University of Alberta

Sodium MRI of the Human Brain: Application to Ischemic Stroke and the Development of Multiple Quantum Filtering

by

Adrian Tsang

A thesis submitted to the Faculty of Graduate Studies and Research
in partial fulfillment of the requirements for the degree of

Doctor of Philosophy

Biomedical Engineering

Fall 2013
Edmonton, Alberta

Abstract

MRI of sodium in the brain is much more challenging compared to hydrogen. However, imaging of brain tissue sodium has been suggested to provide temporal information in acute ischemic stroke that may benefit patients with unknown onset time such as those awake with symptoms. Furthermore, selective imaging of intracellular sodium may provide compartment specific changes early after onset prior to the increase of tissue sodium as demonstrated previously in animal models. Both inversion recovery (IR) and triple-quantum-filtering (TQF) methods have been proposed to probe sodium signal weighted toward intracellular. Unfortunately, signal is greatly reduced (more so for TQF) using compartment specific sodium imaging sequences. Consequently, intracellular-weighted sodium images, especially for TQF, are poor in spatial resolution with low signal-to-noise ratio (SNR).

TQF signal is only ~10% of tissue sodium, or single quantum (SQ), signal in brain. In this thesis, SNR optimization for TQF sodium brain imaging is presented. The strategy of using longer RF pulses with smaller first flip angle and shorter repetition time is shown to improve SNR relative to the ‘standard’ implementation. In addition, inhomogeneous B_0 field causes TQF signal loss. Results are shown to demonstrate that TQF signal loss due to off-resonance in most of the cerebrum is well within 10% and thus implementation of correction methods that incur significant scan time increase is not necessary.

One aspect of potential sodium signal loss, which has mostly been ignored, is caused by sodium interactions in anisotropic ordered environments. Anisotropic sodium signal can be detected using the double-quantum magic angle (DQ-MA) sequence, which is similar to TQF with different flip angle and RF pulse phase cycling. Preliminary results show DQ-MA signals to appear throughout the brain and future studies are required to investigate the distribution of this signal.

Sodium MRI performed in acute stroke patients in this thesis demonstrated that SQ sodium signal was unchanged in the ‘at-risk’ tissue but increased in the lesion core. However, the increase was not correlated with perfusion deficits. Additionally, IR sodium signal showed greater increase than SQ signal within the first fourteen hours after onset suggesting IR signal to reflect intracellular compartment changes.

Acknowledgements

I am extremely grateful to have the opportunity to learn about MRI under the supervision and guidance of a brilliant scientist, Dr. Christian Beaulieu – thank you so much! I also want to express my gratitude to my co-supervisor, a distinguished clinical scientist – Dr. Ken Butcher. Thank you for getting me started on my first research project and manuscript. Thank you also for all the time spent in supervising patient scans.

I also want to thank Dr. Alan Wilman and Dr. Richard Thompson who had taught me the course on MRI (BME 564).

I am also fortunate to have a great mentor, Dr. Rob Stobbe, who has developed all the sodium software tools (described in Appendix 1) used in this thesis. I greatly appreciate for all your efforts in editing my conference abstracts and manuscripts.

I want to express my sincere thanks to Maisie Goh and Catherine Leung for dealing with scholarship applications and making sure that I get paid on time.

Thank you Karim Damji, Peter Seres, and Carol Hartle for maintaining the MRI centre and to keep the MRI scanners operational, debugging problems when things go wrong (which seemed to always happen when I am about to scan volunteers).

It is my pleasure to have worked with all the colleagues (present and past) in the department and I enjoyed the great friendship developed through the last few years: Dr. Rebecca Feldman, Hongfu Sun, Kelvin Chow, Dr. June Cheng-Baron, Corey Baron, Min Liu, Hazlin Zaini, Yushan Huang, Nasir Uddin, Dr. John Chen, Dr. Myrlene Gee, Sarah Treit, Dr. Andrew Walsh, Kelly McPhee, Russell Lagore, Drs. Marc and Catherine Lebel, and Dr. Yusuf Bhagat. I also enjoyed the company of great officemates: Dr. Jacob Ellegood, Ander Watts, and Dr. Dongming Zhou.

I would like to acknowledge the funding sources for the projects carried out in this thesis: an operating grant from the Heart and Stroke Foundation of Alberta, Northwest Territories, and Nunavut as well as scholarship award from the Natural Sciences and Engineering Research Council (NSERC).

Lastly, I am also thankful for the support of my parents and in-laws, siblings, and especially my wife who is willing to come with me to Edmonton. We enjoyed all the moments with wonderful friends we met in the last six years. Thank you for all the prayers and encouragement through all these times. Thank you to our heavenly Father and Lord Savior Jesus Christ by putting so many wonderful people around me!

Table of Contents

List of Tables

List of Figures

List of Abbreviations and Symbols

ADC	Apparent Diffusion Coefficient
ATP	Adenosine Triphosphate
B_0	Main static magnetic field
BBB	Blood Brain Barrier
CBF	Cerebral Blood Flow
CBV	Cerebral Blood Volume
$CMRO_2$	Cerebral Metabolic Rate of Oxygen
CPP	Cerebral Perfusion Pressure
CVF	Cell Volume Fraction
CSF	Cerebrospinal Fluid
δ	Evolution time of the MQF sequence
DQF	Double-Quantum-Filter
DQ-MA	Double-Quantum Magic Angle
DWI	Diffusion Weighted Imaging
ECC	Extra-Cellular sodium Concentration
EFG	Electric Field Gradient
FDA	Food and Drug Administration
FLAIR	Fluid Attenuation Inversion Recovery
FOV	Field of View
G/cm	Gauss/centimeter
GM	Gray Matter
γ	Gyromagnetic ratio
$\hbar$	Plank’s constant
I	Nuclear spin angular momentum
ICC	Intra-Cellular sodium Concentration
IR	Inversion Recovery
IV	Intra-venous
k	Boltzmann’s constant

k_{max}	Maximum extent of k-space sampled (1/m)
μ	Magnetic moment
mM	Millimolar
M_0	Equilibrium magnetization
M_{xy}	Transverse magnetization
M_z	Longitudinal magnetization
MCA	Middle Cerebral Artery
MQF	Multiple-Quantum-Filter
Na-PASS	Sodium Projection Acquisition in the Steady-State
NIHSS	National Institutes of Health Stroke Scale
NMR	Nuclear Magnetic Resonance
OEF	Oxygen Extraction Fraction
p	Twist parameter
PWI	Perfusion Weighted Imaging
rCBF	Regional Cerebral Blood Flow
rCBV	Regional Cerebal Blood Volume
r-tPA	Recombinant Tissue Plasminogen Activator
RF	Radiofrequency
ROI	Region of Interest
SAR	Specific Absorption Rate
SIRFLA	Soft Inversion Recovery Fluid Attenuation
SNR	Signal-to-Noise Ratio
SQ	Single Quantum
τ	preparation time of the MQF sequence
T	Tesla
T_1	Longitudinal (spin-lattice) relaxation
T_2	Transverse (spin-spin) relaxation
T_{max}	Time to peak on deconvolved curve
TE	Echo Time
TR	Repetition Time
TPI	Twisted Projection Imaging

TSC	Tissue Sodium Concentration
TQF	Triple-Quantum-Filter
WM	White Matter
ω_o	Larmor frequency
ω_{off}	Off-resonance frequency
ϖ_Q	Residual time averaged quadrupolar interaction frequency

Chapter 1

Introduction and Background

1.1. Thesis Introduction

Sodium ions (Na^+) along with other elements such as potassium (K^+) and calcium (Ca^{2+}) are tightly regulated in the nervous system under normal cellular metabolism. The distribution of sodium and potassium ions across cell membrane plays a pivotal role to generate a resting membrane potential at approximately -70 mV (i.e. more negative inside the cell). Under normal homeostatic conditions, the concentration of Na^+ is 15 mM and 150 mM and that of K^+ is 150 mM and 5 mM in the intracellular and extracellular compartments, respectively. The maintenance of these ionic concentration gradients is essential to permit propagation of action potentials along the nerve fibers. The distribution of ions is maintained through an active transport mechanism, based on an energy dependent Na^+/K^+-ATPase, which pumps three Na^+ out of the cell for every two K^+ entering at the expense of one ATP molecule (Vander et al., 2001).

Under pathological conditions such as cerebral ischemia, blood flow is restricted leading to hypoxia, uncoupling of the oxidative phosphorylation chain and arrest of ATP production, resulting in ion pump failure. The concentration gradient collapses and sodium ions redistribute along with water, which follows the osmotic gradient created by cation influx into the intracellular space. Thus, a gradual elevation of tissue sodium concentration (TSC) develops. TSC is a volume-fraction weighted mean of intra- and extracellular sodium concentration (ICC and ECC) determined with interstitial volume of the brain ~0.2 and cell volume fraction (CVF) ~0.8 as (Thulborn et al., 2009)

$$\mathrm{TSC} = \mathrm{ICC} \cdot \mathrm{CVF} + (1 - \mathrm{CVF}) \cdot \mathrm{ECC} \quad . \qquad \text{Eq. 1-1}$$

It is desirable to non-invasively detect changes of TSC or more compartment specific sodium from intracellular space as a marker of compromised ionic homeostasis using an imaging modality such as magnetic resonance imaging (MRI). MRI is used presently in routine clinical diagnosis for various diseases. The strength of the magnetic field in clinical scanners ranges from 1.5 to 3 Tesla (T) and techniques based on the imaging hydrogen nuclei produce images with excellent spatial resolution and tissue contrast.

Despite the fact that sodium is the second most biological sensitive element detectable using NMR, imaging of this element is challenging. This is due to its smaller gyromagnetic ratio and much lower concentration in vivo compared to hydrogen (protons). MRI of sodium yields inferior image quality and requires longer scan time than proton MRI. Therefore, sodium imaging has not been applied clinically. These problems can be improved by imaging at a higher magnetic field strength because of the linear relationship between the main field strength with MR signal. Recently, there have been reports of in-vivo sodium human brain imaging studies using 7 T (Fleysher et al., 2009) and 9.4 T scanners (Atkinson et al., 2007). There is continued enthusiasm for research exploring sodium imaging in various diseases such as tumors (Ouwerkerk et al., 2003; Thulborn et al., 1999a; Thulborn, et al., 2009), Alzheimer's disease (Mellon et al., 2009), multiple sclerosis (Inglese et al., 2010), osteoarthritis (Reddy et al., 1998), and cerebral ischemia (Hussain et al., 2009; Shimizu et al., 1993; Thulborn et al., 1999b). Sodium MRI may one day be incorporated into standard diagnostic workup, as clinical scanners migrate to higher field strengths. During the course of this thesis, all sodium imaging experiments were performed using a moderately high field strength of 4.7 T.

As MRI of sodium is different from proton, it is helpful to provide a brief description here of the pulse sequences as well as the sodium NMR signal behavior for those who are not familiar with sodium imaging. A more detailed description of sodium MRI is presented in section 1.4. The sodium nucleus has a spin angular momentum of 3/2, which is associated with 4 allowed energy states and 3 transitions between adjacent states. The sodium signal decays much more rapidly than proton after RF excitation where the transverse T_2 relaxation is also influenced by the sodium interaction with charged molecules. In fluid environments where this interaction is extremely rapid such as in saline or cerebrospinal fluid, the sodium signal decays following a single exponential at a rate described by one T_2 relaxation parameter. However, in environment where the interaction is slow such as in agar gel or expected in brain tissue, the sodium signal decays following two exponentials with two T_2 relaxation parameters. The short (or fast) component of T_2 (T_{2f}) accounts for 60% of the signal and the long (or slow) component of T_2 accounts for the remaining 40%. Sodium signal relaxation with T_{2f} originates with the two outer energy state transitions and T_{2s} from the central state transition. It is important to note that the source of biexponential T_2 sodium signal relaxation is not from two different pools of sodium but from the energy state transitions. In brain tissue, T_{2f} of sodium is extremely rapid (~1-2 ms) and thus pulse sequence with extremely short TE is required to minimize signal loss. Brain tissue sodium, or commonly referred to as single quantum (SQ), image is acquired using a single RF excitation pulse sequence. The sequence is typically implemented with a short non-selective (rectangular) RF pulse and rapid k-space acquisition that starts from the centre of k-space such as twisted projection imaging (TPI).

One method to selectively acquire sodium signal weighted toward intracellular compartment uses a pulse sequence known as triple-quantum filter (TQF) (Jaccard et al., 1986). This imaging method is even more challenging as the TQF signal is only a small fraction of bulk tissue sodium, or single-quantum (SQ), signal resulting in longer scan time and images with poor resolution and low signal-to-noise ratio (SNR). At the time of this thesis preparation, there are only two published journal articles (Fleysher et al., 2012; Hancu et al., 1999) of in vivo TQF sodium brain imaging. A strategy to optimize SNR for in vivo TQF brain imaging at 4.7 T under the constraint of specific absorption rate (SAR) is presented in **Chapter 2**.

Inhomogeneous B_0 static magnetic field can cause detrimental TQF signal loss due to off-resonance. Thus severe signal dropout artifacts may be present in TQF sodium brain images if the problem is not mitigated. Three correction algorithms were proposed previously and demonstrated in agar gel phantoms (Fleysher et al., 2010b; Matthies et al., 2010; Tanase et al., 2005), but the contribution of B_0 inhomogeneity to TQF signal loss is unknown in humans. The downside of implementing these strategies is either doubling or quadrupling of scan time, which is not feasible if TQF sodium imaging is to be used clinically. In addition, the correction algorithms do not offer improvement in SNR as expected for increased scan time. Implementation of two algorithms that incur doubling in scan time to evaluate the necessity of B_0 correction in TQF sodium brain imaging is presented in **Chapter 3.**

Sodium ions diffuse and interact with negatively charged macromolecules in biological tissue. The fluctuating electric field gradients at the nuclei affect the relaxation characteristics of sodium magnetization. In addition, the orientation and order of these interactions cause the sodium NMR spectrum to split and result in non-zero (residual) time averaged quadrupolar interaction frequency ϖ_Q. The classification of sodium NMR spectra shapes influenced by quadrupolar interactions is described in section 1.4.1. In macroscopic ordered environments such as in liquid crystals where residual ϖ_Q exists, sodium nuclei quantum state energy levels are shifted, leading to the spectrum with one central peak and two satellites. The spectrum splitting may result in a portion of sodium NMR signal being undetected when soft or narrow bandwidth RF excitation pulses are implemented (Joseph et al., 1987). Although biological environments are not expected to be macroscopically ordered, but there is evidence to show that residual quadrupolar interactions do exist in human skeletal muscle and brain (Reddy et al., 1995). Residual quadrupolar interactions can be selectively detected using a double-quantum filter (DQF) sequence implemented with a judicious choice of RF flip angle (Eliav et al., 1992). This special implementation is known as a double-quantum magic angle (DQ-MA) sequence. **Chapter 4** describes the work undertaken in this thesis to implement the DQ-MA sequence to visualize distribution of residual ϖ_Q in the brain.

Sodium imaging was performed at the University of Alberta Hospital (UAH) on ischemic stroke patients scanned within the first week after symptom onset. A paper (Hussain, et al., 2009) demonstrated progressive elevation of relative SQ sodium signal intensity within the water diffusion restricted lesion (core) to contralateral hemisphere with respect to symptom onset time. However, SQ sodium signal change within the potentially salvageable tissue (i.e. perfusion-diffusion mismatch region or the penumbra) is unknown. Consequently a study was carried out in this thesis, and described in **Chapter 5**, to explore relative SQ sodium signal intensity evolution in the core and penumbra with respect to time after symptom onset. In addition, relative SQ sodium signal change is tested for correlation with perfusion deficits in the ischemic core, as defined by hemodynamic parameters of cerebral blood flow and volume (CBF and CBV, respectively). Stroke patients recruited were brought to the imaging facility (Peter S. Allen MR Research Centre) to be scanned using two MRI field strength scanners. First, patients undergo a 1.5 T MRI scan with clinically available proton sequences such as diffusion- and perfusion-weighted imaging (DWI and PWI) that permit the identification of infarct core and ‘at-risk’ (penumbra) tissue regions. Second, patients with sizeable DWI lesion (core) were transferred to the adjacent 4.7 T MRI scanner for sodium imaging. Sodium images were acquired using the sodium projection acquisition in steady-state (Na-PASS) sequence that has been optimized for SNR at 4.7 T (Stobbe et al., 2008b). In addition, some patients were also imaged using inversion recovery and multiple-quantum-filtering sequences (describe in section 1.4) that are supposed to weight sodium signal toward intracellular compartment. The total time of imaging is within 1 hour for each subject. It should be pointed out that all patients eligible for thrombolysis received treatment prior to imaging. Currently, the treatment window opportunity is within 4.5 hours after the onset of symptom (Hacke et al., 2008). Therefore, scan duration of 1 hour is not feasible to be used in clinical stroke diagnosis.

Measurement of compartment specific sodium signal increase in the lesion core over contralateral region may demonstrate greater changes than SQ sodium signal. This phenomenon occurs early after the onset of ischemia when sodium ions are shifted into the intracellular space but TSC remains unchanged. Intracellular-weighted sodium signal may be acquired using a soft inversion recovery fluid attenuation (SIRFLA) sequence that has been optimized for SNR at 4.7 T (Stobbe et al., 2005). **Chapter 6** presents a retrospective study to compare relative SIRFLA and SQ Na-PASS signal changes in patients.

1.2. Stroke

1.2.1. Basics of stroke

Stroke is a devastating neurological disease defined by the World Health Organization as '*a syndrome of rapidly developing clinical signs of focal (or global in the case of coma) disturbance of cerebral function lasting more than 24 hours or leading to death with no apparent cause other than a vascular origin*' (Hatano, 1976). It is the third leading cause of death and the most frequent cause of adult disability in North America. Stroke affects 300,000 people annually in Canada (Canada, 2011) and 6.8 million in the United States (Go et al., 2013). In Canada alone, stroke morbidity costs the health care system an estimated $3.6 billion each year (Canada, 2011). Stroke can be broadly classified as either hemorrhagic or ischemic, where the former results from intracranial blood vessel rupture, and the latter results from vessel occlusion that interrupts blood flow. Hemorrhagic stroke, which accounts for 15-20% of all strokes, can be further divided based on location of bleed into intracerebral (often caused by hypertension and occurs generally in small arteries or arterioles) or subarachnoid (bleeding on the surface of the brain often due to rupture of developmental aneurysms). Ischemic stroke, which accounts for 80-85% of all strokes, can be classified by mechanism, as either embolic or thrombotic. Embolic stroke occurs when a blood clot (thrombus) travels through the bloodstream to the brain (embolization), eventually occluding the lumen of an artery supplying brain tissue. The source of emboli can be more proximal arteries, following rupture of an atherosclerotic plaque, or the heart, most often in patients suffering from atrial fibrillation. Thrombotic stroke (clinically referred to as cerebral thrombosis or cerebral infarction) occurs when a blood clot (thrombus) forms in situ, in areas damaged by atherosclerosis. Cerebral thrombosis can be further divided into additional two categories that correlate to the location of the blockage within the brain: large-vessel thrombosis (blockage in one of larger blood supplying arteries such as the carotid or middle cerebral) resulting in cortical infarction and small-vessel thrombosis (deeper penetrating arteries) also referred to as lacunar stroke resulting in subcortical infarction (Hennerici et al., 2005). All ischemic stroke patients recruited in this thesis as described in **Chapters 5** and **6** had large cortical infarction.

1.2.2. Stroke Pathophysiology and Treatment

The brain relies on continuous flow of blood to carry oxygen and glucose to meet its metabolic requirements. Regional cerebral blood flow (rCBF) refers to the volume of blood flowing to a portion of the brain per unit time, which is dependent on collateral flow and microcirculatory changes. In healthy individuals, rCBF is maintained at approximately 50-80 mL/100 g/min in normal gray matter (GM) and 22 mL/100 g/min in white matter (WM). Autoregulation maintains CBF via vasodilatation or constriction of precapillary vessels in response to changes in cerebral perfusion pressure (CPP – typically equal to mean arterial blood pressure). Autoregulation may temporarily protect ischemic tissue following arterial occlusion as shown in Figure 1-1.

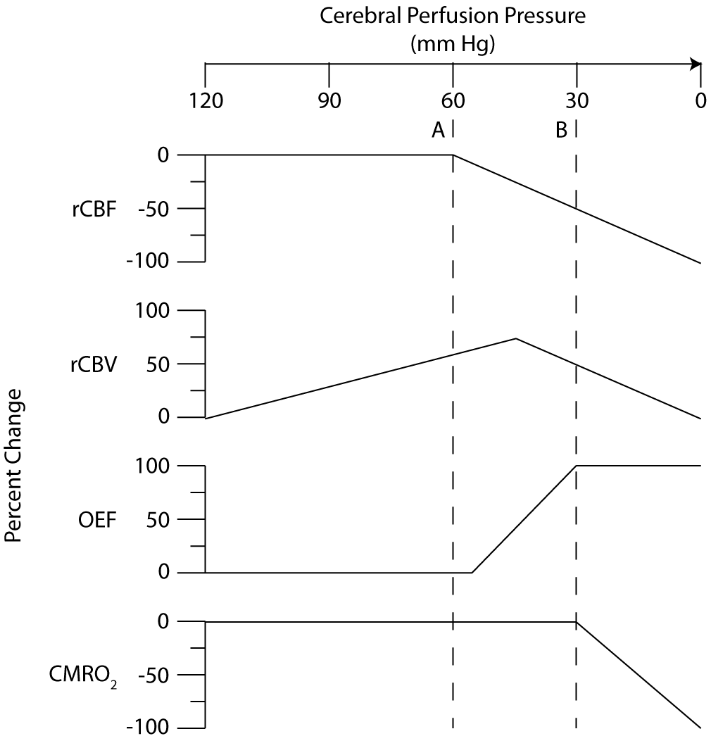

Figure 1-1: Percent change of hemodynamic parameters as a compensatory response to decrease of CPP adapted from Figure 2-1 and Fig.1 in Ahmed et al. and Powers et al. respectively (Ahmed et al., 2001; Powers, 1991). rCBF remains constant during the initial decline of CPP while regional cerebral blood volume (rCBV) increases due to vasodilatation. rCBF begins to decline when autoregulation mechanism fails (A) shortly before the maximal vasodilatation is reached as CPP further decreases, at this point rCBV reverses as vessels collapse. During this time oxygen extraction fraction (OEF) increases to maintain cerebral metabolic rate of oxygen ($CMRO_2$). When OEF change is maximized and cannot sustain aerobic metabolism (B), $CMRO_2$ begins to fall together with decrease of both rCBF and rCBV.

As CPP continues to decline during cerebral ischemia beyond the point when compensatory vasodilatation has reached its maximum, rCBF is progressively reduced and the pathophysiologic events due to the ischemia can be studied in relation to rCBF thresholds (Figure 1-2). Oligemia occurs when rCBF is reduced to between 35 and 45 ml/100 g/min with concomitant elevation of oxygen extraction fraction (OEF) to maintain a normal cerebral metabolic rate of oxygen ($CMRO_2$). At lower rCBF thresholds (20-35 ml/100 g/min), tissue metabolic demands exceed the maximum available oxygen supply (i.e. OEF is at maximum) resulting in $CMRO_2$ decrease. In this mild ischemic state, tissue lactate is increased due to anaerobic glycolysis. This form of glycolysis can maintain energy production of adenosine triphosphate (ATP) in the absence of oxygen and temporarily support tissue function. Very low rCBF thresholds (<20 mL/100 g/min) result in electrical failure, OEF remains maximally elevated and $CMRO_2$ is further reduced. At this threshold the electroencephalogram (EEG) is flat and neurologic deficits are observed. Excitatory amino acids (glutamate and aspartate) are released into the extracellular space, which induce intracellular Ca^{2+} influx in channels associated to glutamate receptor N-methyl-D-aspartate (NMDA). Tissue in a state of electrical failure but with sustained energy metabolism and structural integrity is referred to as penumbral. The ischemic penumbra is potentially salvageable, if reperfusion occurs in a reasonable time frame. (Astrup et al., 1981)

Tissue with rCBF below the threshold of about 10 – 12 ml/100 g/min forms the ischemic core with complete deterioration of transmembrane ionic gradients (indicated as 'Severe' ischemia in Figure 1-2). In this region, there is a marked increase in extracellular K^+ and decrease in both extracellular Na^+ and Ca^{2+} indicating failure of energy-dependent membrane pumps and transport systems (e.g. Na^+/K^+-ATPase, Ca^{2+}-ATPase and the Na^+-Ca^{2+} antiporter) as illustrated in Figure 1-3. Increased extracellular K^+ (and concomitant increased intracellular Na^+ indicative of cytotoxic edema) results in rapid anoxic depolarization and can lead to irreversible cellular injury by: 1) depolarizing neighboring neurons, which may provide a trigger for electrical spreading the injury beyond region of severe ischemia; 2) promoting vascular permeability of sodium, which allow the movement of Na^+ and water into interstitial space leading to cytotoxic edema; 3) promoting vasoconstriction, which further restricts residual blood flow; 4) increasing intracellular Ca^{2+}, which is related to cell necrosis by way of irreversible damage to cell membranes, mitochondria, and enzymes. Cytotoxic edema develops within minutes after the onset of ischemia. Vasogenic edema, where permeability of the blood–brain barrier (BBB) is increased allowing fluid and protein in plasma to accumulate in extracellular space, may also develop in some cases of ischemic stroke. (Ahmed, et al., 2001; Betz et al., 1994; Klatzo, 1987)

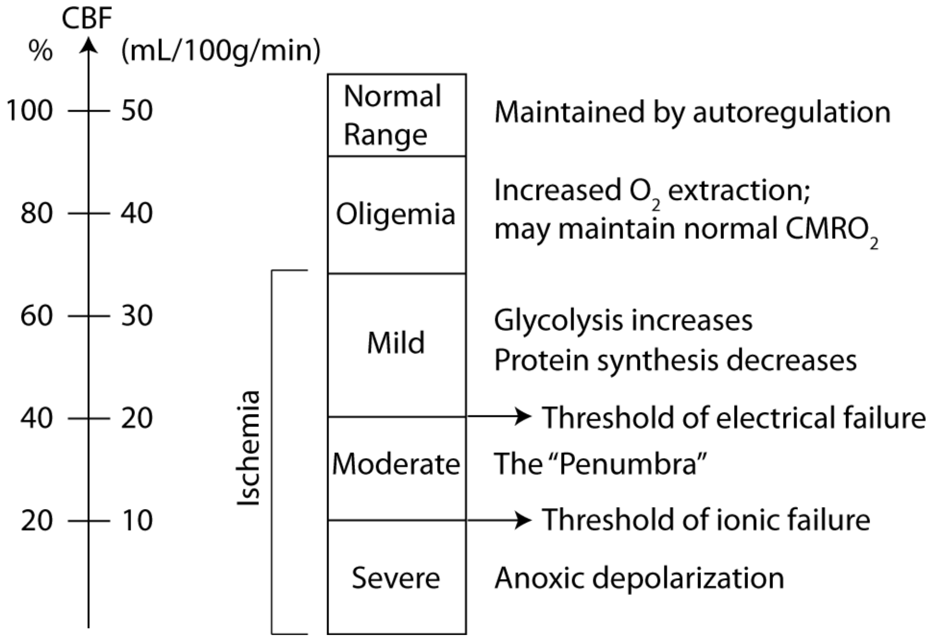

Figure 1-2: rCBF thresholds that correspond to severity of ischemic brain injury adapted from (Ahmed, et al., 2001)

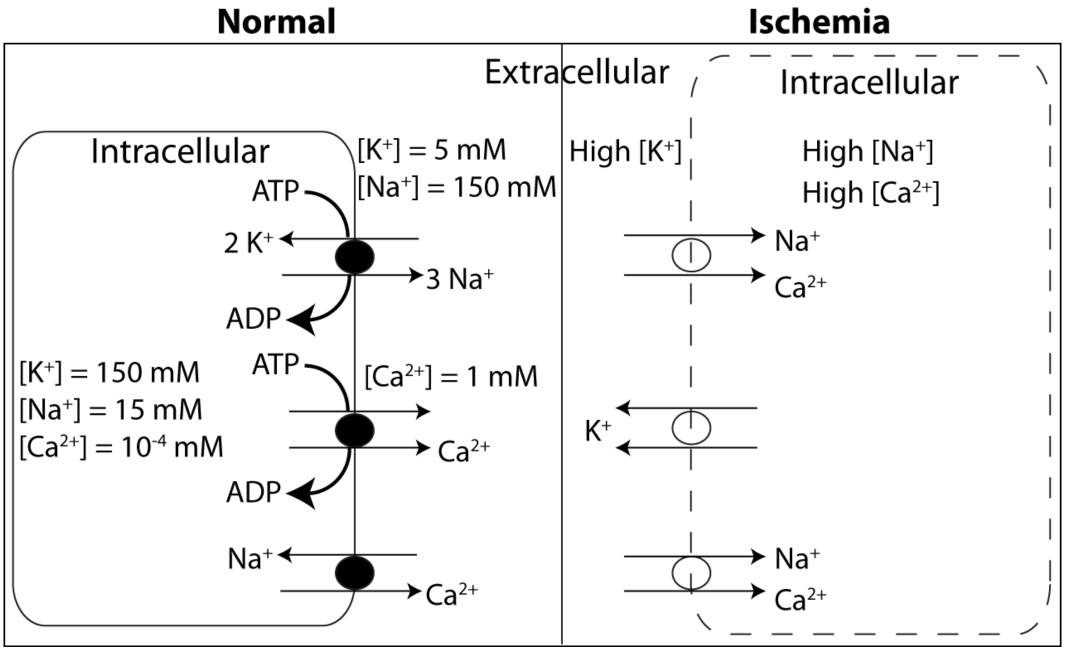

Figure 1-3: (Left) Under normal cellular metabolism, Na^+, K^+, and Ca^{2+} ions concentrations between the intra- and extracellular space are maintained by active transport mechanism using the Na^+/K^+-ATPase and Ca^{2+}-ATPase. Ca^{2+} ions also move out the cell via the Na^+-Ca^{2+} antiporter. (Right) Under cerebral ischemia, the ion pumps fail due to the lack of ATP supply resulting in Na^+ and Ca^{2+} concentrations to increase inside the cell while the K^+ concentration increases outside. The ions redistribute into the cell along with water causing cell swelling (cytotoxic edema).

Currently, recombinant tissue plasminogen activator (alteplase) is the only Food and Drug Administration (FDA) and Health Canada approved thrombolytic therapy to restore blood flow in acute ischemic stroke patients. This approval in 1996 was based on a trial conducted by *The National Institute of Neurological Disorders and Stroke rt-PA Stroke Study Group* which demonstrated improved clinical outcome at three months in patients administered with rt-PA within three hours of onset despite increased incidence of intracerebral hemorrhage (The National Institute of Neurological Disorders and Stroke rt-PA Stroke Study Group, 1995). Subsequent clinical trials demonstrated evidence to extend the narrow therapeutic window beyond 3 hours. The European Cooperative Acute Stroke Study (ECASS III) showed significant improved clinical outcome in patients when intravenous alteplase is administered between 3 and 4.5 hours after symptom onset (Hacke, et al., 2008). The American Heart/Stroke Association has recently published a recommendation to extend the treatment to 4.5 hours after onset (del Zoppo et al., 2009). Despite the efficacy of alteplase to recanalize the occluded vessel, only about 3.4 – 5.2% of ischemic stroke patients are treated with rt-PA in the United States in 2009 (Adeoye et al., 2011). It has been suggested that more patients could benefit from rt-PA treatment in some stroke centers by reducing delays to diagnosis and increasing the availability of neurologists with expertise in stroke treatment (Cocho et al., 2005). Currently, the decision to proceed with treatment is based on clinical presentation, symptom duration, and negative findings on non-contrast computed tomography (CT) to rule out hemorrhage. However, advances in neuroimaging techniques, by using either CT or MRI, to identify the ischemic penumbra may allow treatment decisions to be made based on pathophysiology (or tissue window), rather than the current standard of symptom duration (or temporal window) (Gonzalez, 2006). Two clinical trials, DEFUSE (Albers et al., 2006) and EPITHET (Davis et al., 2008), were performed using MRI to evaluate treatment response from alteplase administered within 3-6 hours after onset and demonstrated a significant correlation of favourable outcome in patients to substantial penumbral tissue, defined as mismatch between abnormalities on diffusion- and perfusion-weighted images. Perfusion-diffusion mismatch is a commonly used definition of ischemic stroke penumbra, which will be discussed further in section 1.3.4. These results suggest that imaging of the penumbra may permit the selection of patients for reperfusion therapy beyond the currently accepted treatment window. However, treatment beyond 4.5 hours is still only limited to clinical trials (Goldemund et al., 2010).

1.3. Magnetic Resonance Imaging

1.3.1. Magnetic Resonance Imaging Principles

Magnetic resonance imaging (MRI) is a non-invasive imaging modality. It does not use ionizing radiation as in CT and permits multiple contrast mechanisms over an arbitrary imaging plane that can be tailored to allow easier detection of tissues affected by pathologic conditions. There are numerous texts that offer excellent description of the principles of nuclear magnetic resonance (NMR) (e.g. (Brown et al., 2003; Nishimura, 2010)), and only a brief description is presented here. The net magnetic moment (μ) of a nucleus is a fundamental property determined by the protons and neutrons of an atom. This moment can be non-zero if either or both of the number of nucleon type is odd. The nucleus of a 'magnetically visible' element has a characteristic known as spin angular momentum, or simply spin, which is denoted as ***I***. ***I*** can take on values in the range from 1/2 to 9/2 measured in units of $\hbar = h/2\pi$ (h = Planck's constant = $6.63\text{x}10^{-34}$ J s). The ratio of the magnetic (or dipole) moment (μ) and spin angular momentum (***I***) give rise to the gyromagnetic ratio (γ)

$$\gamma = \frac{\mu}{I\hbar}. \qquad \text{Eq. 1-2}$$

The value of γ is unique to each element isotope.

Hydrogen (^{1}H) is the most abundant naturally occurring isotope in human, which is present in both water and fat molecules. ^{1}H is, by far, the most NMR-sensitive element in vivo as shown in Table 1-1. Imaging of ^{1}H using NMR in human (proton MRI) constitutes the majority of research in the field and the basis of all clinical MRI sequences at present. Sodium (^{23}Na) is the second most NMR sensitive nucleus to be observed in biological environment after ^{1}H, but it appears after phosphorus (^{31}P) in Table 1-1. The reason for this was that the signal of ^{31}P normally disperses into multiple resonances (Springer, 1987), and hence the signal detected in vivo is lower than ^{23}Na. The ^{31}P NMR signal could be associated with different macromolecules (e.g. phosphocreatine, adenosine triphosphate, etc.) that have different resonance frequencies.

Table 1-1: Biologically interesting and magnetically visible elements

Element	*I*	Larmor frequency at 1.0T (MHz) [a]	γ (radians *$T^{-1}s^{-1}$) [a]	Natural isotopic abundance (%) [b]	Normalized NMR receptivity [b]	Concentration in human body (mM) [b]	Normalized BIONMR receptivity [b]
^{1}H	1/2	42.5775	267.5	100.0	100	99.9 x 10^{3}	100
^{31}P	1/2	17.2515	108.4	100.0	6.65	387	25.74 x 10^{-3}
^{23}Na	3/2	11.2688	70.8	100.0	9.27	44	4.08 x 10^{-3}
^{13}C	1/2	10.7084	67.3	1.1	0.18 x 10^{-1}	15.0 x 10^{3}	2.70 x 10^{-3}
^{14}N	1	3.0777	19.3	99.6	0.1	2.3 x 10^{3}	2.10 x 10^{-3}
^{17}O	5/2	5.7742	36.3	0.037	0.11 x 10^{-2}	40.6 x 10^{3}	0.45 x 10^{-3}
^{35}Cl	3/2	4.1765	26.2	75.5	3.56 x 10^{-1}	56	0.20 x 10^{-3}
^{39}K	3/2	1.9893	12.5	93.1	0.48 x 10^{-1}	47	0.23 x 10^{-4}
^{25}Mg	5/2	2.6083	16.4	10.13	2.72 x 10^{-2}	21	5.71 x 10^{-6}
^{43}Ca	7/2	2.8697	18.0	0.145	8.67 x 10^{-4}	374	3.24 x 10^{-6}

[a] Larmor frequency values obtained from ("CRC Handbook of Chemistry and Physics," 2011) and multiplication by 2π yields gyromagnetic ratio (γ)

[b] data taken from Table 1 in (Springer, 1987). NMR receptivity measures sensitivity of NMR signal as a percentage of ^{1}H; BIONMR receptivity is calculated by multiplying NMR receptivity of the element and its concentration in human, which is also expressed as a percentage of ^{1}H.

In the presence of a strong magnetic field (B_0), a number of nuclear magnetic moments (μ), or simply spins, in the sample being imaged are oriented either parallel or anti-parallel to the direction of the field (z). The number of spins in each orientation is determined by a temperature-dependent Boltzmann distribution as

$$\frac{n_{\uparrow}}{n_{\downarrow}} = \exp\{-E_z / kT\}. \qquad \text{Eq. 1-3}$$

In Eq. 1-3, k is the Boltzmann constant (1.38x10^{-23} J K^{-1}), *T* is temperature in Kelvin, and E_z is the energy difference between the two orientations (i.e. Zeeman energy). The number of spins aligned parallel with B_0 ($n_{\downarrow}$) occupy a lower energy state relative to the anti-parallel ($n_{\uparrow}$) configuration. Typically, the ratio is very close to unity (0.999993) implying that there are very few (only 7 out of 10^{6})

excess spins in the parallel orientation (Nishimura, 2010). The summation of all μ in the sample produces a net equilibrium magnetization, M_0, in the direction of B_0 that contributes to a detectable signal. The magnetization M_0 is calculated as

$$M_0 = N\gamma^2\hbar^2 I(I+1)B_0/3kT \quad , \qquad \text{Eq. 1-4}$$

where N is the number of spins in the sample.

MRI is not a very sensitive approach, but the abundance of hydrogen (^{1}H) in the body is large enough to permit proton images to be created with excellent spatial resolution. However, sensitivity becomes an issue for ^{23}Na imaging. Despite being the second most biological sensitive element visible using MRI, the ratio of sodium magnetization signal over hydrogen is only 35% when one substitutes γ and $\boldsymbol{I}$ into Eq. 1-4. This simple calculation assumes all other parameters in the equation as well as species concentration are identical, which is not true. In vivo sodium abundance is much less than that of hydrogen and M_0 is many orders of magnitude smaller. Since M_0 is improved by increasing B_0, a stronger magnetic field in general will result in larger sodium signal.

Energy is related to frequency as

$$E = hv \qquad \text{Eq. 1-5}$$

and also to the transition between the states (the number of states is $2\boldsymbol{I}+1$) as

$$E_z = \Delta E = \gamma\hbar B_0 . \qquad \text{Eq. 1-6}$$

From Eq. 1-5 and Eq. 1-6, an important relationship arises for the nuclear precession frequency known as the Larmor frequency (ω_0). This frequency, unique for each element isotope and proportional to static magnetic field strength, is given by

$$\omega_0 = \gamma B_0 . \qquad \text{Eq. 1-7}$$

To obtain an MR signal, an excitation radiofrequency (RF) pulse is used to rotate the net magnetization onto the x-y (transverse) plane. This results in a signal that can be detected by the receiving RF coil. The process of relaxation returns the nuclear spins back to equilibrium and is characterized by two timing parameters, in both longitudinal and transverse directions known as T_1 and T_2, respectively. The T_1 (spin-lattice) relaxation is the time constant describing the recovery or return to equilibrium of longitudinal magnetization (M_z) due to the interaction of nuclear spins with surrounding environment. The T_2 (spin-spin) relaxation characterizes the decay of transverse magnetization due to spins de-phasing (primarily from dipole-dipole interactions). In addition, T_2^* accounts for static field inhomogeneity, which is another source that causes spins to de-phase. Both relaxation time constants follow an exponential model as

$$M_z(t) = M_0[1 - \exp(-t/T_1)] \qquad \text{Eq. 1-8}$$

and

$$M_{xy}(t) = M_{xy}(0)\exp(-t/T_2^*) \ . \qquad \text{Eq. 1-9}$$

Within an MR pulse sequence, the repetition time (TR) and echo time (TE) parameters are adjusted to create various contrasts that allow the desired delineation of tissue. TR defines the time between repeated RF excitation for a particular slice (2D) or slab (3D) and TE specifies the time between the middle of the RF excitation pulse and acquisition of signal from the centre of k-space where the maximum signal is expected. T_1-weighted images are created with both short TE and short TR. This minimizes signal loss due to spin de-phasing, however, the longitudinal magnetizations of certain tissues with long T_1 do not fully return to equilibrium. Tissues with long T_1 appear dark on the reconstructed magnitude image. T_2-weighted images are created with both long TE and long TR. Tissues with long T_2 appear bright on the reconstructed magnitude image.

Imaging gradients are used for spatial localization of spins within the object in three orthogonal directions (x,y,z). Gradient pulses, measured in mT/m or G/cm (1 G/cm = 10 mT/m), produce relatively small variations to the main magnetic field in a known position dependent pattern. During gradient application, the Larmor frequency is unique at each position along the specified gradient axis. Traditionally, MR signal is acquired in the frequency-encoding (read-out direction) and repeated for all increments of phase encoding steps in an orthogonal direction forming a Cartesian grid in 2D imaging. The signal acquisition can also be repeated for phase encoding steps in a third direction for 3D imaging. The raw data points are collected and then an inverse Fourier transform is applied to create an image. K-space notation is commonly used to describe the trajectories of signal acquisition in a pulse sequence, where k is defined as phase accumulation per distance from the origin in units of radians/meter:

$$k_i = \gamma \int G_i dt \,. \qquad \text{Eq. 1-10}$$

In Eq. 1-10, G is the magnitude of the gradient applied along the i^{th} axis and k is the position in k-space on the i^{th} axis.

The Nyquist requirement specifies that the signal must be sampled at least two times the maximum frequency for accurate image reconstruction. Sampling the MR signal below the Nyquist frequency leads to aliasing artefacts. When frequency-encoding rectangular gradient pulses are used, relationships between the field of view (FOV), dwell time (Δt), or phase encoding step gradient duration (τ), are

$$G = 1/(\gamma \, \mathrm{FOV} \, \Delta t) \qquad \text{Eq. 1-11}$$

and

$$\Delta G = 1/(\gamma \, \mathrm{FOV} \, \tau) \,. \qquad \text{Eq. 1-12}$$

Position in k-space is related to the image FOV and spatial resolution as:

$$\Delta k = 1/FOV \qquad \text{Eq. 1-13}$$

and

$$\Delta x = 1/(2k_{\max}) \,. \qquad \text{Eq. 1-14}$$

1.3.2. Clinical MRI of Ischemic Stroke

The goal of neuroimaging of stroke is to quickly provide clinicians with information that they can use to properly diagnose and guide treatment for a patient. The sequence of clinical events following injury can be summarized as four P's: a) parenchyma, b) pipes, c) perfusion and d) penumbra. (Rowley, 2001) The first 'P', parenchyma status, can be assessed by using T_2^*-weighted gradient-echo (GE) or T_2-weighted fluid-attenuation inversion recovery (FLAIR) (Decoene et al., 1992) sequences, but these methods are less sensitive compared to diffusion-weighted imaging. Currently, computed tomography (CT) is the preferred imaging modality in acute stroke diagnosis to distinguish between ischemia and hemorrhage. Nevertheless, both GE and FLAIR MRI sequences have been reported to permit this differentiation (Mitchell et al., 2001). A GE sequence is sensitive to MR signal loss due to susceptibility effects caused by the paramagnetic deoxyhemoglobin molecules to highlight regions of acute hemorrhage. It has been shown to be sensitive to detect hemorrhage in the hyperacute stage (Patel et al., 1996), and more accurate than CT at the chronic stage of intracerebral hemorrhage (Kidwell et al., 2004). The MR FLAIR sequence can be used to reveal intracranial hemorrhage (Parizel et al., 2001), cytotoxic edema in cortical gyri (which appear hyper-intense during the acute and subacute stages of ischemia, but insensitive as compared to DWI), and also intra-arterial thrombus or slow arterial flow (as a "hyper-intense vessel sign" representing impending infarction) (Makkat et al., 2002). FLAIR signal intensity, measured within the ischemic lesion, has also been shown to rise with time after onset suggesting it is able to differentiate acute from chronic lesions (Aoki et al., 2010; Lansberg et al., 2001).

Time-of-flight (TOF) MR angiography is an established technique used clinically to visualize the second 'P': pipes (vessels). This evaluation is based on contrast between 'strength' of longitudinal magnetization. TOF MR angiography is done using a GE sequence with short TR and small RF excitation angle such that stationary spins in the imaging slice or slab (depending on 2D or 3D) are saturated and spins in fresh blood (flowing into the region) yield high signal. However, as the blood travels through the imaging volume, the signal from the excited spins is reduced due to exposure to multiple RF excitations. In a typical imaging protocol, a three-dimensional TOF MR angiography is performed. The data is processed using maximum intensity projection (MIP). MIP is used to extract the highest pixel signal intensity for a projection through the imaging volume. This technique permits the visualization of blood vessels. (Dumoulin et al., 1989)

The final two ‘Ps’, perfusion and penumbra visualization, can be assessed using diffusion- and perfusion-weighted imaging (DWI and PWI). These two techniques provide insight into ischemic pathophysiology and have already been incorporated clinically for stroke diagnosis protocols. The high sensitivity and specificity of DWI to clearly depict the ischemic lesion (region of suspected infarction) in the hyperacute stage (0-6 hours) is a major breakthrough in stroke imaging because signal changes in conventional sequences, mentioned above, do not reliably detect the injury within the first 8 hours after stroke onset. (Yuh et al., 1991) PWI is able to provide information about blood flow at the capillary level and other metrics to characterize oligemic tissue. Using PWI and DWI, at-risk tissue exhibiting decreased perfusion but has not evolved to irreversible injury may be identified and potentially salvaged with prompt treatment. These advanced techniques are described in more detail in subsequent sections.

1.3.3. Diffusion-Weighted Imaging (DWI)

Diffusion-weighted imaging is a technique that can detect ischemic lesions within minutes of onset, based on imaging random (Brownian) motion of water molecules, with high sensitivity. This technique as applied in ischemia was first demonstrated using surgical arterial occlusion in cats (Moseley et al., 1990) and since then numerous studies have included DWI as part of acute stroke imaging protocol. Measurement of water diffusion was introduced by Stejskal and Tanner in 1965 by using two magnetic field gradients in a spin echo experiment (Stejskal et al., 1965). The DWI sequence, which is based on the Stejskal and Tanner experiment and including imaging gradients, was demonstrated in healthy subjects and patients with neurological disorders by Le Bihan et al. in the mid-1980s (Lebihan et al., 1986). The DWI sequence uses two diffusion-sensitizing gradient pulses of equal strength and duration inserted into a spin-echo (SE) sequence. One gradient pulse is inserted on each side of the refocusing pulse as shown in Figure 1-4. The 'weight' of the applied diffusion gradients (*b*) is related to the gyromagnetic ratio (γ), the gradient strength (G), the time between onset of diffusion gradients (Δ), and the duration of gradient pulse (δ). The parameters are calculated using

$$b = \gamma^2 G^2 \delta^2 (\Delta - \delta / 3) . \qquad \text{Eq. 1-15}$$

The quantity ($\Delta - \delta/3$) is known as diffusion time for rectangular gradients.

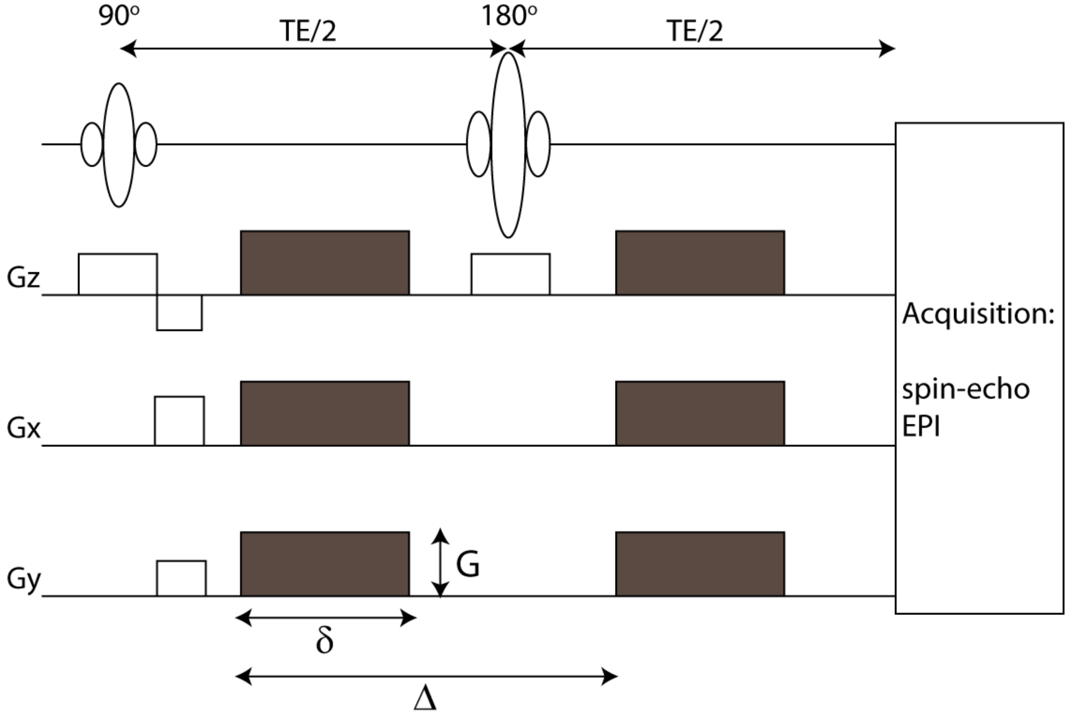

Figure 1-4: A Stejskal-Tanner DWI pulse sequence diagram adapted from (Moritani et al., 2009) with colored area indicating diffusion gradients. The TE is typically ~100 ms and the images are heavily T_2-weighted. The gradients are applied in the desired direction to measure diffusion. For diffusion imaging in three-orthogonal directions, the gradients are applied in x, y, and z separately.

The first diffusion-sensitizing gradient de-phases spins, where the degree of de-phasing is position dependent. The second identical gradient pulse re-phases the spins. Spins that are stationary during the diffusion period (Δ) will be completely re-phased ('refocused') by the second gradient. In contrast, spins in freely diffusible environments, such as cerebrospinal fluid (CSF), move randomly and are not completely re-phased. This movement manifests as signal loss on diffusion-weighted images. The signal intensity on diffusion-weighted images is related to the diffusion sensitivity value *b* and apparent diffusion coefficient (ADC) as

$$S = S_0 \cdot \exp(-b \cdot ADC). \qquad \text{Eq. 1-16}$$

S_o and S are the signal intensities measured with zero and non-zero diffusion weighting, respectively. The ADC coefficient is expressed in units of mm^2/s. This is not the true diffusion because the ADC varies depending on the interactions of water molecules with the geometry of the local environment (e.g. diffusion is hindered in direction perpendicular to fiber tracts). Thus, the diffusion gradients are applied in three orthogonal or more directions (non-collinear and non-coplanar) and then averaged to produce direction bias-free (trace) diffusion-weighted images and ADC maps. A map of ADC for each voxel can be computed by acquiring two sets of images, one without diffusion weighting (i.e. $b = 0$) and the other with a non-zero *b* (typically $b = 1000$ s/mm^2), and using the re-arranged equation from above as (Stejskal, et al., 1965)

$$\ln(S / S_0) = -b \cdot ADC. \qquad \text{Eq. 1-17}$$

The time dependence of signal intensity on DWI images and ADC values have been discussed in review literature to correspond with different stages in ischemic tissue pathophysiology as summarized in Table 1-2 (Abe et al., 2003; Baird et al., 1998; Beauchamp et al., 1999; Roberts et al., 2003). In the hyperacute phase, failure of the Na^+/K^+-ATPase is immediately followed by the accumulation of fluid in the intracellular compartment. This accumulation results in bright region on DWI and dark region on corresponding ADC map. This pattern serves as a marker for bio-energetic compromised tissue. However 'T_2-shine through', a region of increased T_2 that appears bright on DWI but has normal ADC, is an artefact that complicates the evaluation of ischemic stroke using DWI. As ischemia is prolonged further into the acute phase, intravascular fluid enters the extracellular space and results in cytotoxic edema. ADC remains decreased in the acute phase and the ‘light-bulb’ effect is still apparent on DWI images. In the subacute to chronic stage, the ADC appears to pseudo-normalize (i.e. tissue goes on to infarction) initially, then elevates due to cell necrosis. (Garcia et al., 1995)

Table 1-2: Intensity change in ischemic lesion (region of restricted diffusion) on T_2, DWI and ADC map (Baird, et al., 1998).

Stage	**T_2 (b=0)**	**DWI (b=1000 s/mm^2)**	**ADC**
Hyperacute (0-6 hours)	↔	↑	↓
Acute (6-96 hours)	↔/↑	↑	↓
Subacute (4-10 days)	↑	↔ to ↑	↓ / ↔ (pseudo-normalized)
Chronic	↑	↓ to ↑	↑

DWI is increasingly used in the clinical diagnosis of stroke because of its sensitivity to depict the ischemic lesions over other MRI sequences (e.g. FLAIR) in the acute stage (Jauch et al., 2013). In fact, the sensitive and specific of DWI for acute infarct identification is far better than non–contrast-enhanced computed tomography (NECT) (Fiebach et al., 2002).

1.3.4. Perfusion-Weighted Imaging (PWI)

Perfusion, the delivery of blood to capillary bed, is measured in units of mL/100g of tissue/min (units of CBF) (Sorensen et al., 2000). Since the introduction of the penumbra concept in ischemia (Astrup, et al., 1981), there has been great interest in pursuing perfusion imaging (using MRI, CT, or positron emission tomography (PET)) to identify the tissue at risk of proceeding to infarction but which may be salvageable if blood flow is restored. The current treatment criteria limit thrombolysis to patients with a definitive symptom onset time up to 4.5 hours (del Zoppo, et al., 2009). However, studies have demonstrated the existence of viable tissue in the ischemic penumbra up to 17 hours after stroke onset (Furlan et al., 1996; Marchal et al., 1996). This conflict suggests that the identification of tissue with decreased perfusion may be an effective way to select patients for treatment even beyond the narrow time window.

MR perfusion imaging typically utilizes an exogenous tracer (i.e. intravenous injection of a gadolinium-based contrast agent) and a rapid imaging sequence (spin- or gradient-echo echo planar imaging) to follow the passage of the tracer through the brain. This rapid perfusion imaging technique is known as dynamic susceptibility contrast (DSC) imaging (Villringer et al., 1988). This method is used in this thesis to acquire perfusion images of stroke patients and will be discussed in more details in the next section. The three important, and most commonly used, hemodynamic parameters are: regional cerebral blood flow (rCBF), regional cerebral blood volume (rCBV) and mean transit time (MTT – mean transit time of tracer through the tissue). These values are derived from the raw perfusion images based on the central volume theorem (Meier et al., 1954).

Alternatively, MR perfusion can be measured using blood as an endogenous tracer known as arterial spin labelling (ASL). Although ASL is completely non-invasive, it is limited by the small amount of fresh blood delivery to a tissue volume (typically ~1 percent) within the imaging time that results in low signal-to-noise ratio (SNR). In ASL, the proton spins in blood are inverted, or saturated, prior to their entry into the imaging slice of interest. Cerebral blood flow is calculated from the magnetization difference between two acquired images. The first image is ‘tagged’ image acquired after a delay (typically of 1 second) to allow ‘tagged’ blood to be delivered in the tissue volume of interest. The second ‘control’ image is acquired without tagged spins. (Liu et al., 2007)

An operational definition of the penumbra was initially assessed by Schlaug et al. based on the mismatch between the perfusion deficit region and the ischemic core depicted by DWI (Schlaug et al., 1999). Although this definition has been used in subsequent studies to delineate the penumbra, there has been no consensus on the optimal hemodynamic parameter, or optimal threshold, to best highlight the penumbral tissue and exclude benign oligemic tissue (Butcher et al., 2010; Butcher et al., 2005).

1.3.4.1. Dynamic Susceptibility Contrast (bolus tracking)

Perfusion MRI by dynamic susceptibility contrast is done by tracking the first pass of gadolinium-based contrast agent bolus through the capillaries. The gadolinium (Gd) produces transient signal loss due to susceptibility effects. Gd (a toxic paramagnetic element) contrast agent is manufactured by chelating with a large organic molecule such as diethylenetriamine penta-acetic acid (Gd-DTPA) to produce a construct that can be safely used for in vivo imaging purpose (FDA; Weinmann et al., 1984). The concentrated Gd-based contrast agent (typically 0.5 molar) causes shortening of T_1 (enhance signal on T_1-weighted images). However, it is the T_2^* effect that is used to derive the interested hemodynamic parameters in DSC.

Tracking of the bolus requires a rapid imaging pulse sequence capable of repeatedly acquiring T_2^*-weighted images such that the Gd within each tissue voxel can be sampled with adequate temporal resolution, typically every 1-2 seconds. It is typical in DSC perfusion imaging to use a TR of ~1 second because a short TR enhances T_1 weighting and dominates the T_2 effects. A TR value of 1 second also allows adequate time for multi-slice coverage.

Postprocessing of the raw perfusion images is done in offline software package (in this thesis, the Matlab (MathWorks, Natwick, MA) based software package PGUI developed by the Center of Functionally Integrative Neuroscience group from Aarhus University is used). This software displays the perfusion images in a time series which can show signal intensities change with the arrival, and departure, of the bolus of a particular brain slice (signal intensity time curve). This software is also used to compute hemodynamic parameters for each brain voxel. A graph of ΔR_2^* (or ΔR_2 if spin-echo is used) versus time is obtained based on an equation relating the signal intensity to the exponential transverse relaxation rate of change as (Wu et al., 2005)

$$S(t) = S(t_0)\exp(-TE \cdot \Delta R_2^*(t)), \qquad \text{Eq. 1-18}$$

where $S(t_0)$ is the baseline signal intensity. Eq. 1-18 assumes the effect on T_1 relaxation is negligible, as the blood-brain-barrier is largely intact in the hyperacute phase of most stroke patients. The expression can be rearranged such that

$$\Delta R_2^*(t) = \frac{-\ln(S(t)/S(t_0))}{TE}. \qquad \text{Eq. 1-19}$$

If a linear relationship is assumed to exist between $\Delta R_2{}^*(t)$ and tissue contrast agent concentration $C_t(t)$, then $C_t(t)$ can be expressed as

$$\Delta R_2^*(t) = k \cdot C_t(t). \qquad \text{Eq. 1-20}$$

The value of proportionality constant *k* is unknown but it is dependent on the particular tissue, field strength and pulse sequence. In practice, *k* is not usually measured and is assumed to be the same for all tissues of interest. This means that the concentration values are reported in relative terms. Tissue concentration during bolus transit can be calculated by using Eq. 1-21 (Rosen et al., 1990; Weisskoff et al., 1994). The results from a concentration calculation can then be fitted to a gamma-variate function to eliminate recirculation in order to obtain true first bolus passage (Thompson et al., 1964)

$$C_t(t) = -\frac{\ln(S(t)/S(t_0))}{k \cdot TE}. \qquad \text{Eq. 1-21}$$

Hemodynamic parameters are computed from the tissue concentration time curve (C_t). rCBV can be estimated simply as an integration of the area under the C_t curve in each voxel using (Sorensen, et al., 2000)

$$rCBV \approx \int_0^t C_t(\tau)d\tau. \qquad \text{Eq. 1-22}$$

The computation to extract blood flow from tissue contrast agent concentration is more complicated because $C_t(t)$ is related mathematically to rCBF multiplying the convolution of an arterial input function (AIF) and a residue function (*R(t)*) as (Ostergaard et al., 1996)

$$C_t(t) = rCBF \cdot \int_0^t C_a(\tau) R(t-\tau) d\tau \, . \qquad \text{Eq. 1-23}$$

The AIF, which represents tracer concentration in the feeding artery ($C_a(t)$), is typically selected from voxels near the middle cerebral artery (MCA) on the contralateral hemisphere. This single AIF is used to compute rCBF for all brain voxels (Copen et al., 2011). The residue function represents the amount of tracer remaining at each instant after the arrival and passage of the bolus. The function is related to $h(t)$, a transport function representing the probability density function of transit times through the tissue

$$R(t) = 1 - \int_0^t h(\tau) d\tau \, . \qquad \text{Eq. 1-24}$$

rCBF can be extracted from Eq. 1-23 by deconvolution using a technique known as singular value decomposition (SVD) (Wu et al., 2003). SVD minimizes the effect of delay and dispersion of the bolus. The peak of the deconvoluted curve is assumed to represent rCBF (Wu, et al., 2005). Finally from the central volume theorem, mean transit time (MTT) can be derived as the ratio of blood volume to flow as (Meier, et al., 1954)

$$MTT = \frac{rCBV}{rCBF} \, . \qquad \text{Eq. 1-25}$$

Another parameter to characterize bolus arrival delay is T_{max}, which is the time to reach the peak on the deconvolved curve. It has been shown that using T_{max} reduces overestimation of the hypoperfused tissue volume (Butcher, et al., 2005). In this thesis, T_{max} with +4s threshold is used to define the mismatch tissue volume to represent the penumbra. Application of a threshold is used to reduce the inclusion of benign oligemic tissue as the penumbra (Butcher, et al., 2005). Changes to the hemodynamic parameters that characterize perfusion within the penumbra and core regions during acute ischemia are shown in Table 1-3 below.

Table 1-3: Changes of hemodynamic parameters in penumbra and core regions in acute ischemic stroke (Butcher, et al., 2010).

Perfusion Parameter	**Penumbra (Potentially Salvageable)**	**Core (Irreversibly Injured)**
Cerebral Blood Flow (CBF)	↓	↓
Cerebral Blood Volume (CBV)	↑ / ↔	↓
Mean Transit Time (MTT)	↑	↑
T_{max}	↑	↑

1.3.5. Using MRI to Estimate Stroke Onset Time

The knowledge of definitive symptom onset time in ischemic stroke is critical for treatment. Approximately 25% of stroke patients initially experience symptoms upon awakening and therefore have an indeterminate onset time (Serena et al., 2003). These patients are arbitrarily assigned an onset time based on when they were last seen well (usually time before going to bed the night before) and consequently are ineligible to receive thrombolytic treatment (Fink et al., 2002; Serena, et al., 2003). However, there is evidence to suggest the presence of circadian variation in stroke onset with significant higher risk in the morning (Elliott, 1998). This implies that some ‘wake-up’ stroke patients may be eligible and benefit from thrombolytic treatment. Thus, the estimation of onset time by means of imaging would potentially extend treatment to this patient cohort.

It was demonstrated in one study that quantitative proton T_2 measurement may be used to predict onset time because of the strong correlation between T_2 increase and lesion age (Siemonsen et al., 2009). In two other studies, a lesion which was detected on DWI images but failed to show on FLAIR was found to be due to an ischemic stroke less than 3 hours old (Aoki, et al., 2010; Thomalla et al., 2009). However, another study did not find FLAIR signal intensity to be a good predictor of onset time within the first 4.5 hours of stroke (Ebinger et al., 2010). Alternatively, brain sodium concentration within the lesion was measured and demonstrated to rise linearly with time after induced focal cerebral ischemia in rats (Jones et al., 2006; Wang et al., 2000). This linear pattern of tissue sodium concentration increase was also observed in a non-human primate study (Thulborn, et al., 1999b). These animal studies followed the sodium concentration for a few hours immediately after ischemia was induced. However, the linear pattern of sodium concentration increase was not observed in patients imaged with much wider range of onset times (4 to 161 hours) (Hussain, et al., 2009). The sodium intensity, measured on images acquired with a single quantum Na-PASS sequence (Stobbe, et al., 2008b) (see section 1.4.3 for additional details) within the ischemic lesion, demonstrates a non-linear increase with time after onset, relative to contralateral homologous region. There is a lag in the initial 4 to 6 hours, then sodium intensity rises rapidly, and finally levels off after approximately 40 hours. Thus patients with subtle relative sodium Na-PASS intensity increase (<10%) are likely within the therapeutic time window and larger increase in Na-PASS intensity indicates an older stroke. There is no consensus to date of methodology to estimate stroke onset time. It appears that sodium MRI in stroke offers not only temporal information about the ischemic lesion but also the physiological status of cell membrane integrity. This information complements data available from existing proton MRI stroke sequences. These findings provide the impetus for continued research in sodium MRI and to bring it closer clinically to diagnose and guide treatment in acute ischemic stroke.

1.4. Sodium Magnetic Resonance Imaging

1.4.1. Sodium NMR

The sodium nucleus has a spin angular momentum ***I*** = 3/2 with magnitude $|I| = \sqrt{I(I+1)} = \sqrt{15}/2$. There are four quantized energy levels or ‘spin-states’ (2***I***+1) with magnetic quantum number ***m*** taking values of -3/2, -1/2, 1/2, and 3/2. A sodium nucleus possesses a non-zero electric quadrupole moment (eQ) (ellipsoidal charge distribution (Nave, 2010)) and interacts with all electric field gradients (EFG) generated by other charged particles in the surroundings. Consequently sodium ions exhibit unique relaxation characteristics dependent on the fluctuations of the quadrupolar interactions with the environment. Quadrupolar interactions occur only in nuclei with spins ***I*** ≥ 1, such as sodium. The time-averaged quadrupolar interaction frequency is defined as (Rooney et al., 1991)

$$\varpi_Q = \frac{1}{4}\chi(3\cos^2\theta(t) - 1). \qquad \text{Eq. 1-26}$$

χ is the quadrupole coupling constant ($e^2qQ/\hbar$), θ is the polar angle between the orientation of the EFG and the direction of the static magnetic field B_0. From Eq. 1-26, the quadrupolar interaction vanishes if $\theta \approx 54.7^o$.

There are three single quantum (SQ) energy transitions of the sodium nucleus in response to excitation of radiofrequency pulse within a static magnetic field. The central energy transition (between m = -1/2 to 1/2) accounts for 40% of the sodium NMR signal and the outer transitions (between m = -3/2 to -1/2 and m = 3/2 to 1/2) each contribute 30%. The energy levels are modulated by EFGs which fluctuate in time due to thermal motions. The source of EFG fluctuations that influences the sodium NMR spectra shapes are described in the works of Berendsen (Berendsen et al., 1973) and Rooney (Rooney, et al., 1991). The Berendsen model proposed that a single species of sodium ions contributes to the shifting of energy transitions due to diffusion of these ions between regions of different average quadrupolar interactions and sample domain order. Rooney et al.

elaborated further the works of Berendsen and suggested the Debye model to explain the progression of spectrum from “Type d” to “Type a” (Figure 1-5) as the correlation time (τ_c) is increased. Since energy is related to frequency (Section 1.3.1), the three equally spaced transitions in the extreme narrowing limit condition lead to a single peak “Type d” spectrum. In this case, all NMR sodium signals are detected. Under this condition, the fluctuation of EFG is very rapid with respect to the Larmor period (inverse of the Larmor frequency, ω_0^{-1}). τ_c is much smaller than ω_0^{-1}, usually in the order of nanoseconds. In addition, ϖ_Q is zero because the environment of the quadrupolar interaction is isotropic. This scenario is observed when sodium ions are in aqueous solution (e.g. NaCl in water or biologically sodium ions in cerebrospinal fluid).

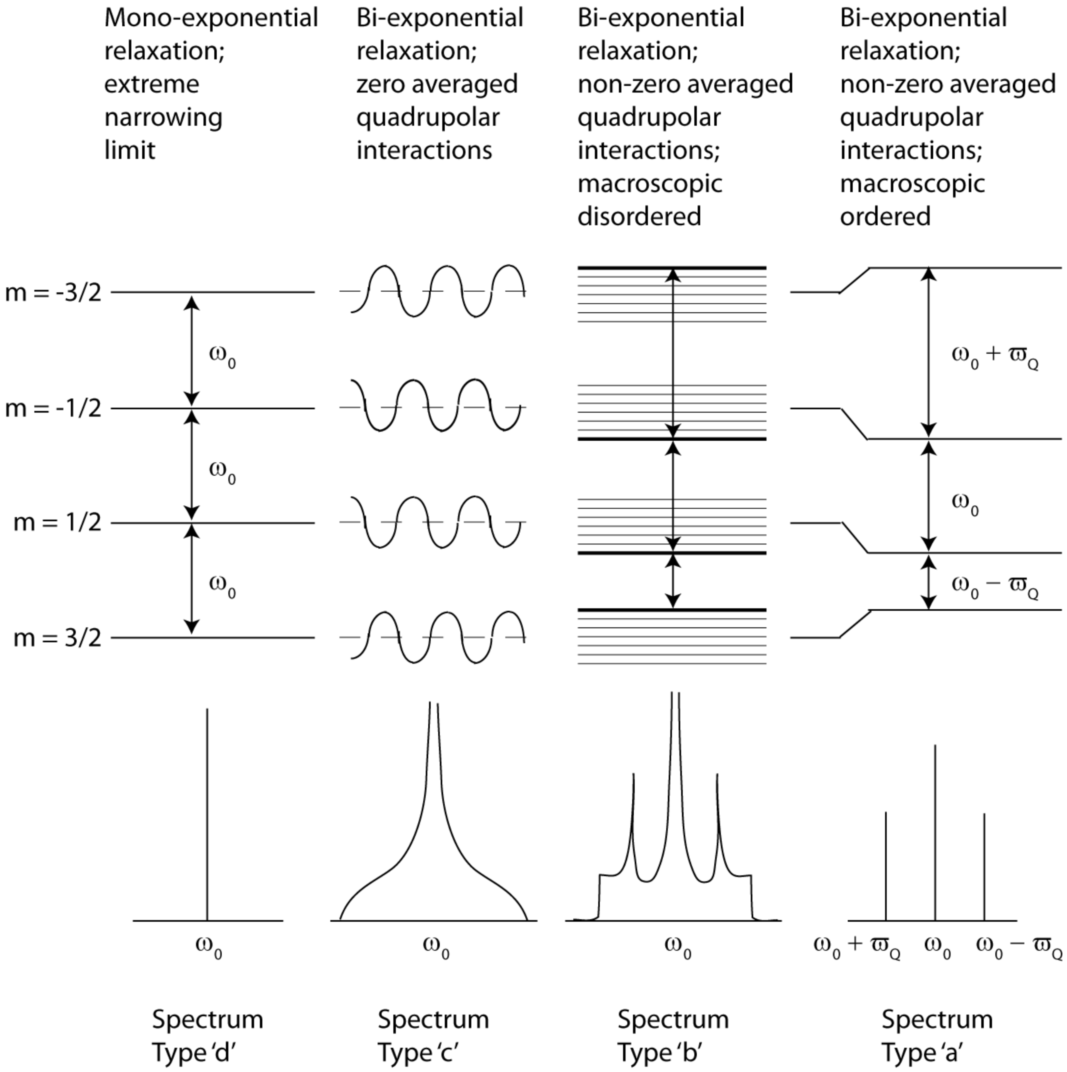

Figure 1-5: Energy levels for spin ***I***=3/2 systems and corresponding spectra to illustrate sodium ions in different environment order as adapted from Rooney et al. (Rooney, et al., 1991)

In biological tissues, sodium ions are not stationary but diffuse and encounter negatively charged macromolecules. This results in producing slower periodic quadrupolar interactions relative to and superimposed on the rapidly fluctuating hydration shells. A "Type c" spectrum is generated in this case, with τ_c greater than the Larmor period. Under this condition, ϖ_Q is zero over the whole period of the slow fluctuating quadrupolar interactions, but it is non-zero when only accounting for half the period. The half period duration of the slow fluctuation is similar in value to τ_c, but is less than ϖ_Q^{-1}. The "Type c" spectrum is comprised of three homogeneous resonances with a narrow peak produced by the central transition (m = -1/2 to m = 1/2) that is superimposed on two broadened out resonances from the outer transitions (Lorentzian). The energy levels oscillate in a slow sinusoid about the mean, as shown in Figure 1-4 (Rooney, et al., 1991). This spectrum shape occurs in disoriented biological tissues.

In other environments or domains such that the EFG fluctuation is even slower, ϖ_Q is not zero either over whole or half period of the slow fluctuation. A "Type b" spectrum is produced in this case, with the half period time and τ_c larger than ϖ_Q^{-1} (and much greater than the Larmor period). The shape of this spectrum is comprised of homogeneous central resonance and heterogeneous 'powder' pattern of the satellite resonances. A "Type b" spectrum can occur when sodium aquo ions remain in regions of non-zero ϖ_Q for times longer than ϖ_Q^{-1} (domain with local order but macroscopic disorder) (Rooney, et al., 1991). This means there exist distinct pools of sodium nuclei where ϖ_Q is never zero, but the ϖ_Q in each may be different. This spectrum type has been observed in human skeletal muscle and brain indicating the existence of sodium ions interactions with ordered structures (Reddy, et al., 1995). This also provides evidence for the well-known sodium invisibility problem present in biological environments (Joseph, et al., 1987). However, this problem is often ignored for in vivo human sodium NMR imaging.

When ϖ_Q is never zero for the slow fluctuating EFG and there are no distinct pools of sodium nuclei with different ϖ_Q, a "Type a" spectrum with two distinct satellite peaks and one central peak is generated. The satellite peaks (outer energy transitions) are shifted due to quadrupolar interactions in both locally and macroscopically ordered (anisotropic) environments, such as liquid crystals, but is unlikely to occur in biological tissue. Therefore, the transition from "Type c" to either “Type b” or “Type a” spectrum depends on the macroscopic order of the sample environment (Springer, 1996).

The longitudinal and transverse relaxation of sodium nuclei in the extreme narrowing limit, with very short τ_c, follow a simple single exponential decay; in fact T_1 is equal to T_2. However, the relaxation characteristics due to quadrupolar interactions with long correlation time (i.e. “Type c” to “Type a” spectra) are comprised of two (***I***+1/2) exponential components (Hubbard, 1970). In this case, the slow component of T_2 is attributed to the central transition between m = -1/2 and 1/2 states and the fast component is attributed to the two outer transitions:

$$M_z \propto 0.8 \cdot \exp(-t/T_{1s}) + 0.2 \cdot \exp(-t/T_{1f}) \qquad \text{Eq. 1-27}$$

$$M_{xy} \propto 0.6 \cdot \exp(-t/T_{2f}) + 0.4 \cdot \exp(-t/T_{2s}) . \qquad \text{Eq. 1-28}$$

T_1 and T_2 are components of the spectral density functions $J(\omega)$, which are Fourier transforms of the correlation function, as (Berendsen, et al., 1973)

$$T_{1f} = \frac{1}{2J(\omega)} ; \; T_{1s} = \frac{1}{2J(2\omega)} \qquad \text{Eq. 1-29}$$

$$T_{2f} = \frac{1}{J(0)+J(\omega)} ; \; T_{2s} = \frac{1}{J(\omega)+J(2\omega)} .$$

Experimentally, it is likely that only one T_1 exponential component is measured because the difference between the two components is small and the amplitude of the slow component is four times larger than the fast component.

1.4.2. In vivo Sodium MRI of the Human Brain

Although sodium is the second most NMR sensitive element in biological environment, in vivo ^{23}Na imaging is a challenging endeavor due to low concentration ($[Na^+]_{tissue}$ ~45 mM; $[Na^+]_{intracellular}$ ~15 mM; $[Na^+]_{extracellular}$ ~150 mM), small gyromagnetic ratio γ (γ_{Na} about 1/4 of γ_H), low sensitivity (35% relative to proton), and short T_1 and T_2 (slow component of T_2^* in brain tissue was measured previously ~21 ms (Bartha et al., 2004b)). Consequently conventional methods tend to produce inferior sodium MR image quality with poor signal-to-noise ratio (SNR) and low spatial resolution. There had been many strategies to "squeeze" as much SNR increase as possible through judicious manipulation of the imaging parameters that affect SNR,

$$SNR \propto M_0 \Delta x \Delta y \Delta z (N_{av} T_{acquisition})^{1/2}. \qquad \text{Eq. 1-30}$$

It is desirable to perform sodium MRI at high static magnetic field strength (B_0), such as 4.7 T, due to the linear relationship of magnetization M_0 to SNR (recall M_0 is also linearly related to B_0, Eq. 1-4). Although SNR is increased by choosing larger voxel dimension (Δx, Δy, Δz), but this leads to poor spatial resolution. Similarly, SNR can be improved by either increased averaging (N_{av}) or data acquisition time, but results in extending the total scan length and thus make sodium MRI unfeasible for clinical applications. It is important to note that the constraint of specific absorption rate (SAR), or tissue heating, (measured in Watts per kilogram) needs to be taken into consideration when one optimizes a sodium MRI sequence for SNR. SAR can be estimated as

$$SAR \propto \frac{B_0^2 \theta^2}{TR \cdot \tau_{RF}}. \qquad \text{Eq. 1-31}$$

SAR at high field (about 10 times increase from common clinical scanner field strength of 1.5T to 4.7T) must be compensated by adjusting other sequence parameters, such as flip angle (θ), TR, or RF pulse duration (τ_{RF}). However, reduced flip angle or increased RF pulses both result in smaller detected signal. A low flip angle means that less transverse magnetization is produced, and a long RF pulse means signal lost due to rapid T_2 decay. On the other hand, increasing TR is also undesirable because scan length is extended. It appears that conventional implementation of sodium MRI sequences use $\theta = 90^o$, short τ_{RF}, and long TR to avoid relaxation weighting. However, a strategy to manipulate these parameters that deviate from the conventional implementation leads to the development of a SNR optimized single quantum imaging sequence known as projection acquisition in steady-state (Na-PASS) (Stobbe, et al., 2008b).

The first clinical human sodium MRI study in healthy volunteers and patients was published in 1985 using a 1.5T scanner. This study demonstrated pronounced signal intensity increase within the pathologic regions in patients with tumors, cerebral infarction and edema (Hilal et al., 1985). The study used a spin-echo sequence with three echoes at TE of 12 ms, 28.5 ms, and 43.8 ms to acquire data, in 34 minutes, that was reconstructed into images with resolution of 4x4x10 mm^3. Sodium transverse relaxation was first measured in rat brain with the fast component T_{2f} = 0.75 ms and the slow component T_{2s} = 10 ms (Cope, 1970). An optimal ^{23}Na MRI sequence will have as short a TE as possible. A short TE will minimize signal loss due to rapid transverse relaxation (fast component of T_2 accounts for 60% of total signal). In 1988, another group demonstrated the use of a 3D FLASH gradient-echo sequence to reduce TE to 4.5 ms (Grodd et al., 1988).

An acquisition approach that deviates from the common Cartesian k-space sampling to minimize TE for detection of short T_2 component was first proposed and demonstrated by Ra in 1986 (Ra et al., 1986). The study used a 1.5T scanner and a three dimensional spin-echo projection imaging (PI) sequence with TE of 3.6 ms. The sodium images acquired with short TE (3.6 ms) showed much higher signal obtained from brain parenchyma than images acquired with longer TE of 14 ms. Two decades later, in 2007, another proposal was made by Nielles-Vallespin (Nielles-Vallespin et al., 2007) to use three-dimensional gradient-echo PI sequence to obtain a ultra-short TE of 0.2 ms. The authors in the study used a short TR of 4 ms to obtain data to reconstruct images with nominal isotropic resolution of 4 mm in 10 minutes. Data points were acquired uniformly in time along each projection, resulting in a k-space more densely sampled centre and sparsely sampled edge. However, this non-uniform k-space sampling was shown to yield ~29% increase in standard deviation of noise relative to uniform sampling (Stobbe, 2010). Unfortunately, a large number of projections are required to isotropically sample k-space, therefore projection imaging is impractical for quantitative tissue sodium concentration (TSC) measurement. For quantitative imaging, TR must be long enough to allow full T_1 recovery (typically ~100 ms or 5 times T_1).

Another acquisition strategy, proposed by Boada in 1997 (Boada et al., 1997), is known as three-dimensional twisted projection imaging (TPI). TPI addresses the sampling inefficiency of PI, retains the property of short TE, and also reduces the number of projections to sample all k-space. A very short TE is achieved when a short (hard) RF pulse is used because sampling of k-space begins at the centre. This technique was based on the extension of two dimensional twisted radial line imaging, known as TWIRL (Jackson et al., 1992) and was proven to be well-suited for TSC quantification in humans (Ouwerkerk, et al., 2003; Thulborn et al., 2005). In this scheme, the trajectories sample k-space with constant density minimizes noise variance. Each trajectory begins at the k-space origin and traverses, in a straight line, up to a fraction p (p<1) of total radial distance k_{max}. After p, the path twists to follow the surface of a cone (Figure 1-6). Sampling density (SD) for the straight radial projection is

$$SD(p) = \frac{1}{p^2}\,. \qquad \text{Eq. 1-32}$$

In the TPI approach, this sampling density is maintained in the twisted portion by making the radial portion of the trajectory evolve according to

$$r(\tau) = (3p^2\tau + p^3)^{1/3}\,. \qquad \text{Eq. 1-33}$$

τ is the dimensionless fraction of time required for a projection to reach k_{max}, and r represents the projection evolution beginning at $r = p$. In TPI, the number of projections is reduced by a factor of p and the acquisition time is reduced by (1-p). It is intuitive that the twisted projection length is longer than the standard straight radial line, and the total relative projection length (τ_{Total}) as a function of p is

$$\tau_{Total} = \frac{1-p^3}{3p^2} + p\,. \qquad \text{Eq. 1-34}$$

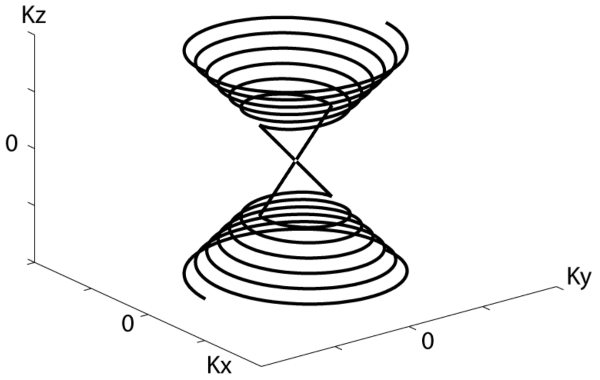

Figure 1-6: Illustration of twisted projection path for non-Cartesian k-space coverage used in sodium imaging with very short TE.

Gibbs' ringing artefact always exists for uniformly sampled k-space and can be detrimental in sodium images because voxel dimension is large to compensate for low SNR. One method to correct this problem is by applying a post-acquisition apodization filter to a uniformly sampled k-space dataset. An alternate approach, with SNR advantage of 17% over the former, is a modification to the 3D-TPI implementation to change the sampling density filter shape to match the desired apodizing function (sampling density weighted apodization [SDWA]) (Stobbe et al., 2008a). All 3D-TPI projections used in this thesis for sodium imaging were created in a custom-designed MATLAB software named NL-PRODS (a description of this software is provided in Appendix 1).

1.4.3. Single Quantum Sodium Sequences and Stroke Imaging

Single-quantum (SQ) sodium MRI has been explored in cerebral ischemia in both animals (Bartha et al., 2004a; Boada et al., 2005; Hilal et al., 1983; Jones, et al., 2006; Lin et al., 2001; Moseley et al., 1985; Thulborn, et al., 1999b; Yushmanov et al., 2009) and humans (Grodd, et al., 1988; Hilal, et al., 1985; Hussain, et al., 2009; Shimizu, et al., 1993; Thulborn, et al., 2005; Thulborn, et al., 1999b). This technique does not distinguish sodium from different compartments but acquires signal from overall tissue sodium. It is typical to use a more conventional approach, with a 90^o non-selective RF excitation pulse of short duration and longer TR, to minimize T_1-weighting for TSC quantification. The T_1 of sodium is short for average brain tissue (37 ms measured at 4.7T (Stobbe et al., 2006)); a TR value of 5 times T_1 (~150 ms at 4.7T and shorter at lower field) in the sequence is adequate to minimize T_1 saturation. A new gradient spoiled steady-state projection acquisition sodium imaging sequence (Na-PASS), with TPI acquisition, was developed (Stobbe, et al., 2008b) to optimize SNR (experimentally measured ~38% increase relative to TSC method at 4.7T for healthy human brain) under the constraint of SAR. The SNR advantage of Na-PASS may be used to improve spatial resolution such that partial volume effects can be decreased.

Several animal models of cerebral ischemia (performed by occlusion of the middle cerebral artery and imaged at 3T using TPI acquisition with TR/TE = 100 ms/0.4 ms) demonstrated that TSC within the ischemic region increases linearly with time in the early hours (1-7 hours) after stroke (Boada, et al., 2005; Jones, et al., 2006; Thulborn, et al., 1999b; Yushmanov, et al., 2009). This finding is consistent with other reports of linear elevation of TSC measured using flame photometry (Betz, et al., 1994; Wang, et al., 2000). However, the rate of increase is heterogeneous between individual animals and also within the ischemic region, so a common TSC increase rate cannot be established. This elevation may reflect the increased diffusion of sodium ions through plasma membrane into the interstitial space during cytotoxic edema leading to higher TSC (Young et al., 1987). The pathologic process that contributes to the increased TSC appears to be time dependent. Elevated sodium concentration can be detected and quantified by MRI to identify potentially viable tissue. In fact, Thulborn et al. (Thulborn, et al., 1999b) have established a viability threshold in a primate study that TSC above 70 mM represents infarcted tissue. This threshold was also shown clinically by Thulborn et al. in a patient who underwent imaging at 5 hours demonstrating an initial TSC of 42 mM and then increased to above 70 mM in follow-up scans at 76 hours and 6 months.

The first clinical study of sodium MRI in cerebral ischemia involved imaging 7 patients from 4 to 82 hours after onset for an initial scan and then a follow-up scan from 38 hours to 39 days. One patient underwent additional imaging at 57 days and 101 days (Shimizu, et al., 1993). The sodium images were acquired at 1.5 T using a spin-echo sequence (TR/TE = 100 ms/13 ms) that yielded slice thickness of 20 mm (in-plane resolution not specified). The sodium signal intensity did not show any changes for the first 13 hours but rapidly increased afterward, up to 82 hours, and then remained elevated in the chronic stage. This pattern differs from the evolution of TSC in animal studies, where it was found to increase linearly in the early hours after stroke. The acute phase insensitivity to intensity changes in this study is likely caused by the long TE used that results in undetected signal due to rapid T_2 relaxation (T_{2f} accounts for 60% of the total signal). Another study by Thulborn et al. investigated TSC increase in patients imaged across a wide span of time after symptom onset (Thulborn, et al., 1999b). The authors did not find time dependence elevation of TSC but demonstrated that all had a minimum increase of 25%.

Sodium sensitivity in acute stroke was improved in a recent study that reported similar sodium intensity evolution pattern in twenty-one patients. The initial scans were obtained from 4 to 104 hours after stroke and follow-up scans were obtained at 23 to 161 hours after symptom onset (Hussain, et al., 2009). Sodium images were acquired at 4.7 T using the Na-PASS method (TR/TE = 25 ms/0.5 ms). Signal intensities were measured within the ischemic lesions defined by restricted diffusion (hyper-intense on DWI and hypo-intense on corresponding ADC map) and in contralateral homologous regions. Relative signal intensity did not change in the first 4 to 6 hours, but then progressively increased, and plateaued beyond 40 hours. Clearly, short TE improves the sensitivity to detect sodium changes than the first clinical study mentioned above. It is possible that in the first 4 to 6 hours, the initial influx of sodium ions has begun (hyper-intense DWI) but sodium ions from plasma may not yet have entered the interstitial space (no change in TSC).

1.4.4. Intracellular-weighted Sodium MRI

Homeostasis of sodium ions between the intra- and extracellular compartments is maintained by the energy intensive Na^+/K^+-ATPase. The concentration gradient collapses when ATP production cannot keep up with the demand, such as in cerebral ischemia, resulting in the influx of sodium ions into the intracellular space. The ability to discriminate sodium signals selectively would potentially provide valuable information about the physiologic impairment that precedes any detection of tissue sodium changes. Three methods have been proposed for in vivo sodium NMR imaging, or spectroscopy, to achieve this purpose: shift reagents (SR), inversion recovery, and relaxation-based techniques known as multiple-quantum filtering (MQF).

Shift reagents (SR) are negatively charged paramagnetic molecules composed of rare earth metals (e.g. dysprosium or thulium). Several animal studies explored the separation of sodium signal by injection of SR to shift the sodium Larmor frequency in the extracellular space. This is effective because SR is not permeable through the cell membrane (Bansal et al., 1992; Gupta et al., 1982; Navon, 1993; Winter et al., 2001a). Despite their ability to discriminate sodium from different compartments, however SRs are not suitable for in vivo human applications due to toxicity and an impassable blood-brain-barrier.

Another approach for selective sodium imaging is based on the assumed T_1 relaxation differences between the intra- and extracellular environments. Sodium ions in extracellular space diffuse more freely and may exhibit longer T_1 than those in intracellular. A sodium sequence implemented with both non-selective 180^o inversion and 90^o excitation pulses (TI = 25 ms; TR/TE = 100 ms/5.6 ms) was demonstrated previously to monitor chemotherapy response in mouse where the signal is weighted toward intracellular (Kline et al., 2000). However inversion recovery sodium signal is greatly reduced compared to SQ signal. As a result, a soft inversion recovery fluid attenuation (SIRFLA) sequence was developed to optimize SNR under the constraint of SAR at 4.7 T for intracellular weighted sodium human brain imaging at 4.7 T (Stobbe, et al., 2005). This sequence uses longer inversion pulse to permit shortening of TR that results in more signal averages acquired in a giving scan length. An advantage of this method for intracellular-weighted (although not proven) signal detection is the higher signal yield than MQF, which is described next.

1.4.4.1. Multiple Quantum Filter

Sodium nuclei that exhibit bi-exponential relaxation are assumed to be mainly in the intracellular space, where the quadrupole interaction lengthens the correlation time to be near the inverse Larmor frequency. Bi-exponential relaxation can be detected and distinguished using the MQF approach (Jaccard, et al., 1986). The filter consists of three RF excitation pulses and an optional refocusing pulse as shown in Figure 1-7. The filter can select either double or triple quantum (DQ or TQ) coherences, which can only be created by sodium nuclei with bi-expontential relaxation, and suppresses SQ coherence. A coherence is related to energy transition between the four states, where transition between two adjacent states (with the difference in magnetic quantum number (Δm) equals ±1) leads to a directly observable transverse magnetization (Bodenhausen et al., 1984). On the other hand, DQ ($\Delta m = \pm 2$) or TQ ($\Delta m = \pm 3$) coherences are not directly observable but are created and passed through the filter and then transformed into observable transverse magnetization. The DQ or TQ signal is summed by repeating the experiment to incrementally step through the transmitter phases in each RF pulse as shown in Table 1-4. The phase cycling steps are chosen for the RF phase dependent of the double- and triple-quantum coherences ($\cos 2\phi$ and $i\sin 3\phi$ respectively) (Chung et al., 1990). As a result, the total imaging time of DQF or TQF experiment is extended by four or six times respectively relative to SQ for same sequence parameters and k-space acquisition scheme where the reconstructed images are identical in spatial resolution.

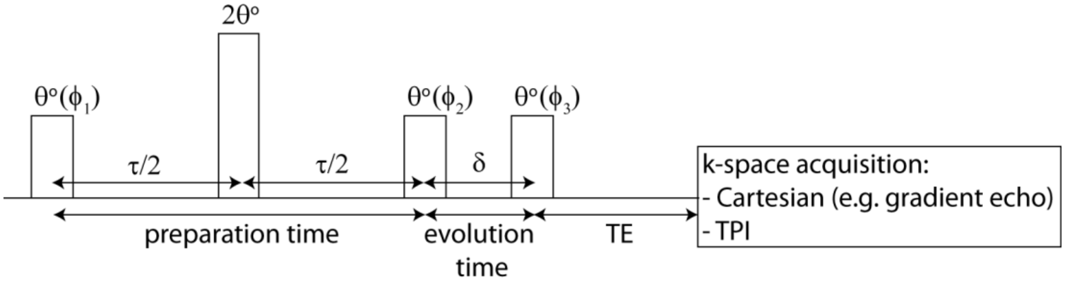

Figure 1-7: Multiple-quantum filter sequence diagram. All RF excitations use non-selective rectangular pulses. The 2θ pulse is optional to refocus magnetic field inhomogeneities. Conventionally, $\theta = 90^o$ and pulse duration is short (e.g. 0.5 ms for in vivo brain imaging). A delay is added after the last RF pulse such that TE is equal to the preparation time. As a result, k-space acquisition may use the more common Cartesian sampling approach or TPI.

Table 1-4: Conventional phase cycling steps used in DQF and TQF experiments for each RF excitation pulse as specified in (Chung et al., 1990). The receiver phase alternates between 0 and 180^o such that SQ coherences are suppressed and higher-order coherences are summed constructively.

	ϕ_1	ϕ_2	ϕ_3	**Receiver phase (ψ)**
DQF	0, 90^o, 180^o, 270^o	0, 90^o, 180^o, 270^o	0	0, 180^o, 0, 180^o
TQF	30^o, 90^o, 150^o, 210^o, 270^o, 330^o	120^o, 180^o, 240^o, 300^o, 0, 60^o	0	0, 180^o, 0, 180^o, 0, 180^o

DQF/TQF signal evolution is governed by the two transverse relaxation components according to (Hancu, et al., 1999)

$$I = a \cdot [\exp(R_2^{(1)}t) - \exp(R_1^{(1)}t)] \qquad \text{Eq. 1-35}$$

$$T_{2s} = \frac{1}{R_2^{(1)}}\ ;\ T_{2f} = \frac{1}{R_1^{(1)}}\ .$$

The optimal preparation time, τ_{opt}, in the filter must be determined for different sodium environments and can be calculated using Eq. 1-36 with the assumption that off-resonance is negligible (Navon, 1993)

$$\tau_{opt} = \frac{\ln(T_{2s} / T_{2f})}{1/T_{2f} - 1/T_{2s}}. \qquad \text{Eq. 1-36}$$

Alternatively, the value for τ_{opt} can be estimated based on the plot as shown in Figure 1-8 where the time that the DQF/TQF signal is at its maximum. The evolution time, δ, is kept as short as possible to minimize signal loss from higher-order coherences transforming back into SQ coherences. TE is typically equal to τ_{opt}, with a delay added after the last RF pulse.

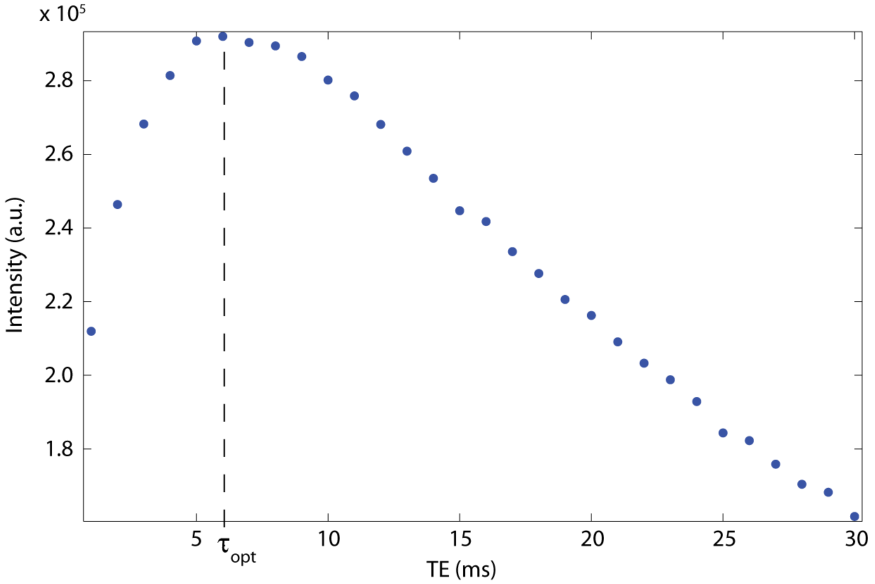

Figure 1-8: Evolution of TQF signal from repeated relaxometry experiments to estimate T_2 in healthy human brain at 4.7T. The experiments used a non-imaging 4-pulse TQF sequence (see Appendix 2) with TE from 1 to 30 ms and acquisition duration of 60 ms. The acquisition begins at 0.6 ms after the middle of the last RF pulse. The pulse duration is 0.5 ms for the excitation pulses and 1 ms for the refocusing pulse. The maximum intensity for each acquired FID is plotted against TE. τ_{opt} = 6 ms is used for in vivo human brain TQF imaging in this thesis.

A simple demonstration of the MQF approach in literature typically uses a spherical phantom that is filled with NaCl solution (saline) in one compartment and agar gel in another, such as shown in Figure 1-9. In this phantom the sodium signal from saline (extreme narrowing limit condition that exhibit mono-exponential relaxation) is quenched while signal from agar (bi-exponential relaxation) passes through the filter (Hancu, et al., 1999; Wimperis et al., 1992;

Wimperis et al., 1991). Both DQF and TQF can selectively extract bi-exponential relaxing sodium nuclei. For some reason investigators in early studies all adopted the DQF approach for intracellular sodium spectroscopy experiments (Jelicks et al., 1989; Lyon et al., 1991; Pekar et al., 1986). However, TQF was shown to be 50% more sensitive than DQF (Chung, et al., 1990) and it is the preferred approach for intracellular-weighted sodium imaging to maximize SNR (although still very limited even at high field) and reduce scan time.

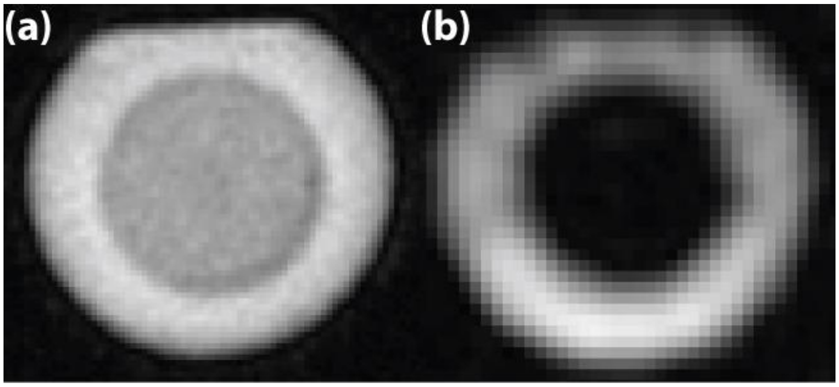

Figure 1-9: A spherical phantom constructed in this thesis that is filled with 500 mL of NaCl solution ([Na$^+$] = 60 mM) in the inner compartment and 5% agar gel (w/v) in 1450 mL of NaCl solution ([Na$^+$] = 70 mM) in the outer compartment. (a) SQ image of the phantom that shows sodium signal from both compartments and (b) TQ image with only extracted signal from bi-exponential relaxing sodium nuclei in agar gel and suppressed mono-exponential relaxing sodium nuclei in saline. The images were acquired at two different sessions.

Coherence transfer through the TQF sequence has been described extensively in literature using irreducible spherical tensor operators. These tensor operators describe the nuclear magnetic moment as an expansion of spherical harmonic moments (Bowden et al., 1986; Chung, et al., 1990; Hancu et al., 2000; Muller et al., 1987). Spin-3/2 nuclei requires 16 basis tensor operators, T_{lp} where l represents the rank (l = 0, 1, 2, 3) and p the order (p = 0, 1, 2, 3), to completely describe spin dynamics (Muller, et al., 1987). These operators are added or subtracted together to form symmetric and anti-symmetric combinations. They are also transformed into orthonormal sets denoted as $\hat{T}_{lp}$ by multiplying with normalizing coefficients a_l that have the values 1/2 (l = 0), $1/\sqrt{5}$ (l = 1), $1/\sqrt{6}$ (l = 2) and $\sqrt{2}/3$ (l = 3) for convenience in the differential equations calculation to describe spin evolution as follows (Hancu, et al., 2000):

$$T_{lp}(s) = (1/\sqrt{2})(T_{l-p} + T_{lp}) \qquad \text{Eq. 1-37}$$

$$T_{lp}(a) = (1/\sqrt{2})(T_{l-p} - T_{lp})$$

$$\hat{T}_{lp} = a_l T_{lp}.$$

Each operator in the basis set takes on the interpretation as: $\hat{T}_{00}$ (identity), $\hat{T}_{10}$ (longitudinal magnetization), $\hat{T}_{11}(a)$ and $\hat{T}_{11}(s)$ (transverse magnetization), $\hat{T}_{20}$ (quadrupolar spin polarization), $\hat{T}_{21}(a)$ and $\hat{T}_{21}(s)$ (second-order SQ coherences), $\hat{T}_{22}(a)$ and $\hat{T}_{22}(s)$ (second-order DQ coherences), $\hat{T}_{30}$ (octopolar spin polarization), $\hat{T}_{31}(a)$ and $\hat{T}_{31}(s)$ (third-order SQ coherences), $\hat{T}_{32}(a)$ and $\hat{T}_{32}(s)$ (third-order DQ coherences), $\hat{T}_{33}(a)$ and $\hat{T}_{33}(s)$ (third-order TQ coherences). All simulations in this thesis are performed in a custom MATLAB (MathWorks, Natick, MA) software named TRIPLE-S (Appendix 1) that implements a set of differential equations involving these operators to describe the spin dynamics under the influence of an RF excitation and relaxation given in (Hancu, et al., 2000; van der Maarel, 2003). It is important to point out that the rank (l) of a tensor operator may change under relaxation where the order (p) is changed only by RF excitation.

TQF sodium imaging had been explored in cerebral ischemia in two earlier reports. These reports demonstrated large TQF signal increase but slight decrease or negligible SQ signal intensity changes within the first hour after onset in dog (Kalyanapuram et al., 1998) and monkey (LaVerde et al., 2007). These results reflect the promising utility of TQF as a non-invasive method to detect early pathophysiology of ischemia when impaired Na^+/K^+-ATPase lead to redistribution of sodium ions from extracellular to intracellular compartment prior to TSC increase. However, TQF sodium imaging is hampered by extremely low SNR due to only a small fraction of TQF signal generated (~1/10 of SQ for brain) with longer acquisition time. This is a major hurdle for TQF sodium imaging applications in clinical setting. The first paper for in vivo human brain TQF sodium imaging in healthy volunteers was published in 1999 by Hancu et al. (Hancu, et al., 1999). This study used a three-pulse TQF sequence (i.e. no refocusing of B_0 inhomogeneities which is better suited for in vivo brain imaging because of less SAR and less prone to B_1 field variation) with TPI acquisition to acquire brain images in 20 minutes at 3T. The spatial resolution for TQF brain images was not specified, but the voxel size was significantly larger compared to SQ images (ironically labelled high resolution in the study) to compensate the small TQF signal in order to produce images with sufficient SNR. Since the publication by Hancu et al., there has only been one additional published paper (Fleysher, et al., 2012) of in vivo TQF sodium brain imaging. TQF sodium imaging, in conjunction with other sequences, may potentially be used to identify suitable candidates in stroke patients with unknown onset time for thrombolytic treatment if similar results as animal studies can be demonstrated. The next chapter discusses necessary optimization strategy of the TQF sequence for in vivo human brain imaging to improve SNR. SNR optimization together with the advantage of higher magnetic field strength at 4.7T and beyond is critical also to improve spatial resolution.

1.4.5. In vivo Sodium MRI of Ordered Environments

Bulk sodium NMR signals from all environments with mono- or bi-exponential relaxation characteristics can be detected using SQ acquisition methods, such as Na-PASS or the conventional TSC pulse sequences as described earlier. These environments include sodium ions in the extreme narrowing limit, as well as those in isotropic (zero time-averaged ϖ_Q) and anisotropic (non-zero time averaged ϖ_Q) motions. Methods to selectively acquire sodium signal weighted toward the intracellular compartment can use the TQF sequence as described in previous section. However, the TQF sequence is not capable to differentiate isotropic and anisotropic sodium signals, as both exhibit bi-exponential relaxations. Further selective detection of sodium NMR signal to distinguish the sodium 'orderness' is desirable, as it may serve as an indicator of disease, such as shown for the degeneration of cartilage (Jelicks et al., 1993). Sodium NMR spectra obtained using a DQF sequence provided evidence that residual quadrupolar splitting exists in human skeletal muscle, brain, breast, and cartilage (Duvvuri et al., 1999; Reddy, et al., 1995; Reddy et al., 1997b). Residual quadrupolar splitting of sodium NMR spectra is caused by the interactions of sodium ions with ordered structures. The observed residual splitting in the lab frame, ω_Q, is (Eliav et al., 1994)

$$\omega_Q = \omega_Q^{loc}\frac{1}{2}(3\cos^2\theta - 1), \qquad \text{Eq. 1-38}$$

where ω_Q^{loc} is the quadrupolar interaction frequency in the local frame of reference of the nucleus, and θ is the angle between this local frame and static magnetic field. Sodium quadrupolar interactions in environment such as liquid crystal with completely macroscopic ordering and uniform orientation results in NMR spectrum that constitute of a central peak and two distinct satellite peaks. In biological environments, where the order changes markedly from one compartment to another (macroscopically disordered), the spectrum is expected to be a 'powder' pattern that includes quadrupolar interactions in all orientations.

Sodium NMR signals from ordered (anisotropic) environments can be selectively detected using a DQF pulse sequence and with the judicious selection of θ for the last RF pulse to be 54.7^{o}, which is often referred to as double-quantum magic angle (DQ-MA) sequence (Eliav, et al., 1992). The evolution of quadrupolar nuclei under the influence of RF excitation and relaxation can be understood using irreducible spherical tensor operators as briefly described in the previous section. After the first RF pulse is applied in the DQF sequence, sodium ions in isotropic environments produce only odd-rank single-quantum tensor operators, $T_{1\pm1}$ and $T_{3\pm1}$, from the outer transitions of energy states. On the other hand, even-rank single-quantum tensor operators, $T_{2\pm1}$ (the only even-rank SQ coherence tensors in $\boldsymbol{I} = 3/2$ nuclei), are formed only in anisotropic environments such as liquid crystals (Jaccard, et al., 1986). $T_{2\pm1}$ operators are formed during the preparation time τ and are transferred into $T_{2\pm2}$ by the second θ non-selective RF pulse excitation. The last RF pulse converts the higher order coherences back to SQ coherence where signals are acquired. The conventional implementation of DQF where $\theta = 90^o$ for all RF pulses detects both odd- and even-rank quantum coherences. The DQF signal contains contribution from both isotropic and anisotropic environments. However, for the DQ-MA sequence where the last RF pulse has $\theta = 54.7^o$, only even-rank tensor operators are extracted while the odd-rank operators are suppressed. This technique is employed in this thesis to obtain DQ-MA sodium images to demonstrate only anisotropic quadrupolar interactions, or non-zero ϖ_Q, in the human brain.

1.5. Brief Summary

Sodium is intricately involved in the proper functioning of normal cellular metabolism where a concentration gradient is maintained between intra- and extracellular compartments by the Na^+/K^+-ATPase. Alteration of this ionic concentration gradient is manifested in many neurological disorders. In addition, the exploration of compartment specific sodium changes is beneficial to allow further understanding of pathophysiological progression. Unfortunately, the nature of the sodium nucleus and its low concentration in biological environments makes in vivo sodium MRI of the human brain a challenging endeavor. The attempt for intracellular-weighted or compartment specific sodium imaging by using the TQF sequence is further more difficult. The following chapters present methods that I have spent considerable time in this thesis to develop in order to increase TQF sodium signal as well as demonstrating for the first time DQ-MA sodium images to show residual ϖ_Q in the brain. In addition, the potential clinical utility of sodium MRI in ischemic stroke patients is also presented.

Chapter 2

Triple Quantum Filtered Sodium Imaging of the Human Brain at 4.7T[1]

2.1. Introduction

One of the motivations for pursuing triple quantum filtered (TQF) sodium NMR (Jaccard, et al., 1986) in cerebral ischemia, or any other neurological disorder, is the potential to selectively measure intracellular sodium changes, which could be a direct marker of compromised ionic homeostasis. Stroke model studies (Kalyanapuram, et al., 1998; LaVerde, et al., 2007) have shown much larger changes in the ischemic lesion relative to the non-affected hemisphere for TQF NMR than for single-quantum (SQ) NMR, consistent with a sodium shift to intracellular space following anoxic depolarization. TQF sodium NMR has also shown signal increases in animal models of tumors (Babsky et al., 2007; Griffey et al., 1990; Winter et al., 2001b). Despite the proportionally greater and potentially more compartment specific changes, TQF imaging is challenging as the TQ sodium signal is typically one tenth that of SQ (Wimperis, et al., 1992), and hence the resulting sodium images suffer from poor spatial resolution and require long scan times to achieve sufficient signal-to-noise ratio (SNR).

The TQF sodium sequence has scarcely been explored for human brain imaging. At the time of the manuscript preparation, there is only one published paper on healthy volunteers (Hancu, et al., 1999), and a conference proceeding with one example of a brain tumor (Boada et al., 2004), both acquired by the same group at 3 T in 16-20 minutes using three radiofrequency (RF) pulses with conventional phase cycling and three dimensional twisted projection imaging (TPI) k-space

---

[1] A version of this chapter has been published. A. Tsang, RW. Stobbe, C. Beaulieu, 2012. Triple-quantum-filtered sodium imaging of the human brain at 4.7 T. Magnetic Resonance in Medicine. 67(6):1633-1643. Dr. Stobbe was involved in this study with verifying the simulation results as well as editing the manuscript.

coverage. These publications use what will be described as the ‘standard’ TQF sequence approach, which includes 90^o flip angles for all excitation pulses, and short (0.5 ms in this case) RF pulse widths. The consequence of using the so called ‘standard’ TQF sequence at a higher field strength such as 4.7T is the need to substantially increase repetition time (TR) to accommodate specific absorption rate (SAR), which in turn increases scan time and limits the number of averages that can be acquired in a given scan duration. The use of smaller flip angle, longer RF pulses, and shorter TR has shown a substantial SNR advantage for a steady-state SQ sodium imaging approach when SAR is a constraint (Stobbe, et al., 2008b). This ideology is extended here to the TQF sequence.

The goal here is to optimize the three-pulse TQF sequence with 6 phase cycling steps (Jaccard, et al., 1986) and TPI to yield improved TQF sodium images of the human brain at 4.7T, given the constraint of SAR, within a feasible scan time. First, simulations of the evolution of the single and triple quantum coherences are performed for the ‘standard’ parameters as well as longer RF pulse lengths, smaller first RF flip angles, and shorter TR in order to choose a set of optimized parameters that yield enhanced SNR of TQ signal while minimizing SQ signal. Second, the predictions of the simulations are confirmed experimentally in agarose gel phantoms. Third, the SNR and image quality of the TQF images from the two parameter sets are compared in five healthy volunteers. Given an observation of non-zero intensity in the fluid spaces of the brain (i.e. ventricles) in the TQ images acquired with both parameter sets, a supplementary study was conducted. Simulation and imaging experiments were performed to assess two contributing effects: spatial blurring (i.e. the spatial smearing of the TQ-passing signal arising from voxels adjacent to CSF space such that the transverse magnetization of the brain tissue contributes to the intensity observed in the CSF space) and SQ signal ‘breakthrough’ from sodium nuclei in the CSF space (Keltner et al., 1994).

2.2. Methods

This sodium imaging project at 4.7T was approved by the Health Research Ethics Board. Written consent was obtained from all volunteers in the study. All MRI was performed on a 4.7T Varian Inova with a single-tuned birdcage head coil. The TQF sequence implemented here includes three RF excitation pulses with standard 6-step phase cycling such that a set of projections is sequentially acquired with a constant set of RF and receiver phases, followed by re-acquisition with the next set of phases in the phase-cycling regime (Figure 2-1).

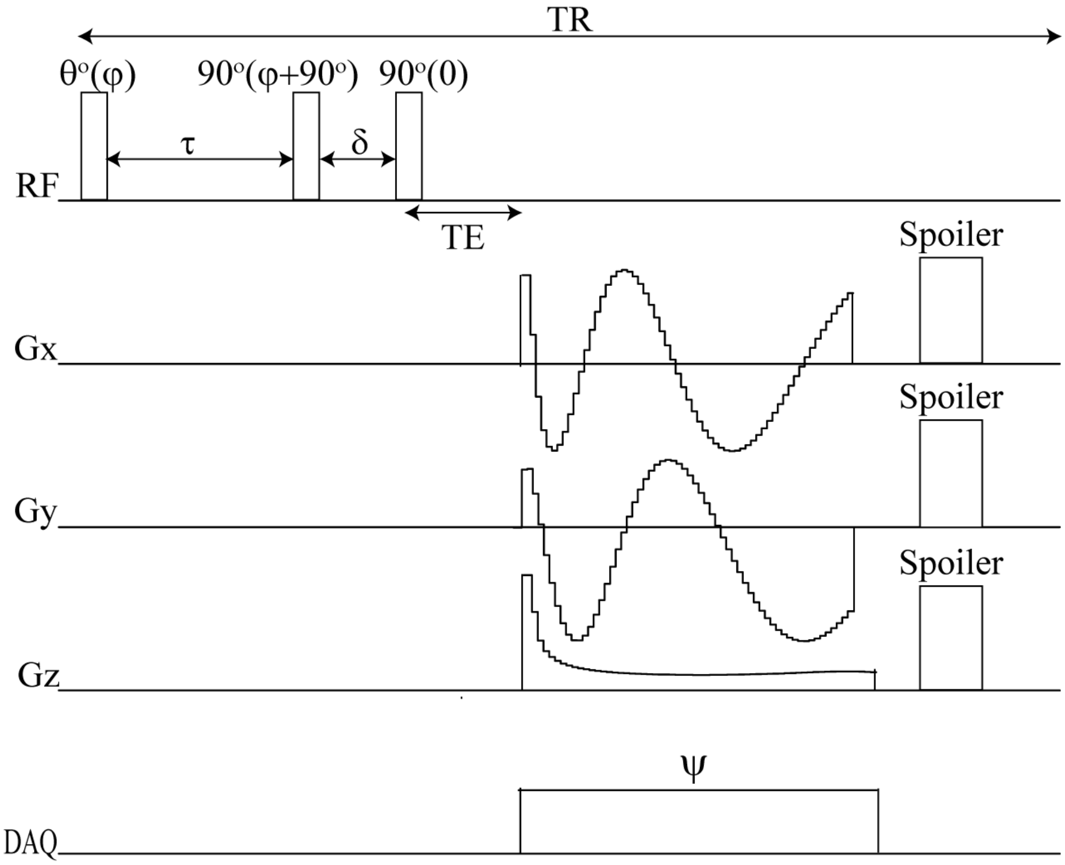

Figure 2-1: Sequence diagram of the three-pulse triple-quantum filter implementing TPI with standard six-step phase cycling φ=30°, 90°, 150°, 210°, 270°, 330°. The receiver phase alternates between ψ=0 and 180° for successive acquisitions. Only the first flip angle was varied in the optimization, while the second and third pulses remain unchanged at 90°. The pulse length is adjusted similarly for all three RF pulses. The interval τ is optimized to yield maximum signal and TE is set to τ, while δ is kept as short as possible. Note that the sequence is not drawn to scale along the time axis.

2.2.1. Simulations

Optimization of the TQF sequence under the constraint of SAR used custom-designed simulation software (Matlab), which solves the set of differential equations describing the evolution of spin-3/2 nuclei in terms of tensor operators under the influence of RF pulses and relaxation (Hancu, et al., 2000). In this sequence, the first RF pulse creates single quantum coherence (T_{11}), or observable transverse magnetization, from the longitudinal magnetization (T_{10}). Note that the combination of irreducible tensor ‘T’ operators can be thought of as describing the magnetic polarization of the sodium spin 3/2 ensemble. The process of bi-exponential relaxation creates rank three single quantum coherence (T_{31}) from T_{11}, and following a ‘preparation’ time τ to maximize T_{31}, a second RF pulse with appropriate relative phase converts T_{31} into rank three triple quantum coherence (T_{33}). As quickly as possible, to minimize T_{33} decay, a third constant phase RF pulse is applied to convert T_{33} back into the single quantum T_{31} coherence. Finally, the bi-exponential relaxation process converts the T_{31} coherences back into observable transverse magnetization T_{11}. Acquisition begins following a delay to maximize T_{11} such that the echo time (TE) is usually the same as τ (Jaccard, et al., 1986). Phase cycling of the receiver (i.e. 0^{o} and 180^{o}) cancels all transverse magnetization (T_{11}) produced by the last RF pulse as a result of simple longitudinal magnetization 'flipping'. However, the T_{11} re-produced from T_{31} through bi-exponential relaxation following the last RF pulse is not cancelled by summation of the phase-cycles, a result of 'phase conversion' through the triple-quantum state. As such, all nuclei in environments that do not produce bi-exponential relaxation, and hence do not experience a triple-quantum state, should not produce measurable signal following phase-cycling summation. The evolution of the magnitude of these tensor operators through the sequence is shown in Figure 2-2.

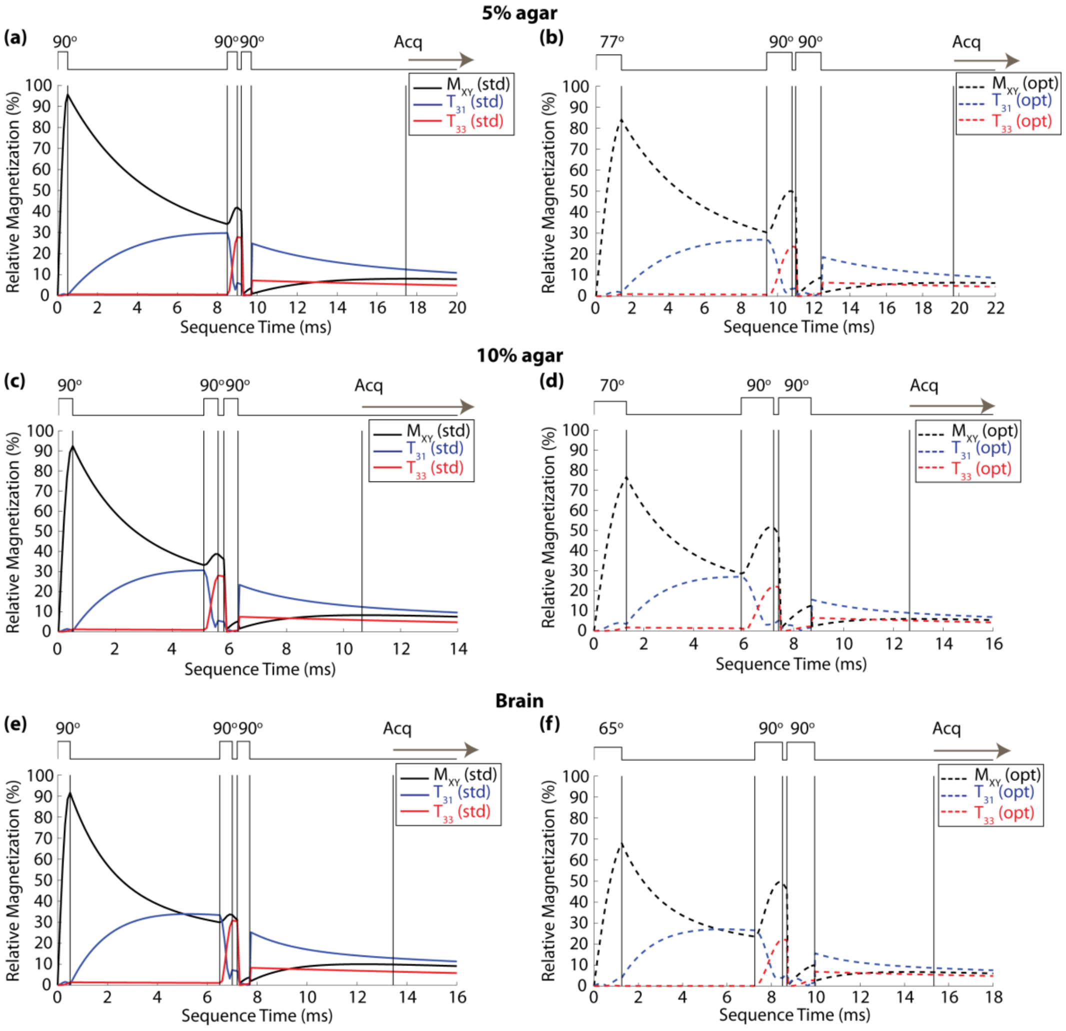

Figure 2-2: Evolution of the relative magnetization of the tensor operators (T_{11} - black, T_{31} - blue, T_{33} - red) through the TQF sequence for different sodium environments that exhibit bi-exponential relaxation. The creation of these tensor operators can be visualized as they are shown together with the timing of the RF pulses. The graphs on the left (a,c,e) (with solid lines) demonstrate the evolution through the sequence using 'standard' parameters (i.e. 90° flip angle and 0.5 ms pulse length with long TR=330 ms) and the graphs on the right (b,d,f) (with dash lines) used optimized parameters (i.e. smaller first flip angle and longer pulse length for all three pulses with shorter TR=110 ms). The plots are the sum of all 6 phase cycling experiments and acquisition of the transverse magnetization T_{11} (i.e. M_{xy}) begins at the dash vertical line indicated by 'Acq' when the TQ signal has evolved to its maximum. Note that transverse magnetization during acquisition for a mono-exponential relaxing environment (not shown) is zero at long TR and negligible (0.1-0.2%) in the optimized (TR=110 ms) case.

Different sodium environments were modeled by a set of spectral density parameters (to be specified in the next sections on the phantom and human brain experiments). The simulations of the TQF sequence varied the first excitation flip angle (between 60^{o}–90^{o} in 1^{o} increments) as well as the duration of all three RF pulses (between 0.5–2.5 ms in 0.1 ms increments) while adjusting TR to maintain constant average power deposition (optimization was performed for a SAR of ~2 W/kg at 4.7T assuming the head weighs ~3 kg). The reason for modifying only the first flip angle is that the generation of T_{33} from T_{31} by the second RF pulse, and the re-regeneration of T_{31} by the third RF pulse, each have a $\sin^2(\theta)$ dependence. Flip angle reduction for these two pulses would lead to excessive signal loss (van der Maarel, 2003). Theoretical relative SNR improvement was calculated with respect to the 'standard' TQF sequence approach according to:

$$rSNR = \sqrt{\frac{TR_{std}}{TR}} \times \frac{M_{XY}}{M_{XY_{std}}} \times 100\% \qquad \text{Eq. 2-1}$$

where TR_{std} is the repetition time of the 'standard' approach with a 90^{o} first flip angle and 0.5 ms RF pulse length. A TR_{std} of 330 ms was required to attain a SAR of ~ 2W/kg at 4.7T. $M_{XY_{std}}$ is the transverse magnetization obtained from simulation at TE for the 'standard' approach. M_{XY} is the transverse magnetization at TE for each combination of first flip angle and RF pulse length when TR has been adjusted for constant SAR.

2.2.2. Phantoms

Two 100-mL cylindrical phantoms (4x9 cm) containing 5% and 10% agar gels (500 mM $[Na^{+}]$) were used to represent different sodium environments. The spectral density parameters for the 5% agar ($J_0(0)$=265 Hz, $J_1(\omega_o)$=21 Hz, and $J_2(2\omega_o)$=18 Hz) and 10% agar ($J_0(0)$=492 Hz, $J_1(\omega_o)$=35 Hz, and $J_2(2\omega_o)$=24 Hz) were derived from the transverse and longitudinal relaxation measurements (Table 2-1). The relaxometry experiments were repeated five times in each agar phantom. T_1 was measured using a non-imaging inversion recovery sequence with a 180^{o} inversion sinc pulse of 26 ms, a non-selective 90^{o} excitation pulse of 1 ms, TR=300 ms, and 10 values for TI between 3 to 100 ms. The magnitudes of the first points in the acquired FIDs for all TI times were fit to a mono-exponential longitudinal relaxation model to yield an estimate of T_1. The two components of T_2 were measured using a non-imaging 4-pulse TQF sequence (Chung, et al., 1990), which is similar to that shown in Figure 2-1 with the addition of a 180^o refocusing pulse of 1 ms between the first and second excitation RF pulses. The three non-selective 90^o excitation pulses were each of 0.5 ms in duration. The preparation time (τ) was varied between 1 to 30 ms in 1 ms increments (TR=300 ms and evolution time (δ) fixed at 0.1 ms), and acquisition began at 0.6 ms after the last RF pulse for 60 ms. The maximum magnitudes of the transverse magnetization from acquired FIDs for all values of τ were fit to a bi-exponential relaxation model to yield estimates of T_{2s} and T_{2f} (Hancu, et al., 1999). Assuming magnetic field inhomogeneities are not significant, the optimal preparation time (τ_{opt}, also equal to TE) was calculated to be 8.0±0.2 ms and 4.6±0.1 ms for the 5% and 10% agar, respectively, using the relation (Navon, 1993)

$$\tau_{opt} = \frac{\ln(T_{2s}/T_{2f})}{1/T_{2f} - 1/T_{2s}} \qquad \text{Eq. 2-2}$$

Alternatively, the maximum magnitudes of the transverse magnetization from all acquired FIDs can be plotted as a function of τ to qualitatively determine τ_{opt} when the TQ signal is at maximum.

The agar phantoms were also imaged three times to compare theoretical and experimental SNR improvement using optimized parameters, selected as outlined in the Results section regarding the simulations, (5% agar: first flip angle=77^o, pulse width=1.4 ms, TE/TR=8/110 ms, δ/τ_{opt}=0.2/8 ms; 10% agar: first flip angle=70^o, pulse width=1.3 ms, TE/TR=4.6/110 ms, δ/τ_{opt}=0.2/4.6 ms) and 'standard' parameters (flip angle=90^o, pulse width=0.5 ms, TR=330 ms, δ/τ_{opt}/TE for 5% and 10% agar same as above). A twisted projection set with a sampling density designed filtering shape (Stobbe, et al., 2008a) (868 projections, twist=0.16, field of view=120 mm, readout duration=17 ms) yielding nominal resolution of 3 mm isotropic was used for the TQ images of the phantoms that were acquired with 3 averages in 28 minutes for each scenario.

Table 2-1: Sodium relaxation parameters measured in 5% and 10% agar phantoms with 500 mM Na (n=5) and taken from the literature for human brain.

	T_{2f} (ms)	T_{2s} (ms)	T_1 (ms)	τ (ms)
5% agar	3.5±0.1	26±0.3	27.4±0.1	8.0±0.2 [a]
10% agar	1.9±0.04	16.9±0.4	19.2±0.2	4.6±0.1 [a]
Brain	1.7 [b]	22.7 [b]	37 [b]	6 [a]

[a] For agar phantoms, τ is calculated using Eq. 2-2 but for brain the τ that yielded maximum TQ signal based on imaging 5 volunteers was chosen.

[b] T_{2f} and T_1 measured in (Bartha, et al., 2004b) and T_{2s} taken from relaxation model used in (Stobbe, et al., 2008b).

2.2.3. In Vivo Human Brain

Optimization of in vivo TQ brain imaging used a one-compartment model with spectral density parameters of $J_0(0)$=558 Hz, $J_1(\omega_o)$=32 Hz, and $J_2(2\omega_o)$=12 Hz (Stobbe, et al., 2008b). The model is based on relaxation parameters measured previously at 4.0T (Bartha, et al., 2004b) and 4.7T (Stobbe, et al., 2006) (T_{2s} was taken from the T_{2s}^* value measured at 4T (Bartha, et al., 2004b) and was lengthened to account for decay associated with static inhomogeneity) (Table 2-1). Five volunteers (30±4 years) were measured with the non-imaging 4-pulse TQF sequence, as described above in phantoms, to estimate τ_{opt} with TR adjusted accordingly to limit SAR below ~2W/kg. τ_{opt} was visually chosen to be 6 ms from observation of the maximum TQ signal, which is nearly the same as the 5.5 ms observed in the previous human brain TQ study at 3T (Hancu, et al., 1999).

Another five volunteers (28±5 years) were imaged with the 3-pulse TQ-filtered sequence (Figure 2-1) using both optimized parameters, selected as outlined in Results section regarding the simulations (first flip angle=65^o, pulse width=1.25 ms, TE/TR=6/110 ms, δ/τ_{opt}=0.2/6 ms, averages=3) and 'standard' parameters (first flip angle=90^o, pulse width=0.5 ms, TE/TR=6/330 ms, δ/τ_{opt}=0.2/6 ms, averages=1) to compare the SNR improvement with the theoretical predictions. This set of optimized parameters was chosen to keep TR and number of averages the same as phantom experiments. Four additional volunteers (31±3 years) were imaged with another possible set of optimized parameters (first flip angle=75^o, pulse width=0.9 ms, TE/TR=6/165 ms, δ/τ_{opt}=0.2/6 ms, averages=2) and 'standard' parameters for the SNR comparison. A twisted projection set (340 projections, twist=0.12, field of view=235 mm, readout duration=18 ms) with a sampling density designed filtering shape (Stobbe, et al., 2008a) that yields nominal 8.4 mm isotropic resolution was created for all in vivo human brain imaging. Each TQ brain image set was acquired in 11 minutes. SQ sodium images were also acquired (90^o flip angle, TE/TR=0.5/120 ms, pulse width of 0.8 ms, and 1 average) with resolution identical to TQ images in 40 seconds for identifying gross anatomy. Region of interests (ROIs) were manually drawn on SQ images (and overlaid on TQ images) in the brain tissue (avoiding cerebrospinal fluid (CSF) space) and the background noise to calculate SNR.

2.2.4. Supplementary Study

As will be evident in the Results, the CSF spaces on sodium brain images produced with either the optimized or 'standard' TQ-filtered sequence parameters were not void of intensity. This is also the case in the previously published TQ-filtered human brain images which implemented short 90^o RF pulses and a TR of 130 ms at 3T (Hancu, et al., 1999), even though phase cycling should completely cancel all signal from mono-exponentially relaxing nuclei. However, we recently presented TQF sodium images of the human brain in which the CSF spaces were void of intensity (Tsang et al., 2009). This prompted further investigation into the combined effect of the first flip angle and TR on the SQ signal breakthrough in saline/CSF space for a TQF image. Using simulation based on optimized TQF sequence parameters for brain, the evolution of the transverse magnetization in saline (T_1=T_2=54 ms measured at 4.7T)/5% agar and CSF (based on T_1=T_2=64 ms measured using a different method in the human brain at 4T (Bartha, et al., 2004b))/brain tissue (using the one-compartment brain model described above) was explored for different first flip angle (50^o, 65^o and 90^o) and TR (82, 110, and 200 ms). Note that a saline/agar model was also simulated for first flip angle of 60^o, 70^o, 80^o, and TR=50 ms. Pulse width was adjusted to 2 ms for CSF/brain tissue to accommodate for the greatest SAR associated with the 90^o flip angle at short TR of 82 ms.

Imaging experiments were performed first in a saline phantom (550-mL 100 mm diameter sphere filled with 500 mM [Na^+]) to explore SQ signal breakthrough and then in a two compartment phantom (10-mL 20 mm diameter sphere filled with 500 mM [Na^+] saline immersed in a 450-mL 70 mm diameter cylindrical container of 5% agar gel with 100 mM [Na^+]) to investigate the interaction of SQ signal breakthrough with TQ blurring signal. Both phantoms were imaged with the following parameters: first flip angle=$50^o/65^o/90^o$, pulse width=1.25 ms, TE=6 ms, TR=50/82/110/200 ms, δ/τ_{opt}=0.2/6 ms, averages=1. The same twisted projection set above for brain imaging was used to acquire images in 1.7, 2.8, 3.7, and 6.8 minutes for TR of 50, 82, 110, and 200 ms, respectively.

Furthermore, five new volunteers (28±5 years) were imaged with the TQF sequence (first flip angle=$50^o/65^o/90^o$, pulse width=2 ms, TE/TR=6/82 ms, δ/τ_{opt}=0.2/6 ms, averages=4) to explore the effect of SQ signal breakthrough and its interaction with TQ blurring signal from brain tissue in the short TR case. The acquisition times of TQ and SQ images were same as described above. Average signal intensities were measured within ROIs drawn in the ventricles, eyes, and brain tissue on TQ images to calculate the proportion of SQ signal breakthrough (assumed to be the case in the fluid-filled ventricles and the vitreous humor of the eyes) and/or blurring relative to the surrounding brain tissue signal.

2.3. Results

2.3.1. Simulations

The evolution of T_{11}, T_{31}, and T_{33} coherences through the TQF sequence with optimized (to be outlined in next paragraph) and ‘standard’ parameters for the agar gel phantoms and brain is shown in Figure 2-2. The relative transverse magnetization (T_{11} or M_{xy}) at TE, following summation of the six TQF phase-cycles, was lower using the optimized parameters (5% agar=6.4%; 10% agar=6.0%; brain=6.6%) compared to ‘standard’ parameters (5% agar=8.0%; 10% agar=8.3%; brain=9.8%). This is the result of reduced first flip angle, increased RF pulse length and very minor T_1 related weighting. However, because of the lower powered RF pulse, a shorter TR is permitted in the optimized case which enables increased averaging for the same scan duration (and reduced noise variance). Note that TQF signal produced is only a fraction (~6-10%) of the available longitudinal magnetization. It is this small signal fraction that provides the impetus for TQF sequence SNR optimization. It is also important to note that TQ signal loss by $\sin^5\theta$ shown in previous work (Hancu, et al., 1999) resulted from reducing flip angle of all 3 RF pulses and cannot be used to describe the signal loss (prior to averaging) obtained in our optimization approach.

Relative transverse magnetization after a single average (Figure 2-3a-c) and relative SNR after multiple averages for equivalent scan time (Figure 2-3d-f) is plotted for different combinations of pulse length, first flip angle and TR that have equivalent time-averaged power deposition. Relative M_{xy} loss of ~16% for brain (Figure 2-3c) is observed when the RF pulse length is increased from 0.5 ms to 0.9 ms for the first flip angle of 90^o, consistent with results in previous work (Hancu, et al., 2000). The associated TR for each sodium environment is given in Figure 2-3g for each first flip angle and pulse width combination. For experimental verification of optimization, the first flip angle and pulse width for each environment (marked with “**X**”, “+”, “*” and “#” for 5% agar, 10% agar, and brain on Figure 2-3, respectively) were chosen to achieve SNR benefit such that the associated TR was 110 or 165 ms, an integer factor of the 330 ms required for the ‘standard’ approach (marked with “**O**”). At TR of 110 ms, theoretical SNR improvements of 40%, 26%, and 16% are predicted for 5% agar, 10% agar, and brain (optimized parameters are first flip angle of 65° and an RF pulse length of 1.25 ms), respectively, when three averages are implemented for the same scan duration as the ‘standard’ approach. An alternate set of parameters (marked with “#”, first flip angle=75°, pulse length=0.9 ms and TR=165 ms) could have been chosen for the brain, accommodating 2 averages within the same scan time with predicted theoretical SNR improvement of 18%.

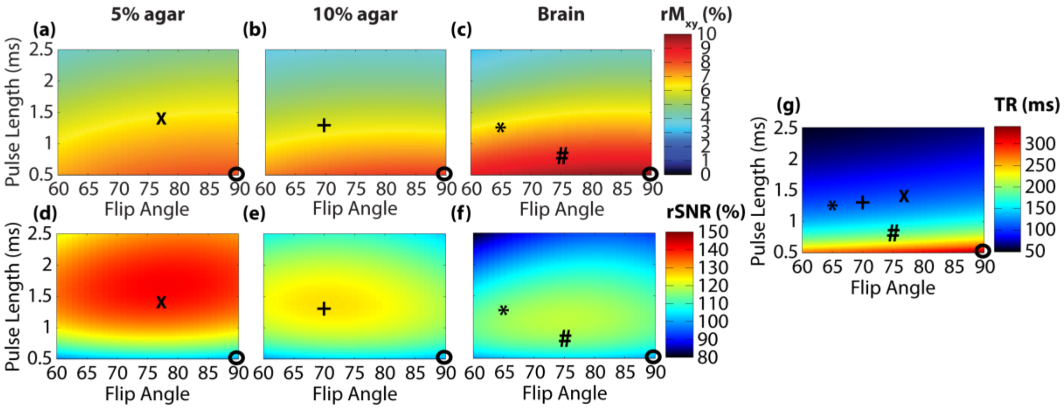

Figure 2-3: Simulations showing relative transverse magnetization at beginning of acquisition in the 3-pulse TQF after one average and relative SNR increase associated with shorter TR and multiple averages. The optimized parameters chosen are marked with ‘X’, ‘+’, ‘*’ and ‘#’ for 5% agar (a,d), 10% agar (b,e), and brain (c,f) respectively, and that with ‘standard’ parameters is marked with ‘O’. Note that the relative SNR for the 'standard' parameters is 100% for each environment (i.e. absolute comparisons of SNR cannot be made between environments). The corresponding TR for each environment is marked with the same symbol shown on (g). In (g), the TR values for the optimized cases (110 ms – ‘X’, ‘+’, ‘*’; 165 ms – ‘#’) were chosen to be integer multiples of the TR of 330 ms needed to satisfy SAR for the 0.5 ms, 90° flip angle ‘standard’ case in order to allow 3 or 2 averages in the same scan time. This in turn led to the choices of flip angle/pulse length combinations shown in (d-f).

2.3.2. Phantoms

SNR increase observed in the homogeneous phantoms imaged three times with ‘standard’ and optimized TQ sequence parameters were 39±2% for the 5% agar and 27±2% for the 10% agar (Figure 2-4), which is consistent with the theoretical SNR increase of 40% and 26% predicted from simulation.

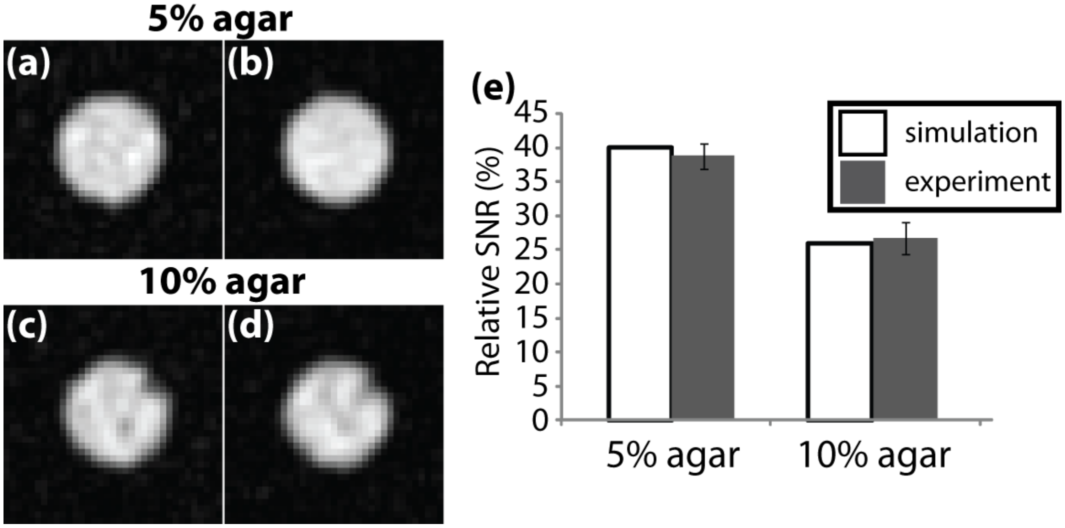

Figure 2-4: One representative transverse slice of the 5% and 10% agar phantoms imaged with the ‘standard’ TQ sequence parameters (a,c) and optimized parameters (b,d) to demonstrate the SNR advantage in the latter case. (e) The relative SNR predicted from simulation is in excellent agreement with that obtained experimentally.

2.3.3. In Vivo Human Brain

The mean TQ brain SNR in all five volunteers was 13.1±0.9 acquired with 'standard' parameters and 15.9±1.3 for the optimized parameters to yield an observed SNR increase of 22±5% (Figure 2-5). In the four subjects imaged with an alternate set of optimized parameters (first flip angle=75^o, pulse width=0.9 ms, TR=165 ms), the measured SNR benefit over standard parameters was 20±7%. These are higher than the simulation predicted 16% or 18% improvement, possibly due to differences in the model to describe average brain tissue relaxation characteristics. Image intensity is non-zero in the ventricular space using either TQ approach but appears to be eliminated in the vitreous humor, more in line with the expected suppression of sodium nuclei in a mono-exponential T_2 environment.

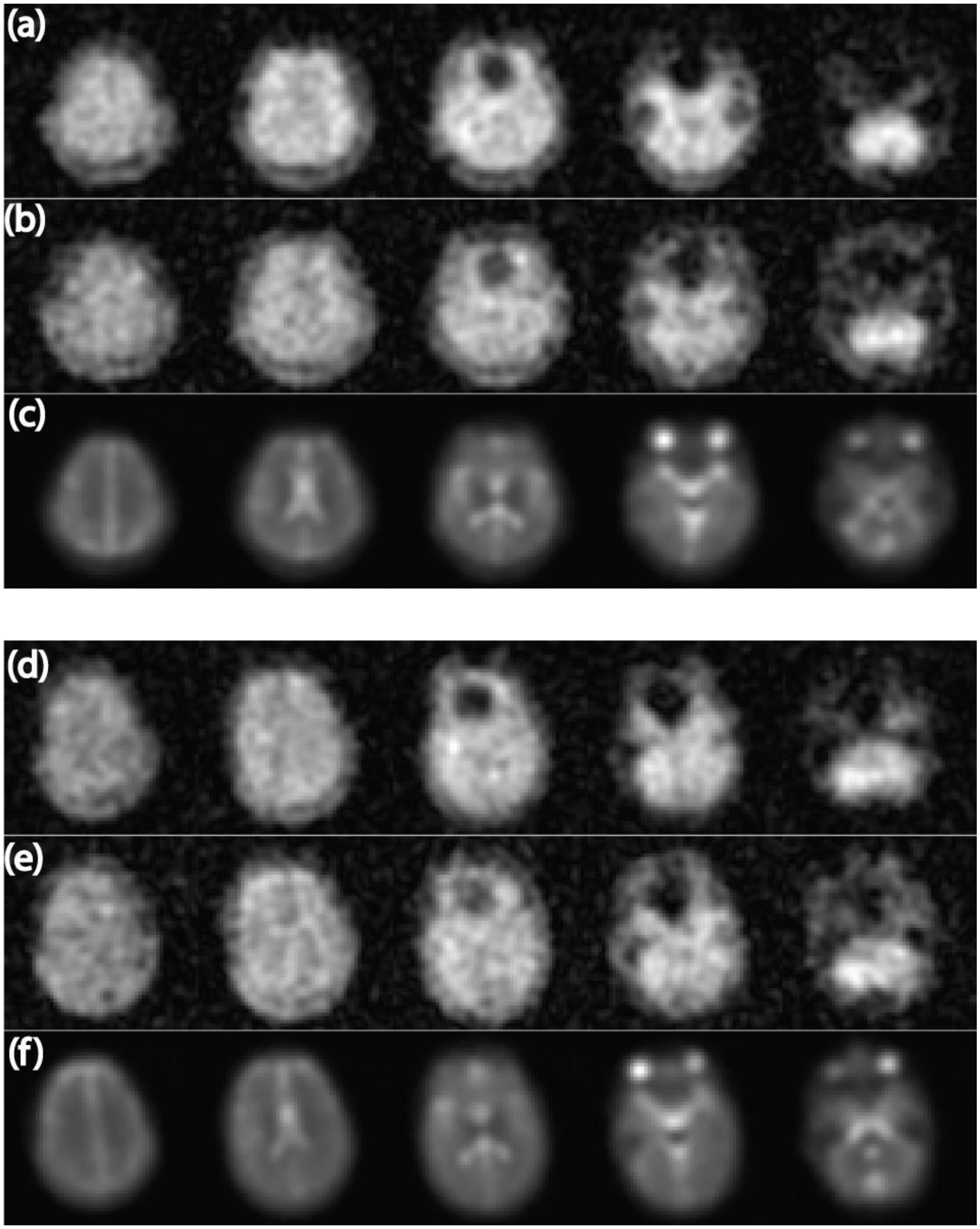

Figure 2-5: Selected in vivo TQ sodium images from two volunteers showing slices at different brain levels demonstrating SNR benefits of 18 and 24% acquired with the optimized parameters (first flip angle=65^{o}, pulse width=1.25 ms, TR=110 ms) (a,d) over the ‘standard’ parameters (b,e). SQ sodium images are shown (c,f) for comparison. The TQ images had identical scan time of 11 minutes and nominal spatial resolution of 8.4x8.4x8.4 mm^{3}. The SQ images had the same spatial resolution but were acquired in 40 seconds.

2.3.4. Supplementary Study

Investigation of SQ signal breakthrough in the saline/CSF spaces began with simulation, and the anti-symmetric (or 90^o out-of-phase) component of transverse magnetization, i.e. $T_{11}(a)$, is shown in Figure 2-6. Simulation suggests that no resultant signal should be produced from sodium nuclei in saline or CSF when the TR is 200 ms. However, the magnitude and sign of SQ signal produced at short TR (i.e., 50 or 82 ms) is dependent on the first flip angle. For CSF with TR=82 ms, this transverse magnetization at the beginning of acquisition is -1.3%, -0.1% and 0.9% (of the available longitudinal magnetization) for the first flip angles of 90^o, 65^o and 50^o respectively (Figure 2-6d-f). This is significant given that CSF has a sodium concentration of 2 to 5 times that of gray and white matter as measured from quantitative sodium MR approaches (Lu et al., 2010; Ouwerkerk, et al., 2003). Multiplication of CSF transverse magnetization values by this factor yields significant signal that can either enhance or counteract the spatial 'blurred-in' TQ sodium signal from brain tissue. It is important to note that the magnitude of relative $T_{11}(a)$ is only reduced slightly between first flip angle of 90^o and 50^o in agar (Figure 2-6a-c) and brain (Figure 2-6d-f) because a constant pulse width was used to simulate each environment. On the other hand, the large decrease of relative transverse magnetization between the 'standard' and 'optimized' cases shown in Figure 2-2 results from the combined effect of increasing pulse width together with shortening TR and reducing the first flip angle.

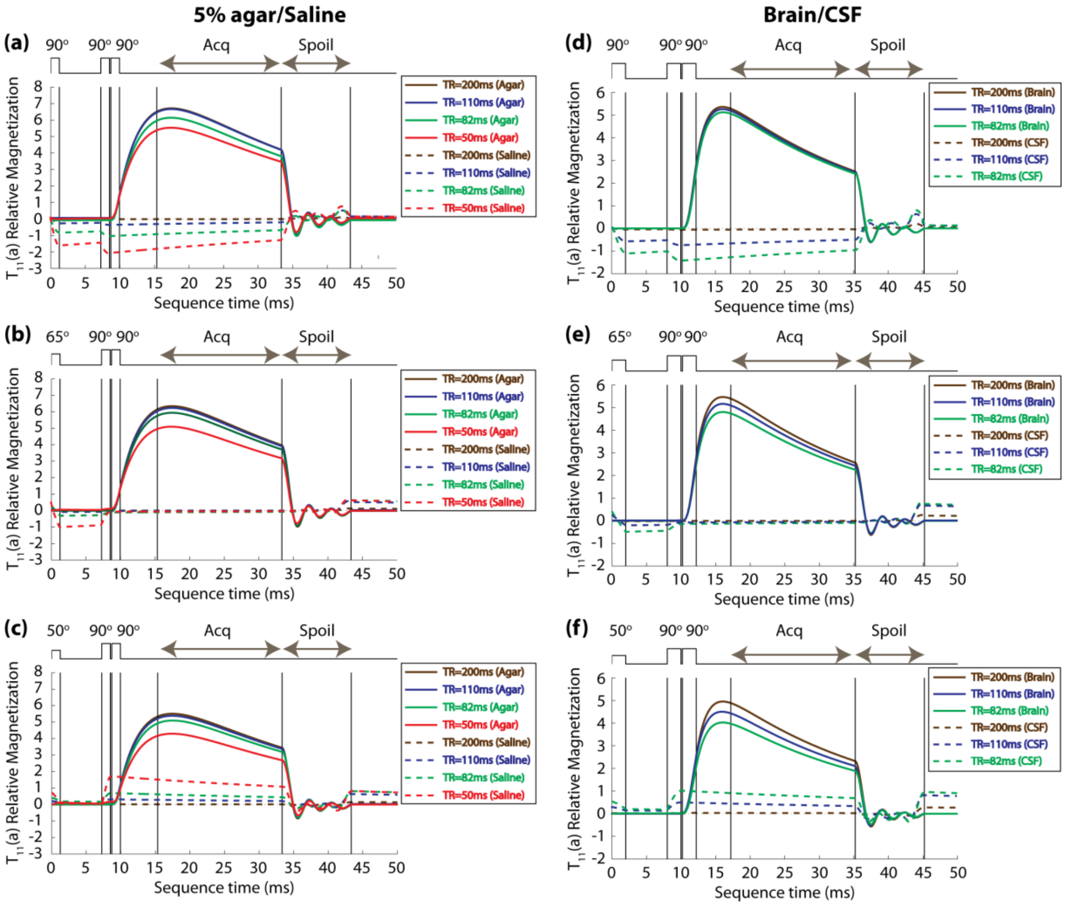

Figure 2-6: Quantum simulation of 90^{o} out-of-phase T_{11}(a) transverse magnetization component in saline/CSF (dash line) and agar/brain tissue (solid line) as it evolves through the TQ-filtered sequence (displayed following phase-cycle summation). Note that the in-phase component of transverse magnetization, T_{11}(s), is negligible during the acquisition period in each case. Note also that the pulse width has no effect in the sign and magnitude of SQ signal produced. The duration of TQ signal acquisition is indicated by ‘Acq’ with horizontal arrow. Gradient spoiling of the transverse magnetization (indicated by ‘Spoil’) follows after acquisition. No SQ sodium signal was predicted to pass through the filter using long repetition time (200 ms) with 90^{o} (a,d), 65^{o} (b,e), or 50^{o} (c,f) for the first RF pulse. However, the sign and magnitude of SQ ‘breakthrough’ signal from saline (a-c) or CSF (d-f) varies as the first flip angle is reduced from 90^{o} to 50^{o} when shorter repetition times are used in the TQ filter.

SQ signal breakthrough was demonstrated in the saline phantom (Figure 2-7). Relative mean M_x intensity (representing relative $T_{11}(a)$) measured on TQ images is similar and negligible for all first flip angle at TR=200 ms. The sign and magnitude of the relative intensity at TR=50 ms (1.7% and -1.7% for first flip angle of 50^o and 90^o respectively) is also consistent with simulation. Note that SNR gain due to SQ signal breakthrough in the first part of this study is unlikely as the relative $T_{11}(a)$ of first flip angle of 65^o at TR=110 ms is similar to that of first flip angle of 90^o at TR=200 ms. This SQ signal breakthrough and its interaction with 'blurred-in' TQ signal from agar was demonstrated in the two-compartment phantom (Figure 2-8). With 5 times more concentration of sodium in saline than agar in this phantom, the TQ blurring signal in the saline compartment is enhanced with the positive SQ signal breakthrough (M_x intensity = 155±10) for first flip angle of 50^o (Figure 2-8j) and offset with the negative SQ signal breakthrough (M_x intensity = -35±33) for first flip angle of 90^o (Figure 2-8l) at TR=50 ms, which is consistent with simulation and the previous saline experiment.

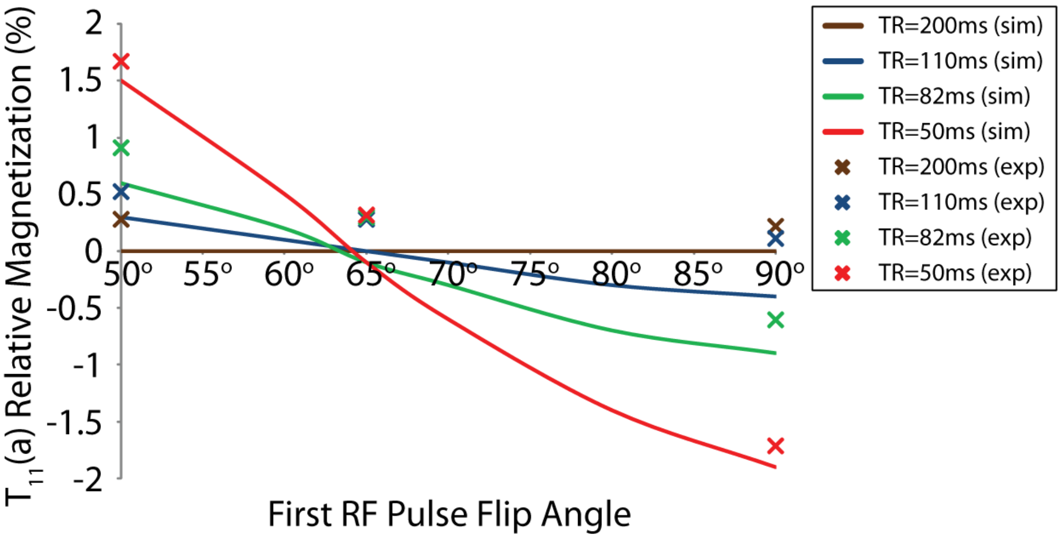

Figure 2-7: Mean M_x intensity (real component of the Fourier transformed data in each voxel) in the saline region was measured relative to the SQ image of saline phantom. The SQ image was acquired with TR=200 ms, pulse width=0.5 ms, RF pulse=90^o, averages=6, using identical twisted projection set as TQF imaging in 6.8 minutes. Efficiency of the TQ-filter to ‘block’ the SQ breakthrough signal is decreased when the first flip angle is not 65^o at short TR. Experimental results are slightly higher than simulations possibly due to noise and imperfection of RF pulse phase cycling.

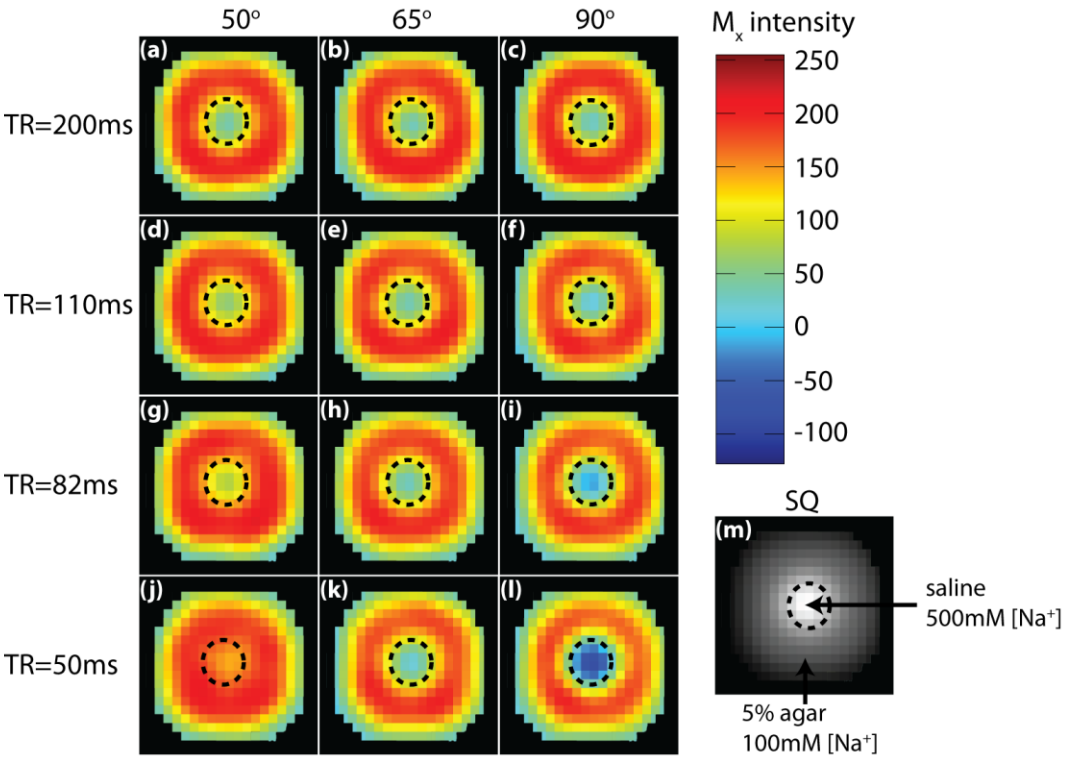

Figure 2-8: One representative transverse slice of the two-compartment phantom imaged with various TR and first flip angle to demonstrate the interaction of SQ signal breakthrough of saline with the TQ agar blurring signal into the center compartment. A corresponding SQ image was acquired (m) with the 2 compartments labelled. The nominal resolution for all images is 8.4 mm isotropic. The M_x component of the acquired FID is shown in images a-l to represent T_{11}(a). The positive T_{11}(a) intensity (69±20, 69±20, and 61±21 for first flip angle of 50^o, 65^o, and 90^o respectively; 8a-c) in the center compartment for TR=200 ms is most likely blurring TQ signal from surrounding agar. At TR=50 ms, the TQ blurring signal in the saline compartment is enhanced with the positive SQ signal breakthrough (155±10) for first flip angle of 50^o (j) and offset with the negative SQ signal breakthrough (-35±33) for first flip angle of 90^o (l). Note the sign and magnitude of T_{11}(a) intensities in the center compartment for all combinations of TR and first flip angle is consistent to the simulation results shown in Figure 2-6.

Furthermore, TQ images of five volunteers also demonstrated that image intensity in the ventricles depended on the first flip angle when TR was reduced (two examples are shown in Figure 2-9). Intensity in the lateral ventricles is not voided in the images acquired with first flip angle of 65^o and TR of 82 ms (Figure 2-9a,d). Recall from Figure 2-6e that only a small (-0.1%) SQ signal breakthrough is expected for CSF at a first flip angle of 65^o. In the same imaging session, the volunteers were also imaged with first flip angle of 90^o keeping all other sequence parameters constant; in this case the intensity in the lateral ventricles has clearly been voided (Figure 2-9b,e) likely due to negative SQ signal of the CSF offsetting the blurred-in TQ brain signal. However, there is variability in the amount of image intensity ‘voiding’ amongst the subjects. Because we expected the 'blurring-in' of signal from surrounding brain tissue to be more prominent in the ventricles than in the eyes, given the isolation of the eyes from brain tissue, we measured the image intensities on the TQ images in both regions among the five subjects. The proportion of intensity in the vitreous humor/brain tissue was found to be 0.16±0.04, 0.25±0.15 and 0.39±0.18 for the first flip angle of 90^o, 65^o, and 50^o, respectively, whereas the proportion in the ventricles in relation to brain tissue was 0.48±0.13, 0.89±0.05 and 1.21±0.08.

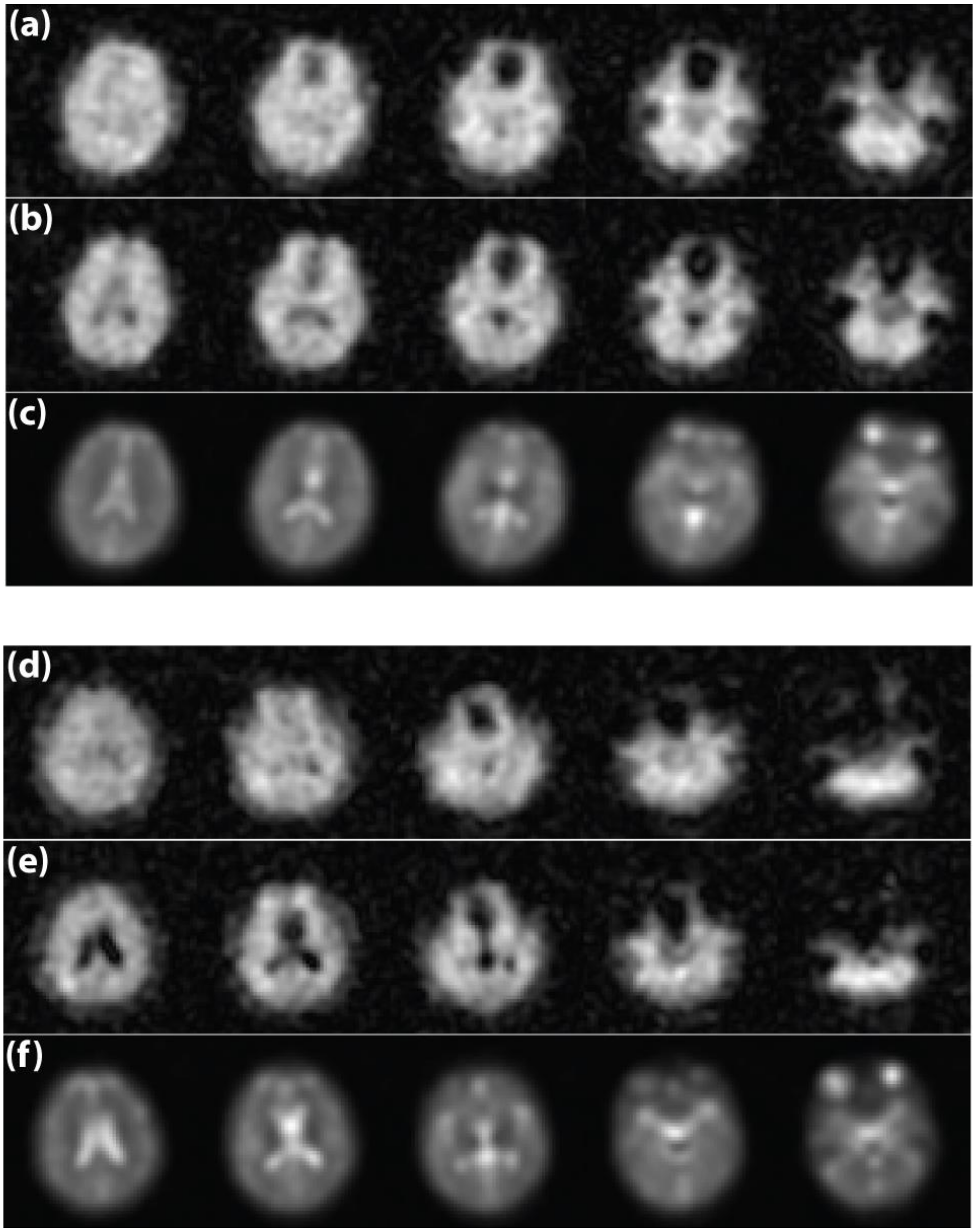

Figure 2-9: Selected in vivo TQ sodium images over multiple slices from two volunteers demonstrating image intensity remaining in the CSF compartment most likely due to TQF signal blurring from adjacent brain tissue when imaged with first flip angle=65^o and pulse length=2 ms (a,d). The image intensity in CSF is minimized when imaged with a first flip angle=90^o and pulse length=2 ms (b,e), likely due to cancellation from negative SQ signal breakthrough from ventricular saline with positive TQF blurring signal from surrounding brain tissue. All TQ images were acquired with TR=82 ms. However the amount of cancellation between the two volunteers is not consistent. Notice that the residual image intensity in the vitreous humor in the eyes is quite small for all TQ images. Corresponding SQ images acquired in 40 seconds with the same projection set are presented to show gross anatomy (c,f).

2.4. Discussions

The goal of TQ filtering is to weight the acquired image towards signal from intracellular-sodium, however, the TQF signal produced is only a small fraction (< 10%) of the available longitudinal magnetization making TQ imaging particularly daunting given the already low sensitivity and concentration of sodium in tissue such as the brain. Therefore, much effort is still required to increase the SNR for TQF sodium MRI. In the past, the optimal flip angles to acquire maximum TQF signal were found to be 90^{o} in phantom experiments (Reddy et al., 1994; Van Der Veen et al., 1993). Also, short RF pulse lengths of 100 μs were demonstrated to yield approximately 15% higher TQF signal than longer pulse lengths of 500 μs due to rapid relaxation during longer RF pulses (Hancu, et al., 2000). However, when considering the SAR constraint, higher SNR TQF images can be obtained when substantially larger RF pulse lengths are implemented in combination with a reduced first flip angle. Although this reduces the signal produced following the TQ-filter, the reduced RF power associated with these two aspects enable shorter TR and increased averaging, with concomitant noise variance reduction and ultimately higher SNR, for a given scan length. Experimentally, we obtained SNR increase of 39±2% and 27±2% for the 5% and 10% agar gel phantoms respectively measured from TQ images acquired with optimized over ‘standard’ parameters, which agrees very well with simulation. Similarly higher SNR of 22±5% in brain was measured among 5 volunteers. It is shown that in vivo TQ brain images can be acquired in a clinically relevant scan time of 11 minutes at 4.7 T with a nominal resolution of 8.4 mm isotropic (Figures 5, 9), almost half the scan time of the previous TQ-filtered human brain image at 3T (Hancu, et al., 1999). However, it is acknowledged that even with these SNR improvements, TQF sodium imaging will still be relegated to the study of large lesions for patient applications.

A supplementary study was carried out to explore the effect of TR and first pulse flip angle on image intensity within the lateral ventricles, given that they could not be visualized on either optimized or 'standard' TQF images (or on previously published images at 3T (Hancu, et al., 1999)), but could be visualized on a previously presented abstract (Tsang, et al., 2009). A previous study (Keltner, et al., 1994) has suggested that SQ signals can pass through the TQ-filter when TR is sufficiently short. In this paper we show that depending on the flip angle of the first RF pulse and at short TR, this breakthrough can either be in-phase or 180^o out-of-phase from signal produced in the presence of bi-exponential relaxation. Image intensity present in the ventricular space may be the result of 'blurring-in' from surrounding brain tissue signal since intensity is non-zero in the ventricles even at long TR when simulation predicts no SQ breakthrough. It is important to note that SQ breakthrough within the fluid (CSF) space is a completely different, but off-setting, effect from the spatial blurring (or smearing) of adjacent TQ signal. This 'blurred-in' signal in central fluid spaces can be cancelled by negative SQ breakthrough when a 90^o first RF pulse is used in combination with a short TR (Figure 2-9b,e). However, we do not suggest this to be an appropriate approach, as essentially we have two artifacts cancelling each other.

The blurring effect assumed to be the source of image intensity in the ventricle locations is caused by long readout time and rapid transverse signal decay in addition to large voxel size. One could reduce this adverse blurring effect by using a shorter readout time and smaller voxel size but would require substantial increase to the total scan time for more averaging to compensate SNR. Image intensity in the ventricle locations may also be due to pulsation in CSF which could potentially corrupt the phase cycling; this should be investigated in future studies.

It should be noted that gradient spoiling following acquisition was used in this implementation of TQ-filtering for both simulation and experiment resulting in negligible SQ breakthrough (~0.1% from simulation) for the optimized brain imaging parameters (first flip angle of 65^o at TR=110 ms). It should also be noted that SQ breakthrough can be described in terms of a stimulated echo, and is dependent on residual transverse magnetization remaining at the end of TR. While the application of a gradient may dephase transverse magnetization following one acquisition, this 'left-over' magnetization can be re-phased through subsequent gradients. We have shown in the supplementary study that SQ signal breakthrough may be developed (if a first flip angle of 65^{o} is not selected; Figures 2-6,2-7) because the reduced TR leads to a steady-state, ‘stimulated-echo-like’ effect for mono-exponentially relaxing nuclei exhibiting relatively ‘long’ T_2 decay. However, the steady-state process that causes SQ breakthrough in fluid environments will essentially be non-existent in relevant bi-exponentially relaxing environments. It is important to note that the proposed optimized brain TQF sequence with phase cycling, which uses a short TR, and can eliminate SQ signals with judicious choice of flip angle, is not equivalent to the steady-state free precession (SSFP) sequence which has shown complex sodium spin responses (Kharrazian et al., 2006).

The effect of B_0 inhomogeneities in TQF imaging has been investigated previously and strategies have been proposed and demonstrated in phantoms (Fleysher, et al., 2010b; Matthies, et al., 2010; Tanase, et al., 2005). However, we did not implement the above correction schemes in this work as the total scan time would become impractical for patient scans, because of the need for additional phase cycling steps. Manual shimming (x,y,z,z^2) was performed prior to imaging, and off-resonance effects are not apparent in most of brain tissue. However B_0 correction schemes could be implemented if required.

Some of the improvements in the TQ image quality and reduced scan time reported here are due to inherent increases of SNR at 4.7T relative to the earlier study at 3T (Hancu, et al., 1999). Sites with a 7T MRI scanner should expect a 50% improvement of SNR versus our 4.7T, with an additional advantage related to an increasing of the bi-exponential relaxation proportion (Fleysher et al., 2010a; Qian et al., 2010). However, tissue heating (i.e. SAR) is further constrained at 7T as it depends on B_0^2 which must be mitigated by the adjustment of flip angle, pulse length, and TR. Simulation (not shown) of brain at 7T estimates that optimized parameters (first flip angle=70^o, pulse width=1.3 ms, TR=247 ms, 3 averages) yields ~23% higher SNR over standard parameters. The optimization method presented here can also be applied for TQF sodium MRI at other field strengths for in vivo brain imaging or even for other anatomies such as cartilage (Borthakur et al., 1999; Reddy et al., 1997a), or spinal disc tissue (Ooms et al., 2008), but note that this has not been evaluated in pathologic conditions. The results presented here suggest that using a first RF flip angle of 65^o leads to a minimization of SQ signal breakthrough for mono-exponential relaxing nuclei in fluid at short TR. In this work, we propose the sequence parameters of first flip angle=65^o, pulse length=1.25 ms, and TR=110 ms to be the optimal choice for 3-pulse TQF human brain sodium imaging at 4.7T to maximize SNR and minimize SQ breakthrough from sodium in CSF. Alternatively, although we chose to focus on shorter TR parameter sets, inspection of Figure 2-3f suggests that using 90^o RF pulses all with longer pulse lengths of 1 ms, and TR=165 ms can also yield ~14% higher SNR with SQ signal suppressed. If more projections were needed in a given time, the previously mentioned shorter TR set may be preferable. Further marginal increase in SNR (15%) is possible if all three flip angles were also reduced to 85^o (simulations not shown). However, even smaller flip angles for the last two RF pulses are not desirable due to the excessive loss of TQ signal (Reddy, et al., 1994) which cannot be recovered by increased averaging in a limited scan time. Further improvements in spatial resolution and minimization of blurring are necessary to bring triple quantum sodium imaging of the brain closer to clinical application.

Chapter 3

Evaluation of B_0-Inhomogeneity Correction for Triple-Quantum-Filtered Sodium MRI of the Human Brain at 4.7T[2]

3.1. Introduction

Triple-quantum-filtered (TQF) sodium imaging may offer a non-invasive method to detect intracellular sodium concentration changes in neurological disorders. TQF sodium signal in animal models of tumor (Griffey, et al., 1990; Winter, et al., 2001b) and ischemia (Kalyanapuram, et al., 1998; LaVerde, et al., 2007) have demonstrated greater changes than single quantum (SQ), or bulk sodium, signal changes. The TQF sequence is typically implemented with three non-selective radiofrequency (RF) pulses and six-step phase cycling (Jaccard, et al., 1986) to 'extract' signal from sodium nuclei producing TQ coherence, or those nuclei which exhibit bi-exponential T_2 relaxation, while suppressing signal from mono-exponentially relaxing nuclei. This sequence, without a 180^o RF pulse during the preparation period to refocus B_0 inhomogeneities, is particularly suited for human brain imaging because of its reduced specific absorption rate (SAR) and smaller TQF signal loss due to flip angle variation (Hancu, et al., 1999). However, a potential problem with this sequence is that B_0 inhomogeneity may lead to undesirable signal loss. Three correction methods have been proposed to rectify TQF signal loss due to B_0 inhomogeneities (Fleysher, et al., 2010b; Matthies, et al., 2010; Tanase, et al., 2005), but the disadvantage of implementing any of these methods is a significant (2 or 4 times) increase of scan time, *without the expected increase of SNR*. The primary problem of TQF imaging is that the TQF signal is only a small fraction (typically ~1/10 for brain) of the SQ sodium signal, and

---

[2] A version of this chapter has been published. A. Tsang, RW. Stobbe, C. Beaulieu, 2013. Evaluation of B_0-inhomogeneity correction for triple-quantum-filtered sodium MRI of the human brain at 4.7 T. Journal of Magnetic Resonance. 230:134-144. Dr. Stobbe was involved in this study with verifying the simulation results as well as editing the manuscript.

hence TQF images suffer low signal-to-noise ratio (SNR) and poor spatial resolution when compared to standard SQ sodium imaging. Given the very low SNR/voxel-volume relationship for human brain TQF sodium imaging, the effective SNR loss associated with B_0 inhomogeneity correction for a constant scan duration is of particular concern. What remains unknown is the extent to which B_0 inhomogeneity correction is necessary for TQF sodium imaging of the human brain, given that these correction methods have only been demonstrated in the context of agar phantoms.

This exploration of the impact of off-resonance on healthy human brain TQF imaging and the recovery of signal using two different correction methods (from Fleysher et al. (Fleysher, et al., 2010b) and Matthies et al. (Matthies, et al., 2010)) is performed at 4.7 Tesla, a moderately high field. Simulation of signal loss for both ‘Standard’ (Hancu, et al., 1999), and ‘SNR-optimized’ (Tsang et al., 2012) TQF sequence parameters, as well as simulation of the effectiveness of correction for each set of sequence parameters, is verified with agar phantom imaging. Using simulation results, resonant frequencies are divided into three pools based on expected signal loss for both sets of TQF sequence parameters. The average signal intensity on healthy human brain images within each of these three different resonant frequency ranges, as identified on B_0 maps, is then compared to expected signal loss. The average signal intensity in these pools is also measured when the two correction methods have been applied. Finally, the proportion of voxels in the off-resonant pools where signal loss is mitigated by off-resonance correction methodology is determined to assess its need for TQF human sodium brain imaging at 4.7T.

3.2. Methods

Imaging experiments were performed in this study using a 4.7T Varian Inova Scanner (Walnut Creek, CA) and an in-house designed and manufactured single-tuned bird-cage head coil.

3.2.1. TQF Sequence Parameters

Two different sets of TQF sequence parameters were chosen to evaluate signal loss as a result of off-resonance and its correction. Each was associated with the 3-pulse TQF sequence shown in Figure 3-1. Note that in this paper τ and δ is referred to as the preparation and evolution times respectively. The first sequence is labelled the 'Standard' TQF sequence. It includes 90^o flip-angles for each of the three RF pulses in the sequence and RF pulse widths of 0.5 ms, TR = 330 ms to satisfy SAR at 4.7T, τ = TE = 6 ms, and δ = 0.2 ms. The value τ = TE = 6 ms was selected from TQF signal optimization for the human brain at 4.7 Tesla. The second sequence is labelled the 'SNR-optimized' sequence, and was introduced in (Tsang, et al., 2012) as well as presented in the previous chapter. This sequence employs longer RF pulses of 1.25 ms and a first RF pulse flip angle of 65^o to facilitate TR reduction to 110 ms under SAR constraint. Reduced TR allows increased averaging and noise power reduction within a constant scan duration. The value of τ = TE was also 6 ms for this sequence and δ = 0.2 ms. Sequence parameters are summarized in Table 3-1.

Each TQF image (and SQ sodium image used for B_0 mapping) was acquired using 3D twisted projection acquisition (340 projections, twist = 0.12, field of view = 235 mm, readout duration = 18 ms) with a sampling density designed filtering shape (Stobbe, et al., 2008a) that yields nominal 8.4 mm isotropic resolution. Image reconstruction was performed using standard convolution based gridding.

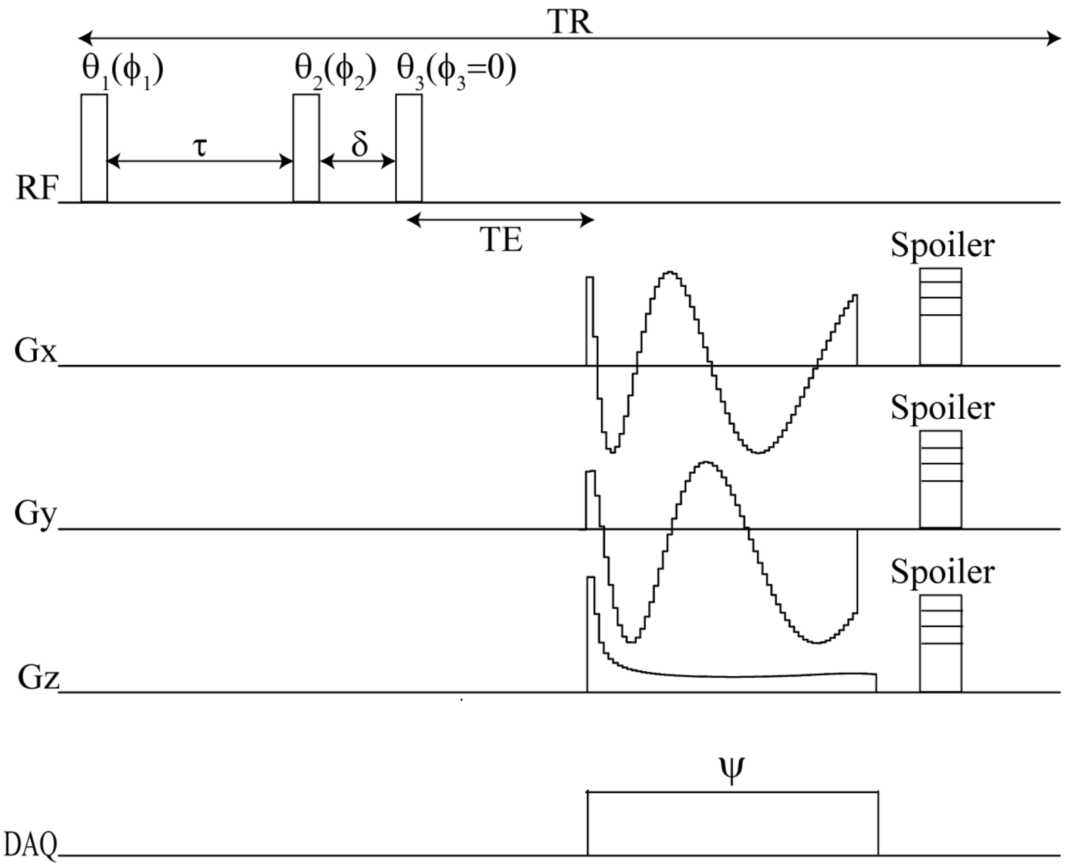

Figure 3-1: RF pulse timings of the 3-pulse TQF sequence. The values of flip-angle, RF pulse length, and TR for the 'Standard' and 'SNR-optimized' TQF sequences are given in Table 3-1. The phases for the first and second RF pulses (ϕ_1 and ϕ_2) along with the receiver phase ψ are indicated in Table 3-2 for the two off-resonance correction methods implemented. The spoiler gradients are turned on for 10 ms after data acquisition.

Table 3-1: Summary of TQF sequence parameters used in this study

TQF sequence	**RF flip angles**	**RF pulse length**	**TR / TE**	**NEX**	**τ / δ**
SNR-optimized	65^o,90^o,90^o	1.25 ms	110 / 6 ms	2	6 / 0.2 ms
Standard	90^o,90^o,90^o	0.5 ms	330 / 6 ms	1	6 / 0.2 ms

3.2.2. TQF Off-Resonance Correction Methods Tested

Two different methods of mitigating TQF signal loss as a result of off-resonance were tested in this study for each of the two TQF sequences described above. *Method 1* is that of Fleysher et al. (Fleysher, et al., 2010b) and *Method 2* that of Matthies et al. (Matthies, et al., 2010). The phases of the RF pulses, labelled as ϕ in Figure 3-1, associated with each TQF acquisition are listed in Table 3-2. Note that a 'TQF acquisition' in this paper is equivalent to one phase cycling *set*, which consists of six steps. Two different TQF acquisitions (referred to as *1a*, *1b*, and *2a*, *2b* in Table 3-2 for *Method 1* and *Method 2* respectively) are required for each method and combined in post-processing to construct a B_0 corrected image (see section 3.2.6). Note that by itself, the TQF acquisition *2a* is used to acquire TQF images without B_0 inhomogeneity correction.

Table 3-2: RF pulse phase cycling steps and receiver phase of the TQF acquisitions for B_0 correction *Method 1* (Fleysher, et al., 2010b) and *Method 2* (Matthies, et al., 2010)

TQF acquisition[a,b]	First RF pulse phase (φ_1)[c]	Second RF pulse phase (φ_2)[c]	Third RF pulse phase	Receiver phase (ψ)[c]
1a	$k(\pi/3)$	$k(\pi/3)$	0	0
1b	$\pi/2 + k(\pi/3)$	$k(\pi/3)$	0	0
2a	$\pi/6 + k(\pi/3)$	$2\pi/3 + k(\pi/3)$	0	$k\pi$
2b	$2\pi/3 + k(\pi/3)$	$2\pi/3 + k(\pi/3)$	0	$k\pi$

[a] TQF acquisition *2a* is the classic phase cycling steps used to acquire TQF images without B_0 inhomogeneity correction

[b] The two TQF acquisitions *1a*, *1b* each contain six separate FIDs (i.e. one for each phase cycling step) whereas TQF acquisitions *2a*, *2b* each contain one FID that is summed by the scanner from the six phase cycling steps

[c] k = 0,1, 2, 3, 4, 5 in all cases for six-step phase cycling

3.2.3. Simulation

Simulations of signal loss as a result of off-resonance used custom-designed software (Matlab, MathWorks, Natwick, MA) (Stobbe, et al., 2005), which solves the sets of differential equations describing the evolution of spin-3/2 nuclei in terms of spherical tensor operators under the influence of RF pulses, frequency offset, and relaxation (Hancu, et al., 2000). The simulations assumed no quadrupolar splitting (i.e. $\omega_Q = 0$ in the equations defined by (Hancu, et al., 2000)). For each sequence, and for each off-resonance correction method, the relative transverse magnetization at TE was recorded for off-resonance frequency ($\Delta\omega$) values from -600 to 600 Hz in 1 Hz increments.

In addition to the two TQF sequences described above, a sequence labeled 'Ideal' was also tested for simulation only, in which the RF pulses were very short (0.1 μs). This sequence is not applicable for imaging experiments, but allows exploration of negligible off-resonance effect during RF pulses. The remaining aspects of the 'Ideal' sequence are the same as the 'Standard' TQF sequence given above (i.e. flip angle = 90^o for all three RF pulses, TR = 330 ms, TE = τ = 6 ms, and δ = 0.2 ms).

Simulations were performed for 4.7T models both of brain tissue and 4% agar. The relaxation power spectral density parameters used for brain tissue were: J_0 = 558 Hz, J_1 = 32 Hz, and J_2 = 12 Hz (Stobbe, et al., 2008b). The relaxation power spectral density parameters for the 4% agar model and their calculation are described below (Section 3.2.4).

3.2.4. Phantom

Phantom experiments were included in this study to verify the TQF signal loss with off-resonance predicted from simulation. The ~250 mL spherical phantom contained 4% agar gel and 500 mM [^{23}Na], with the high sodium concentration being chosen to increase experiment SNR. Relaxation power spectral density parameters were determined by first fitting bi-exponential T_2 decay, obtaining values of T_{2f} = 7.3 ms and T_{2s} = 31.4 ms. The J_1 parameter was then found by fitting the bi-exponential T_1 relaxation of Eq. 3-1.

$$M_z(t) = 1 - 2 \times (0.2\exp(-2J_1 t) + 0.8\exp(-2(\frac{1}{T_{2s}} - J_1)t)) \qquad \text{Eq. 3-1}$$

The parameters J_0 and J_2 were determined from the following assignments:

$$J_0 = \frac{1}{T_{2f}} - J_1 \qquad \text{Eq. 3-2}$$

$$J_2 = \frac{1}{T_{2s}} - J_1 \qquad \text{Eq. 3-3}$$

This relaxation power spectral density fitting procedure directly follows from the relationships described in (Hubbard, 1970). For the 4% agar phantom used in this experiment, J_0 = 119 Hz, J_1 = 18 Hz, and J_2 = 14 Hz. The bi-exponential T_1 values associated with these values of J_1 and J_2 are: T_{1f} = 28.6 ms, and T_{1s} = 34.9 ms. Note that $T_{2s} = 1/(J_1+J_2)$, and including T_{2s} in the regression of bi-exponential T_1 relaxation facilitates differentiation of the J_1 and J_2 values, and hence T_{1f} and T_{1s}.

To verify the TQF signal loss with off-resonance predicted from simulation, the agar phantom was imaged for both the ‘Standard’ and ‘SNR-optimized’ sequences with the system resonant frequency manually adjusted from -100 Hz to 100 Hz in 5 Hz increments. This was a non-imaging experiment, i.e. no imaging gradients were applied for spatial localization, and 25 FID averages were acquired for each phase cycling value. A non-imaging experiment was conducted to reduce total scanning duration. Relative TQF signal loss was calculated by dividing the magnitude of the FID for all offset frequencies by the corresponding magnitude at on-resonance. This procedure was also performed for both the ‘Standard’ and ‘SNR-optimized’ sequences using off-resonance correction *Method 2*. Only *Method 2* was used because simulation suggested the responses of the two correction methods are simply mirror images of each other.

Because both simulation and experiment showed an unexpected asymmetric signal loss with respect to off-resonant frequency, an additional experiment was included to further verify the response predicted by the simulation. Simulation and experiment were repeated for τ = 8 ms using both the ‘Standard’ and ‘SNR-optimized' TQF sequences. A different value of τ yields unique asymmetric signal loss patterns.

3.2.5. Human Imaging

All human imaging was performed using the same hardware as phantom experiments. Written consent approved by the institution's health research ethics board was obtained from all ten healthy volunteers in the study. Note that only manual shimming (x, y, z, z^2) on the sodium signal (taking approximately 2-3 minutes) was performed prior to imaging to yield an average line width over the entire head of ~34 Hz (±17 Hz). The use of only manual shimming on the sodium signal provides a 'worst case scenario' in terms of off-resonance.

Five healthy subjects were imaged using the TQF sequence with 'SNR-optimized' parameters. For each volunteer, all four of the TQF acquisitions of Table 3-2 were acquired with two averages each (TQF acquisition time per row = 7.5 minutes). B_0 corrected TQF images (with associated scan times of 15 minutes) were produced with post-processing as described below (Section 3.2.6). Uncorrected TQF images were produced from only the TQF acquisition *2a* in Table 3-2. Another five volunteers (including one from the previous group) were imaged using 'Standard' TQF sequence parameters. In this case, each TQF acquisition was obtained with 1 average for a scan duration of 11 minutes. The B_0 corrected TQF images constructed from *Method 1* and *Method 2* are thus associated with scan times of 22 minutes each.

A frequency offset map was obtained from each volunteer by acquiring 2 SQ images using a pulse-acquire (3D twisted projection acquisition – see section 3.2.1) sequence with TE values of 0.5 and 5.5 ms. The acquisition time for each SQ image was 40 seconds (RF flip angle = 90^{o}, pulse width = 0.8 ms, TR = 120 ms, average = 1). The off-resonance ($\Delta\omega$) value in each voxel was computed from phase differences of the two SQ images using

$$\Delta\omega = \frac{\phi_2 - \phi_1}{TE_2 - TE_1} \qquad \text{Eq. 3-4}$$

However, the choice of echo time difference (5 ms used in this study) was arbitrary and may not be optimal as it could produce phase wrapping artefacts. A smaller echo time difference would have minimized this artifact. In this study, phase unwrapping was performed on the phase differences of the two SQ images using the FSL software (FMRIB, Oxford, UK). In the frequency offset map computation, a threshold of 10% of the maximum intensity on the SQ image acquired using TE = 0.5 ms was applied to exclude voxels outside the head.

3.2.6. Image Reconstruction

Method 1 – The four coherence transfer pathways that contribute to the final TQF signal were extracted as two pairs denoted by (B_{+1+3} + B_{+1-3}) and (B_{-1+3} + B_{-1-3}), where $B_{\pm1\pm3}$ represent the pathways' amplitudes from the two TQF acquisitions as indicated in Table 3-2. Both TQF acquisitions (each contains six FIDs from the six phase cycling steps) were inverse Fourier transformed along the phase cycle index, and then combined as described by equation 14 in (Fleysher, et al., 2010b). The two pairs were then processed (i.e. grid, zero-fill, inverse Fourier transform) and their magnitudes added together to create B_0 corrected TQF images such that

$$\left|S_{\text{TQF corrected}}\right| = \left|B_{+1+3} + B_{+1-3}\right| + \left|B_{-1+3} + B_{-1-3}\right| \qquad \text{Eq. 3-5}$$

Method 2 – The B_0 corrected TQF images were constructed directly from the two TQF acquisitions as indicated in Table 3-2. The two acquisitions were processed (i.e. grid, zero-fill, inverse Fourier transform) and then combined together to form the final B_0 corrected images as follows:

$$S_{\text{TQF corrected}} = \sqrt{S^2_{TQFAcquisition2a} + S^2_{TQFAcquisition2b}} \qquad \text{Eq. 3-6}$$

Note that the knowledge of off-resonance is not required for both methods.

3.2.7. Analysis

SNR was measured within the brain tissue voxels in each volunteer in order to compare the uncorrected TQF images with the two B_0 corrected images. This measurement was performed by calculating the ratio between signal intensity in brain tissue and the standard deviation of noise in the background of the image, which was multiplied by 0.655 to account for the fact that the background noise in an absolute value image has a Rayleigh distribution (Kaufman et al., 1989).

Using the frequency offset maps generated from each volunteer, brain tissue voxels were divided into three different off-resonant frequency pools corresponding to uncorrected TQF signal loss predicted from simulation. Pools ‘a’, ‘b’, and ‘c’ include the resonant frequencies for which simulation predicts signal losses less than 10%, 10% to 50%, and greater than 50% respectively. This pooling was done for both the ‘Standard’ and ‘SNR-optimized’ TQF parameters. A histogram was created for each subject to show off-resonance distribution over brain tissue voxels, and to highlight the number of voxels within each of the resonant frequency pools described above. Note that CSF voxels were excluded from analysis using visual inspection on the SQ image (TE = 0.5 ms) acquired from each volunteer (as part to the B_0 mapping). The CSF yields much higher signal intensity on SQ sodium images than the cellular brain tissue.

The experimental average relative signal intensity within each resonant frequency pool was determined by dividing the average signal magnitude of all voxels in each pool by the average signal magnitude of on-resonance voxels. Measured average signal loss in the resonant frequency pools is compared to signal loss predicted from simulation, as is the compensation of the off-resonance correction methods. Finally, a map of resonant frequency pools is overlaid on corresponding SQ image slices for a representative subject to show regions in which off-resonance correction may or may not be necessary.

3.3. Results

3.3.1. Simulations

Simulation of uncorrected TQF sodium signal loss in human brain tissue as a result of off-resonance is shown in Figure 3-2 (dotted line). The relative signal off-resonance drops off more rapidly with longer RF pulse lengths. The 'SNR-optimized' case shows greatest signal loss for off-resonance (Figure 3-2a). It is interesting to note that the TQF signal loss is asymmetric about on-resonance and becomes increasingly more so as the duration of the RF pulse is lengthened.

For the 'Ideal' TQF parameters, B_0 inhomogeneity correction works very well for both *Method 1* and *Method 2* within ±40 Hz (Figure 3-2c). However, as RF pulse lengths are increased, the two B_0 inhomogeneity correction methods become less effective. For the 'Standard' parameters (Figure 3-2b), large improvements beyond 20 Hz are still observed and correction extends the 10% TQF signal loss range from ~±10 Hz (uncorrected) to ~±20-30 Hz (corrected). However, for the 'SNR-optimized' case with longer 1.25 ms RF pulses, correction yields only marginal improvement. Note that both correction methods can result in minor 'over-correction', i.e. signal greater than that on-resonance.

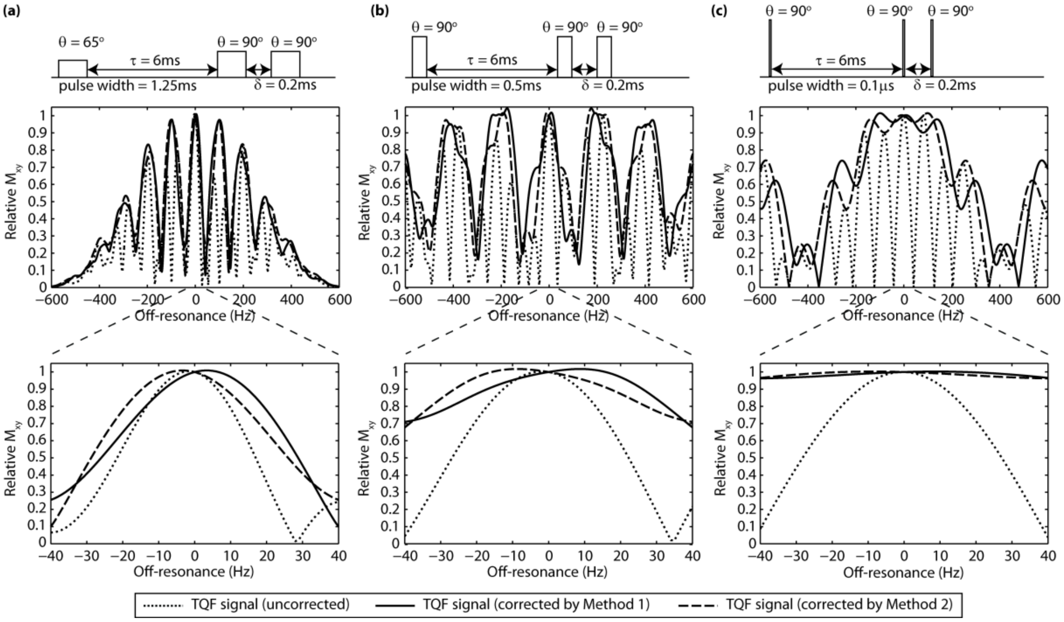

Figure 3-2: Simulated TQF signal loss in brain tissue (dotted line) due to off-resonance using (a) ‘SNR-optimized’, (b) ‘Standard’, and (c) ‘Ideal’ sequence parameters as described in the Methods section. The expected signal associated with B_0 correction using *Method 1* (solid line) and *Method 2* (long dash line) is shown in corresponding plots. Each plot is scaled relative to on-resonance (i.e. 0 Hz) such that relative M_{xy} values below 1 indicate TQF signal loss.

3.3.2. Phantom

The asymmetric simulated TQF signal loss as a result of off-resonance frequency was verified using a 4% agar gel phantom. For both the ‘SNR-optimized’ and ‘Standard’ TQF parameters with a τ of 6 ms (Figures 3-3a and 3-3b), experiment very closely matched simulation for both the corrected (*Method 2*) and uncorrected considerations. Both simulation and experiment were shown to also match with τ = 8 ms (generating a different off-resonance profile) to further verify the asymmetry TQF signal loss and correction by *Method 2*.

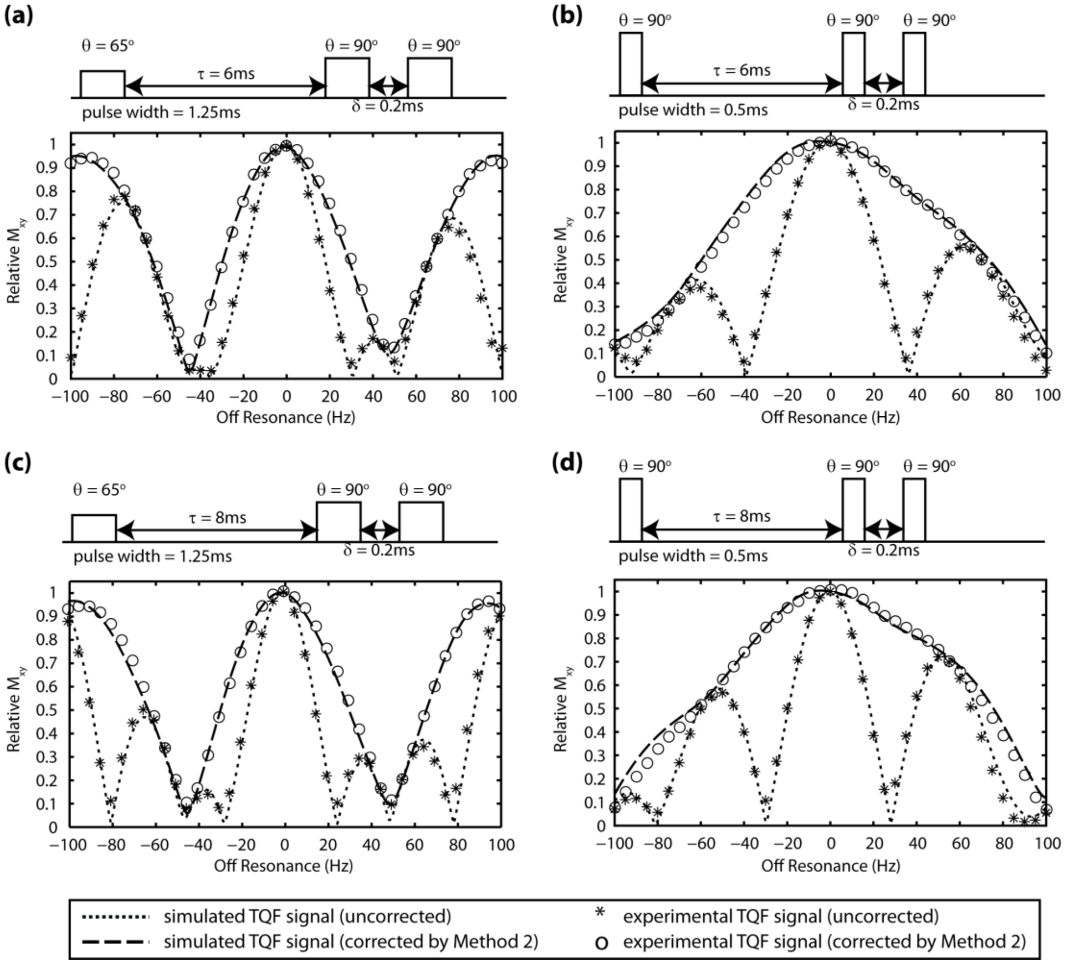

Figure 3-3: Validation of simulated TQF signal loss in a 4% agar phantom (500 mM [Na^+]). The experimental results matched very well with simulation for both off-resonance corrected (*Method 2*) and uncorrected TQF sequences. This validation of simulation used both (a) ‘SNR-optimized’ and (b) ‘Standard’ parameters. The experiments/simulations were also performed with τ = 8 ms (c and d) to provide a different signal loss profile with off-resonance for further validation.

3.3.3. Image Analysis

Visual inspection of representative TQF sodium images and the corresponding frequency offset map from one healthy subject imaged with ‘SNR-optimized’ parameters (Figure 3-4), and another subject imaged with ‘Standard’ parameters (Figure 3-5), show that frontal areas around the nasal sinuses and in the petrous bone region of the temporal lobe are most severely impacted by static field inhomogeneities (as expected). This is also observed in other image modalities such as proton echo planar imaging. Off-resonance related signal losses are not apparent in the upper brain slices, as uncorrected and corrected images appear similar. SNR value of 13±2 was measured from five volunteers imaged with the ‘SNR-optimized’ parameters for both uncorrected TQF images (total scan duration of 7.5 minutes) and correction *Method 1* and *Method 2* (total scan duration of 15 minutes for each method). SNR measured from the other five volunteers imaged with the ‘Standard’ parameters (total scan duration of 11 minutes for uncorrected TQF images and 22 minutes for *Method 1* and *Method 2*) was also 13±2 for all images. Note that while the SNR for the ‘Standard’ parameters is the same as that for the ‘SNR-optimized’ parameters, this is only the case because the scan durations are almost 50% longer for the ‘Standard’ parameters.

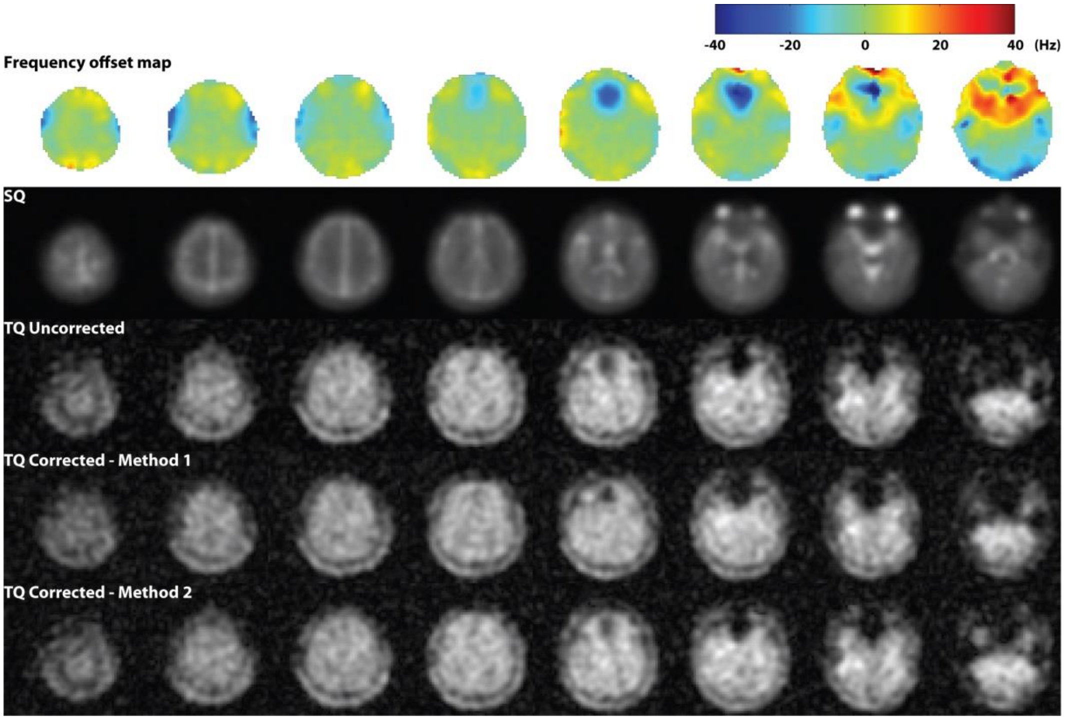

Figure 3-4: Selective TQF sodium brain images acquired using ‘SNR-optimized’ parameters from one volunteer (#4 in Figure 3-6) showing slices at different brain levels. The B_0 corrected TQF images of *Method 1* and *Method 2* are each constructed from two TQF acquisitions obtained in 15 minutes, which is double the scan time of the uncorrected TQF images. The corresponding frequency offset map shows that most brain voxels have off-resonance within ±5 Hz. There is a signal drop on the uncorrected TQF images in the usual areas affected by B_0 inhomogeneity such as the prefrontal cortex and temporal lobe, but B_0 corrections only partially restore the signal intensity. The SQ sodium images with the same spatial resolution as the TQF images were acquired in 40 seconds to show gross anatomy.

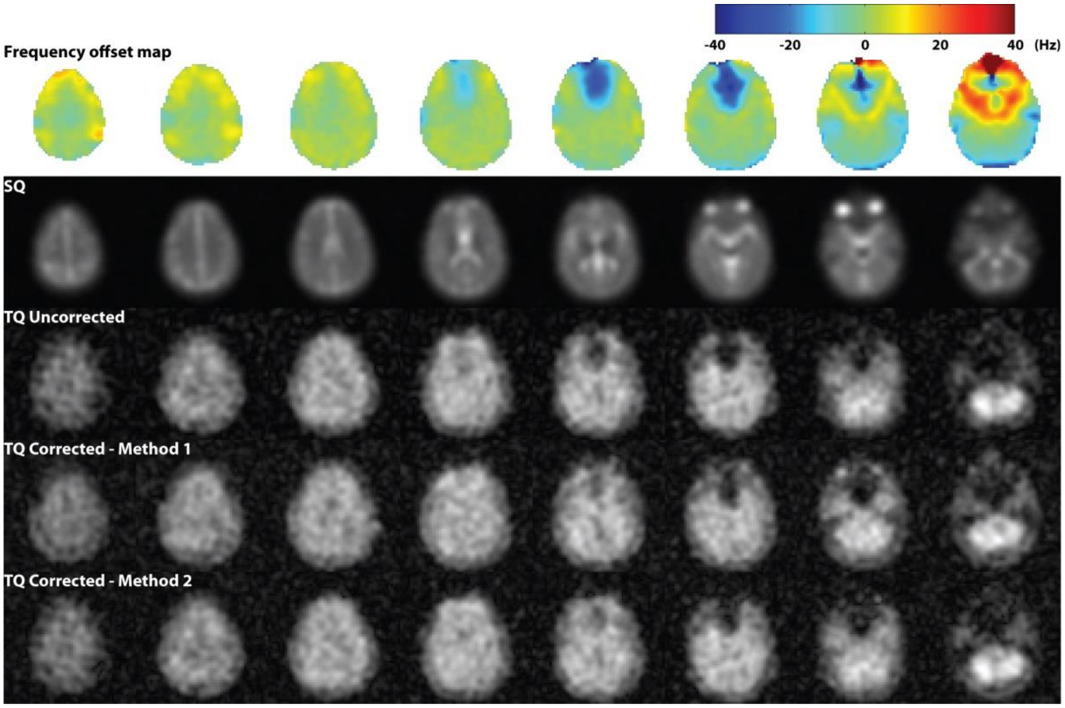

Figure 3-5: Selective TQF sodium brain images from one volunteer (#7 in Figure 3-6) imaged with 'Standard' parameters. The B_0 corrected TQF images of *Method 1* and *Method 2* are each constructed from two TQF acquisitions totalling 22 minutes whereas the uncorrected image is acquired in 11 minutes.

All subjects demonstrate off-resonance distribution mostly between ±5 Hz (78±6% among all ten volunteers) (Figure 3-6). The resonant frequencies associated with each pool (i.e. 'a', 'b', and 'c', which included predicted uncorrected signal losses less than 10%, 10% to 50%, and greater than 50%, respectively) are demarcated in Figure 3-6f and 3-6l for the 'SNR-optimized' and 'Standard' sequence parameters, respectively. In the 'SNR-optimized' case, the proportion of voxels in pool 'a', 'b', and 'c' is 87±4%, 11±2%, and 2±2%, respectively, whereas in the 'Standard' case, the proportions are 94±2% (pool 'a'), 6±2% (pool 'b'), and 0.2±0.2% (pool 'c'). As expected from simulation (Figure 3-2), the 'SNR-optimized' protocol with longer RF pulse lengths shows more voxels in the pools with greater predicted signal loss.

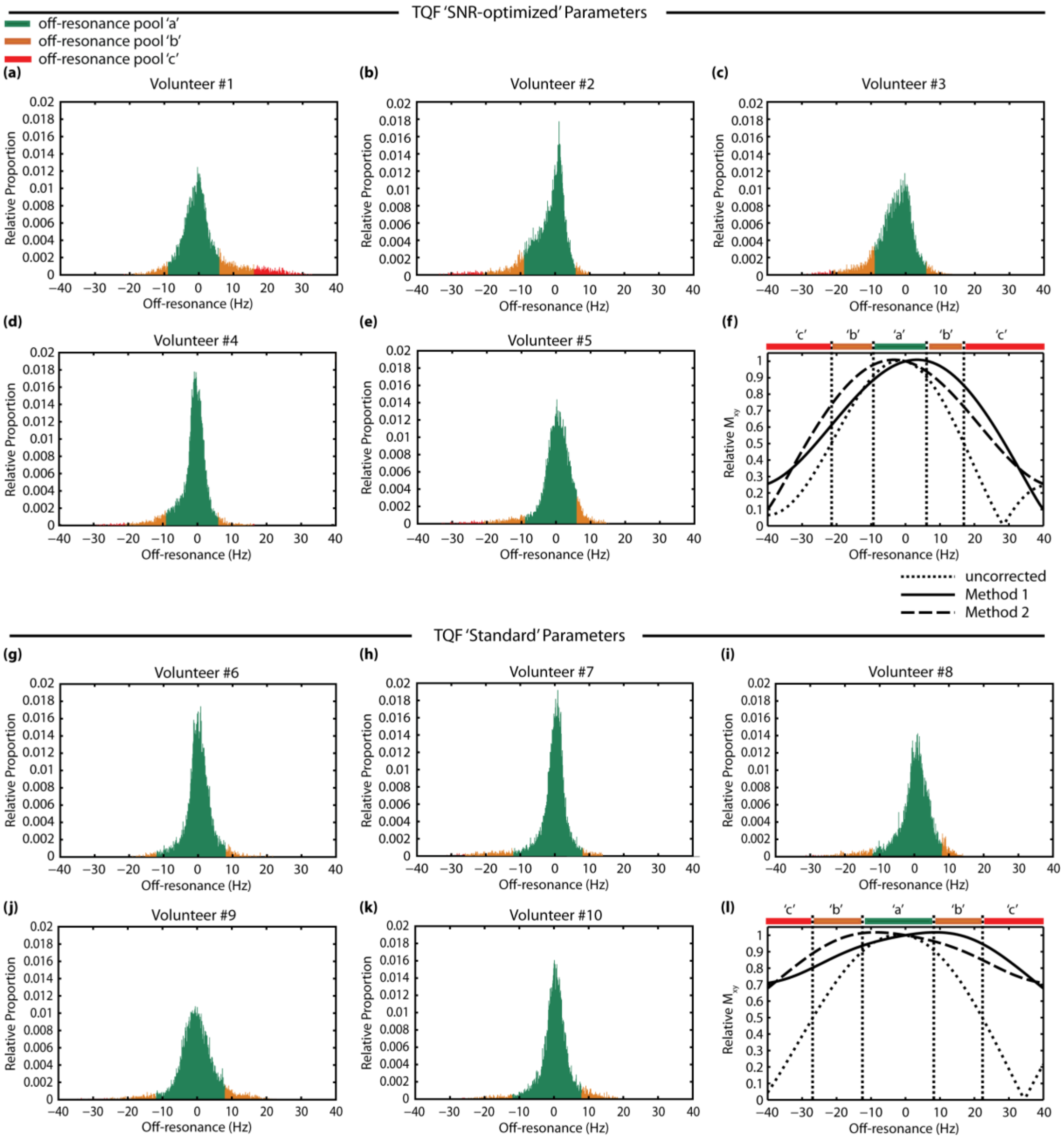

Figure 3-6: Histogram of off-resonance distribution over brain tissue voxels in each volunteer for the 'SNR-optimized' (a-e) and 'Standard' (g-k) TQF sequence parameters. The vertical axes indicate relative proportion such that the sum of total voxels is equal to one. Frequency offset measured in brain voxels among all subjects is mostly between ±5 Hz. The colors green, orange, and red correspond to the resonant frequency pools 'a' (≤10% predicted signal loss), 'b' (10%-50% predicted signal loss), and 'c' (≥50% predicted signal loss), respectively as demarcated in (f) for 'SNR-optimized' sequence parameters and (l) for 'Standard' sequence parameters.

The average relative signal intensities measured in each resonant frequency pool are shown in Figure 3-7. In each case, signal intensity is given relative to that measured in on-resonant voxels (within ±0.1 Hz). These on-resonant voxels, which are scattered throughout the images in each case, account for 2.4±0.4% of the total voxels in the five volunteers imaged with ‘SNR-optimized’ parameters. The proportion of on-resonant voxels in the five volunteers imaged with ‘Standard’ parameters is 2.7±0.6%. In each pool, and for each TQF sequence, the measured uncorrected relative signal intensity is within the range of predicted relative signal intensity (i.e. signal loss) associated with that pool. Additionally, in each pool, and for each TQF sequence, the correction methods perform as expected from observation of Figures 3-6f and 3-6l. Figure 3-7 suggests that for pool ‘b’ the average measurement accuracy has been increased from 80% to 90% of full value for both ‘SNR-optimized’ and ‘Standard’ parameters on account of off-resonance correction. For pool ‘c’ the average measurement accuracy is increased from 40% to 60% of full value for ‘SNR-optimized’, and 50% to 70% for ‘Standard’ parameters on account of off-resonance correction.

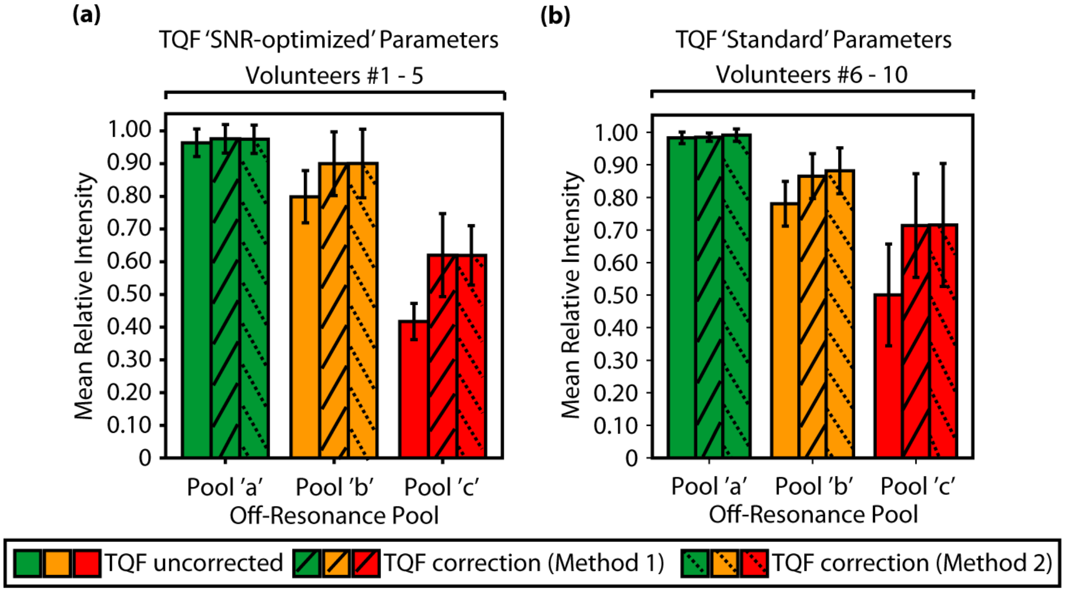

Figure 3-7: Average signal intensities (mean ± standard deviation) relative to on-resonance measured on uncorrected and corrected images. The colors green, orange, and red correspond to the three resonance frequency pools demarcated in Figure 3-6. In each uncorrected pool, measured average signal intensity is within the range of predicted relative signal intensity associated with that pool. Also, in each pool the average signal intensity associated with off-resonance correction is within the range predicted for that pool in Figure 3-6. Note that for large off-resonance (red pool) adequate correction for 'accurate' measurement with respect to off-resonance is no longer achievable.

A map illustrating regions in which off-resonance correction may be necessary and beneficial is shown in Figure 3-8. The regions in green effectively do not require off resonance correction at 4.7T. The regions in orange have an average accuracy of ~80% of full value on account of off-resonance and can be corrected to ~90% of full value (depending on the TQF sequence). The regions in red have an average accuracy of only ~40-50% of full value, but can only be corrected to ~60-70% of full value (depending on the TQF sequence).

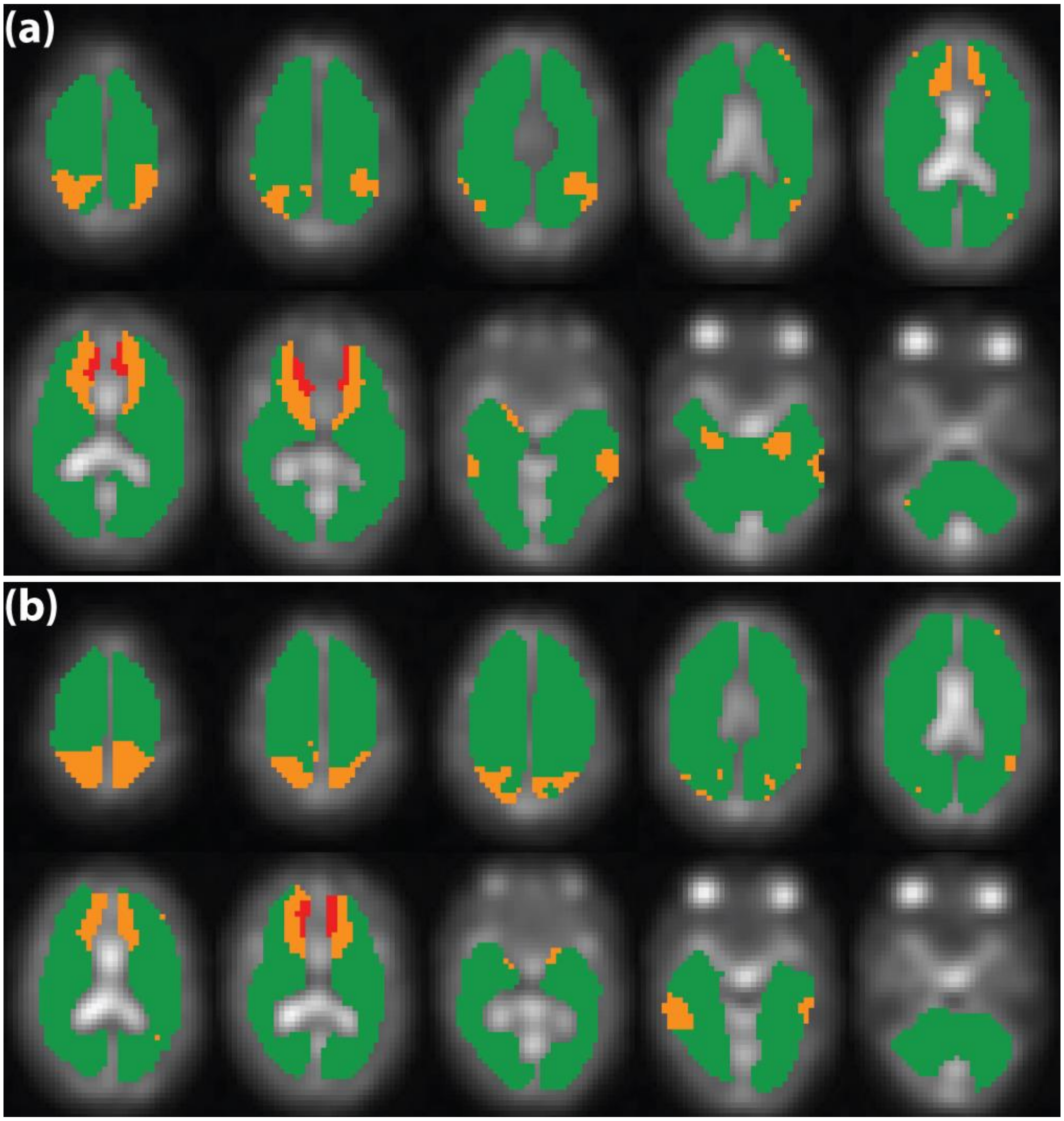

Figure 3-8: Maps for the ‘SNR-optimized’ (a) and ‘Standard’ (b) sequence parameters from the same subject (volunteer #5 and #9 in Figure 3-6) highlighting regions where off-resonance correction may be necessary for accurate signal measurement at 4.7T. Regions in green (pool ‘a’) experience little signal loss from off-resonance. Regions in orange (off-resonance pool ‘b’) and red (off-resonance pool ‘c’) experience larger off-resonant signal loss and may require off-resonant correction for more accurate signal analysis.

3.4. Discussion

Off-resonance signal loss correction methods have previously been proposed for TQF sodium imaging and were demonstrated to be effective in agar phantoms (Fleysher, et al., 2010b; Matthies, et al., 2010). However, this is the first study to quantitatively match off-resonance signal loss and its correction with theory, which has led to the observation of an unexpected asymmetric signal loss profile about on-resonance via simulation that has been verified with agar phantom experiment. This is also the first study to implement and evaluate the necessity and effectiveness of B_0 inhomogeneity correction for human brain TQF sodium imaging. At 4.7T (and likely for lower magnetic field strength scanners) off-resonance correction appears unnecessary in the vast majority of brain tissue (87% - 94% depending on TQF sequence parameters). In these regions the expected TQF signal loss is well within 10% with mean relative signal intensities of 0.96±0.04 and 0.98±0.02 for TQF 'SNR-optimized' and 'Standard' parameters, respectively, relative to on-resonance. In regions of greater off-resonance, ~10 Hz to ~20 Hz (depending on the TQF sequence parameters used), the correction methods did effectively mitigate the TQF signal loss (from ~80% of full value to ~90% of full value). However, in regions beyond ~20 Hz off-resonance, the correction methods were not effective in fully restoring TQF signal loss. Scan time is doubled for each B_0 correction method without SNR improvement, and in cases where small lesions or specific regions of the brain are of interest, this additional time may be better spent to increase image resolution while maintaining SNR. Improving resolution is necessary to reduce partial volume averaging (i.e. smearing of the point-spread-function) with adjacent tissue as it can lead to very large errors in signal measurement. When regions with known susceptibility problems are to be evaluated, the use of off-resonance correction may be important for more accurate signal analysis, while acknowledging that regions where off-resonance is too great will not be fully compensated.

The other off-resonance correction method proposed by Tanase et al. (Tanase, et al., 2005) (not tested in this study) is also not expected to improve SNR. In that method, the four coherence transfer pathways that form the final TQF signal are acquired separately (each with different starting phase in the six-step phase cycling) and then combined together in post-processing with the knowledge of frequency offset in each voxel to construct the final B_0 corrected TQF image. SNR is expected to be the same as that of uncorrected TQF images despite a four-fold increase in scan length plus the time to acquire two SQ images to produce a B_0 map. Here we limited our study to two methods that incur a doubling of scan time.

For both the ‘SNR-optimized’ and the ‘Standard’ TQF sequences, the asymmetric signal loss predicted from spherical tensor based simulation very closely matched that measured from 4% agar phantom experiment, both with and without off-resonance correction and with an alternative τ value of 8 ms, thus validating simulation (Figure 3-3). For the human brain experiments (with and without off-resonance correction), the measured average relative signal intensity in each resonant frequency pool (Figure 3-7) was within the range for that pool predicted from simulation (Figure 3-6f and 3-6l). For the ‘SNR-optimized’ TQF sequence, the proportion of off-resonance voxels that require B_0 correction (i.e. the voxels in pools ‘b’ and ‘c’) is only ~13% of the total number of brain tissue voxels (5 subjects) whereas the proportion is ~7% for the ‘Standard’ TQF sequence (5 subjects).

While we simulate off-resonance during the RF pulses using spherical tensors, others (Fleysher, et al., 2010b; Matthies, et al., 2010; Tanase, et al., 2005) have considered the effect of off-resonance during practical (non-infinitesimally short) RF pulses using substitution of ideal RF pulses. Tanase et al. (Tanase, et al., 2005) had suggested to include effective delays ($T_{eff,}$ a delay before and after an infinitesimally short RF pulse) to account for phase accumulation during practical RF pulses. If the value of $T_{eff} = 2T_p/\pi$ (Tanase, et al., 2005) (where T_p is the pulse duration) is included both before and after infinitesimally short RF pulses in our simulation, the signal loss profiles both with and without off-resonance correction are very similar to those shown in Figure 3-2 and 3-3 (for consideration within 100 Hz off-resonance). For the TQF 'Standard' sequence, the effective δ (δ_{eff}) is 0.836 ms, and for the 'SNR-optimized sequence δ_{eff} is 1.79 ms. Note that the effectiveness of off-resonance correction is proportional to δ_{eff} as described in (Tanase, et al., 2005), thus explaining the reduced effectiveness of off-resonance correction for the 'SNR-optimized' sequence. At very high off-resonance frequencies (with respect to RF pulse length) the ideal RF pulse substitution model breaks down, and reduced T_{11} generation by the first RF pulse, and more complicated coherence loss during the triple-quantum conversion pulses eventually results in no M_{xy} generation. This effect is seen at 600 Hz in Figure 3-2a.

The general pattern of signal annihilation with off-resonance (Figures 3-2 and 3-3) is primarily the result of modulation of the T_{31} magnetic moment as it is being created from bi-exponential T_2 decay during the period defined by τ. The second RF pulse of the TQF sequence, 90^o out of phase from the first, converts the portion of T_{31} in-phase with the first RF pulse (i.e. $T_{31}(s)$) to in-phase triple quantum coherence (i.e. $T_{33}(s)$). If the nuclear ensemble is off-resonant, oscillation of $T_{31}(s)$ such that its value is zero at the second RF pulse results in no T_{33} generation, and ultimately no signal. TQF signal may also be annihilated by T_{33} modulation (at 3x the off-resonant frequency) during the period defined by δ. The average (over the full phase-cycled sequence) magnitude of T_{31} recreated by the third RF pulse is proportional to $T_{33}(s)$. Thus, if $T_{33}(s)$ is zero at the third RF pulse no signal will be produced by the filter. These two aspects of signal loss associated with off resonance are demonstrated in combination in Figure 3-9. The arrows in Figure 3-9 indicate that reduction in $T_{31}(s)$ during τ (solid arrow) or $T_{33}(s)$ during δ (dash arrow) would result in smaller $T_{31}(s)$ recreated from the third RF pulse. This has the consequence of reducing the magnitude of M_{xy} at the start of acquisition. A long $\delta = 3$ ms period is shown for demonstration purpose. Typically, δ would be as small as possible. Note that the effects of off-resonance are identical for both the positive and negative off-resonance frequency when T_1 is assumed to be mono-exponential.

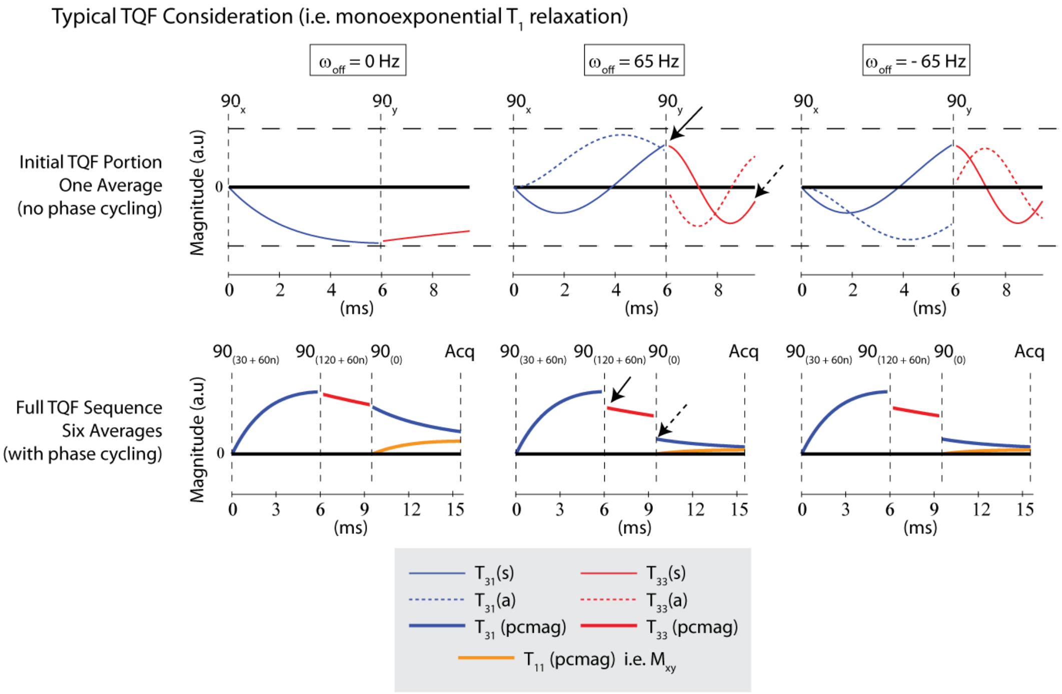

Typical TQF Consideration (i.e. monoexponential T_1 relaxation)

pcmag = magnitude over six phase cycling steps

Figure 3-9: For typical theoretical consideration of TQF, mono-exponential T_1 relaxation is assumed and the creation of a T_{30} magnetic moment is ignored. The plots in each row are scaled identically. In this case the signal produced by the filter (M_{xy}) is independent of the sign of off-resonance (ω_{off}). Note that in the off-resonance case (second column), phase offset accumulation during τ yields a reduction in $T_{31}(s)$ at the time of the second RF pulse (solid arrow), creating less $T_{33}(s)$. Similarly, phase offset accumulation during δ also yields a reduction in the $T_{31}(s)$ recreated by the third RF pulse (dashed arrow).

The asymmetry in the TQF response to off-resonance (Figures 3-2 and 3-3) is the result of a non-zero T_{30} value present at the time of the second RF pulse in the TQF sequence, a ^{23}Na aspect not included in the formal equations of (Fleysher, et al., 2010b; Matthies, et al., 2010; Tanase, et al., 2005). There are two mechanisms for the creation of T_{30}. The first is bi-exponential T_1 relaxation during the preparation period τ. Typical TQF sequence analysis and design includes the approximation that T_1 is mono-exponential, and for fundamental development and optimization this is a very reasonable approximation. The fast component of bi-exponential T_1 relaxation accounts for only 20%, and the two components are similar. Experimental T_1 relaxation in typical model environments and tissue appears mono-exponential. However, while difficult to measure, bi-exponential T_1 relaxation likely does exist in real environments. The method of relaxation power spectral density calculation described in equations (3-1 to 3-3) makes use of the difference between T_{2s} and what looks like a mono-exponential T_1 to determine J_1 and J_2 parameters that describe the bi-exponential T_1 relaxation. Note that in Figure 3-9, where T_1 is considered to be mono-exponential and no T_{30} is created during τ, the M_{xy} magnitude at acquisition is same for an offset frequency on either side about on-resonant. The second mechanism of T_{30} generation does not require bi-exponential T_1 relaxation. If the first RF pulse is not infinitesimally short, creation of T_{31}(s) during the RF pulse as a result of bi-exponential T_2 decay will be simultaneously converted into T_{30} by the RF pulse. This effect is not captured by the 'ideal RF and delay substitution' used in previous theoretical considerations (Fleysher, et al., 2010b; Matthies, et al., 2010; Tanase, et al., 2005) mentioned above.

The mechanism by which T_{30} creates an asymmetric off-resonance response is demonstrated in Figure 3-10. For this demonstration with simulation, very short RF pulses are used and T_{30} is generated during τ as a result of bi-exponential T_1 relaxation. The second RF pulse in the TQF sequence converts T_{30} into a 90^o out-of-phase triple-quantum-coherence (i.e. T_{33}(a)). In the absence of off-resonance, the production of T_{30} and the generation of T_{33}(a) has no impact on the signal generated through the filter, as the average magnitude of T_{31} (and ultimately M_{xy}) is proportional to T_{33}(s). However, that is not the case when the nuclear ensemble is off-resonant. The effect of the creation of T_{33}(a) from T_{30} (which is unaffected by resonant frequency) is to increase the magnitude and alter the initial phase of T_{33} directly following the second RF pulse. As a result of initial phase change, subsequent off-resonance T_{33} evolution no longer yields the same T_{33}(s) evolution for positive and negative off-resonance frequencies. Figure 3-10 demonstrates a case where T_{33}(s) is zero at the third RF pulse for positive off-resonance (producing no M_{xy}), but $T_{33}(s)$ has a large negative value (producing substantial M_{xy}) for negative off-resonance. If δ could be made infinitesimally small, there would be no T_{33} evolution as a result of off-resonance, and no asymmetry effect. However, even for small δ, some off-resonance asymmetry effect can be observed, particularly for large off-resonance frequencies. Note that the slight over-compensation observed in the simulation of Figure 3-2, can also be explained by the creation of $T_{33}(a)$ as a result of T_{30} and the small magnitude increase in triple-quantum-coherence.

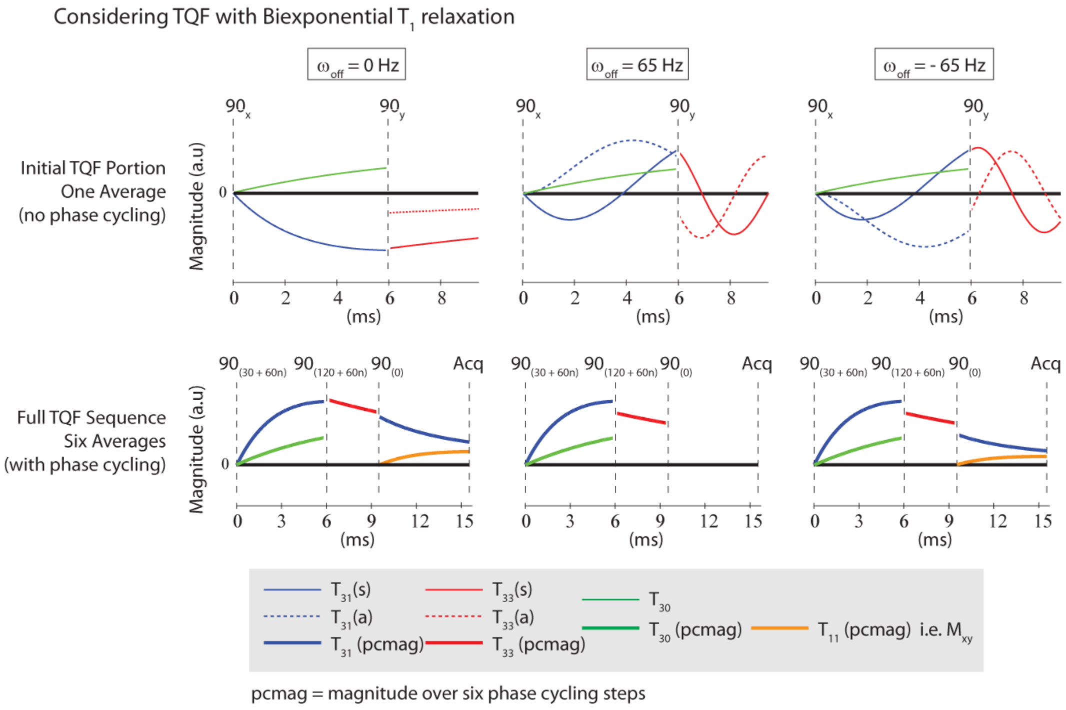

Figure 3-10: T_{30} is created as a result of bi-exponential T_1 relaxation. In this case T_{30} is converted to a small 90° out-of-phase triple quantum coherence ($T_{33}(a)$). The effect is to change the magnitude and initial phase of T_{33} evolution following the second RF pulse (i.e. during δ). Because of the initial phase change, positive and negative ω_{off} can yield *different* values of $T_{33}(s)$ at the end of the period δ, which is effectively proportional to the magnitude of M_{xy} produced by the filter. The label ‘pcmag’ in the figure denotes magnitude of tensor operator after averaging from six-step phase cycling.

This study was performed at 4.7T, where off-resonance as a result of B_0 inhomogeneity is likely to be greater than 3T, but presumably less than at 7T or 9.4T. Note that only manual shimming (x, y, z, z^2) on the sodium FID over the entire brain volume was performed prior to imaging in this study. It is likely that more sophisticated shimming would even further decrease off-resonance effects and may ameliorate the situation at higher fields. It should also be noted that the value of δ used in the two TQF sequences was 0.2 ms. The effectiveness of the correction methods at larger off-resonance frequencies can also be improved if this value is decreased. Finally, an additional source of signal loss for both the corrected and uncorrected TQF sequences may be off-resonance variation within large voxels (i.e. a dephasing effect). However, this additional signal loss contribution is expected to be small. A relatively large off-resonance variation of 10 Hz is associated with an additional maximum signal loss of 2% for the 'Standard' TQF sequence, and 3% for the 'SNR-optimized' sequence (data from simulation not shown).

For the analysis of lesions not located in brain regions with known susceptibility problems (i.e. the majority of brain tissue), the requirement of B_0 correction to improve imaging accuracy seems unnecessary on TQF sodium images acquired at field strengths up to 4.7T. The additional acquisition time for B_0 correction is likely better spent acquiring a second average to increase the image SNR or improve the spatial resolution. However for patients with compromised B_0 inhomogeneity or the use of longer preparation times at higher field strengths (expected due to increase of T_{2s}), greater TQF signal losses are likely to be observed than described in this study. The necessity of B_0 correction would need to be evaluated for these scenarios. Future studies should also evaluate whether B_0 correction methods in TQF sodium imaging warrant the additional scan time in other anatomies such as cartilage (Borthakur, et al., 1999; Reddy, et al., 1997a) or spinal disc tissue (Ooms, et al., 2008).

Chapter 4

In Vivo Double Quantum Filtered Sodium Magnetic Resonance Imaging of the Human Brain at 4.7T[3]

4.1. Introduction

Quadrupolar interaction of the spin 3/2 sodium nucleus with fluctuating electric field gradients produces nuclear longitudinal and transverse relaxation that is characterized by either mono-exponential or bi-exponential depending on the correlation time (τ_c). In addition, the ‘order’ or anisotropy of molecular structure affects the time-averaged quadrupolar interaction splitting frequency (ϖ_Q). It is well known that in macroscopically ordered and oriented environments, such as in liquid crystal, ϖ_Q is non-zero and causes the sodium NMR spectrum to split with two clearly distinct satellite peaks separated from the central peak (Rooney, et al., 1991). Such quadrupolar splitting is the cause of signal magnitude reduction by 60% in NMR spectroscopy measurements as only the signal produced from the central spin state transition is detected (Shporer et al., 1972). Signal loss due to splitting could be even worse when finite radiofrequency (RF) pulse duration is used as typically the case in imaging applications such that only 20% of signal may be detected (Joseph, et al., 1987). In human, the line shapes of sodium spectra acquired using a double-quantum filter (DQF) sequence varied with respect to preparation time providing evidence that residual (non-zero) quadrupolar interaction of sodium exist in skeletal muscles (Reddy, et al., 1995), brain (Reddy, et al., 1995), cartilage (Reddy, et al., 1997b), and breast (Duvvuri, et al., 1999). However sodium quadrupolar splitting is expected to be less distinct in human,

---

[3] An abstract version of this chapter has been published. A. Tsang, RW. Stobbe, C. Beaulieu, 2013. Double Quantum Magic Angle Sodium MRI of the Human Brain, Abstract #4130. Proceedings of the International Society for Magnetic Resonance in Medicine, 21st Annual Meeting, Salt Lake City, Utah. Dr. Stobbe was involved in this study with verifying the simulation results as well as editing the abstract.

where multiple locally ordered domains exist with overall ϖ_Q suggested to be characterized by a Gaussian distribution (Woessner et al., 1998), than macroscopically ordered and oriented crystals.

There has been no report to date of any imaging studies performed to show residual quadrupolar interaction in either human or animal. Nevertheless, selective imaging of anisotropic sodium interaction may be desirable in pathologies such as cartilage degeneration in the knee or tissue microstructure alteration in the brain. In addition, the exploration of residual quadrupolar interaction in human is pertinent to tissue sodium concentration (TSC) quantification to evaluate the extent of signal loss due to 'invisible' sodium. This problem has not been considered in previous human imaging applications to quantify TSC (e.g. (Lu, et al., 2010; Madelin et al., 2012; Ouwerkerk, et al., 2003; Thulborn, et al., 2009)) as its effect on signal loss is assumed to be insignificant.

Selective sodium signal acquisition from different quadrupolar interaction environments may use a 3-pulse multiple quantum filter (MQF) sequence as shown in Figure 4-1 by a judicious choice of phase cycling scheme and RF excitation pulse flip angle. A DQF or triple-quantum filter (TQF) sequence, with typical implementation of using 90^o flip angle for all three RF pulses, is often used to extract signal from sodium nuclei that exhibit bi-exponential transverse (T_2) relaxation. It has been shown that sodium in intracellular compartment produces bi-exponential T_2 signal that can be detected using a TQF sequence (Tauskela et al., 1997). Further selective acquisition of sodium quadrupolar interaction with non-zero ϖ_Q may use a double-quantum magic angle (DQ-MA) sequence. DQ-MA is same as the DQF sequence but use a special flip angle of 54.7^o to extract even-rank tensor operator produced only in anisotropic ordered environments (Jaccard, et al., 1986). The advantage of extracting only even-rank operator, while suppressing the odd-rank, is that signal can be isolated to reflect only sodium quadrupolar interaction with non-zero ϖ_Q. This work begins with simulations to show the unique extraction of spherical tensor operators produced in two quadrupolar interaction models (i.e. isotropic and anisotropic) through the 3-pulse MQF sequence (Figure 4-1) using different phase cycling scheme and RF pulse flip angle. In addition, simulation also shows the effect of τ and ϖ_Q on DQ-MA signal at the beginning of acquisition (i.e. echo time TE) for different quadrupolar interaction frequency distributions environments. Correct functioning and implementation of DQ-MA is verified by first imaging phantoms and then is applied in three healthy volunteers. Since white matter (WM) fiber tracts are oriented and hence anisotropic, it is expected that the DQ-MA signal in WM will be greater than in cerebral gray matter (GM).

4.2. Methods

This sodium imaging project was approved by the Health Research Ethics Board at the University of Alberta. Written consent from all volunteers was obtained prior to imaging. All imaging experiments in this study were performed using a 4.7 T Varian Inova whole-body MRI scanner (Walnut Creek, CA) and an in-house manufactured single-tuned birdcage head coil.

4.2.1. MRI Sequences

A 3-pulse MQF sequence is used in this study for simulations and imaging experiments as shown in Figure 4-1. The preparation and evolution times are denoted as τ and δ respectively. Detection of bi-exponential T_2 relaxing sodium nuclei in both disordered and ordered (i.e. isotropic and anisotropic) environments use either a DQF or TQF sequence. Typical implementation of DQF and TQF sequences use 90^o flip angle for the three RF pulses, but the former uses a 4-step phase cycling and the latter uses a 6-step phase cycling scheme as indicated in Table 4-1. The receiver phase is alternated between 0^o and 180^o between each phase cycling step. In both filters, signal is acquired for a set of projections with a constant set of RF and receiver phases, followed by re-acquisition with the next set of phases in the phase-cycling regime. The final free induction decay signal is the summed average signal acquired at each phase cycling step. Selective extraction of anisotropic sodium signal is achieved by the DQ-MA sequence, which is the same as the DQF sequence except that the last RF pulse flip angle is set to 54.7^o.

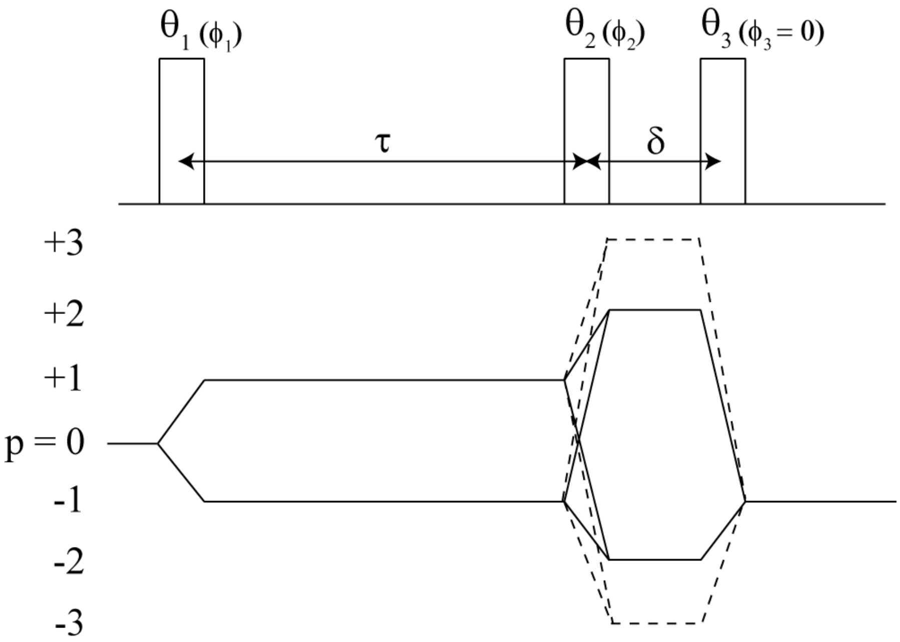

Figure 4-1: The 3-pulse MQF sequence that is implemented as triple-quantum-filter (TQF), double-quantum-filter (DQF) or double-quantum magic angle (DQ-MA) sequence. The preparation and evolution times are denoted by τ and δ respectively. The transmitter phase for each RF pulse is indicated by ϕ. The TQF sequence extracts third-order coherences indicated by the dashed lines where the DQF and DQ-MA sequences both extract second-order coherences indicated by solid lines. The phase cycling steps for each RF pulse in different MQF implementation is described in Table 4-1.

Table 4-1: RF pulse phase cycling steps and receiver phase of TQF, DQF, and DQ-MA acquisitions

Sequence	First RF pulse phase (ϕ_1)	Second RF pulse phase (ϕ_2)	Third RF pulse phase (ϕ_3)	Receiver phase (ψ)
TQF [a]	$\pi/6 + k(\pi/3)$	$2\pi/3 + k(\pi/3)$	0	$k\pi$
DQF / DQ-MA [b]	$k(\pi/2)$	$k(\pi/2)$	0	$k\pi$

[a] k = 0, 1, 2, 3, 4, 5 for six-step phase cycling TQF acquisition
[b] k = 0, 1, 2, 3 for four-step phase cycling DQF and DQ-MA acquisition

4.2.2. Simulations

Sodium signal detection in different quadrupolar interaction environments using the 3-pulse MQF sequence was simulated in a custom-designed software in Matlab (MathWorks, Natick, MA) (Stobbe, et al., 2005). Two quadrupolar interaction models were arbitrarily designed to represent anisotropic (spectral density parameters: $J_0 = J_1 = J_2 = 0.001$ Hz with $\varpi_Q = 500$ Hz) and isotropic ($J_0 = 975$ Hz, $J_1 = 75$ Hz, $J_2 = 25$ Hz, $\varpi_Q = 0$) ordered environments. A single-valued residual quadrupolar interaction frequency for the anisotropic model was used for simplicity and does not reflect that in biological tissues. In addition, signal loss due to relaxation through the filter can be ignored in this case. The isotropic model was designed to yield an optimal τ value of 2.5 ms. The parameters τ = TE = 2.5 ms, $\delta = 0.5$ ms. TR = 200 ms, and pulse length = 0.1 μs were used for TQF, DQF, and DQ-MA sequences. The interval $\delta = 0.5$ ms was used to demonstrate the evolution of higher order coherences (i.e. T_{22} and T_{32}) in the DQ filters but should be made as short as possible in practice. The extremely short pulse length was chosen to minimize relaxation during RF and is not applicable for imaging experiments.

The effect of τ and ϖ_Q on DQ-MA signal at TE was simulated for 2 scenarios. The first scenario, labeled as ‘Ideal’, used the same anisotropic model and sequence parameters as described above, except that $\delta = 0.01$ ms. Signal loss due to relaxation is negligible in this ‘Ideal’ case. The second scenario, labeled as ‘Practical’, used a brain model (spectral density parameters J_0=558 Hz, J_1=32 Hz, and J_2=12 Hz (Stobbe, et al., 2008b)) with practical imaging sequence parameters (i.e. pulse width = 0.5 ms, $\delta = 0.5$ ms, TR = 300 ms). The two scenarios were considered in three anisotropic environments: 1). completely ordered and oriented interaction such as in liquid crystal where ϖ_Q is characterized by a single (Delta distribution) value; 2). moderately long range ordered interaction where ϖ_Q is characterized by a Gaussian distribution with small standard deviation (e.g. 50 Hz); 3). macroscopic disorder (i.e. no long range order) interaction that is relevant for biological environment where ϖ_Q is represented by a zero mean Gaussian distribution with varying standard deviation (e.g. 0 to 500 Hz). For the first two environments, ϖ_Q was adjusted from 0 to 500 Hz in 10 Hz increments. This range was chosen as previously reported to be relevant in biological environments (Laustsen et al., 2010). The DQ-MA sequence was repeated using τ = 1, 2, 6, and 10 ms for the 'Ideal' and 'Practical' scenarios along with the three environments considered. For each Gaussian distributed ϖ_Q consideration in the DQ-MA sequence, the signal at TE was averaged over 100 randomly generated ϖ_Q of specified mean and standard deviation to simulate the various residual quadrupolar interactions within a voxel.

4.2.3. Phantoms

Three cylindrical phantoms (60 mm diameter and 130 mm height) of 250 mL containing saline, 4% agar gel, and 3% xanthan gum were constructed with [Na^+] of 200 mM in each to represent different sodium environments. The agar and xanthan gum reflect disordered and ordered macromolecular environments respectively (Woessner, 2001). The phantoms were imaged together to test the correct functioning of DQ-MA using the following parameters: pulse width = 0.26 ms, τ = TE = 1, 2, 6, and 10 ms, δ = 0.27 ms, and TR = 300 ms. Signal acquisition used a twisted projection set with a sampling density designed filtering shape (Stobbe, et al., 2008a) (168 projections, twist = 0.17, field of view = 240 mm, readout duration = 12.5 ms) that yield nominal isotropic spatial resolution of 15 mm. Acquisition time for one τ value was 3.4 minutes. In addition, the phantoms were imaged with DQF and TQF sequences (τ = TE = 10 ms, δ = 0.27 ms, TR = 300 ms) as well as single-quantum (SQ) sequence (flip angle = 90^o, TE/TR = 0.23/120 ms, pulse width = 0.26 ms) using the same twisted projection set as above. Acquisition time for DQF, TQF, and SQ was 3.4, 5, and 0.3 minutes respectively.

4.2.4. In Vivo Human Brain

Three healthy volunteers (age 35, 39 and 58 years) were scanned with DQ-MA, TQF, and TSC sequences using parameters chosen to maintain specific absorption rate (SAR) below 6 W (assume SAR ~2 W/kg at 4.7 T and head weighs ~3 kg). The DQ-MA sequence (pulse width = 0.5 ms, δ = 0.5 ms, TR = 300 ms, and TE = τ) was repeated in each subject with τ = 1, 2, 6, and 10 ms to explore optimal value for in vivo brain imaging. DQ-MA images for one τ value were acquired with 2 averages in 7 minutes using same twisted projection set as applied in phantoms. In addition, TQF images of identical spatial resolution were acquired in the same imaging session from each volunteer using the following parameters: TR = 330 ms, τ = TE = 6 ms (optimal τ determined previously at 4.7 T (Tsang, et al., 2012)), δ = 0.5 ms, and pulse width = 0.5 ms. TQF brain images were obtained with 1 average in 5 minutes. In order to identify brain slice location, SQ sodium images were obtained using a typical TSC sequence implementation with flip angle = 90^o, TE/TR = 0.3/120 ms, and pulse width = 0.5 ms. A twisted projection set (2500 projections, twist = 0.15, field of view = 244 mm, readout duration = 18 ms) that yield higher nominal spatial resolution of 2.9 x 2.9 x 5.8 mm^3 in 5 minutes was used.

4.3. Results

4.3.1. Simulations

Evolution of tensor operators for two quadrupolar interaction models was simulated for TQF, DQF, and DQ-MA sequences (Figure 4-2). Either symmetric or anti-symmetric component of the tensor operators are shown to depict the oscillating nature due to residual quadrupolar interaction. In all three sequences, the first RF pulse converts longitudinal magnetization (T_{10}) into observable transverse magnetization (T_{11}). Bi-exponential T_2 relaxation or residual ϖ_Q converts T_{11} into T_{31} during the time interval τ for the two modelled environments. The even-rank single quantum operator (T_{21}) is created during τ only in the anisotropic model. In the TQF sequence, the second RF pulse extracts T_{31} and converts it into third order coherence T_{33}. It is important to note that T_{21} is not converted into higher order coherence using the 6-step phase cycling scheme and does not contribute to the final detected signal. After a short evolution time interval δ, the last RF pulse transforms the third order coherence into T_{31} and then bi-exponential T_2 relaxation turns it back into T_{11}. In the DQF and DQ-MA sequences, the second RF pulse converts T_{31} into T_{32} for both environments but T_{22} is created from T_{21} only in the anisotropic model. The last 90^o RF pulse in DQF converts both T_{22} and T_{32} back into T_{21} and T_{31} respectively which are then transformed into T_{11}. Since TQF has been shown to be ~50% more sensitive than DQF (Chung, et al., 1990), the signal magnitude of the isotropic model at acquisition is about half that of TQF. It is important to note the signal magnitude in the anisotropic model at acquisition depends on τ and ϖ_Q due to the oscillating nature of tensor operators produced. In the DQ-MA sequence, the last RF pulse of 54.7^o extracts only T_{22} and then converts into T_{11}. The resultant transverse magnetization for isotropic model is zero since no T_{22} is created during δ.

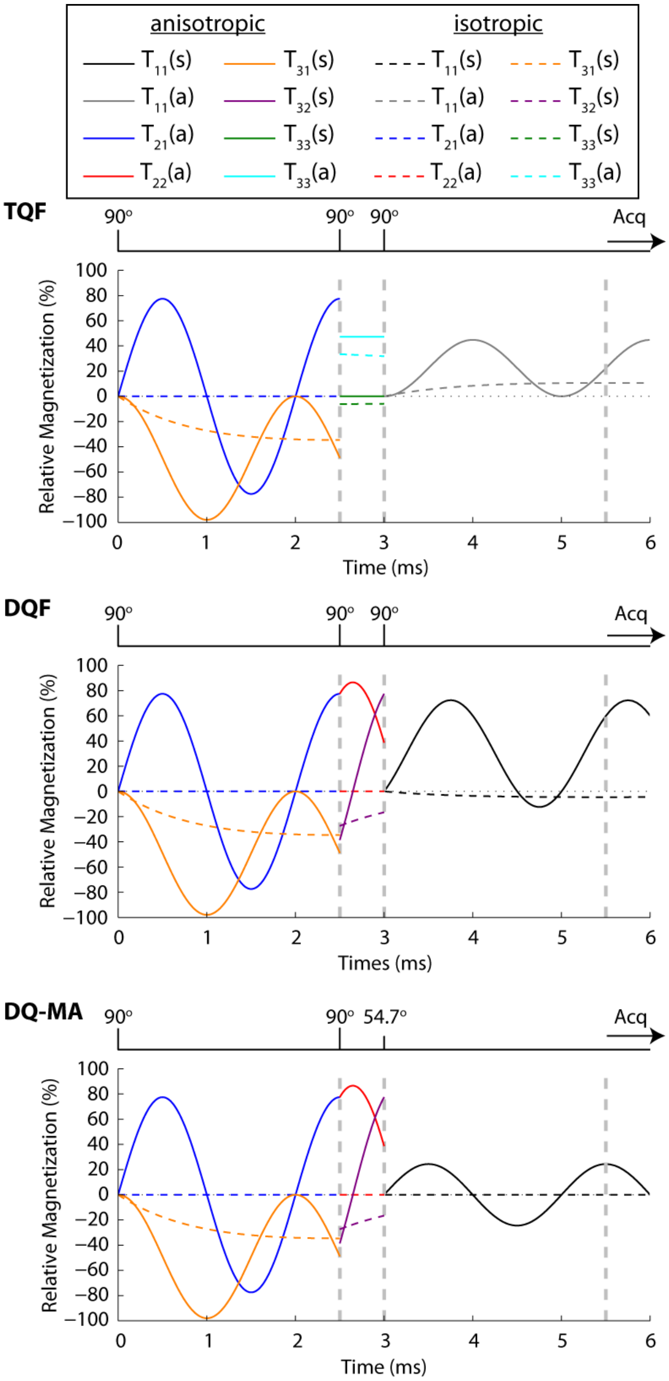

Figure 4-2: Evolution of tensor operators through the 3-pulse MQF sequence. Even-rank single quantum tensor (T_{21}(a)) is created only in the anisotropic model (solid lines) but the odd-rank tensor (T_{31}(s)) is created in both anisotropic and isotropic (dash lines) models. In this simulation where the anisotropic model is described by a single-valued residual quadrupoar interaction frequency, the amplitude of tensor operators T_{21}(a) and T_{31}(s) at the second RF pulse is dependent on τ due to their oscillating nature which consequently affects the final signal magnitude.

The effect of τ and ϖ_Q on DQ-MA signal magnitude at TE is presented in Figure 4-3. The DQ-MA signal is dependent on ϖ_Q in an oscillatory manner and proportional to $\sin(2\pi\varpi_Q\tau)$. This pattern is observed in the 'Ideal' (no relaxation) scenario with ϖ_Q characterized by a single value (top) to represent completely ordered and oriented environments such as crystal. In this case, a long τ (10 ms) yields the highest signal as it is sensitive for a wide range of ϖ_Q. Similarly in the other two environments where ϖ_Q is Gaussian distributed to represent moderately long range ordered (middle) and macroscopic disorder (bottom), the DQ-MA signal increases for longer τ value when relaxation is negligible. However, in the 'Practical' scenario, a short τ value yields the highest DQ-MA signal when bi-exponential relaxation is rapid such as in brain irrespective of the ϖ_Q distribution. DQ-MA signal is greatly reduced in the 'Practical' scenario for long τ value because T_{21} decays at the rate of T_{2f}.

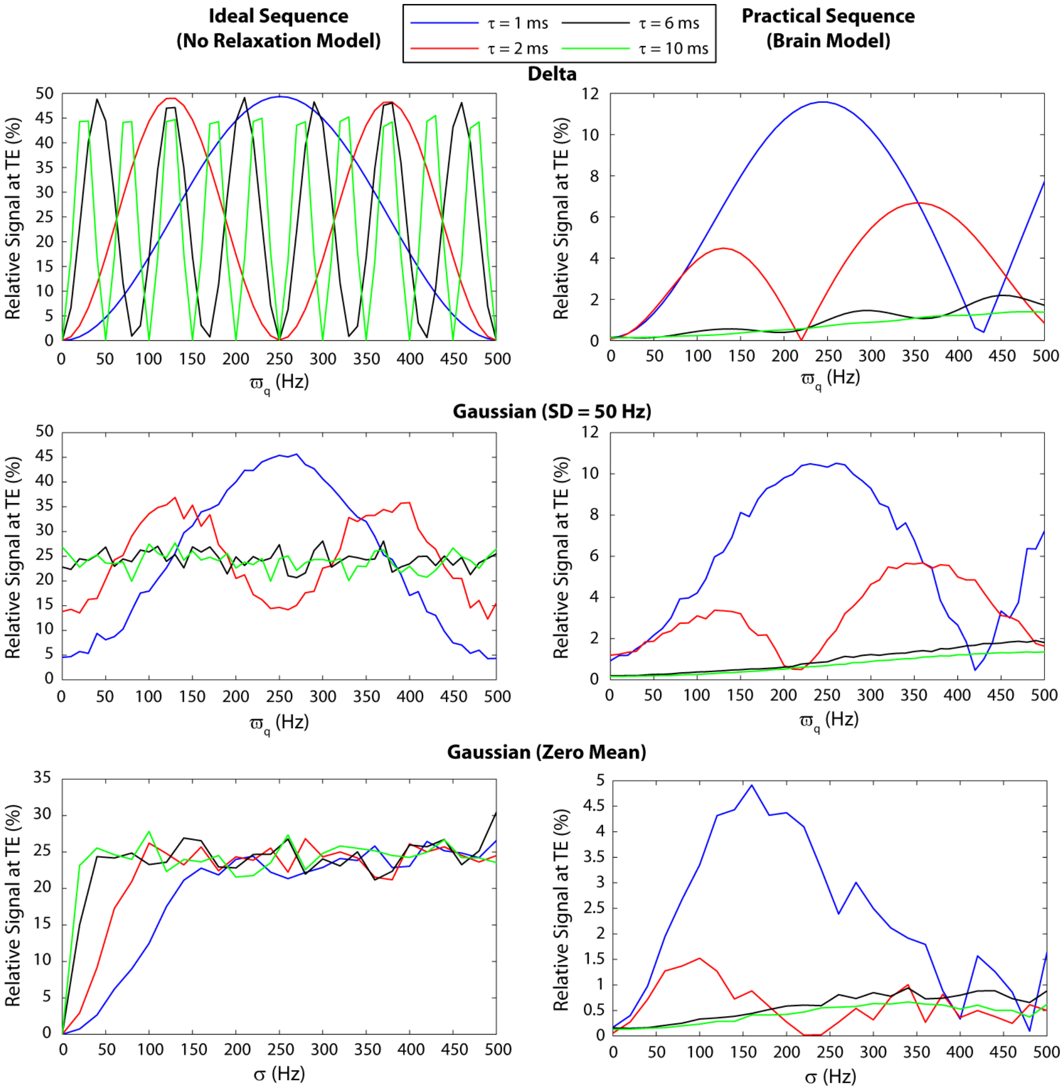

Figure 4-3: The effect of τ and ϖ_Q on DQ-MA signal magnitude at TE for various distributions of mean residual quadrupolar interaction frequency (ϖ_Q).When relaxation is negligible, the DQ-MA signal increases with τ. However, the DQ-MA signal is greatly reduced in the 'Practical' scenario for long τ due to rapid decay of T_{21} with T_{2f}.

4.3.2. Phantoms

The DQ-MA images shown in Figure 4-4(a-d) are scaled relative to the maximum signal acquired using τ = 6 ms and demonstrate that only signals from the xanthan gum phantom are observed while intensities in both saline and agar gel phantoms are suppressed. The results confirmed correct implementation of DQ-MA to selectively detect anisotropic ordered sodium signal. On both DQF and TQF images acquired with τ = 10 ms (Figure 4-4e,f), signals from agar (isotropic ordered environment) and xanthan gum phantoms are observed while intensity in saline is still suppressed. This confirms the selection of bi-exponential T_2 relaxing sodium signal and residual quadrupolar interactions. The non-selective signal acquisition using a SQ TSC sequence (Figure 4-4g) shows signal intensities from all three phantoms.

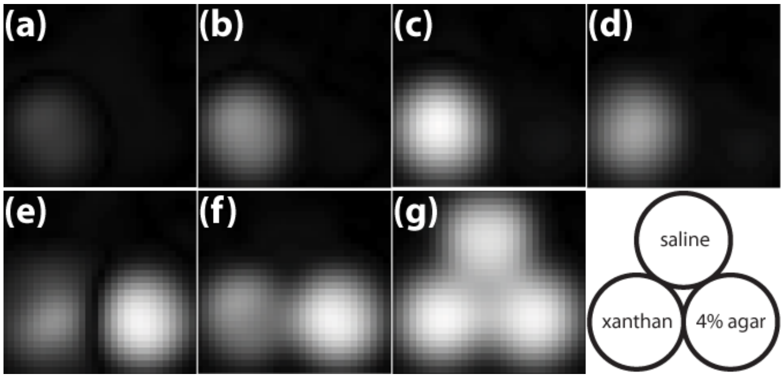

Figure 4-4: An image slice of the three phantoms demonstrates the correct functioning of the DQ-MA sequence to select anisotropic ordered sodium signal. The DQ-MA sodium images acquired with τ values = 1, 2, 6, and 10 ms (a – d respectively) show only sodium signal in the xanthan gum phantom irrespective of τ used. On the other hand, DQF and TQF sodium images both acquired with τ = 10 ms (e and f respectively) show non-zero signal intensity in agar and xanthan gum. The SQ image (g) shows signal in all three phantoms.

4.3.3. In Vivo Human Brain

Selected brain slices from one representative volunteer are shown in Figure 4-5. Signal intensities on TQF and DQ-MA images are reasonably uniform throughout the brain. All DQ-MA images were scaled relative to the maximum signal acquired using τ = 2 ms. In all subjects, DQ-MA signal in brain is lowest acquired with τ = 10 ms which agrees with simulations (Figure 4-3). On both TQF and DQ-MA images, sodium signal in cerebrospinal fluid and vitreous humor, where the T_2 relaxation is expected to be mono-exponential, is suppressed as it is confirmed in phantom experiments. However, the intensity in the lateral ventricles is not completely nulled due to spatial blurring of signal smearing from neighboring voxels, an adverse effect from large voxel dimensions, and not from breakthrough of single-quantum signal.

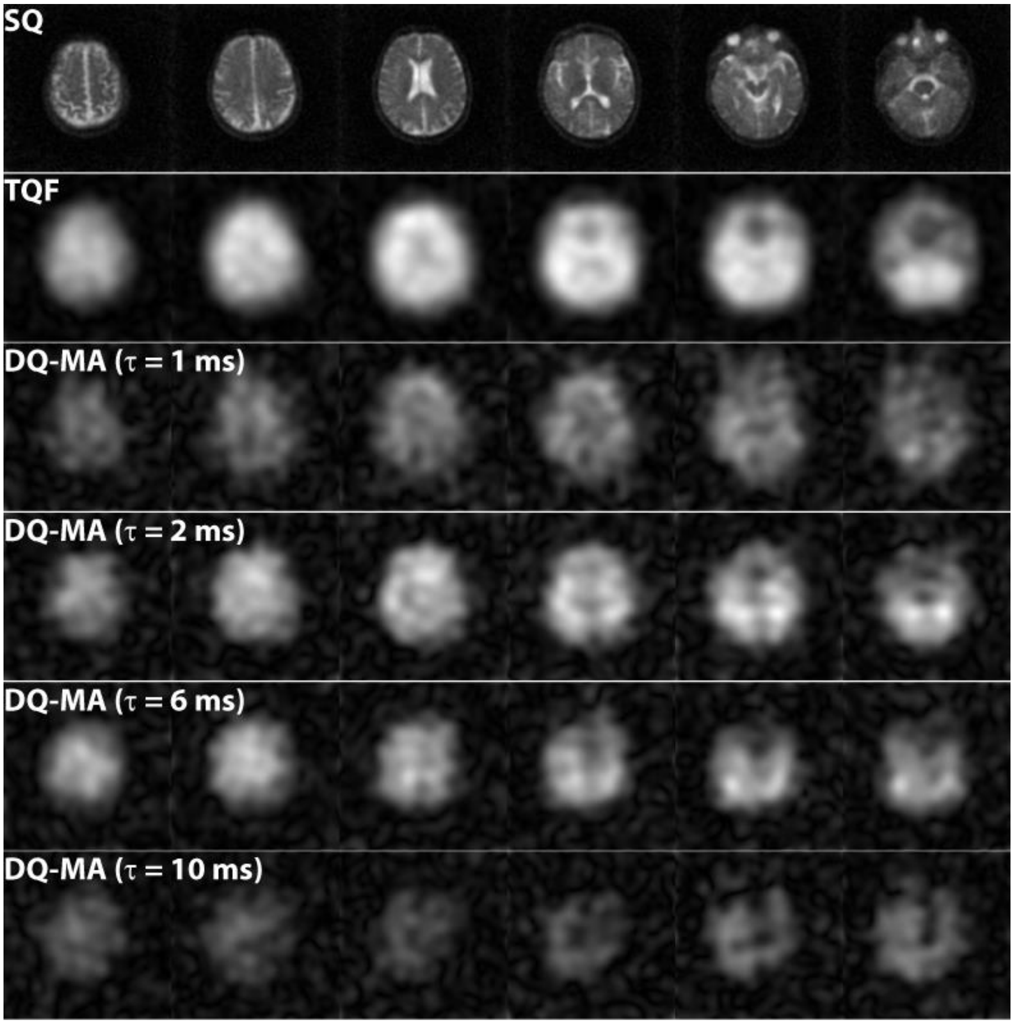

Figure 4-5: Selective image slices of a volunteer at different brain level acquired using SQ, TQF and DQ-MA sequences. DQ-MA images were acquired using four τ values (1, 2, 6, and 10 ms). The DQ-MA images for one value of τ were acquired in ~7 minutes using the projection set to yield nominal isotropic spatial resolution of 15 mm. All DQ-MA images were scaled relative to the maximum signal intensity acquired using τ = 2 ms. TQF images were acquired using same projection set in 5 minutes. SQ images were acquired in 5 minutes using projection set designed to yield higher nominal spatial resolution of 2.9 x 2.9 x 5.8 mm^3 to identify brain slice location.

4.4. Discussion

Previous in vivo human spectroscopy studies (Duvvuri, et al., 1999; Reddy, et al., 1995; Reddy, et al., 1997b) suggested that sodium nuclei in anisotropic ordered environment can be selectively detected when the preparation time in the DQF sequence is short. The rationale is that the broad component of the DQF sodium spectrum, which arises from the satellite transitions and results from the formation of T_{21} during τ, is dominant only at short τ values. As τ increases, the narrow component of the DQF sodium spectrum, which arises from the central transition and results from T_{31}, becomes dominant (Eliav, et al., 1994; Eliav, et al., 1992). However, the dependency on τ for the filtering capability of anisotropic ordered sodium signal is lifted when the magic angle of 54.7^o is used (Eliav, et al., 1992). Consequently, the DQ-MA sequence was chosen in this study to explore residual qudarupolar interaction in the brain that is 'free' from contamination of isotropic sodium signal. The phantom results (Figure 4-4) clearly demonstrated that sodium signal from anisotropic ordered environment in xanthan gum, where ϖ_Q is non-zero, can be selectively extracted by using the DQ-MA sequence independent of τ. On the other hand, the DQF images show sodium signal intensity from both xanthan gum and agar gel phantoms because the sequence selects both T_{21} and T_{31} created during τ and thus the transverse magnetization detected contains signal from both anisotropic and isotropic ordered sodium.

The implementation of DQ-MA in this study (Figure 4-1) uses $\theta_1 = \theta_2 = 90^o$ and $\theta_3 = 54.7^o$. Other implementations for selective extraction of anisotropic ordered sodium signal include using flip angle values of $\theta_1 = 90^o$, $\theta_2 = 54.7^o$, $\theta_3 = 90^o$, or $\theta_1 = 90^o$, $\theta_2 = \theta_3 = 54.7^o$. It has been shown previously (Kemp-Harper et al., 1997) that the sensitivity of DQ-MA filter is higher when either θ_2 or θ_3 is set to 54.7^o compared to the case when both $\theta_2 = \theta_3 = 54.7^o$. In addition, it has also been shown that a potential pitfall of DQ-MA is incomplete suppression of the third-rank tensor operator (T_{31}) when precise RF pulse flip angle is not achieved, which is especially problematic when using a surface coil. However, the 'clean' suppression of both mono-exponential and bi-exponential T_2 relaxing sodium signal in isotropic ordered environment in phantoms (Figure 4-4) is evident that the B_1 field is reasonably homogeneous throughout the sample volume using the birdcage coil. Incomplete suppression of T_{31} may also occur when finite RF pulse duration is used where ω_1 is close in value relative to ϖ_Q . Under such circumstances, suppression of T_{31} may be better achieved by using another proposed method known as the Jeener-Broekaert (JB) sequence (Kemp-Harper et al., 1994). The selection of even-rank tensor operator (T_{21}) using JB is based on relative phase of the first and third RF pulses being 90^o out of phase. The second RF pulse is used to refocus B_0 inhomogeneities during τ. The transformation of T_{21} into second order coherence by the third RF pulse and then back into single order coherence by the fourth RF for detection is independent of flip angle, which has an advantage over DQ-MA when B_1 is non-uniform over the sample volume. It should be noted that an 180^o refocusing pulse was included in previous implementation of DQ-MA and JB sequences (Kemp-Harper, et al., 1997; Kemp-Harper, et al., 1994). However, the addition of this pulse is not suitable for in vivo imaging application as RF power deposition to tissue is substantially increased. In theory, the 180^o refocusing pulse does not change the coherence order during τ and can be eliminated in imaging application to reduce RF power while retaining the same filtering capability. In vivo human imaging using the JB sequence should be tested in the future and compare to images acquired using DQ-MA.

Given the highly oriented WM fiber tracts, it was hypothesized that DQ-MA signal in WM would be much higher than cerebral GM. However, differentiation of GM and WM on DQ-MA sodium brain images acquired in this study is limited by spatial resolution. The in vivo DQ-MA brain images (Figure 4-5) does not allow detection of spatially varying ϖ_Q in cerebral tissue. Higher resolution DQ-MA brain imaging or other methods to increase anisotropic signal detection (Choy et al., 2006) is required to achieve this purpose. It should be noted that the detection of ϖ_Q is dependent on the orientation of the quadrupolar interaction as $3\cos^2\theta - 1$, where θ is the angle between the electric field gradient and static magnetic field B_0. When θ is at 54.7°, no quadrupolar splitting is observed. The DQ-MA signal is much lower than that of TQF, where the latter is only about 1/10 that of SQ signal in brain (Hancu, et al., 1999). While TQF has been shown to be ~50% more sensitive than DQF (Chung, et al., 1990), the selective extraction of only even-rank tensor operator in DQ-MA is expected to further reduce the signal to less than 5% that of SQ in brain as demonstrated from simulations (Figure 4-3). It is possible that other sites with higher magnetic field strength MRI scanners can improve DQ-MA image resolution to distinguish between the two tissue types. As well, the choice of τ value use in the DQ-MA sequence is important to optimize the signal. A short τ value (2 ms) appears to be optimal for DQ-MA signal detection in brain as demonstrated from 3 healthy subjects (Figure 4-5) in this study. This agrees with simulations that when T_{2f} is short such as in brain, a long τ value greatly reduces DQ-MA signal due to rapid decay of T_{21} during this period.

Sodium quadrupolar splitting (i.e. non-zero ϖ_Q) in biological tissue has only been scarcely explored in the past. One study has shown that such splitting can be observed by measuring the signal strength as a function of flip angle and comparing that to saline (Joseph, et al., 1987). Theoretical simulations in that study showed in quadrupolar splitting situation, a doubling of flip angle effect is observed with maximum transverse magnetization signal intensity reaching only 20% of the unsplit case. NMR imaging experiments in that study did not show any flip angle effect in cat brain and pig skeletal muscle where the authors believed that sodium quadrupolar splitting is non-existent in these specimens and suggested that 100% of sodium signal is ‘visible’. Conversely, NMR spectroscopic studies in human brain (Reddy, et al., 1995), muscles (Reddy, et al., 1995), cartilage (Reddy, et al., 1997b), and breast (Duvvuri, et al., 1999) demonstrated the change in line shapes of DQF sodium spectra as preparation time period τ was varied compared to the consistent TQF signal spectra irrespective of τ, suggesting the existence of residual ϖ_Q in these biological environments. DQ-MA images acquired with different τ values from 3 subjects in this study also clearly show that residual ϖ_Q exists throughout the brain, where the choice of τ only affects the signal magnitude. Perhaps the reason that spectral splitting was not found in the biological samples tested in (Joseph, et al., 1987) was due to the one-dimensional gradient echo imaging method used where spatial resolution obscures the signal measurement between GM and WM. Recent in vivo sodium MRI studies in human brain (Lu, et al., 2010; Ouwerkerk, et al., 2003; Thulborn, et al., 2009) had all demonstrated the capability to perform TSC quantification but yet neglected to consider the effect of residual quadrupolar splitting. Preliminary results showed that signal loss independent of bi-exponential T_2 relaxation was observed in WM regions (posterior limb of the internal capsule or corpus callosum) of the human brain on single quantum images acquired using 'standard' TSC sequence (Stobbe et al., 2009). Future studies should explore the extent of signal loss due to quadrupolar splitting such that accurate measurement of sodium concentration can be made that is unbiased from NMR contrast.

Chapter 5

Relationship Between Sodium Intensity and Perfusion Deficits in Acute Ischemic Stroke[4]

5.1. Introduction

An important goal of magnetic resonance imaging (MRI) in acute ischemic stroke patients is the identification of threatened tissue that remains amenable to salvage following reperfusion therapy, i.e. the penumbra (see section 1.2.2). In general, the "at risk" tissue is still viable when cerebral blood flow remains above the critical threshold (10-15 ml/100 g/min) (Hossmann, 1994), but failure to reperfuse in a timely manner may lead to irreversible injury. Diffusion-weighted imaging (DWI) and corresponding Apparent Diffusion Coefficient (ADC) maps (section 1.3.3) can easily delineate the tissue with water diffusion restriction within minutes after the ischemic onset reflecting cytotoxic edema (Abe, et al., 2003). Perfusion-weighted imaging (PWI) with paramagnetic contrast agent bolus tracking (section 1.3.4) yields metrics that characterize regional cerebral blood flow (Grandin et al., 2002). An operational definition of the ischemic penumbra, based on the PWI-DWI mismatch has been developed (Schlaug, et al., 1999). In this model, the area at risk is identified using hemodynamic parameters derived from raw PWI data. In this study, a time to peak of the deconvolved curve, Tmax, with a +4s threshold was used. The DWI lesion indicates the extent of largely irreversibly injured ischemic 'core' tissue. Mismatch between a larger PWI abnormality and a smaller DWI lesion has been postulated to represent the ischemic penumbra, in which tissue is at risk for infarction, but also potentially amenable to salvage (Kidwell et al., 2003). There is evidence that PWI-DWI

---

[4] A version of this chapter has been published. A. Tsang, RW. Stobbe, N. Asdaghi, MS. Hussain, YA. Bhagat, C. Beaulieu, D. Emery, KS. Butcher, 2011. Relationship between sodium intensity and perfusion deficits in acute ischemic stroke. Journal of Magnetic Resonance Imaging. 33(1): 41-47. Drs. Stobbe, Asdaghi, Hussain, and Bhagat were involved in this study with patient recruitment and scanning as well as editing the manuscript. Dr. Emery was the neuroradiologist involved with image interpretation.

mismatch is predictive of an enriched response to thrombolysis in stroke patients (Albers, et al., 2006; Davis, et al., 2008).

A major barrier to treatment of acute ischemic stroke is the inability to establish the time of symptom onset, particularly in patients who wake with symptoms in the acute period. DWI and PWI do not provide insight into the duration of symptoms. Furthermore, the significance of penumbral patterns in patients without an established onset time is less clear, as perfusion thresholds for infarction are highly time dependent (Butcher et al., 2003). Although the combination of DWI and fluid attenuation inverse recovery (FLAIR) images may provide some temporal information, this has not been established as an imaging pattern predictive of a good response to reperfusion therapy (Ebinger, et al., 2010; Gauvrit et al., 2006; Oppenheim et al., 2000; Perkins et al., 2001; Ricci et al., 1999; Thomalla, et al., 2009). Unknown onset stroke patients are therefore currently excluded from established thrombolysis protocols. Imaging of sodium, a carefully regulated ion whose compartmental distribution is altered during ischemia, may be of added value in the assessment of these patients, by providing temporal information. It should be pointed out that the change of brain tissue sodium concentration is expected to be gradual after the onset of ischemia, where its increase indicates the failure of Na/K-ATPase. Nevertheless, sodium MRI, in conjunction with DWI, may be used as an imaging biomarker for irreversible damage (see section 1.2.2).

Longitudinal sodium MRI studies in animal stroke models indicate a progressive increase in tissue sodium concentration over the first few hours and days after induction of cerebral ischemia (Bartha, et al., 2004a; Jones, et al., 2006 ; Lin, et al., 2001; Thulborn, et al., 1999b; Tyson et al., 1996). Data from human stroke patients are scarce but it appears that sodium intensity is elevated within the infarcted region, reflecting impaired ionic homeostasis (Hussain, et al., 2009; Shimizu, et al., 1993; Thulborn, et al., 1999b). It has also been demonstrated that sodium intensity progressively increases with duration of symptoms within areas of restricted water diffusion (Hussain, et al., 2009).

The relationship between the degree of hypoperfusion and sodium signal changes within the DWI lesion has not been studied. Although absolute perfusion thresholds have not been identified, the severity of oligemia measured with PWI has been correlated with infarction (Butcher, et al., 2003). We therefore tested the hypothesis that the degree of sodium signal changes is correlated with the decrease of regional cerebral blood flow. In addition, earlier studies have not included sodium signal measurements within the perfusion-diffusion mismatch region. In this study, perfusion, diffusion, and sodium imaging were utilized to evaluate first, whether the severity of perfusion deficits are correlated with tissue sodium increases and second, whether sodium intensity is altered in the putative ischemic penumbra of acute stroke patients.

5.2. Methods

5.2.1. Patients

Acute ischemic stroke patients presenting with definite known time of onset and no contraindications to high field MRI scanning were eligible for this study. Our local Human Research Ethics Board approved the study protocol and written informed consent was obtained from all patients or their next of kin. All patients received standard care including thrombolytic therapy (intravenous tissue plasminogen activator; IV tPA) if clinically indicated. Patients demonstrating signs of hemorrhage, extensive white matter hyper-intensities or small DWI lesions (<1.5 mL) were excluded from this study. Patient demographics were recorded at baseline. In addition, a National Institutes of Health Stroke Scale (NIHSS) score was recorded at the time of each MRI scan.

5.2.2. Magnetic Resonance Imaging Protocol

All patients were initially imaged with a proton stroke protocol using an 8-channel phased array radiofrequency (RF) head coil (MRI Devices, Waukesha, WI) on a 1.5-Tesla (T) whole body Siemens Sonata MRI scanner (Siemens Medical Systems, Erlangen, Germany). DWI was acquired with single-shot spin-echo diffusion echo-planar imaging (EPI) using the following parameters: 220 mm field of view (FOV), nineteen 5-mm axial slices with 1.5 mm gap, b value of 1000 s/mm^2 along three orthogonal directions, repetition time (TR)/echo time (TE) 2600/86 ms, GRAPPA R=2, matrix size of 128x128/256x256. PWI images were obtained at 60 time points per slice also using parallel imaging with single-shot gradient echo-EPI (TR/TE 1320/50 ms) using 13-17 5-mm axial slices with 1.5 mm gap and matrix size and slice orientation identical to DWI during the intravenous injection of Magnevist (Bayer HealthCare Pharmaceuticals, Germany), Gd-DTPA, at the rate of 5 mL/s. Axial T1-weighted images were acquired using a turbo spin-echo with 19 slices, TR/TE 680/17 ms, matrix size 128x256, FOV and slice orientation identical to DWI. Axial T2-weighted, FLAIR, gradient-echo, and time-of-flight angiography images were also acquired as part of the 20 minute stroke protocol.

Immediately after the 1.5 T DWI/PWI scans, patients were then transferred to an adjacent high field 4.7 T Varian Inova MRI scanner (Varian Inc., Palo Alto, CA) for sodium imaging. Sodium images were acquired using an in-house designed and manufactured single-tuned RF birdcage head coil resonating at 53MHz. High quality sodium images were acquired in 10 minutes using a steady-state projection acquisition sequence (Na-PASS) (Stobbe, et al., 2008b) with imaging parameters TR/TE 25/0.6 ms, flip angle 55^o, and nominal voxel size of $2.4x2.4x4.8\ mm^3$. Only patients who were capable of remaining still for the 10 minute acquisition were included in the study. Foam padding was used to support the head to minimize movement and the tendency to tilt towards one side. Sodium imaging at 4.7 T is advantageous to improve signal-to-noise ratio and reduce scan length compared to clinical field strength scanners at 1.5 T or 3.0 T.

5.2.3. Image Post-Processing and Analysis

Post-processing of raw perfusion images to generate PWI maps was performed using a customized MATLAB software package Penguin (Center of Functionally Integrative Neuroscience, Århus C, Denmark) implementing the optimized singular value decomposition (oSVD) method (Wu, et al., 2003), which was proposed to address the inaccurate estimation of cerebral blood flow in the original SVD algorithm (Ostergaard, et al., 1996). This software was used to plot the change in MRI transverse relaxivity, which is linearly related to Gd-DTPA concentration, on a per voxel basis over time. Time to peak of the impulse response curve (Tmax) maps were calculated using oSVD. The impulse response curve was calculated as a deconvolution of the raw perfusion images using an arterial input function (AIF) selected in the middle cerebral artery contralateral to the affected hemisphere. A threshold of +4s was applied to the Tmax maps in order to provide an objective measure of the hypoperfused tissue volume, as previously described (Butcher et al., 2008; Butcher, et al., 2005). The calculation steps for hemodynamic parameters from raw perfusion data is described in section 1.3.4.1.

Sodium and DWI images from the same imaging session were spatially co-registered to PWI images using the software package SPM8b (Wellcome Trust Centre for Neuroimaging, London, UK). Regional PWI and DWI image analysis was performed using the Analyze software package (Biomedical Imaging Resource, Rochester, MN) (Robb, 2001). DWI hyper-intense region boundaries were identified with the assistance of an algorithm that searches for changes in signal intensity within a 7 voxel radius. These regions of interest (ROIs) were manually edited to exclude voxels containing cerebral spinal fluid (CSF). ROIs were defined in a similar manner on PWI maps, but voxels below the Tmax+4s threshold were excluded. Penumbral tissue was defined as tissue included in the Tmax+4s ROI, but outside the DWI lesion. Contralateral homologous ROIs for DWI lesion and penumbral tissue were defined by rotation of DWI and Tmax+4s images 180^o with respect to the midline vertical axis. When necessary, these ROIs were manually edited to exclude CSF spaces and include comparable cerebral topography in both hemispheres.

Mean sodium intensity within the infarct core and penumbra was then measured, based on the ROIs described above, as well as contralateral homologous regions. Mean relative sodium signal intensity was calculated as the ratio of that within either the core (DWI) or penumbral (PWI-DWI mismatch) region to contralateral homologous regions. CBF and CBV maps were normalized to 22 mL/100 g/min and 2 mL/100 g respectively in the centrum semiovale on the contralateral side. Mean relative cerebral blood flow (CBF), cerebral blood volume (CBV) and apparent diffusion coefficient (ADC) were calculated in a similar manner (i.e. ipsilateral value normalized by contralateral value).

As CBF differs in white matter (WM) and gray matter (GM), sodium intensity change in WM and GM within the ischemic core was assessed independently. T_1-weighted images acquired as part of the stroke protocol were segmented using a tissue probabilistic map of WM and GM provided by SPM8b. The segmented T_1-weighted images were spatially co-registered to PWI maps. Ischemic core ROIs, as well as contralateral homologous regions, were then sub-divided into WM and GM. Mean relative sodium signal intensity in GM and WM within the DWI lesion was then calculated.

5.2.4. Statistical Analysis

Statistical analysis was performed using SPSS for Windows (SPSS Inc., Chicago, IL). Paired sample T-tests were used to compare the mean sodium intensity in the core or penumbra to that of corresponding contralateral homologous regions. Two-tailed Spearman bivariate tests were used to test correlations between mean relative sodium intensity and relative ADC, CBV, and CBF within the DWI lesion. Post-hoc analysis using 2-way ANOVA tests (not included in the published manuscript) were performed to compare mean sodium intensity in the two tissue regions (i.e. core and penumbra) with imaging time after onset (i.e. ‘4-7 hours’ and ’17-32 hours’).

5.3. Results

5.3.1. Patient Characteristics

Nine ischemic stroke patients (7 male, 2 female) were included in the study (Table 5-1). Note that Table 5-1 in the published manuscript was split into Tables 5-1 and 5-2 in this thesis for presentation clarity. The median patient age was 54 years (range 30-75). The median NIHSS score was 7 (range 3-22). All patients had large cortical infarcts. Eight patients were treated with IV tPA within 3 hours of symptom onset. Treatment was initiated and completed prior to MR imaging in all cases. Initial MR imaging was performed 4-30 hours after symptom onset. Four patients had follow-up imaging performed 22.5-32 hours after onset.

Table 5-1: Acute stroke patient characteristics

	Age	**Sex**	**NIHSS Score**	**Imaging Time After Onset (hours)**	**Reperfusion Therapy**	**Stroke Location**
1	46	M	7 7	4 25.5	tPA	left MCA
2	48	M	4 3	5.25 22.5	tPA	right PCA
3	56	M	13	6.25	none	left MCA
4	54	M	7 5	6.75 28	tPA	left MCA
5	54	M	6 6	7 32	tPA	right PCA
6	66	M	5	29.5	tPA	left MCA
7	30	M	17	17	tPA	left ICA
8	65	F	10	27	tPA	right MCA
9	75	F	22	6	tPA	right MCA
	Median = 54		Median = 7			

MCA = middle cerebral artery; PCA= posterior cerebral artery; ICA = internal carotid artery

5.3.2. Diffusion Lesion and Perfusion Deficit Volumes

All nine acute stroke patients had acute diffusion and perfusion deficits. In addition, all patients had areas of perfusion–diffusion mismatch at their first imaging time point (Table 5-2, Figures 5-1, 5-2). The mean initial DWI lesion volume for patients imaged at 4-7 hours was 33±19 mL. In patients imaged 17-32 hours after onset, DWI lesion volume was 66±89 mL. Acute mean hypoperfused tissue (Tmax+4s) and PWI-DWI mismatch volumes were 78±54 mL and 54±39 mL respectively, indicating the presence of some penumbral tissue at baseline. At later timepoints (i.e. 17-32 hours), the Tmax+4s tissue and PWI-DWI mismatch volumes were smaller (69±88 mL and 30±26 mL respectively). In the four patients imaged serially, mean DWI lesion increased from 30±24 mL to 45±26 mL while the mean penumbral (Tmax+4s-DWI) volumes decreased from 48±37 mL to 23±24 mL between the first and second scans.

Table 5-2: Summary of acute stroke patient data

Patient	**Imaging Time After Onset (hours)**	**Tmax+4s Volume (mL)**	**PWI-DWI Mismatch Volume (mL)[a]**	**DWI Core Volume (mL)[b]**	**Relative Sodium Intensity (Penumbra)**	**Relative Sodium Intensity (Core)[b]**	**Relative CBF (Core)**	**Relative CBV (Core)**	**Relative ADC (Core)**
1	4	142	92	61	0.97	0.99	0.40	0.79	0.68
	25.5	114	52	77	0.97	1.46	0.41	1.08	0.55
2	5.25	22	19	3	0.99	1.10	0.67	1.14	0.86
	22.5	13	6	13	1.08	1.31	0.81	0.96	0.65
3	6.25	115	90	36	0.85	1.07	0.48	0.94	0.62
4	6.75	38	26	28	0.91	1.01	0.89	1.20	0.74
	28	9	5	42	0.95	1.06	1.16	1.29	0.66
5	7	69	47	29	1.04	1.39	0.53	0.87	0.64
	32	41	23	47	1.10	1.76	0.71	0.71	0.71
6	29.5	27	27	15	0.93	1.46	1.03	2.05	0.72
7	17	248	74	261	0.97	1.33	0.37	1.41	0.47
8	27	22	21	9	0.98	1.78	1.08	0.51	0.81
9	6	51	26	39	1.02	1.10	0.46	0.72	0.62
mean± stdev	4-7	78±54	54±39	33±19	0.96±0.07	1.11±0.14	0.57±0.18	0.94±0.19	0.69±0.09
	17-32	69±88	30±26	66±89	1.00±0.07	1.45±0.26	0.80±0.32	1.15±0.51	0.65±0.11

[a] Note that the penumbral volume need not be the subtracted area of the PWI and DWI lesion volumes if the PWI lesion volume does not fully overlap with the DWI lesions.

[b] DWI lesion volumes and core sodium signal intensities vary slightly from a previous study utilizing some of this data (Hussain, et al., 2009), as they were reanalyzed using different software and diffusion intensity threshold criteria.

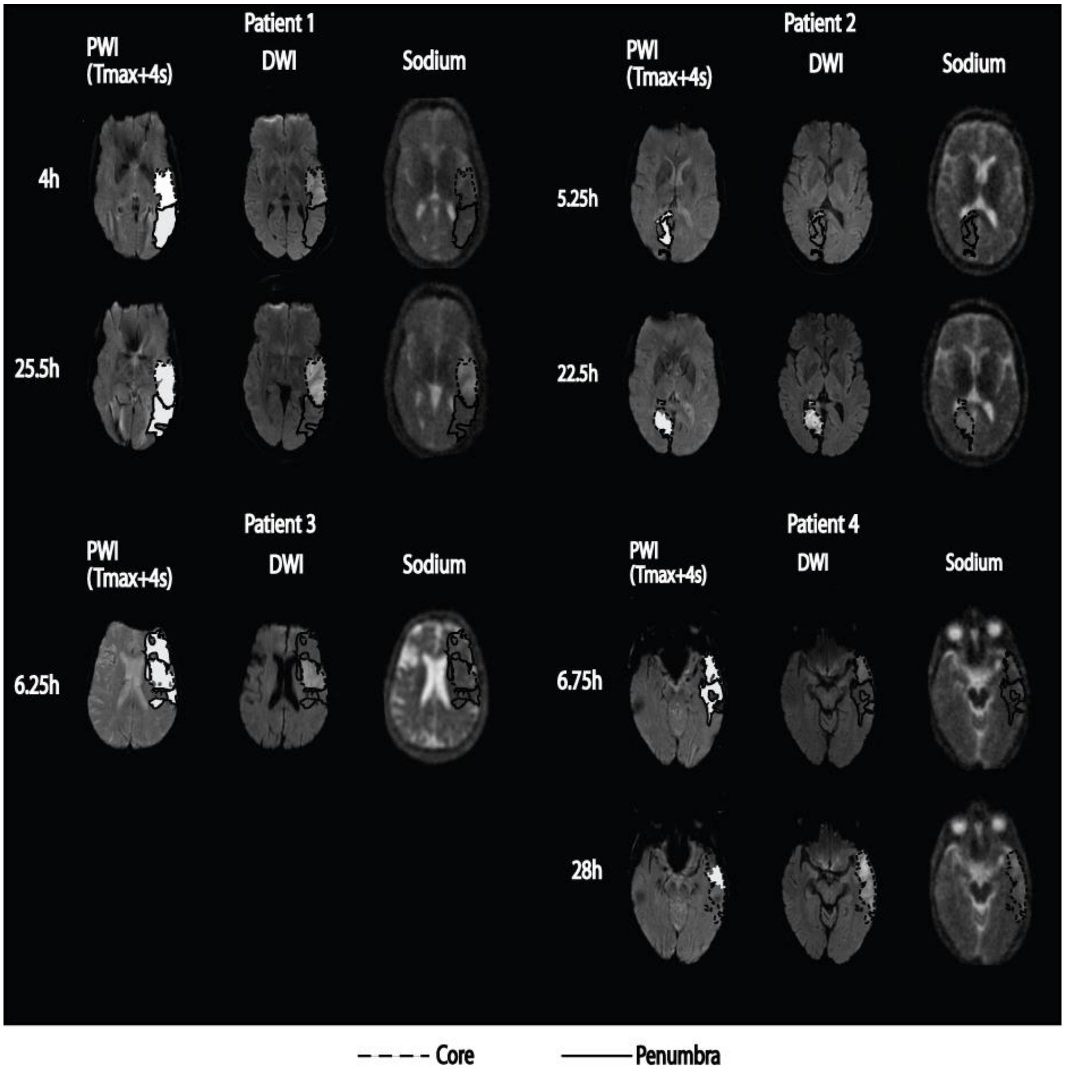

Figure 5-1: Images of a representative slice from ischemic stroke patients #1-4 showing the hypoperfused (Tmax+4s) perfusion maps, the DWI with DWI hyper-intense (core) in dotted outline, the PWI-DWI mismatch tissue (penumbra) in solid outline, and sodium images for all acquisition times.

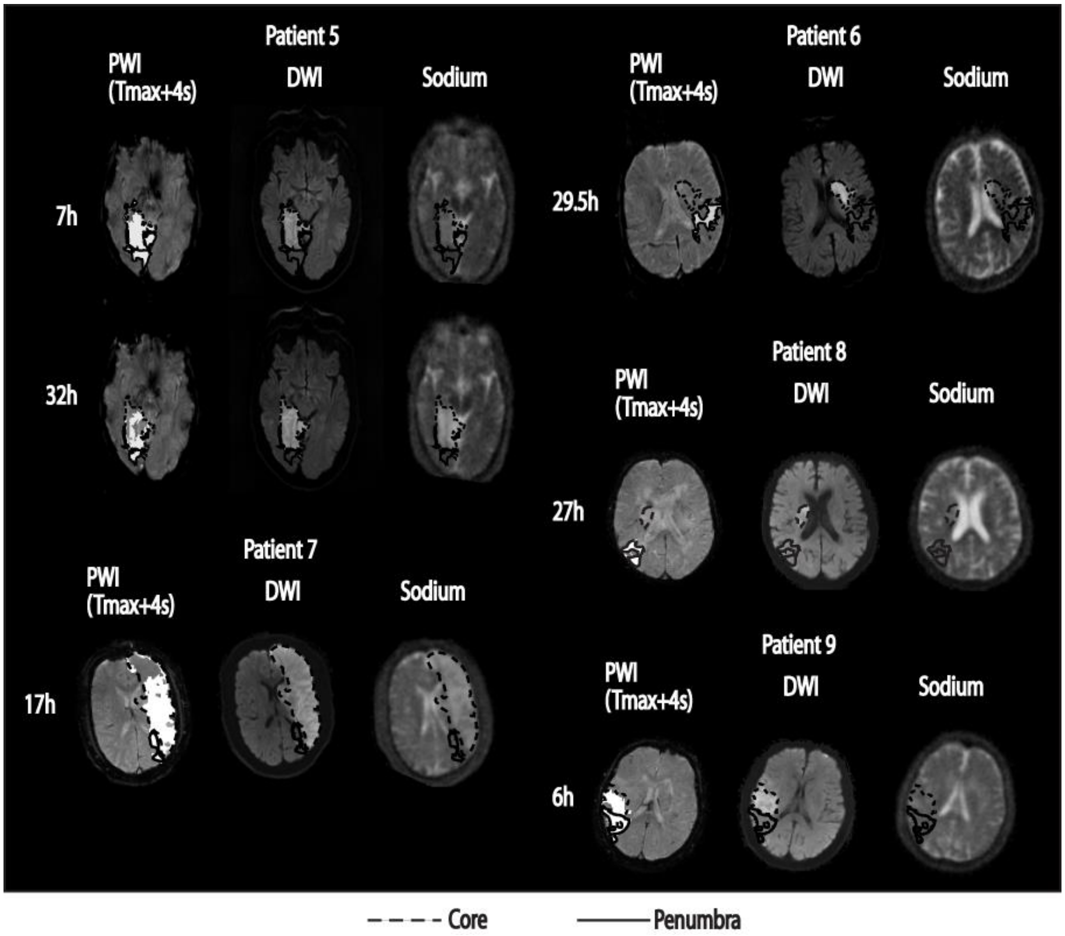

Figure 5-2: Images of a representative slice from ischemic stroke patients #5-9 showing the hypoperfused (Tmax+4s) perfusion maps, the DWI with DWI hyper-intense (core) in dotted outline, the PWI-DWI mismatch tissue (penumbra) in solid outline, and sodium images for all acquisition times. All 9 patients (5 shown here and 4 in Figure 5-1) had perfusion/diffusion mismatches at their first timepoint. Typically, the absolute lesion volume of core enlarged from 4-7 hours to 17-32 hours after symptom onset while the penumbral volume diminished.

5.3.3. Sodium Intensity Changes

Region of interest measurements showed that relative sodium intensity was not correlated with either relative CBF (ρ = 0.157; P = 0.61), CBV (ρ = -0.234; P = 0.44) or ADC (ρ = 0.021; P = 0.95) within the DWI lesion (Figure 5-3). Qualitatively, the increased sodium signal intensity appeared to be limited to the areas of diffusion restriction and did not extend into the mismatch regions (Figures 5-1, 5-2). Quantitative analysis confirmed that sodium signal intensity in the perfusion-diffusion mismatch was not significantly different from that in homologous contralateral regions at any time point with mean relative sodium intensities of 0.96 ± 0.07 (P = 0.28) at 4-7 h and 1.00 ± 0.07 (P = 0.89) at 17-32 h (Figure 5-4). In contrast, sodium intensity in the DWI-defined lesion increased with time after symptom onset. In patients imaged 4-7 hours after onset, mean relative sodium intensity within the DWI lesion was not significantly elevated (1.11 ± 0.14; P = 0.11), but it was at 17-32 hours (1.45 ± 0.26; P = 0.003). The significant sodium intensity increase within the DWI lesion at 17-32 hours was also confirmed from the 2-way ANOVA tests. There were no significant differences in mean relative sodium intensity between GM and WM within the DWI lesion at 4-7 hours (GM 1.12 ± 0.18 and WM 1.14 ± 0.15; P = 0.82) and at 17-32 hours (GM 1.41 ± 0.19 and WM 1.42 ± 0.25; P = 0.97) (Figure 5-5). We also defined ROIs remote from DWI lesion and PWI-DWI mismatch regions in the ipsilateral as well as the contralateral hemisphere, in order to demonstrate similar sodium intensity in non-affected tissue in all patients. Mean relative sodium intensity in these ROIs was 1.00 ± 0.04.

CBF was reduced in the DWI core in all subjects imaged within 4-7 hours. Two of 6 subjects demonstrated elevated CBV during this time. However imaging at 17-32 hours revealed elevated CBF and CBV in 3 of 7 and 4 of 7 patients, respectively (Figure 5-3a,b). ADC was reduced in all subjects within the DWI core and did not change over time (Figure 5-3c).

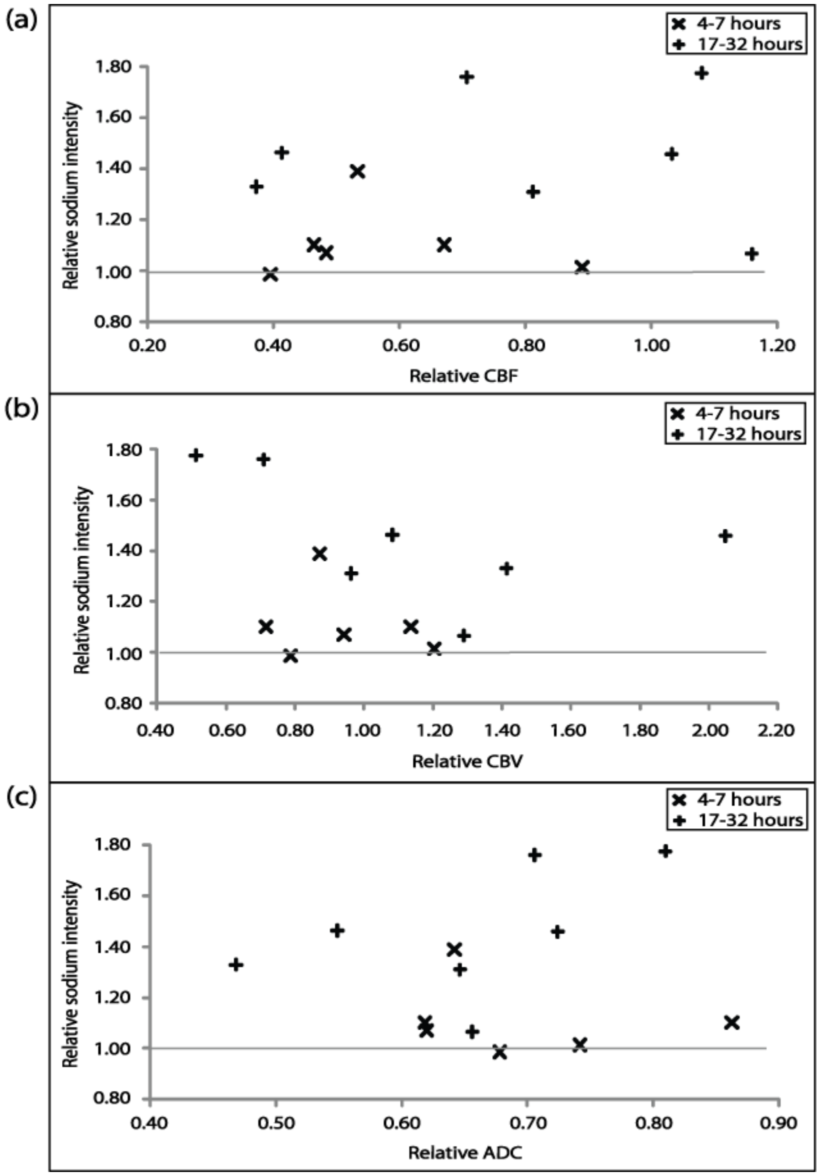

Figure 5-3: There was no correlation between mean relative sodium intensity within the DWI lesion with either relative (a) Cerebral Blood Flow (CBF), (b) Cerebral Blood Volume (CBV), or (c) Apparent Diffusion Coefficient (ADC). All patients demonstrated reduced CBF and CBV at 4-7 hours. ADC was reduced relative to contralateral homologous regions for all patients.

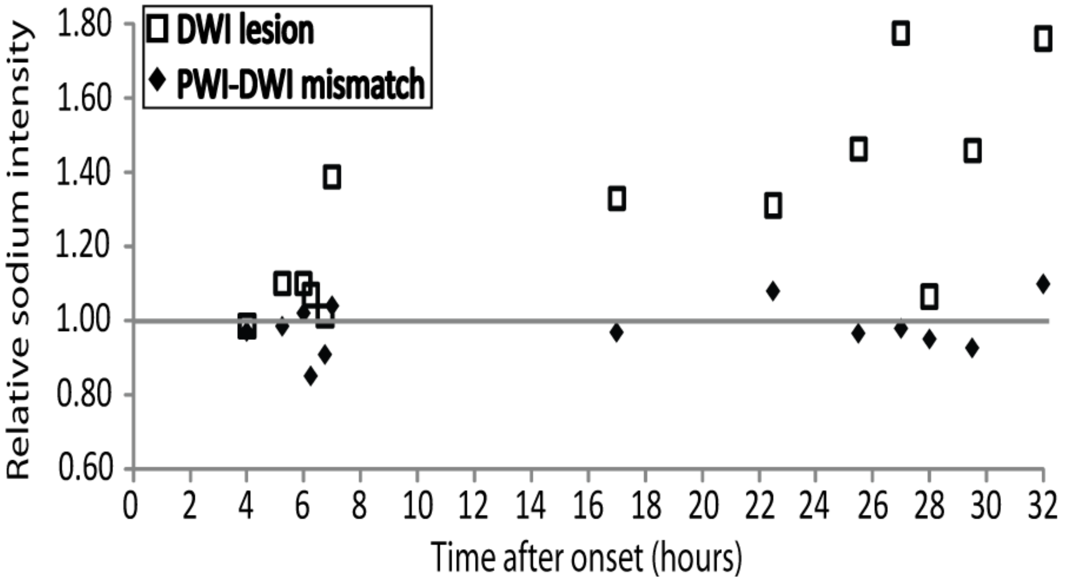

Figure 5-4: Mean relative sodium intensity was progressively elevated within the DWI lesion with increasing duration between symptom onset and time to imaging. There was no significant sodium signal increase within the PWI-DWI mismatch regions at any time.

7s

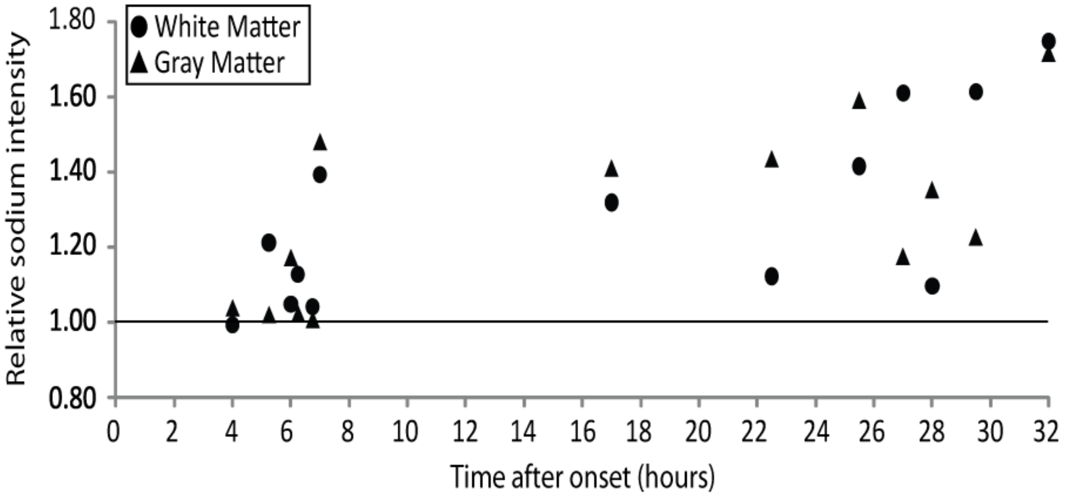

Figure 5-5: Mean relative sodium intensity changes within the DWI lesion were not significantly different between gray matter and white matter at 4-7 hours and 17-32 hours after onset.

5.4. Discussion

It has been shown previously in rats that brain tissue sodium concentration measured using flame photometry increases linearly after arterial occlusion within region with severe reduction in ADC and CBF (Wang, et al., 2000). However this is the first study to examine the relationship between cerebral blood flow/volume and sodium NMR signal intensity changes within the DWI lesion in acute stroke. In addition, previous sodium MRI studies of stroke, in either animals or humans, have examined signal intensity changes only in areas of diffusion restriction and not in penumbral zones indicated by perfusion measurements. Our results indicate that sodium intensity cannot be predicted by any perfusion parameter. Furthermore, sodium intensity is not altered within the PWI-DWI mismatch tissue, irrespective of the interval between symptom onset and image acquisition. Sodium signal does increase in sub-acute ischemic stroke, but only in regions that are already bio-energetically compromised, as demonstrated by water diffusion restriction. However, unlike water ADC, which remains consistently low in the first few days after stroke, the sodium signal intensity increases markedly over the same time period in the core. The lack of sodium change in the putative penumbra suggests preserved ionic homeostasis and is consistent with the lack of water ADC reduction, despite the abnormal cerebral perfusion demonstrated with PWI.

Although PWI-DWI mismatch provides an operational definition of the ischemic penumbra, it is recognized that this model often overestimates the truly at risk tissue volume, due to the inclusion of areas of benign oligemia (Grandin et al., 2001; Kidwell, et al., 2003). It has been shown that a deconvolved parameter (i.e. Tmax) reduces overestimation of the hypoperfused tissue volume due to bolus delay and dispersion (Butcher, et al., 2005). However definitive PWI thresholds for either penumbra or infarct have not been identified. This is nonetheless a challenging endeavour as thresholds for infarction vary with the duration of ischemia and can be modified by both spontaneous and thrombolysis associated reperfusion (Butcher, et al., 2003). In this study, we defined hypoperfusion as a Tmax+4s delay, which was used to define an objective penumbral tissue volume.

The ischemic penumbra contains tissue where CBF is reduced to below the threshold required to sustain normal neuronal functional activity, but remains above that for sodium potassium exchange pump failure (Astrup, et al., 1981; Hossmann, 1994). A previous study revealed only slight elevations of extracellular potassium concentration within the penumbra, indicating that ion pumps are largely functional (Astrup et al., 1977). Our results are consistent with this finding, as penumbral metabolic activity appears sufficient to maintain normal sodium gradients in the PWI-DWI mismatch regions. Identification of the penumbral tissue at the hyper-acute time is critical so that reperfusion treatment may prevent it from progressing to infarction. It is recognized that the PWI-DWI mismatch region at later time points (i.e. 17-32 hours) is likely not penumbral tissue.

We have previously shown in a larger sample, which included five of the subjects in this study, that sodium intensity increases minimally within the first 7 hours after stroke onset and then more substantially with time, eventually reaching a plateau at approximately 48 hours (Hussain, et al., 2009). In this study, we have shown that sodium signal increases in the ischemic core cannot be predicted by the severity of oligemia, as measured with either CBF or CBV. Sodium signal intensity progressively increased over time in core infarct areas, even in cases where reperfusion occurred (Figures 5-1, 5-2). This was seen clearly in patient 4 with follow-up imaging at 28 hours after symptom onset demonstrating slight elevation in sodium intensity associated with elevated blood flow (rCBF 1.16) and volume (rCBV 1.29) in the region of the DWI lesion, consistent with reperfusion.

Sodium intensity changes are subtle within 7 hours of symptom onset, and therefore it is unlikely that a relationship can be established between sodium intensity and perfusion parameters in that time frame. Similarly, ADC changes are not predictive of sodium intensity increases, as the former does not develop in a time dependent fashion. The substantial increase in sodium intensity coexists in regions where ADC is reduced relative to contralateral regions. Unlike sodium intensity, however, ADC values decline suddenly and remain relatively stable for at least 96 hours from stroke onset (Schlaug et al., 1997).

It is known that normal CBF is higher in gray matter than white matter. It is also recognized that the flow thresholds for infarction differ with each tissue type (Arakawa et al., 2006). We therefore assessed sodium changes in gray and white matter separately within the ischemic core (DWI hyper-intensity). Our results did not indicate significant differences in mean relative sodium intensity changes in GM and WM within the DWI lesion at 4-7 h and 17-32 h. There were differences between gray and white matter sodium intensity in individual patients (Figure 5-5). In over half of the patients, gray matter sodium signal was higher than that in white matter, although there was a large degree of heterogeneity. This likely reflects differences in the proportion of gray and white matter involvement in the infarcted tissue. It may be that gray matter sodium increases earlier and to a greater extent than that in white matter, but this will need to be assessed in a much larger sample. Furthermore, avoiding the effects of partial volume averaging (mainly of 3x sodium concentrated CSF) in low resolution sodium imaging is difficult, particularly if there is brain atrophy at older ages.

Normal sodium intensity is consistent with preserved ionic homeostasis within the penumbral tissue. Within the DWI lesion, previous animal studies (Benveniste et al., 1992; Kohno et al., 1995) indicate that the reduced ADC occurs in tandem with the shift of extracellular water and ions into the intracellular compartment due to failure of the sodium-potassium ATPase. Therefore, sodium signal changes, in combination with ADC reduction, likely reflect prolonged ATPase dysfunction and/or a loss of cellular integrity. The subsequent ionic shifts result in additional accumulation of sodium ions within the infarct region and appear to be associated with irreversible injury. There has also been evidence suggesting that apoptosis is regulated by ionic homeostasis, notably that the shift of sodium ions into the intracellular compartment during ischemia is accompanied by efflux of potassium ions and this event triggers cascading processes leading eventually to apoptosis (Yu, 2003).

This study has a number of limitations. The number of patients recruited for DWI, PWI and sodium imaging, was relatively small at nine, reflecting the logistical difficulties involved in serial imaging of acute stroke patients using two different MRI scanners, even if side-by-side. Nonetheless, it is very clear that sodium signal increases are limited to the infarct core, as defined by hyper-intensity on DWI (and reduced ADC) and do not occur in penumbral tissue, as defined by PWI-DWI mismatch. In addition, 8 of 9 patients in this study were treated with tPA shortly prior to their initial MRI scan, and subsequent reperfusion may have affected the penumbral sodium response. Regardless, all patients did have areas of persistent hypoperfusion at the time of sodium imaging. Contralateral homologous regions were carefully defined and manually edited to minimize the effect of left-right asymmetry as well as to avoid sodium signal from CSF. However, low resolution sodium images are prone to partial volume effects which likely resulted in some variability in mean sodium intensity values. Finally, the effect of gadolinium contrast on sodium image acquisition has not yet been evaluated. However, this is unlikely to have affected our results, as no enhancement was observed on post-gadolinium T_1-weighted images.

In conclusion, assessment of sodium intensity may be clinically useful in stroke patients with an unknown time of onset, such as those who wake with symptoms. These patients are currently ineligible for thrombolytic or other reperfusion therapy. Patients with a penumbral (PWI-DWI mismatch) pattern and no sodium intensity changes are likely the ideal treatment candidates. This combination of imaging changes is consistent with the potential for tissue salvage (penumbra) and a total ischemic period of no more than 7 hours.

Chapter 6

Inversion Recovery Sodium Magnetic Resonance Imaging in Human Ischemic Stroke[5]

6.1. Introduction

Sodium ions rapidly redistribute toward the intracellular compartment after the bio-energetic failure of Na^+/K^+-ATPase resulting in anoxic depolarization (Balestrino, 1995). Elevation of intracellular sodium (or loss of ion homeostasis) is followed by catastrophic events that eventually lead to tissue infarction (Brouns et al., 2009). In particular, influx of sodium, and also calcium, ions has deleterious effects that include rapidly exhausting the already depleted adenosine triphosphate to maintain calcium ion balance and activate enzymes that ultimately lead to cell death (Deb et al., 2010). Thus, non-invasive monitoring of intracellular sodium concentration may be an important imaging marker of tissue viability and further enhance our understanding of acute stroke pathophysiology. Previously, a decrease in the amplitude of the sodium magnetic resonance spectrum was observed during transient induced ischemia in dogs (Eleff et al., 1991). A decrease in the sodium spectrum was interpreted as shifting of sodium ions to intracellular compartment. The study also demonstrated that the sodium spectrum amplitude had restored almost fully to pre-ischemic level shortly after reperfusion suggesting sodium efflux and the re-establishment of ionic gradients across cellular compartments. As such, magnetic resonance imaging (MRI) of intracellular sodium may complement perfusion weighted imaging (PWI) to signal reperfusion response in individual acute stroke patients scanned before and after thrombolysis.

---

[5] Manuscript in preparation to be submitted.

In vivo human MRI of sodium allows quantification of *total* tissue sodium concentration (TSC) within the infarcted tissue (Thulborn, et al., 1999b) and assessment of the progressive increase of tissue sodium signal intensity with respect to the contralateral region following stroke (Hussain, et al., 2009). Tissue sodium is the volume weighted mean of sodium concentration from both intra- and extracellular compartments (Christensen et al., 1996). Previously, MRI methods (or sequences) used to acquire tissue sodium signal (Hussain, et al., 2009; Thulborn, et al., 1999b) did not provide information pertaining to compartmental ion shifts (i.e. extra- to intracellular space). However, non-invasive monitoring of intracellular sodium may be possible using alternate MRI sequences that exploit sodium nuclear relaxation characteristics (see section 1.4.4). One method, known as multiple quantum filtering (MQF) (Jaccard, et al., 1986), selectively acquires sodium signal that exhibits bi-exponential transverse (T_2) relaxation. It has been suggested that the sodium MQF signal is weighted towards the intracellular space (Allis et al., 1991; Tauskela, et al., 1997). Another approach for selective compartment sodium imaging is known as soft inversion recovery fluid attenuation (SIRFLA) (Stobbe, et al., 2005). The SIRFLA sequence is sensitive to compartmental differences in both longitudinal (T_1) *and* transverse (T_2) relaxation. The SIRFLA sequence suppresses sodium nuclei with longer T_1 relaxation that is assumed to be the case in extracellular space. To our knowledge, neither the SIRFLA nor MQF ‘intracellular sodium’ MRI methods have been applied in the study of human ischemic stroke. The advantage of the SIRFLA approach for in vivo intracellular weighted sodium imaging is that the signal is greater than MQF so that higher spatial resolution images can be obtained within a given scan time.

In this study, sodium signal intensity was measured within the infarct core relative to the contralateral hemisphere in patients who were imaged with both tissue sodium and the supposed intracellular weighted SIRFLA sodium MRI sequences. We tested the hypothesis that the SIRFLA provides ancillary information to tissue sodium MRI, thereby yielding insights into intracellular sodium concentration changes after stroke onset. We also present an interesting observation concerning the appearance of white-matter hyper-intensities (WMH) on the sodium SIRFLA images.

6.2. Methods

6.2.1. Imaging Subjects

A retrospective study was performed on a cohort of 18 ischemic stroke patients with known symptom onset time and no hemorrhage or contraindications to high field MRI. These patients were part of the previous study (Hussain, et al., 2009), and among them four were also included in the study presented in Chapter 5, as indicated in Table 6-1. The study protocol was approved by the local Human Research Ethics Board and written informed consent was obtained from all patients or their next of kin. All acute stroke patients received standard care including thrombolytic therapy such as intravenous tissue plasminogen activator (IV tPA) if clinically indicated. A National Institutes of Health Stroke Scale (NIHSS) score was recorded at the time of each MRI scan. In addition, three subjects were imaged using the same sodium and proton MRI sequences (describe below) that were performed on the 18 patients due to their presentation with white matter hyper-intensities.

Table 6-1: Summary of patient clinical data

Patient[a]	Age (years)	Sex	NIHSS	Treatment	Imaging time after onset (hours)	Stroke location
1[b]	46	M	7 / 7	IV tPA	4 / 25.5	Left MCA
2[b]	48	M	4 / 3	IV tPA	5.25 / 22.5	Right PCA
3	22	M	1 / 1	None	6 / 52	Left MCA
4[b]	56	M	13 / 7	None	6.25 / 25.5	Left MCA
5[b]	54	M	7 / 5	IV tPA	6.75 / 28	Left MCA
6	72	F	19	IV tPA	9.33	Right MCA
7	54	M	10	None	13	Right MCA
8	52	M	12 / 10	None	14 / 36	Left MCA
9	61	M	7	None	18.5	Right SCA
10	84	M	6	IV tPA	23	Right striatocapsular
11	58	F	11	None	29	Left PCA
12	82	F	6	None	36	Right striatocapsular
13	55	F	6	None	38	Right striatocapsular
14	78	F	1	None	45	Left MCA
15	55	F	7	IV tPA	47	Left striatocapsular
16	73	M	5	None	50	Left MCA
17	73	F	17	IV tPA	98	Right MCA
18	81	F	8	IV tPA	104	Left MCA
	Median = 57		Median = 7			
19	80	F	-	None	-	-
20	88	M	-	None	-	-
21	91	M	-	None	-	-

MCA = middle cerebral artery; PCA= posterior cerebral artery; SCA = superior cerebellar artery

[a] Patients 1-18 were acute stroke patients who were part of previous study (Hussain, et al., 2009). They were identified as patient 5,7,9,3,8,16,13,2,15,6,4,11,14,10,12,20,21,18 respectively. Patients 19-21 were included in this study due to their presentation of white matter hyper-intensities

[b] Patients 1,2,4,5 were included in the study presented in Chapter 5. They were identified as patient 1,2,3,4 respectively.

6.2.2. Magnetic Resonance Imaging

All subjects were initially imaged with a proton (^{1}H) stroke protocol, including diffusion-weighted imaging (DWI) and fluid attenuation inversion recovery (FLAIR) sequences, using an 8-channel phased array radiofrequency (RF) head coil (MRI Devices, Waukesha, WI) on a 1.5-Tesla (T) whole body Siemens Sonata MRI scanner (Siemens Medical Systems, Erlangen, Germany). Image volumes acquired using DWI and FLAIR had nineteen 5 mm-thick axial slices with 1.5 mm gap. DWI used single-shot spin-echo diffusion echo-planar imaging (EPI), field of view (FOV) 220 mm, b value of 1000 s/mm^2 along three orthogonal directions, repetition time (TR)/echo time (TE) 2600/86 ms, GRAPPA R=2, matrix size of 128x128 zero-filled to 256x256. FLAIR sequence used TR/TE 7450/94 ms, inversion time (TI) 2400 ms, FOV 220 mm and matrix size of 256x204.

Immediately following 1.5 T scans, the subjects were transferred to an adjacent 4.7 T Varian Inova MRI scanner (Walnut Creek, CA) for sodium imaging using a single-tuned RF birdcage head coil. Tissue sodium images were acquired in 10 minutes using a steady-state projection acquisition sequence known as Na-PASS (Stobbe, et al., 2008b) with TR/TE 25/0.6 ms and flip angle 55^o for nominal voxel size of 2.4x2.4x4.8 mm^3. As well, SIRFLA images were acquired in 10 minutes using TR/TE 100/0.6 ms, TI 18 ms, flip angles 180^o and 90^o, for nominal voxel size of 5x5x10 mm^3. The ‘soft’ inversion pulse was 26 ms in duration. Sodium signal acquisition used twisted projection imaging (Stobbe, et al., 2008a) in both sequences.

6.2.3. Image Post-Processing

Sodium images from the same imaging session were spatially co-registered to DW images using SPM8 (Wellcome Trust Centre for Neuroimaging). Regional image analysis was performed using Analyze 11.0 software package (Biomedical Imaging Resource, Mayo Clinic, Minnesota) in the eighteen stroke patients. The ischemic core was identified as hyper-intense regions on DWI by means of an auto-trace algorithm. The algorithm searches for neighboring voxels with signal intensity values within a defined range from a seed voxel. These regions of interest (ROIs) were manually edited to exclude voxels containing cerebrospinal fluid (CSF). Presumably healthy homologous brain ROIs were defined on contralateral side by rotation of DW images 180^o with respect to the midline vertical axis and manually edited to exclude CSF and regions outside the brain. Mean relative sodium signal intensity was calculated for both Na-PASS and SIRFLA as the ratio of that within the core to contralateral homologous regions.

6.2.4. Statistical Analysis

Paired sample T-tests were performed in MATLAB (Matlab, MathWorks, Natwick, MA) to test for differences in the mean relative sodium intensity within the core measured on Na-PASS and SIRFLA images among the eighteen patients. In addition, 2-way ANOVA tests were performed to compare relative mean Na-PASS and SIRFLA signal intensities with imaging times of within 14 hours and beyond 14 hours after symptom onset. Furthermore, relative sodium intensities were fitted to a “best fit” line based on weighted nonlinear least squares regression using a modified Morgan, Mercer, Flodin (MMF) model (Ratkowsky, 1990) as in the previous study (Hussain, et al., 2009) to show signal evolution with respect to time after symptom onset. Such nonlinear model was selected because it starts at zero at time zero and also approaches an upper asymptote at later times that is logical to reflect the increase of both intracellular and tissue sodium concentration after the onset of ischemia. This modified MMF model has 3 parameters fitted to the following equation

$$F = \frac{\alpha t^{\delta}}{\exp(\gamma) + t^{\delta}} \qquad \text{Eq. 6-1}$$

where α indicates the upper asymptote of sodium signal leveling off.

6.3. Results

6.3.1. Patients Characteristics

All eighteen stroke patients (median age 57 years, range 22-84 years; male 10, female 8) demonstrated conspicuous DWI hyper-intense regions, with corresponding hypo-intensity on mean diffusivity (MD) maps, for identification of the ischemic lesion core. In addition, six patients had follow-up imaging to yield a total of 24 time points. The DWI lesion volume and other imaging data for each patient are summarized in Table 6-2.

Table 6-2: Summary of acute stroke patient imaging data

Patient	Imaging time after onset (hours)	DWI core volume (mL)	Relative Na-PASS Increase (%)	Relative SIRFLA Increase (%)
1	4 / 25.5	45.9 / 87.7	1 / 43	5 / 27
2	5.25 / 22.5	3.5 / 12.6	5 / 31	9 / 29
3	6 / 52	4.0 / 17.7	17 / 32	10 / 7
4	6.25 / 25.5	30.0 / 43.8	6 / 40	32 / 26
5	6.75 / 28	23.5 / 34.6	1 / 13	2 / 4
6	9.33	146.6	27	46
7	13	6.0	27	40
8	14 / 36	65.2 / 91.0	33 / 50	25 / 39
9	18.5	6.9	57	51
10	23	9.4	55	50
11	29	42.4	43	47
12	36	6.6	85	53
13	38	1.3	63	16
14	45	3.6	60	39
15	47	13.5	99	33
16	50	56.6	61	68
17	98	54.0	108	75
18	104	28.3	44	37
mean±stdev	≤ 14 hours	41±48	15±13	21±17
	≥18.5 hours	42±51	59±28	43±29

6.3.2. Relative Sodium Intensity

Representative sodium image slices co-registered with corresponding proton DW images and MD maps are presented for three selected patients scanned at 4, 47, and 98 hours after stroke onset in Figure 6-1. Sodium signal from CSF is suppressed on the SIRFLA images, reflecting the relaxation-based weighting of the sequence. Sodium signal intensity remained elevated at later times post onset on both Na-PASS and SIRFLA images. Relative signal intensity evolution for all 24 time points is shown in Figure 6-2a. Within the first 14 hours following stroke onset, sodium signal increase within the lesion (compared to the contralateral hemisphere) is generally higher for SIRFLA ('+') than for Na-PASS ('o') (1% - 26% greater for 6 of 8 patients, Figure 6-2b). At later time points (≥18.5 hours), the lesion sodium signal increase (compared to the contralateral hemisphere) is generally lower for SIRFLA than for Na-PASS (2% - 66% less in 14 of 16 patients imaged between 18.5-104 hours after onset). Quantitative analysis showed that sodium signal measured on Na-PASS and SIRFLA images were significantly different between 18.5-104 hours after onset ($P = 0.002$). There was no significant difference ($P = 0.171$) between the signal increases in SIRFLA compared to Na-PASS within the first 14 hours after stroke. The significant difference between Na-PASS and SIRFLA signal intensities at 18.5-104 hours is also confirmed by 2-way ANOVA tests. Furthermore nonlinear curve fitting to a modified MMF growth model suggested that relative SIRFLA signal intensity (dashed line) increases more rapidly within the first 14 hours post onset and levels off at 39 ± 12% thereafter compared to the more gradual increase of Na-PASS (solid line) which levelled off at 72 ± 31% beyond 60 hours. The parameters of fit for Na-PASS are: $\alpha = 72 \pm 31\%$, $\delta = 1.9 \pm 1.2$, $\gamma = 5.5 \pm 2.4$. Similarly, the parameters of fit for SIRFLA are: $\alpha = 39 \pm 12\%$, $\delta = 4.9 \pm 6.4$, $\gamma = 9.4 \pm 11.5$.

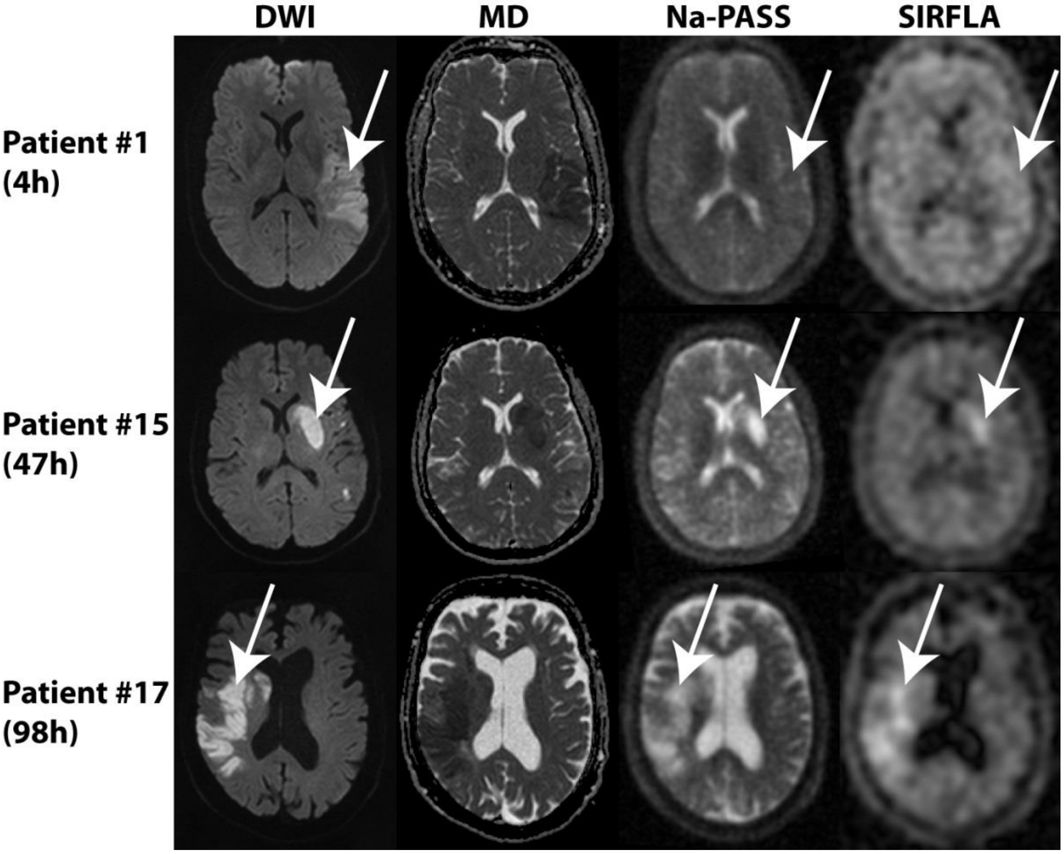

Figure 6-1: Representative axial slices from three patients imaged at different times after symptom onset showing elevated signal intensity on both sodium images within the ischemic core (arrow). The suppression of sodium signal in CSF for SIRFLA reflects the longer T_1 of sodium in CSF relative to brain parenchyma. The patient imaged at 4 hours after onset has greater SIRFLA signal increase (5%) in the DWI lesion compared to Na-PASS (1%). Conversely, the other two patients imaged at 47 hours and 98 hours had greater Na-PASS (99% and 108%, respectively) signal increase compared to SIRFLA (33% and 75%, respectively).

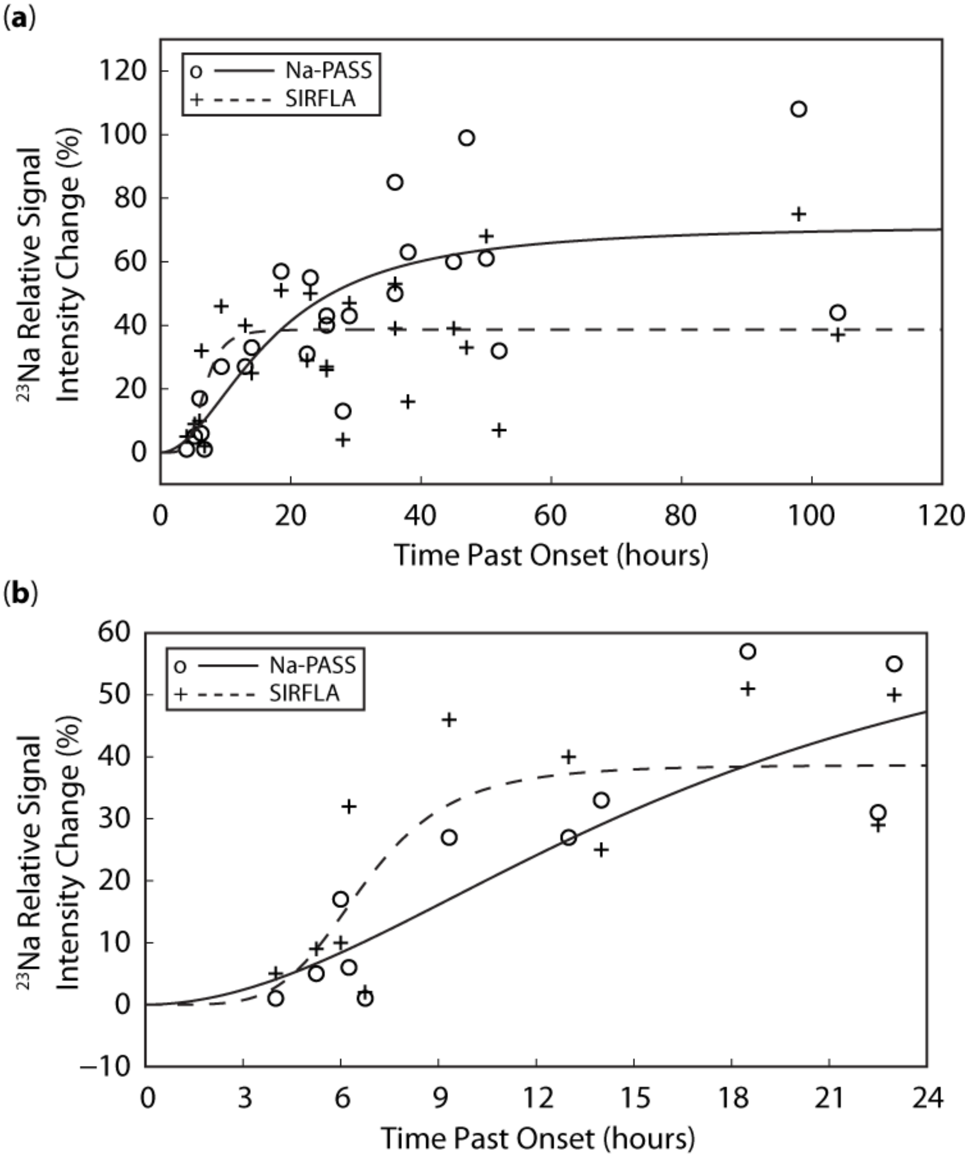

Figure 6-2: (a) Relative sodium signal intensity increase for all 18 patients (24 time points) measured on Na-PASS images is in general lower within the first 14 hours (N=8) after stroke compared to the increase in SIRFLA signal intensity. A reverse trend was observed at 18.5 hours and beyond (N=16). (b) Within the first 14 hours, SIRFLA sodium signal increase is more rapid and levelled off sooner compared to the more gradual increase seen in the Na-PASS data. Nonlinear curve fit to the modified MMF growth model for Na-PASS and SIRFLA signal increase is represented as solid and dashed lines respectively on both graphs.

6.3.3. White Matter Hyper-intensity

Two male (age 88 and 91) and a female subject (age 80) as well as two among the eighteen patients (patient 10 and 14 in Table 6-1) demonstrated conspicuous hyper-intensities on T_2-weighted proton FLAIR images in deep or periventricular WM. A representative slice from the two sodium and corresponding proton image volumes acquired in two subjects is shown in Figure 6-3. On the proton T_2-weighted FLAIR images WMH areas are hyper-intense, while CSF appears dark. However, on the sodium SIRFLA images the same WMH areas are *hypo-intense*, with signal intensity approaching that of CSF.

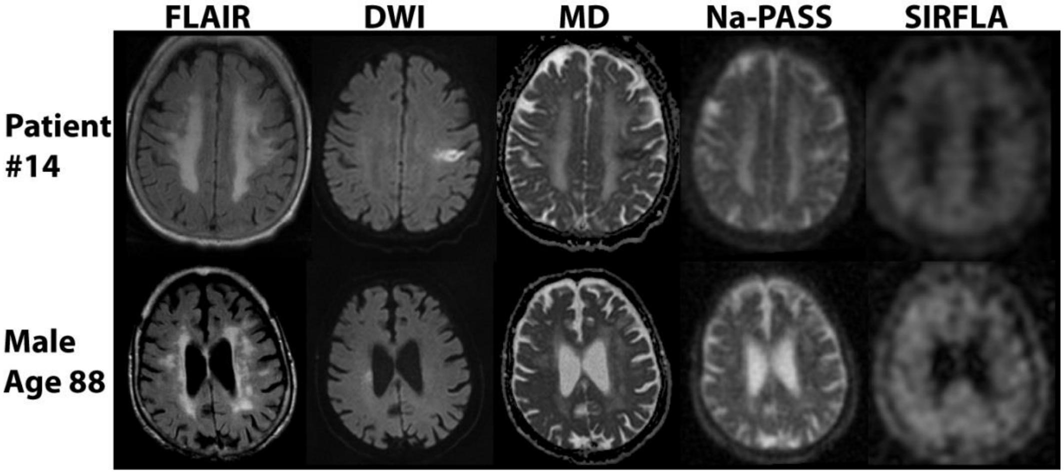

Figure 6-3: Two selected subjects with conspicuous hyperintensity in deep (top row) or periventricular (bottom row) white matter observed on T_2-weighted proton FLAIR images and MD maps. WMH are not conspicuous on DWI due to counterbalancing high MD (loses signal) and long T_2 (gains signal). There is lengthening of sodium T_2 within the WMH region which results in elevated signal intensity on Na-PASS images. The change in T_1 of sodium in the WMH region is similar to that in CSF which shows similar signal intensity suppression on SIRFLA images. However the T_1 change of sodium and proton in WMH region is different.

6.4. Discussion

Sodium inversion recovery imaging has been shown to be particularly sensitive to chemotherapy response in a mouse model (Kline, et al., 2000) and recently applied to human subjects with muscular disorders (Nagel et al., 2011a) where both studies show that the signal is weighted toward intracellular. In this study, sodium SIRFLA MR signal is generally higher and appears to increase more rapidly within the first 14 hours after stroke onset than tissue sodium Na-PASS signal. This is consistent with results from previous studies using the alternate proposed intracellular weighted sodium acquisition method (i.e. MQF), which can be implemented as either a double-quantum filter (DQF) or a triple-quantum filter (TQF). A spectroscopy study in rodent (Tyson, et al., 1996) has shown larger DQ signal increase compared to bulk tissue (SQ) sodium signal during 10 minutes of forebrain ischemia. Similarly, a non-human primate imaging study (LaVerde, et al., 2007) has also shown a much greater TQF signal increase at 0.6 hours after arterial occlusion while there was almost no increase in tissue sodium. The source of early SIRFLA signal increase measured in our data is expected to be attributed to the accumulation of sodium ions within intracellular space and unlikely to be caused by T_1 shortening, where T_1 has been shown previously in isolated perfused rat hearts to remain constant during hypoxia and after reperfusion (Prince et al., 1992). At later time points (i.e. beyond 18.5 hours), the increase of sodium SIRFLA signal measured in the lesion is generally lower and leveled off sooner than Na-PASS signal. This reflects the gradual elevation of tissue sodium within the ischemic lesion after influx of sodium to intracellular compartment and has been suggested to be the result of increased blood-brain-barrier permeability to sodium as well as the diffusion of sodium ion with water from surrounding brain tissue and CSF (Gotoh et al., 1985; Young, et al., 1987). Thus there is evidence here that SIRFLA and Na-PASS signals do seem to be identifying different sodium evolutions in the ischemic lesion and suggesting the former to be preferentially weighted toward intracellular space. It should be noted here that at the time of this thesis preparation, sodium intensities measured from Na-PASS and SIRFLA images were fitted to a modified MMF model. However, there are other growth models that should be considered and will be investigated in the manuscript.

In vivo human MRI of tissue sodium is technically challenging. Compartment specific sodium MRI acquisition is even more difficult due to the further decrease in signal availability. Voxel dimensions must be increased, as seen on the SIRFLA images (Figure 6-1), to produce images with sufficient SNR. Nominal voxel dimension of 5x5x10 mm^3 were acquired in 10 minutes with SIRFLA in this study. Large voxel sizes (low spatial resolution) are also necessary for the other proposed intracellular weighted TQF sodium imaging technique (Allis, et al., 1991; Tauskela, et al., 1997). To date, there are no reports of either SIRFLA or TQF sodium MRI applied to human stroke. Whether SIRFLA and TQF show similar signal intensity time-course following the onset of human stroke, and therefore similar compartmental sodium weightings, remains to be determined.

White matter hyper-intensities may represent demyelination with increases in brain water content (Ovbiagele et al., 2006). While proton T_1s are higher in areas of WMH, as seen by their hypo-intense appearance on T_1-weighted images compared to normal WM (Yoshita et al., 2005), they are not elevated to the extent of CSF T_1s otherwise the signal intensity would be completely nulled on FLAIR images. In fact, WMH areas appear hyper-intense on FLAIR images. On the other hand, WMH areas are hypo-intense on sodium images which can be explained by considerable increase of sodium T_1 in these regions compared to normal WM. It should be noted that the increase of T_1 approaches that of sodium in CSF, where T_1 increase is to be expected in the context of demyelination, thus explaining hypo-intense SIRFLA signal.

There are limitations in this study. First, reperfusion from IV tPA administered prior to imaging in eight of 18 patients included in the analysis may contribute to the data scatter in Figure 6-2, given a potential sodium efflux following reperfusion (Eleff, et al., 1991). However, patients with and without treatment were distributed across imaging time after symptom onset, which minimized bias in the time-dependent signal intensity increase. Second, only three patients (identified as 1, 2, and 5 in Table 6-1) received IV tPA treatment and with subsequent follow-up scans so that evaluation of intracellular weighted and tissue sodium changes due to reperfusion is inconclusive. It is interesting to note that these three patients demonstrated greater SIRFLA signal increase than Na-PASS in the first scan and the reverse was observed in the second scan. Meanwhile, the DWI-defined lesion volume in these patients had enlarged in the second imaging session. Third, the poor resolution of SIRFLA images relative to Na-PASS may result in different partial volume effects. However, the mean ± standard deviation of the DWI lesion volume is similar within the first 14 hours (41 ± 48 mL) and after 14 hours (42 ± 51 mL) such that bias in relative intensity measurement is minimized in either group. Fourth, data acquired in this study did not correct for potential signal loss due to inhomogeneities in the static magnetic (B_0) and RF (B_1) fields, which may influence signal intensity measurement within the lesion relative to the contralateral homologous region. It should also be pointed out that the percentage relative Na-PASS increase measured in this work may differ in some patients presented in our previous studies (Hussain, et al., 2009; Tsang et al., 2011) due to our use of different software and algorithms to select the core and contralateral ROIs. This also resulted in a different curve fitted through the data (Figure 6-2).

In conclusion, the progression of sodium signal in the lesion with time of onset differs between total tissue sodium and inversion recovery sodium. MRI SIRFLA sodium image can be acquired in patients within a clinically feasible scan time showing the progression of sodium inversion recovery signal in the ischemic lesion that potentially reflect changes in intracellular compartment. The relative increase of SIRFLA sodium signal to supposedly normal contralateral hemisphere is in general greater than the change in tissue sodium at the early time point after onset.

Chapter 7

Final Discussions and Conclusion

7.1. Thesis Summary

In vivo sodium MRI of the brain is technically challenging due to the smaller gyromagnetic ratio (~1/4) and much lower signal availability compared to proton (^{1}H) in biological tissue. Sodium signal in brain decays rapidly after excitation with 60% of relaxation characterized by T_{2f} which is less than 2 ms (Stobbe, et al., 2006). Nevertheless, in vivo single-quantum (SQ) or bulk sodium signal images can be obtained using a clinically relevant acquisition time (~10 minutes) (Stobbe, et al., 2008b), with sufficient spatial resolution and signal-to-noise ratio (SNR). This SQ sodium imaging method has also been applied in acute ischemic stroke patients to explore sodium intensity changes with respect to imaging time after symptom onset (Hussain, et al., 2009). A large portion of the work in this thesis tackles a sequence known as multiple-quantum-filter (MQF), which can be implemented as either DQF or TQF, to selectively detect bi-exponential T_2 relaxing sodium signal. As stated in previous chapters, in vivo MQF imaging in brain detects sodium signal weighted toward intracellular that may yield more compartment specific changes in pathology such as stroke. However, the signal magnitude at acquisition is drastically reduced (TQF signal in brain is only ~10% of SQ signal) resulting in images with poor spatial resolution and SNR despite a longer scan time. The TQF sequence is typically implemented using 6-step phase cycling as it was done in this thesis. Consequently, the duration to obtain a TQF image set is 6 times longer than SQ for a given twisted projection set (i.e. same spatial resolution) and identical signal averaging. At the time of writing this thesis, only a few human TQF sodium imaging studies had been published as shown in Table 7-1.

Table 7-1: Summary of TQF imaging studies in human subjects

Anatomy	Reference	Field strength	Scan Time	Resolution / Volume
Brain	(Hancu, et al., 1999)	3T	~20 mins	unspecified
	(Tsang, et al., 2012)	4.7T	11 mins	8.4 mm isotropic
	(Fleysher, et al., 2012)	7T	43 mins	8x8x10mm^3
Cartilage	(Borthakur, et al., 1999)	3T	20 mins	Voxel volume = 500 mm^3

The first in vivo TQF brain study published in 1999 by Hancu et al. (Hancu, et al., 1999) used typical (referred to as 'standard' in this thesis) sequence parameters of 90° flip angle and short (0.5 ms) RF pulses. More recent study at 7 T by Fleysher et al. (Fleysher, et al., 2012) also use a 90° flip angle but with longer pulse widths (~1 ms) such that an excessively long TR is not required to satisfy specific absorption rate (SAR) constraints. An approach to optimize SNR for in vivo TQF imaging of the brain at 4.7 T (a moderately high field), which can also be applied to higher field strengths, under the SAR constraint is described in Chapter 2. The SNR-optimized TQF sequence implemented in this thesis uses smaller first RF flip angle (i.e. 65°) and longer duration (i.e. 1.25 ms) for all three RF pulses to shorten TR. SNR is increased for a given scan duration relative to the 'standard' approach due to more signal averaging and reduced noise variance.

Given the extremely low TQF signal and low SNR/voxel relationship in brain, any factor that would cause further signal loss is a major concern. The three pulse TQF sequence, without the 180° refocusing pulse, is prone to signal loss due to B_0 inhomogeneity. Three correction algorithms were proposed previously, and demonstrated in agar gel phantoms, to rectify signal loss due to inhomogeneous B_0 field (Fleysher, et al., 2010b; Matthies, et al., 2010; Tanase, et al., 2005). However, implementation of these correction algorithms incurs doubling or quadrupling in scan time without the expected SNR improvement. Most of cerebrum among 10 healthy subjects demonstrates frequency offset between ±5 Hz (Chapter 3) with minimal TQF signal loss that does not benefit from B_0 correction. Regions with severe TQF signal loss, which are also susceptible using other imaging sequences such as proton echo-planar, demonstrate only partial signal recovery from B_0 correction. Hence B_0 inhomogeneity appears not to be a major concern for TQF brain imaging at 4.7T or below and the significant increase in scan time associated with correction would be better spent to improve spatial resolution or SNR in the low TQF signal starved image.

TQF has been shown to be 50% more sensitive than a DQF sequence, but the latter can be implemented with a judicious choice of flip angle to selectively detect sodium signal in anisotropic ordered environment where the quadrupolar interaction frequency (ϖ_Q) is non-zero. Chapter 4 presented the results of in vivo human brain sodium MRI using a DQF sequence with flip angle = 54.7^o for the last RF pulse, which is known as a double-quantum magic angle (DQ-MA) sequence. This is the first in vivo DQ-MA human brain images to show the presence of residual ϖ_Q throughout the brain. The optimal τ value of 2 ms is suggested to yield the highest DQ-MA signal for in vivo brain imaging experiments.

Sodium MRI was performed in acute ischemic stroke patients admitted to the UAH during the course of this thesis. Sodium MRI in human stroke is rare with only a limited number of published studies (Table 7-2). Time dependent SQ sodium MRI intensity increase within the diffusion restricted area (i.e. core), where injury is thought to be largely irreversible, may be used to estimate onset time in patients who are awake with symptoms. On the other hand, the ultimate goal in treatment is to identify and salvage viable tissues, which can be operationally defined as the mismatch tissue area between PWI and DWI (commonly referred to as penumbra) as done in this thesis. SQ sodium intensity in the penumbra region was found to remain unchanged irrespective of the interval between symptom onset and image acquisition, suggesting a preservation of ionic homeostasis in this region (Chapter 5). Hence, sodium MRI in conjunction with PWI and DWI, may permit identification of patients with viable tissue, despite an unknown symptom onset time.

Table 7-2: Sodium MRI studies in human ischemic stroke

Reference	**Field Strength**	**Scan Time**	**Resolution / Volume**	**Number of Patients scanned**	**Imaging Time after symptom onset**
(Grodd, et al., 1988)	1.5T	21 min	4.7x4.7x10 mm^3 = 221 mm^3	1	24 hours
(Shimizu, et al., 1993)	1.5T	unspecified	unspecified	7	Initial scan: 4-82 hours
(Thulborn, et al., 1999b)	1.5T and 3T	~10 min	220 mm^3 (1.5T); 64 mm^3 (3T)	42	<24 hours (n=11); >24 hours (n=31)
(Hussain, et al., 2009)	4.7T	10 min	2.4x2.4x4.8 mm^3 = 28 mm^3	21	4 – 161 hours
(Tsang, et al., 2011)	4.7T	10 min	2.4x2.4x4.8 mm^3 = 28 mm^3	9	4 – 32 hours

A previous non-human primate stroke study demonstrated a much greater TQF, or supposedly intracellular-weighted, sodium signal increase in as early as 0.6 hour after arterial occlusion compared to only subtle changes in SQ sodium signal that reflects TSC during that time (LaVerde, et al., 2007). Compartment specific changes of sodium in ischemic stroke patients may be more sensitive to detect disturbed ionic homeostasis while TSC is still not elevated. A retrospective study was performed (Chapter 6) on ischemic stroke patients imaged with the SIRFLA sequence, where sodium signal in CSF is suppressed and assumed to be also the case for extracellular fluid space, as well as an SQ sodium sequence. The increase of SIRFLA signal measured within the DWI core is in general greater than SQ sodium signal at the early time points after onset. Monitoring of intracellular-weighted sodium change in the lesion in patients before and after administration of thrombolysis may potentially indicate tissue reperfusion response as evidence from animal stroke models suggest a reverse of TQF signal change toward pre-ischemic level after restoration of blood flow. Figure 7-1 shows an illustration of the expected ‘intracellular’ and tissue sodium NMR signal intensity changes in relation to the decrease of CBF in acute stroke patients.

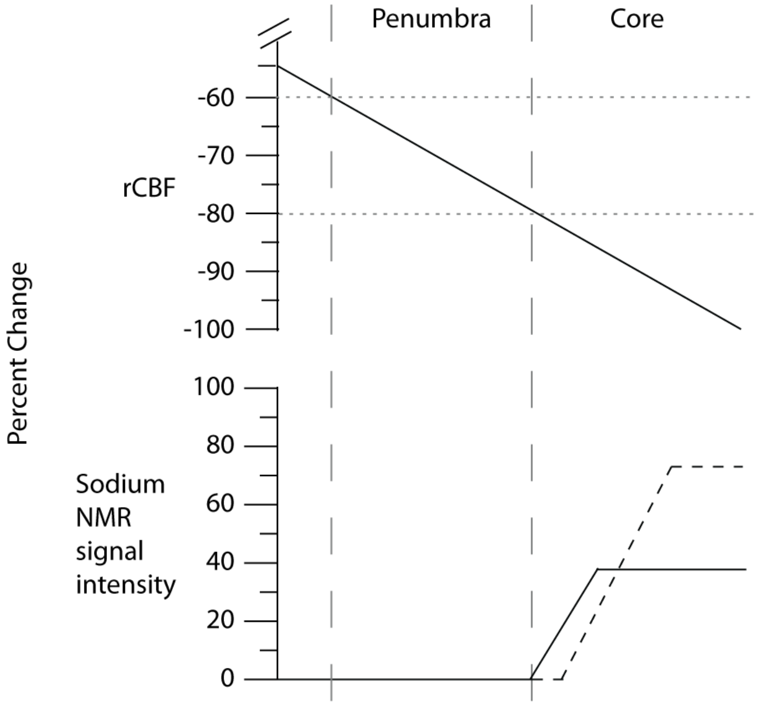

Figure 7-1: Illustration of percentage change of sodium signal intensity in relation to the decrease of CBF due to cerebral ischemia In this case, the horizontal axis implies time and a monotonically decreasing CBF is presented with no reperfusion. Sodium signal remains unchanged within the penumbral tissue between the CBF thresholds that indicate anaerobic mechanism to support the operation of Na/K-ATPase. Sodium signal increases in the core tissue below the CBF threshold of ionic failure (i.e. anoxic depolarization). Solid line for sodium signal increase represents intracellular-weighted sodium (e.g. SIRFLA signal) and the dashed line represents bulk tissue sodium (e.g. Na-PASS signal). For the change of CBF with other hemodynamic parameters, see Figure 1-1.

7.2. Final Discussions

7.2.1. TQF Imaging

The TQF sequence is often implemented using 6-step phase cycling of RF pulses as is done in this thesis to extract bi-exponential T_2 signal. However this scheme to select third order coherences during the evolution time (δ) is susceptible to motion (Van Der Veen, et al., 1993). In order to mitigate this potential problem for in vivo imaging applications, such as in the brain where CSF is known to pulsate (Schroth et al., 1992), gradients can be used instead of RF pulse phase cycling. Because triple-quantum coherences precess at three times the Larmor frequency than single-quantum coherences, a gradient during δ with 1/3 the strength or duration than a corresponding gradient after the last RF pulse can select the third order coherences that lead to the final detected signal (Wimperis, et al., 1991). Unfortunately, TQF signal amplitude acquired using gradient selection is reduced by a factor of 2 because only one of $T_{3,3}$ or $T_{3,-3}$ is detected depending on the sign of the gradients (Van Der Veen, et al., 1993). In addition, Wimperis et al. (Wimperis, et al., 1991) pointed out that the suppression of unwanted coherence is not sufficient by using gradients alone, and suggested an eight step phase cycling scheme of the last RF pulse and alternating receiver phase between 0^o and 180^o together with gradients to extract only the desired coherence. The authors also suggested to using RF flip angle of 109^o for the last RF pulse to obtain optimal TQF signal. Phase cycling also helps to increase SNR. This method proposed by Wimperis et al. (label here as ‘G+PC’ for gradient plus phase cycling) and the ‘standard’ 6-step phase cycling approach were implemented in the simulator using parameters as indicated in Table 7-3. The relative signal magnitude at beginning of acquisition is found to be 6% and 0.01% for the brain and CSF models respectively as described in Chapter 2 using ‘G+PC’. Similarly the relative signal magnitude is 10% and 0.01% for brain and CSF using ‘standard’ TQF sequence.

Table 7-3: TQF sequence parameters used in simulation

TQF sequence[a]	Flip Angle	Pulse width (ms)	τ / TE (ms)	δ (ms)[b]	TR (ms)	ϕ_1 [c]	ϕ_2 [c]	ϕ_3 [d]
Standard	$90^o, 90^o, 90^o$	0.5	6	0.51	330	$\pi/6 + k(\pi/3)$	$2\pi/3 + k(\pi/3)$	0
G+PC	$90^o, 90^o, 109^o$	0.5	6	1	380	0	$\pi/2$	$n\pi/4$

[a] Receiver phase is alternated between 0^o and 180^o for each phase cycling step using both implementation

[b] for 'G+PC', gradient is turned on for 0.5 ms during δ and 1.5 ms after the last RF pulse. Gradient strength is determined such that a dephasing of 2π is achieved for a given voxel size, or mathematically satisfy the relationship $2\pi = 2\pi\gamma Gvt$, where γ is the sodium gyromagnetic ratio, v is voxel dimension, and t is gradient duration.

[c] k = 0, 1, 2, 3, 4, 5 for six-step phase cycling

[d] n = 0, 1, 2, 3, 4, 5, 6, 7 for eight-step phase cycling

Twisted projection imaging (TPI) as it was originally proposed by Boada et al. (Boada, et al., 1997) is critical for SQ sodium MRI in order to obtain the short TE value required to 'capture' signal that would otherwise be lost using conventional acquisition methods. TPI is the preferred approach over radial acquisition due to the reduced number of projections to cover k-space with significant time saving, dependent on the twist *p* value. TQF imaging, however, is less stringent to the use of TPI because a delay is usually inserted after the last RF and before acquisition such that TE is equal to τ. Therefore, conventional gradient echo acquisition may also be used as it has been done in a recent study by Fleysher et al. (Fleysher, et al., 2012).

7.2.2. Concerning Intracellular-Weighted Sodium Imaging in Stroke

Sodium brain images acquired using SIRFLA as shown in Chapter 6 are dependent on TI chosen using relaxation parameters of unbound' sodium signal in CSF, and assumed that nuclei in extracellular space to behave in a similar manner, to produce an intracellular-weighted image. However, sodium relaxation in extracellular space may be quicker than CSF and hence the TI value to achieve optimal suppression may be different (Stobbe, et al., 2005). Alternatively, TQF separates sodium nuclei in a slow interaction environment that exhibit bi-exponential T_2 from those in fast motion with mono-exponential T_2. These two different mechanisms of producing intracellular-weighted images warrant a future study to compare the evolution of TQF and SIRFLA signal changes with respect to onset time in ischemic stroke. Due to the low resolution of TQF images, only patients with large lesions (determined from their diffusion weighted images) would be a good candidate for sodium imaging. In general, recruitment of stroke patients for sodium imaging is extremely challenging because many have contraindications to the moderately high field 4.7 T MRI, and those with large lesions often are too unstable to remain still for the entire scan duration. As a result, TQF data were acquired in only 2 ischemic stroke patients during the course of this thesis. In both subjects, the lesions involved almost the entire hemisphere, and are clearly visible on TQF images (Figures 7-2, 7-3) obtained using two different projection sets that yield 8.4 mm isotropic resolution. A SQ sodium image was also acquired within the same imaging session in each subject for total scan time of less than 20 minutes. Preliminary analysis of these two cases show that the first subject (shown in Figure 7-2) imaged at 17 hours after symptom onset has similar TQF and SQ sodium signal increase (relative signal increase of 29% and 35% for TQF and SQ respectively) within the lesion. However, the second subject (shown in Figure 7-3) imaged at 15 hours after symptom onset (this is the time reported based on last seen well) demonstrate a greater TQF signal increase than that of SQ (relative signal increase of 19% and 57% for TQF and SQ respectively). Future studies should image acute patients within the first 24 hours using TSC, SIRFLA and TQF to compare signal evolution.

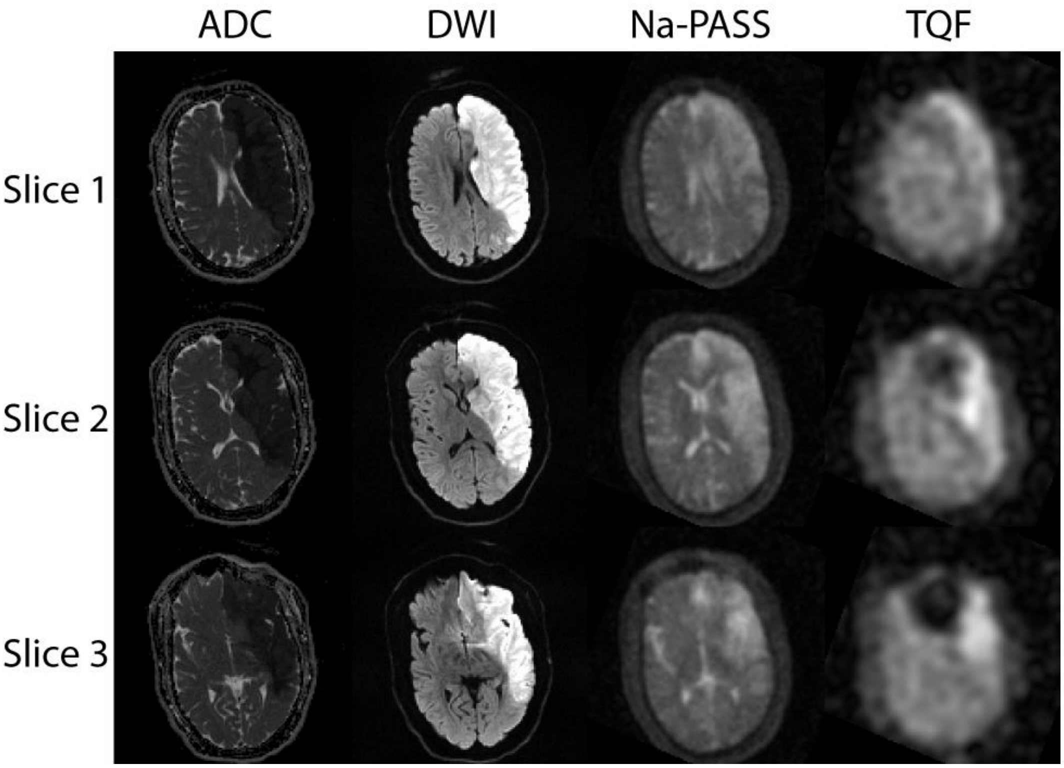

Figure 7-2: Three selected transverse slices obtained from a 30 year old male patient with NIHSS score of 17 at the time of imaging. Sodium imaging at 4.7T was performed at 17 hours post onset. The SQ Na-PASS images of 2.6 x 2.6 x 5.2 mm^3 resolution were acquired in 6 minutes with 35% relative signal increase measured within the lesion. TQF images of 8.4 mm isotropic resolution were acquired in 12 minutes with relative increase of 29%. Sodium images were spatially co-registered to proton (DWI and ADC) images obtained on a 1.5T scanner using SPM.

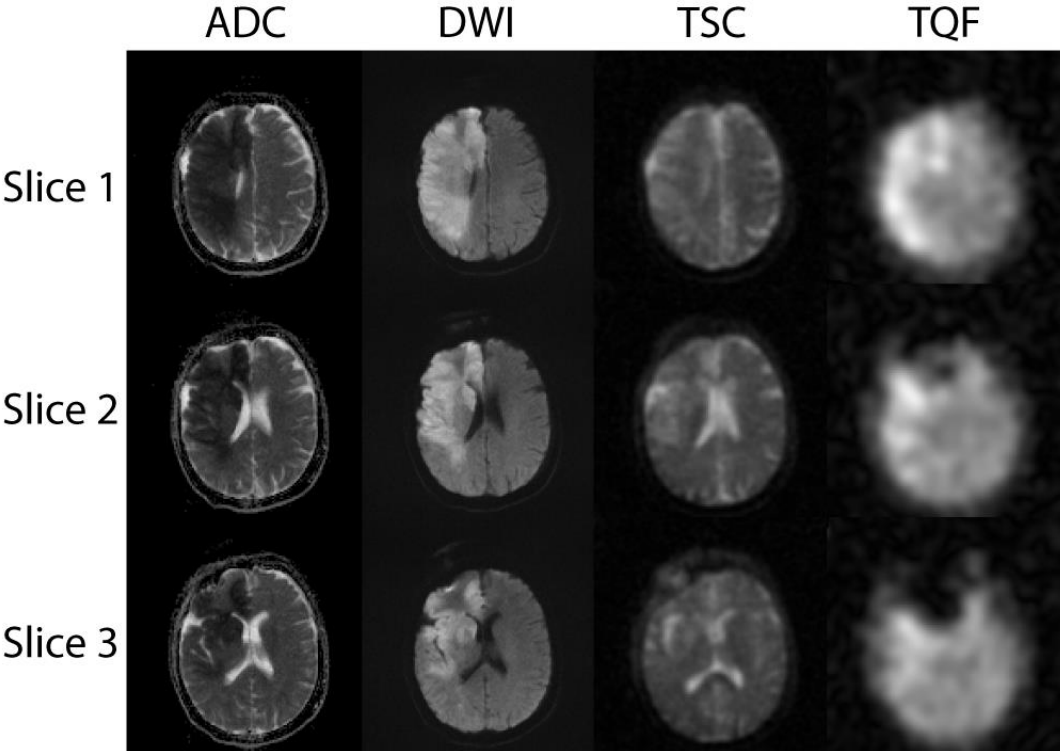

Figure 7-3: Three selected transverse slices obtained from a 66 year old female patient with NIHSS score of 16 at the time of imaging. Sodium imaging at 4.7T was performed at 15 hours post onset based on the time last seen well. The SQ Na-PASS images of 2.9 x 2.9 x 5.8 mm^3 resolution were acquired in 5 minutes with 19% relative signal increase measured within the lesion. TQF images of 8.4 mm isotropic resolution were acquired in 11 minutes with relative increase of 57%.

7.3. Conclusion

In vivo sodium MRI has been perceived by some pundits, particularly in the clinical fields, to have little translational research potential. There are indeed barriers to clinical use, which (I believed) is due to the following causes. First, most clinical MRI scanners are not equipped with broadband synthesizers, amplifiers, and specialized RF coils to image sodium which has a different Larmor frequency than proton (^{1}H). However new scanners (3 T and 7 T) are offered with multi-nuclear capability and this invites more widespread sodium MRI applications in the future. Second, the development of MRI sequences often depend on simulations to study the effect of RF pulses on magnetization, as it has been done extensively in this thesis. Due to the quadrupolar nature of sodium, simulation of sodium MRI sequences is not possible to 'follow' the magnetization evolution using the Bloch equation and require the use of complex irreducible tensor operators. Third, the sampling of k-space for image acquisition requires the use of TPI to achieve very short TE to allow 'capturing' of signals that decay with very rapid T_2. The design of twisted project sets is not trivial compared to the simpler Cartesian k-space sampling. Fourth, reconstruction of images acquired using TPI would need to be regridded onto a Cartesian plane first before Fourier transformation can be performed. Thus, viewing sodium MRI images in real time in patients is not yet feasible in most centres. Nevertheless, despite all these challenges and the fact that the resolution of in vivo sodium images are much lower than those based on proton, sodium MRI can yield unique physiological information related to the sodium ion rather than water using sequences shown in this thesis that appears to provide complementary information to conventional MRI sequences. Sodium is intricately involved in many physiological processes and this ionic homeostasis, which may be disturbed in pathological conditions, can be used as an imaging marker. This is evident in applications such as Alzheimer's Disease (Mellon, et al., 2009), multiple sclerosis (Inglese, et al., 2010; Zaaraoui et al., 2012), hypertension (Kopp et al., 2012), tumors (Cameron et al., 1980; Hashimoto et al., 1991; Jacobs et al., 2010; Nagel et al., 2011b; Ouwerkerk, et al., 2003; Thulborn, et al., 2009; Turski et al., 1987), and stroke (Grodd, et al., 1988; Hussain, et al., 2009; Shimizu, et al., 1993; Thulborn, et al., 2005; Thulborn, et al., 1999b; Tsang, et al., 2011). As more sites are equipped with higher field strength scanners, together with novel acquisition techniques to improve both resolution and SNR, the number of applications for sodium MRI is expected to increase in the near future.

Appendix 1

Description of Sodium Software Tools

Sodium MRI sequence simulation, twisted projection set design, and image analysis tools used in this thesis are all based on custom software written in Matlab by Dr. Rob Stobbe. A screen shot and brief description of each tool used is provided in this appendix.

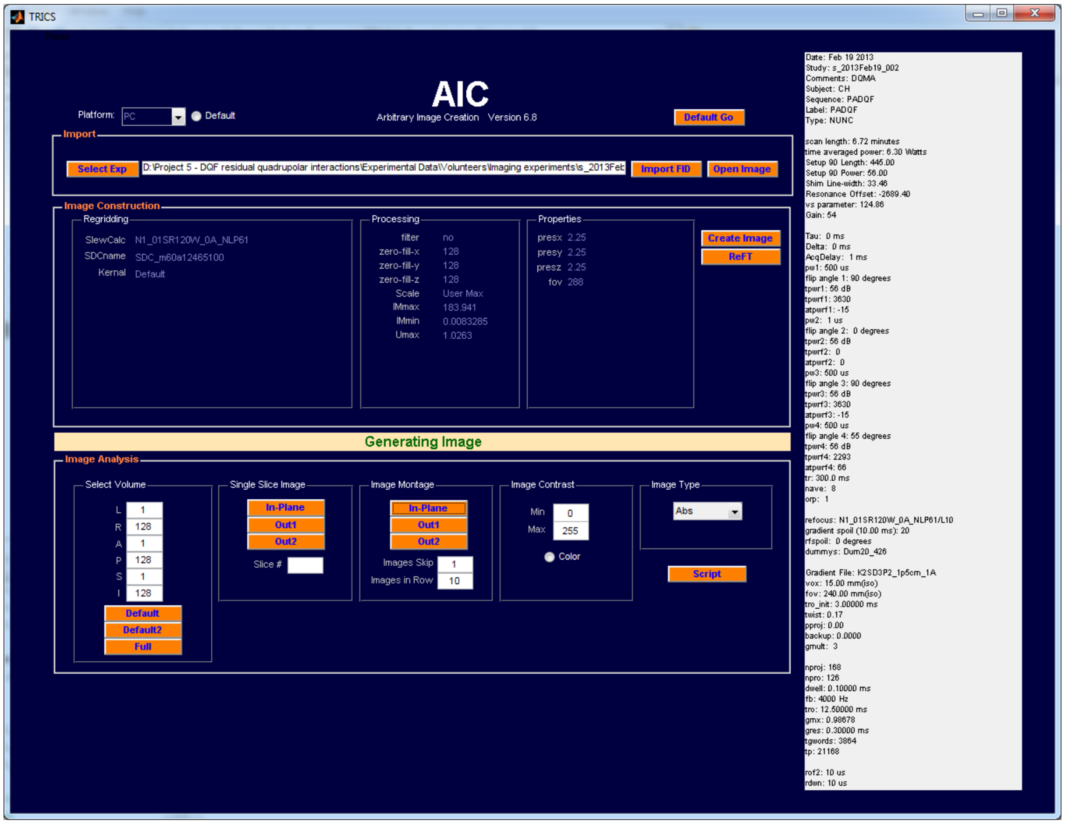

Platform: PC ○ Default

D:\Project 5 - DQF residual quadrupolar interactions\Experimental Data\Volunteers\Imaging experiments\s_2013Feb

SlewCalc N1_01SR120W_0A_NLP61
SDCname SDC_m60a12465100
Kernal Default

filter no
zero-fill-x 128
zero-fill-y 128
zero-fill-z 128
Scale User Max
IMmax 183.941
IMmin 0.0083285
Umax 1.0263

presx 2.25
presy 2.25
presz 2.25
fov 288

L 1
R 128
A 1
P 128
S 1
I 128

Slice #

Images Skip 1
Images in Row 10

Min 0
Max 255
○ Color

Abs

```
Date: Feb 19 2013
Study: s_2013Feb19_002
Comments: DQMA
Subject: CH
Sequence: PADQF
Label: PADQF
Type: NUNC

scan length: 6.72 minutes
time averaged power: 6.30 Watts
Setup 90 Length: 445.00
Setup 90 Power: 56.00
Shim Line-width: 33.46
Resonance Offset: -2689.40
vs parameter: 124.86
Gain: 54

Tau:  0 ms
Delta:  0 ms
AcqDelay:  1 ms
pw1: 500 us
flip angle 1: 90 degrees
tpwr1: 56 dB
tpwrf1: 3630
atpwrf1: -15
pw2:  1 us
flip angle 2:  0 degrees
tpwr2: 56 dB
tpwrf2:  0
atpwrf2:  0
pw3: 500 us
flip angle 3: 90 degrees
tpwr3: 56 dB
tpwrf3: 3630
atpwrf3: -15
pw4: 500 us
flip angle 4: 55 degrees
tpwr4: 56 dB
tpwrf4: 2293
atpwrf4: 66
tr: 300.0 ms
nave:  8
orp:  1

refocus: N1_01SR120W_0A_NLP61/L10
gradient spoil (10.00 ms): 20
rfspoil:  0 degrees
dummys: Dum20_426

Gradient File: K2SD3P2_1p5cm_1A
vox: 15.00 mm(iso)
fov: 240.00 mm(iso)
tro_init: 3.00000 ms
twist: 0.17
pproj: 0.00
backup: 0.0000
gmult:  3

nproj: 168
npro: 126
dwell: 0.10000 ms
fb: 4000 Hz
tro: 12.50000 ms
gmx: 0.98678
gres: 0.30000 ms
tgwords: 3864
tp: 21168

rof2: 10 us
rdwn: 10 us
```

Figure A1-1: Screen shot of the AIC software for sodium image reconstruction

Image reconstruction and display used the AIC (Arbitrary Image Creation) software (Figure A1-1). The raw k-space FID file is loaded where the parameters used for acquisition are displayed on the right. Once the FID is imported, the user must load the corresponding projection set sampling density compensation matrix to reconstruct the image. In this thesis, scripts were written in Matlab to process multiple FID files automatically from relaxometry experiments and B_0 correction algorithms as described in Chapter 3. This software is also used to convert ‘raw’ images reconstructed from the acquired FID to ‘Analyze’ format. This is used for the SPM (Wellcome Trust centre for Neuroimaging, London, UK) tool for co-registration, GALILEO software for SNR measurement, and Analyze (Biomedical Imaging Resource, Rochester, MN) software to define ROIs for DWI stroke lesions analysis.

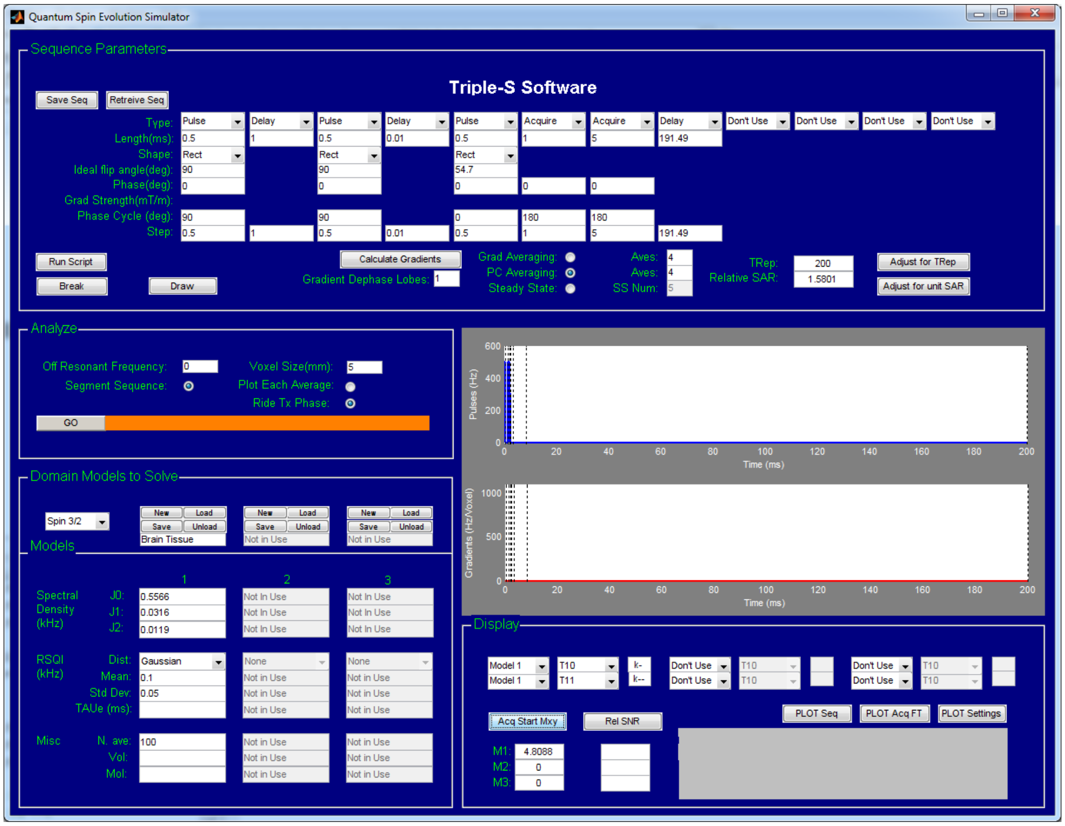

Type:	Pulse	Delay	Pulse	Delay	Pulse	Acquire	Acquire	Delay	Don't Use	Don't Use	Don't Use	Don't Use
Length(ms):	0.5	1	0.5	0.01	0.5	1	5	191.49				
Shape:	Rect		Rect		Rect							
Ideal flip angle(deg):	90		90		54.7							
Phase(deg):	0		0		0	0	0					
Grad Strength(mT/m):												
Phase Cycle (deg):	90		90		0	180	180					
Step:	0.5	1	0.5	0.01	0.5	1	5	191.49				

Gradient Dephase Lobes: 1
Grad Averaging: ○
PC Averaging: ●
Steady State: ○
Aves: 4
Aves: 4
SS Num: 5
TRep: 200
Relative SAR: 1.5801

Off Resonant Frequency: 0
Segment Sequence: ●
Voxel Size(mm): 5
Plot Each Average: ○
Ride Tx Phase: ●

Spin 3/2

		1	2	3
		Brain Tissue	Not in Use	Not in Use
Spectral Density (kHz)	J0:	0.5566	Not In Use	Not In Use
	J1:	0.0316	Not In Use	Not In Use
	J2:	0.0119	Not In Use	Not In Use
RSQI (kHz)	Dist:	Gaussian	None	None
	Mean:	0.1	Not in Use	Not in Use
	Std Dev:	0.05	Not in Use	Not in Use
	TAUe (ms):		Not in Use	Not in Use
Misc	N. ave:	100	Not in Use	Not in Use
	Vol:		Not in Use	Not in Use
	Mol:		Not in Use	Not in Use

Model 1	T10	k-	Don't Use	T10	Don't Use	T10
Model 1	T11	k--	Don't Use	T10	Don't Use	T10

M1: 4.8088
M2: 0
M3: 0

Figure A1-2: Screen shot of the TRIPLE-S software for sodium sequence simulation

TRIPLE-S (Sodium Spin Simulation) (Figure A1-2) software that solves the set of differential equations to follow the evolution of irreducible tensor operators due to RF excitation, relaxation, off-resonance, and residual quadrupolar interaction as defined in (Hancu, et al., 2000; van der Maarel, 2003). Scripts were written to load different sequence parameters automatically, as done in Chapters 2-4 to obtain relative transverse magnetization at the beginning of acquisition. The software is capable to solve up to 3 models (defined by spectral density parameters) simultaneously.

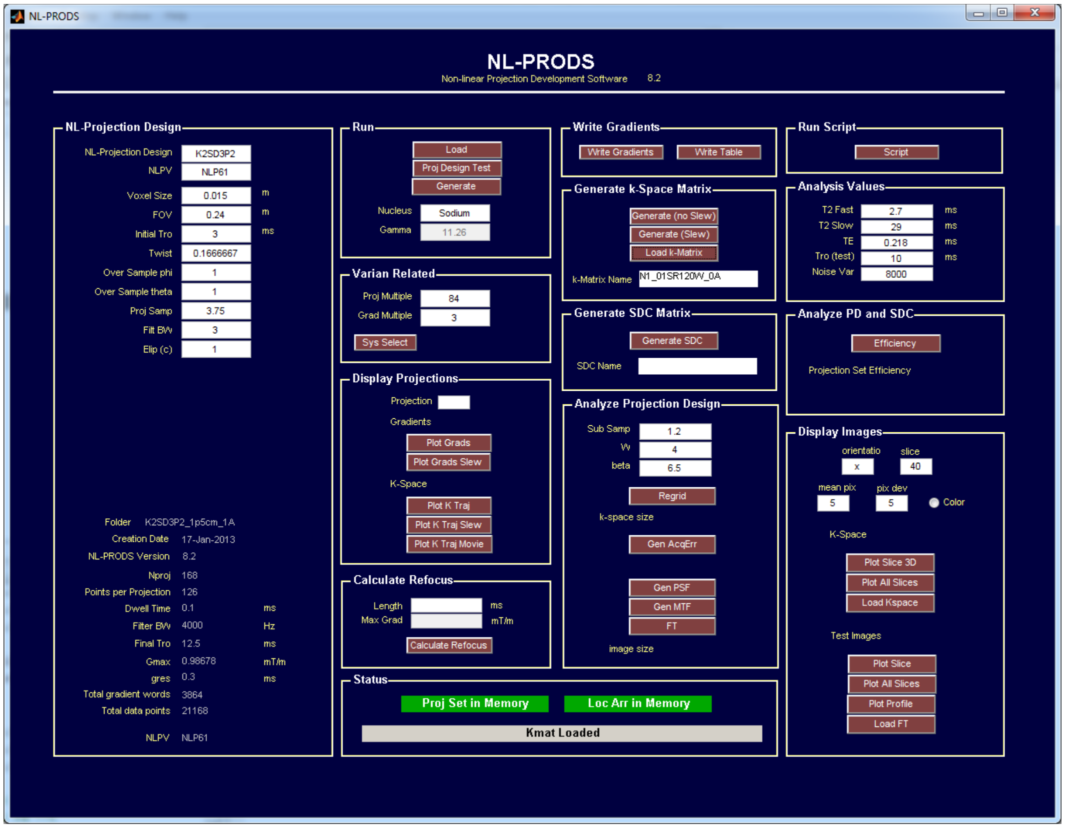

NL-Projection Design: K2SD3P2
NLPV: NLP61
Voxel Size: 0.015 m
FOV: 0.24 m
Initial Tro: 3 ms
Twist: 0.1666667
Over Sample phi: 1
Over Sample theta: 1
Proj Samp: 3.75
Filt BW: 3
Elip (c): 1

Folder: K2SD3P2_1p5cm_1A
Creation Date: 17-Jan-2013
NL-PRODS Version: 8.2
Nproj: 168
Points per Projection: 126
Dwell Time: 0.1 ms
Filter BW: 4000 Hz
Final Tro: 12.5 ms
Gmax: 0.98678 mT/m
gres: 0.3 ms
Total gradient words: 3864
Total data points: 21168
NLPV: NLP61

Nucleus: Sodium
Gamma: 11.26

Proj Multiple: 84
Grad Multiple: 3

Length: ms
Max Grad: mT/m

Proj Set in Memory
Loc Arr in Memory
Kmat Loaded

k-Matrix Name: N1_01SR120W_0A
SDC Name:

Sub Samp: 1.2
Vv: 4
beta: 6.5

T2 Fast: 2.7 ms
T2 Slow: 29 ms
TE: 0.218 ms
Tro (test): 10 ms
Noise Var: 8000

orientatio: x
slice: 40
mean pix: 5
pix dev: 5

Figure A1-3: Screen shot of the NL-PRODS software for twisted projection set design where gradient files are produced and uploaded to the Varian 4.7T console

Twisted projection sets for k-space acquisition is designed using the NL-PRODS (Non-linear projection development software) (Figure A1-3) program. The gradient files and refocusing files are generated based on design parameters such as voxel size, field of view, twist *p*, initial read-out time, out-plane scaling factor, oversampling in phi or theta direction for ‘extra’ cones or projections. The files are uploaded manually to the Varian 4.7T console computer in ‘<username>\vnmrsys\shapelib’ and ‘<username>\vnmrsys\tablib’ folders. The sampling density compensation matrix is also generated based on the design parameters and will be required for image reconstruction.

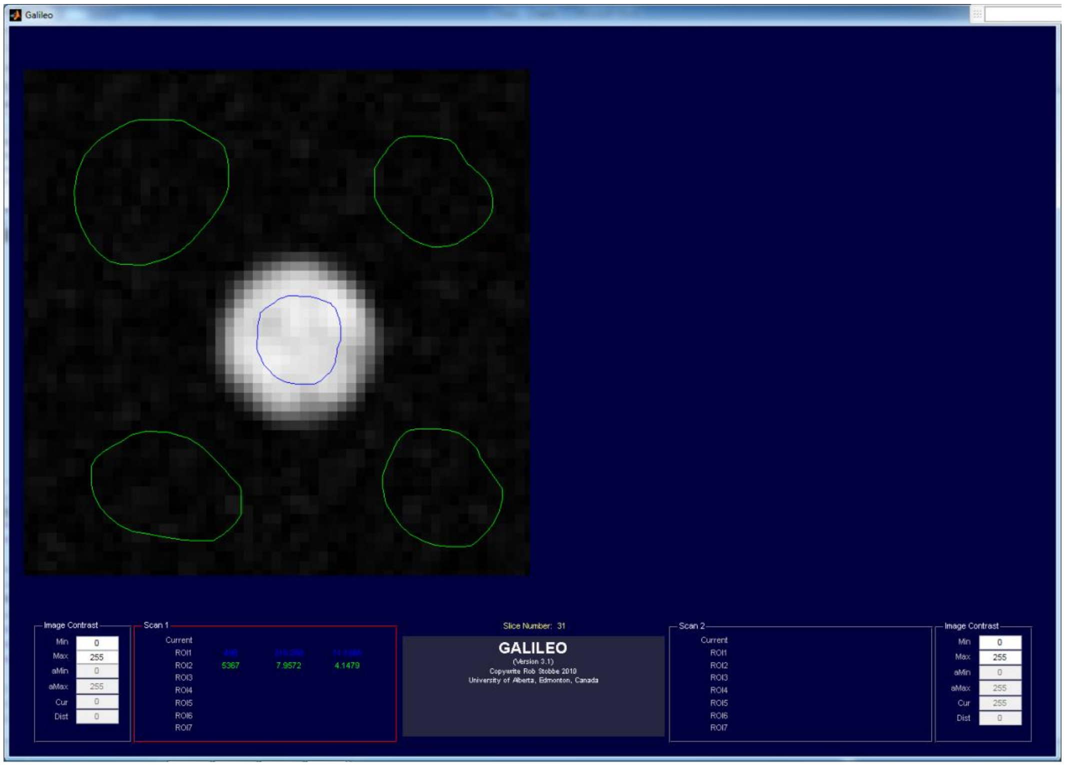

Image Contrast (Scan 1): Min 0, Max 255, aMin 0, aMax 255, Cur 0, Dist 0

Scan 1:
Current
ROI1
ROI2 5367 7.9572 4.1479
ROI3
ROI4
ROI5
ROI6
ROI7

Scan 2:
Current
ROI1
ROI2
ROI3
ROI4
ROI5
ROI6
ROI7

Image Contrast (Scan 2): Min 0, Max 255, aMin 0, aMax 255, Cur 255, Dist 0

Figure A1-4: Screen shot of the GALILEO software used to display sodium images in Analyze format.

SNR measurement on sodium images in this thesis used the software named GALILEO (Figure A1-4). Image volume must be saved in ‘analyze’ format in order to be loaded into the software. Region of interests (ROIs) are manually drawn on different image slices and the mean and standard deviation of signal intensities in voxels enclosed by the ROI circles are calculated.

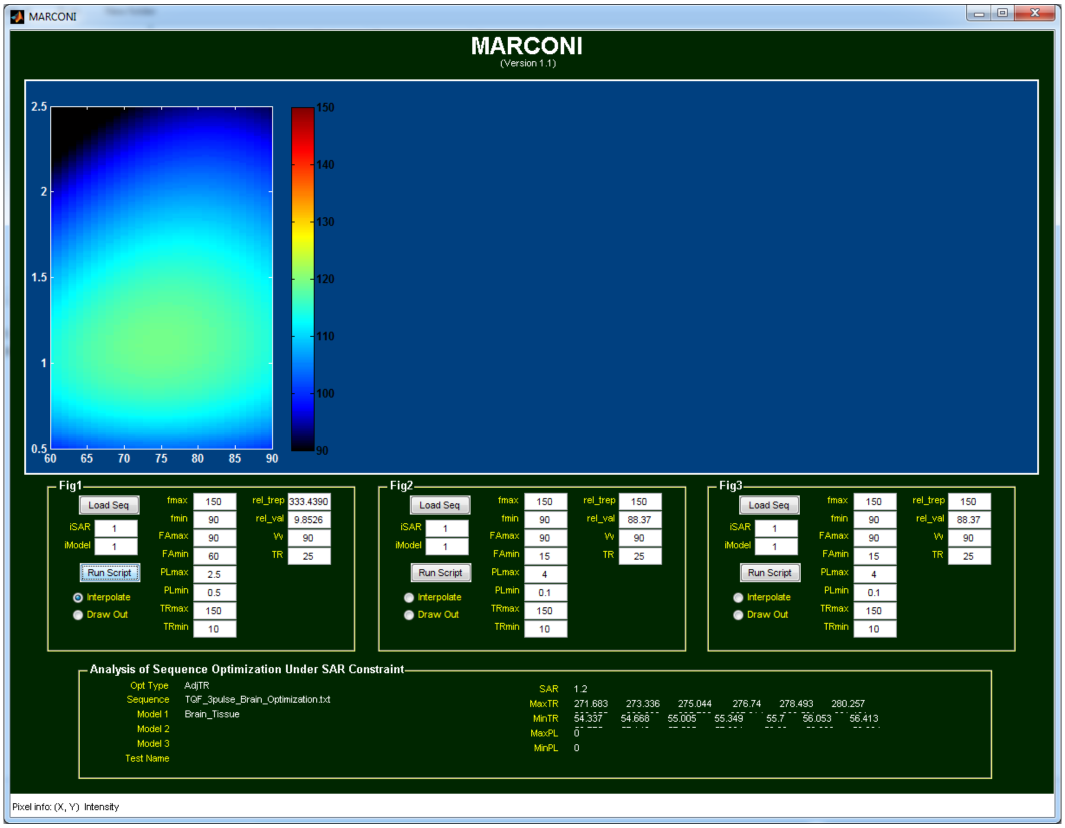

Fig1

iSAR 1
iModel 1
● Interpolate
○ Draw Out
fmax 150
fmin 90
FAmax 90
FAmin 60
PLmax 2.5
PLmin 0.5
TRmax 150
TRmin 10
rel_trep 333.4390
rel_val 9.8526
Vv 90
TR 25

Fig2

iSAR 1
iModel 1
○ Interpolate
○ Draw Out
fmax 150
fmin 90
FAmax 90
FAmin 15
PLmax 4
PLmin 0.1
TRmax 150
TRmin 10
rel_trep 150
rel_val 88.37
Vv 90
TR 25

Fig3

iSAR 1
iModel 1
○ Interpolate
○ Draw Out
fmax 150
fmin 90
FAmax 90
FAmin 15
PLmax 4
PLmin 0.1
TRmax 150
TRmin 10
rel_trep 150
rel_val 88.37
Vv 90
TR 25

Analysis of Sequence Optimization Under SAR Constraint

Opt Type AdjTR
Sequence TQF_3pulse_Brain_Optimization.txt
Model 1 Brain_Tissue
Model 2
Model 3
Test Name

SAR 1.2
MaxTR 271.683 273.336 275.044 276.74 278.493 280.257
MinTR 54.337 54.668 55.005 55.349 55.7 56.053 56.413
MaxPL 0
MinPL 0

Figure A1-5: Screen shot of the MARCONI software used to display 3-dimensional simulation results saved from the TRIPLE-S software.

Visualization of TQF sequence parameters to optimize SNR (Chapter 2) used the MARCONI (Figure A1-5) software. A script was written to repeat the TQF sequence for a range of first RF pulse flip angle and pulse width where the relative transverse magnetization at TE is recorded for each parameter combination. TR is also adjusted in each case such that the SAR remains constant. The resultant matrix contains 3-dimensional data. SNR associated with each pair of first flip angle and pulse width is plotted relative to the 'standard' combination (i.e. pulse width = 0.5 ms and first flip angle = 90^{o}) as reference (i.e. 100%).

Appendix 2

Relaxometry Experiments

Various phantoms containing saline (sodium chloride provided by EMD Chemicals Inc., Gibbstown, NJ), agar gel (agar gel powder from Invitrogen, Carlsbad, CA), or xanthan gum (Keltrol T food grade xanthan gum from CP Kelco, Atlanta, GA), were constructed through the course of this thesis as described in previous chapters. Relaxometry experiments were performed to measure T_1 and T_2 parameters for every phantom in order to determine the spectral density parameters that are used in the TRIPLE-S software.

T_2 can be measured by an imaging experiment using a single-pulse sequence implemented with the following parameters: TR = 200 ms, flip angle = 90^o, multiple TE values between 0.3 to 40 ms. To minimize scan time, a twisted projection set that yields large voxel dimension can be used. In this thesis, either a projection set designed for 8.4 mm or 15 mm isotropic voxel was used. The images are reconstructed identically and scaled relative to the image acquired with the shortest TE using the AIC software. Signal intensity within the phantom volume on all images is measured by manually drawing region of interests (ROIs) using the GALILEO software. The signal intensities vs. TE values are plotted and fitted to the following bi-exponential T_2 relaxation model

$$M_{xy} = a * (0.4 \exp(-t / T_{2s}) + 0.6 \exp(-t / T_{2f})) \qquad \text{Eq. A2-1}$$

where ‘a’ is a scaling factor, T_{2f} and T_{2s} are the fast and slow components respectively. Nonlinear least square fitting of data points to the model used the Levenberg-Marquardt algorithm. The curve fitting tool (cftool) in Matlab can be used.

Alternatively, T_2 of an agar gel phantom can be measured by a non-imaging experiment using a 4-pulse TQF sequence and conventional 6-step phase cycling. The basis for this is that the agar gel is homogeneous throughout the entire phantom volume and T_2 is expected to be the same regardless of location within the object. This approach was also used in healthy volunteers to determine the optimal τ value for TQF imaging. The following sequence parameters can be used: TR = 400 ms, flip angle = 90^o, 180^o, 90^o, 90^o, pulse width = 0.5 ms (90^o pulse) and 1 ms (180^o), τ/TE = 1 – 30 ms (in 1 ms increment), δ should be as short as possible, and no spatially localizing gradients are applied during acquisition. Since only one signal readout is performed for each τ/TE value (i.e. sequence is not repeated for different projections), signal can be averaged multiple times without significantly increasing the total scan duration. In this thesis, 25 averages were used where the acquisition time for each τ/TE value is 60 seconds. The maximum magnitudes of transverse magnetization from all acquired FIDs are fitted to the model (Hancu, et al., 1999)

$$\mathrm{M_{xy}} = \mathrm{a} * (\exp(\mathrm{R}_2^{(1)}\mathrm{t}) - \exp(\mathrm{R}_1^{(1)}\mathrm{t})) \qquad \text{Eq. A2-2}$$

where ‘a’ is a scaling factor, $R_2^{(1)} = 1/T_{2s}$ and $R_1^{(1)} = 1/T_{2f}$ (the superscript denotes the quantum coherence order). In this case, relaxation is dependent on single-quantum relaxation.

Similarly, T_1 can be measured by either an imaging or non-imaging experiment using an inversion recovery sequence. The following sequences parameters can be used: TR = 300 ms, flip angle of 180^o (inversion pulse) and 90^o (excitation), pulse width = 0.5 ms, multiple TI values selected between 3 to 100 ms. The data points are fitted to the model

$$M_{xy} = a * (1 - 2(-TI / T_1)) \qquad \text{Eq. A2-3}$$

where ‘a’ is a scaling factor. Since it is likely that bi-exponential T_1 does exist in agar, the 2 components are found by non-linear regression to Eq. 3-1 and the assignment of spectral density parameters follow Eq. 3-2 and 3-3.

Bibliography

Abe, O., Aoki, S., Shirouzu, I., Kunimatsu, A., Hayashi, N., Masumoto, T., Mori, H., Yamada, H., Watanabe, M., Masutani, Y., & Ohtomo, K. (2003). MR imaging of ischemic penumbra. *European Journal of Radiology, 46*(1), 67-78.

Adeoye, O., Hornung, R., Khatri, P., & Kleindorfer, D. (2011). Recombinant Tissue-Type Plasminogen Activator Use for Ischemic Stroke in the United States A Doubling of Treatment Rates Over the Course of 5 Years. *Stroke, 42*(7), 1952-1955.

Ahmed, S., Hu, C., Paczynski, R., & Hsu, C. (2001). Pathophysiology of Ischemic Injury. In M. Fisher (Ed.), *Stroke Therapy* (Second ed., pp. 25-57): Butterworth-Heinemann.

Albers, G., Thijs, V., Wechsle, L., Kemp, S., Schlaug, G., Skalabrin, E., Bammer, R., Kakuda, W., Lansberg, M., Shuaib, A., Coplin, W., Scott, H., Moseley, M., & Marks, M. (2006). Magnetic resonance imaging profiles predict clinical response to early reperfusion: The diffusion and perfusion imaging evaluation for understanding stroke evolution (DEFUSE) study. *Annals of Neurology, 60*(5), 508-517.

Allis, J., Seymour, A., & Radda, G. (1991). Absolute quantification of intracellular Na+ using triple-quantum-filtered 23Na NMR. *Journal of Magnetic Resonance, 93*(1), 71-76.

Aoki, J., Kimura, K., Iguchi, Y., Shibazaki, K., Sakai, K., & Iwanaga, T. (2010). FLAIR can estimate the onset time in acute ischemic stroke patients. *Journal of the Neurological Sciences, 293*(1-2), 39-44.

Arakawa, S., Wright, P., Koga, M., Phan, T., Reutens, D., Lim, I., Gunawan, M., Ma, H., Perera, N., Ly, J., Zavala, J., Fitt, G., & Donnan, G. (2006). Ischemic thresholds for gray and white matter - A diffusion and perfusion magnetic resonance study. *Stroke, 37*(5), 1211-1216.

Astrup, J., Siesjo, B., & Symon, L. (1981). Thresholds in Cerebral-Ischemia - the Ischemic Penumbra. *Stroke, 12*(6), 723-725.

Astrup, J., Symon, L., Branston, N., & Lassen, N. (1977). Cortical Evoked-Potential and Extracellular K+ and H+ at Critical Levels of Brain Ischemia. *Stroke, 8*(1), 51-57.

Atkinson, I., Renteria, L., Burd, H., Pliskin, N., & Thulborn, K. (2007). Safety of human MRI at static fields above the FDA ST guideline: Sodium imaging at 9.4T does not affect vital signs or cognitive ability. *Journal of Magnetic Resonance Imaging, 26*(5), 1222-1227.

Babsky, A., Zhang, H., Hekinatyar, S., Hutchins, G., & Bansal, N. (2007). Monitoring chemotherapeutic response in RIF-1 tumors by single-quantum and triple-quantum-filtered Na-23 MRI, H-1 diffusion-weighted MRI and PET imaging. *Magnetic Resonance Imaging, 25*(7), 1015-1023.

Baird, A., & Warach, S. (1998). Magnetic resonance imaging of acute stroke. *Journal of Cerebral Blood Flow and Metabolism, 18*(6), 583-609.

Balestrino, M. (1995). Pathophysiology of anoxic depolarization - new findings and a working hypothesis. *Journal of Neuroscience Methods, 59*(1), 99-103.

Bansal, N., Germann, M., Lazar, I., Malloy, C., & Sherry, A. (1992). Invivo Na-23 MR imaging and spectroscopy of rat brain during TmDOTP5 infusion. *Journal of Magnetic Resonance Imaging, 2*(4), 385-391.

Bartha, R., Lee, T., Hogan, M., Hughes, S., Barberi, E., Rajakumar, N., & Menon, R. (2004a). Sodium T2*-weighted MR imaging of acute focal cerebral ischemia in rabbits. *Magnetic Resonance Imaging, 22*(7), 983-991.

Bartha, R., & Menon, R. (2004b). Long component time constant of Na-23 T*(2) relaxation in healthy human brain. *Magnetic Resonance in Medicine, 52*(2), 407-410.

Beauchamp, N., Barker, P., Wang, P., & van Zijl, P. (1999). Imaging of acute cerebral ischemia. *Radiology, 212*(2), 307-324.

Benveniste, H., Hedlund, L., & Johnson, G. (1992). Mechanism of Detection of Acute Cerebral-Ischemia in Rats by Diffusion-Weighted Magnetic-Resonance Microscopy. *Stroke, 23*(5), 746-754.

Berendsen, H., & Edzes, H. (1973). Observation and general interpretation of sodium magnetic resonance in biological material. *Annals of the New York Academy of Sciences, 204*(MAR30), 459-485.

Betz, A., Keep, R., Beer, M., & Ren, X. (1994). Blood brain barrier permeability and brain concentration of sodium, potassium, and chloride during focal ischemia. *Journal of Cerebral Blood Flow and Metabolism, 14*(1), 29-37.

Boada, F., Gillen, J., Shen, G., Chang, S., & Thulborn, K. (1997). Fast three dimensional sodium imaging. *Magnetic Resonance in Medicine, 37*(5), 706-715.

Boada, F., LaVerde, G., Jungreis, C., Nemoto, E., Tanase, C., & Hancu, F. (2005). Loss of cell ion homeostasis and cell viability in the brain: What sodium MRI can tell us. *Current Topics in Developmental Biology, 70*, 77-101.

Boada, F., Tanase, C., Davis, D., Walter, K., Torres-Trejo, A., Couce, M., Hamilton, R., Kondziolka, D., Bartynski, W., & Lieberman, F. (2004). *Non-invasive assessment of tumor proliferation using triple quantum filtered 23Na MRI: Technical challenges and solutions.* Paper presented at the 26th Annual International Conference of IEEE Engineering in Medicine and Biology Society, San Francisco, USA.

Bodenhausen, G., Kogler, H., & Ernst, R. (1984). Selection of coherence-transfer pathways in NMR pulse experiments. *Journal of Magnetic Resonance, 58*(3), 370-388.

Borthakur, A., Hancu, I., Boada, F., Shen, G., Shapiro, E., & Reddy, R. (1999). In vivo triple quantum filtered twisted projection sodium MRI of human articular cartilage. *Journal of Magnetic Resonance, 141*(2), 286-290.

Bowden, G., Hutchison, W., & Khachan, J. (1986). Tensor operator formalism for multiple-quantum NMR. 2. Spins 3/2, 2, and 5/2 and general I. *Journal of Magnetic Resonance, 67*(3), 415-437.

Brouns, R., & De Deyn, P. (2009). The complexity of neurobiological processes in acute ischemic stroke. *Clinical Neurology and Neurosurgery, 111*(6), 483-495.

Brown, M., & Semelka, R. (2003). *MRI: basic principles and applications* (3rd ed.): Wiley-Liss.

Butcher, K., & Emery, D. (2010). Acute Stroke Imaging Part II: The Ischemic Penumbra. *Canadian Journal of Neurological Sciences, 37*(1), 17-27.

Butcher, K., Parsons, M., Allport, L., Lee, S., Barber, P., Tress, B., Donnan, G., Davis, S., & Investigators, E. (2008). Rapid assessment of perfusion-diffusion mismatch. *Stroke, 39*(1), 75-81.

Butcher, K., Parsons, M., Baird, T., Barber, A., Donnan, G., Desmond, P., Tress, B., & Davis, S. (2003). Perfusion thresholds in acute stroke thrombolysis. *Stroke, 34*(9), 2159-2164.

Butcher, K., Parsons, M., MacGregor, L., Barber, P., Chalk, J., Bladin, C., Levi, C., Kimber, T., Schultz, D., Fink, J., Tress, B., Donnan, G., Davis, S., & Investigators, E. (2005). Refining the perfusion-diffusion mismatch hypothesis. *Stroke, 36*(6), 1153-1159.

Cameron, I., Smith, N., Pool, T., & Sparks, R. (1980). Intracellular concentration of sodium and other elements as related to mitogenesis and oncogenesis in vivo. *Cancer Research, 40*(5), 1493-1500.

Canada. (2011). *Tracking Heart Disease and Stroke in Canada – Stroke Highlights 2011*. Ottawa: Public Health Agency of Canada Retrieved from http://www.phac-aspc.gc.ca/cd-mc/cvd-mcv/sh-fs-2011/pdf/StrokeHighlights_EN.pdf.

Choy, J., Ling, W., & Jerschow, A. (2006). Selective detection of ordered sodium signals via the central transition. *Journal of Magnetic Resonance, 180*(1), 105-109.

Christensen, J., Barrere, B., Boada, F., Vevea, J., & Thulborn, K. (1996). Quantitative tissue sodium concentration mapping of normal rat brain. *Magnetic Resonance in Medicine, 36*(1), 83-89.

Chung, C., & Wimperis, S. (1990). Optimum detection of spin-3/2 biexponential relaxation using multiple-quantum filtration techniques. *Journal of Magnetic Resonance, 88*(2), 440-447.

Cocho, D., Belvis, R., Marti-Fabregas, J., Molina-Porcel, L., Diaz-Manera, J., Aleu, A., Pagonabarraga, J., Garcia-Bargo, D., Mauri, A., & Marti-Vilalta, J. (2005). Reasons for exclusion from thrombolytic therapy following acute ischemic stroke. *Neurology, 64*(4), 719-720.

Cope, F. (1970). Spin-echo nuclear magnetic resonance evidence for complexing ions in muscle, brain and kidney. *Biophysical Journal, 10*(9), 843-858.

Copen, W., Gonzalez, R., & Schaefer, P. (2011). Perfusion MRI of Acute Stroke. In R. G. Gonzalez, J. A. Hirsch, M. H. Lev, P. W. Schaefer & L. H. Schwamm (Eds.), *Acute Ischemic Stroke: Imaging and Intervention* (2nd ed., pp. 175-196): Springer.

CRC Handbook of Chemistry and Physics. (2011). W. M. Haynes & D. R. Lide (Eds.), Retrieved from http://www.hbcpnetbase.com/

Davis, S., Donnan, G., Parsons, M., Levi, C., Butcher, K., Peeters, A., Barber, P., Bladin, C., De Silva, D., Byrnes, G., Chalk, J., Fink, J., Kimber, T., Schultz, D., Hand, P., Frayne, J., Hankey, G., Muir, K., Gerraty, R., Tress, B., Desmond, P., & Investigators, E. (2008). Effects of alteplase beyond 3 h after stroke in the Echoplanar Imaging Thrombolytic Evaluation Trial (EPITHET): a placebo-controlled randomised trial. *Lancet Neurology, 7*(4), 299-309.

Deb, P., Sharma, S., & Hassan, K. (2010). Pathophysiologic mechanisms of acute ischemic stroke: An overview with emphasis on therapeutic significance beyond thrombolysis. *Pathophysiology, 17*(3), 197-218.

Decoene, B., Hajnal, J., Gatehouse, P., Longmore, D., White, S., Oatridge, A., Pennock, J., Young, I., & Bydder, G. (1992). MR of the brain using fluid-attenuated inversion recovery (FLAIR) pulse sequences. *American Journal of Neuroradiology, 13*(6), 1555-1564.

del Zoppo, G., Saver, J., Jauch, E., Adams, H., & Amer Heart Assoc Stroke, C. (2009). Expansion of the Time Window for Treatment of Acute Ischemic Stroke With Intravenous Tissue Plasminogen Activator A Science Advisory From the American Heart Association/American Stroke Association. *Stroke, 40*(8), 2945-2948.

Dumoulin, C., Cline, H., Souza, S., Wagle, W., & Walker, M. (1989). 3-Dimensional time-of-flight magnetic resonance angiography using spin saturation. *Magnetic Resonance in Medicine, 11*(1), 35-46.

Duvvuri, U., Leigh, J., & Reddy, R. (1999). Detection of residual quadrupolar interaction in the human breast in vivo using sodium-23 multiple quantum spectroscopy. *Journal of Magnetic Resonance Imaging, 9*(3), 391-394.

Ebinger, M., Galinovic, I., Rozanski, M., Brunecker, P., Endres, M., & Fiebach, J. (2010). Fluid-Attenuated Inversion Recovery Evolution Within 12 Hours From Stroke Onset A Reliable Tissue Clock? *Stroke, 41*(2), 250-255.

Eleff, S., Maruki, Y., Monsein, L., Traystman, R., Bryan, R., & Koehler, R. (1991). Sodium, ATP, and intracellular pH transients during reversible complete ischemia of dog cerebrum. *Stroke, 22*(2), 233-241.

Eliav, U., & Navon, G. (1994). Analysis of double-quantum-filtered NMR spectra of 23Na in biological tissues. *Journal of Magnetic Resonance Series B, 103*(1), 19-29.

Eliav, U., Shinar, H., & Navon, G. (1992). The formation of a 2nd-rank tensor in Na-23 double-quantum-filtered NMR as an indicator for order in a biological tissue. *Journal of Magnetic Resonance, 98*(1), 223-229.

Elliott, W. (1998). Circadian variation in the timing of stroke onset - A meta-analysis. *Stroke, 29*(5), 992-996.

FDA. (Aug 13, 2009). Questions and Answers on Gadolinium-Based Contrast Agents Retrieved February 25, 2013, from http://www.fda.gov/Drugs/DrugSafety/DrugSafetyNewsletter/ucm142889.htm

Fiebach, J. B., Schellinger, P. D., Jansen, O., Meyer, M., Wilde, P., Bender, J., Schramm, P., Juttler, E., Oehler, J., Hartmann, M., Hahnel, S., Knauth, M., Hacke, W., & Sartor, K. (2002). CT and diffusion-weighted MR imaging in randomized order - Diffusion-weighted imaging results in higher accuracy and lower interrater variability in the diagnosis of hyperacute ischemic stroke. *Stroke, 33*(9), 2206-2210.

Fink, J., Kumar, S., Horkan, C., Linfante, I., Selim, M., Caplan, L., & Schlaug, G. (2002). The stroke patient who woke up - Clinical and radiological features, including diffusion and perfusion MRI. *Stroke, 33*(4), 988-993.

Fleysher, L., Oesignmann, N., Brown, R., Wiggins, G., Sodickson, D., & Inglese, M. (2010a). *Intra-cellular sodium fraction in the human brain at 7T in-vivo.* Paper presented at the 18th Annual Meeting of ISMRM, Stockholm, Sweden.

Fleysher, L., Oesingmann, N., Brown, R., Sodickson, D., Wiggins, G., & Inglese, M. (2012). Noninvasive quantification of intracellular sodium in human brain using ultrahigh-field MRI. *NMR in Biomedicine*.

Fleysher, L., Oesingmann, N., & Inglese, M. (2010b). B0 inhomogeneity-insensitive triple-quantum-filtered sodium imaging using a 12-step phase-cycling scheme. *NMR in Biomedicine, 23*(10), 1191-1198.

Fleysher, L., Oesingmann, N., Stoeckel, B., Grossman, R., & Inglese, M. (2009). Sodium long-component T(2)* mapping in human brain at 7 Tesla. *Magnetic Resonance in Medicine, 62*(5), 1338-1341.

Furlan, M., Marchal, G., Viader, F., Derlon, J., & Baron, J. (1996). Spontaneous neurological recovery after stroke and the fate of the ischemic penumbra. *Annals of Neurology, 40*(2), 216-226.

Garcia, J., Liu, K., & Ho, K. (1995). Neuronal necrosis after middle cerebral artery occlusion in Wistar rats progresses at different time intervals in the caudoputamen and the cortex. *Stroke, 26*(4), 636-642.

Gauvrit, J., Leclerc, X., Girot, M., Cordonnier, C., Sotoares, G., Henon, H., Pertuzon, B., Michelin, E., Devos, D., Pruvo, J., & Leys, D. (2006). Fluid-attenuated inversion recovery (FLAIR) sequences for the assessment of acute stroke - Inter observer and inter technique reproducibility. *Journal of Neurology, 253*(5), 631-635.

Go, A., Mozaffarian, D., Roger, V. L., Benjamin, E. J., Berry, J. D., Borden, W. B., Bravata, D. M., Dai, S., Ford, E. S., Fox, C. S., Franco, S., Fullerton, H. J., Gillespie, C., Hailpern, S. M., Heit, J. A., Howard, V. J., Huffman, M. D., Kissela, B. M., Kittner, S. J., Lackland, D. T., Lichtman, J. H., Lisabeth, L. D., Magid, D., Marcus, G. M., Marelli, A., Matchar, D. B., McGuire, D. K., Mohler, E. R., Moy, C. S., Mussolino, M. E., Nichol, G., Paynter, N. P., Schreiner, P. J., Sorlie, P. D., Stein, J., Turan, T. N., Virani, S. S., Wong, N. D., Woo, D., Turner, M. B., Amer Heart, A., & Stroke Stat, S. (2013). Heart Disease and Stroke Statistics-2013 Update A Report From the American Heart Association. *Circulation, 127*(1), E6-E245.

Goldemund, D., & Mikulik, R. (2010). Reperfusion Therapies for Acute Ischemic Stroke. *Current Treatment Options in Neurology, 12*(2), 155-166.

Gonzalez, R. (2006). Imaging-guided acute ischemic stroke therapy: From "time is brain" to "physiology is brain". *American Journal of Neuroradiology, 27*(4), 728-735.

Gotoh, O., Asano, T., Koide, T., & Takakura, K. (1985). Ischemic brain edema following occlusion of the middle cerebral artery in the rat .1: The time courses of the brain water, sodium and potassium contents and bood-brain-barrier permeability to I-125 albumin. *Stroke, 16*(1), 101-109.

Grandin, C., Duprez, T., Oppenheim, C., Peeters, A., Robert, A., & Cosnard, G. (2002). Which MR-derived perfusion parameters are the best predictors of infarct growth in hyperacute stroke? Comparative study between relative and quantitative measurements. *Radiology, 223*(2), 361-370.

Grandin, C., Duprez, T., Smith, A., Mataigne, F., Peeters, A., Oppenheim, C., & Cosnard, G. (2001). Usefulness of magnetic resonance-derived quantitative measurements of cerebral blood flow and volume in prediction of infarct growth in hyperacute stroke. *Stroke, 32*(5), 1147-1153.

Griffey, R., Griffey, B., & Matwiyoff, N. (1990). Triple-quantum-coherence-filtered imaging of sodium-ions in vivo at 4.7 Tesla. *Magnetic Resonance in Medicine, 13*(2), 305-313.

Grodd, W., & Klose, U. (1988). Sodium-MR-imaging of the brain: initial clinical results. *Neuroradiology, 30*(5), 399-407.

Gupta, R., & Gupta, P. (1982). Direct observation of resolved resonances from intra- and extracellular sodium-23 ions in NMR studies of intact cells and tissues using Dysprosium(III) tripolyphosphate as paramagnetic shift reagent. *Journal of Magnetic Resonance, 47*(2), 344-350.

Hacke, W., Kaste, M., Bluhmki, E., Brozman, M., Davalos, A., Guidetti, D., Larrue, V., Lees, K., Medeghri, Z., Machnig, T., Schneider, D., von Kummer, R., Wahlgren, N., Toni, D., & Investigators, E. (2008). Thrombolysis with alteplase 3 to 4.5 hours after acute ischemic stroke. *New England Journal of Medicine, 359*(13), 1317-1329.

Hancu, I., Boada, F., & Shen, G. (1999). Three-dimensional triple-quantum-filtered Na-23 imaging of in vivo human brain. *Magnetic Resonance in Medicine, 42*(6), 1146-1154.

Hancu, I., van der Maarel, J., & Boada, F. (2000). A model for the dynamics of spins 3/2 in biological media: Signal loss during radiofrequency excitation in triple-quantum-filtered sodium MRI. *Journal of Magnetic Resonance, 147*(2), 179-191.

Hashimoto, T., Ikehira, H., Fukuda, H., Yamaura, A., Watanabe, O., Tateno, Y., Tanaka, R., & Simon, H. (1991). In-vivo sodium-23 MRI in brain tumors evaluation of preliminary clinical experience. *American Journal of Physiologic Imaging, 6*(2), 74-80.

Hatano, S. (1976). Experience from a multicenter stroke register - preliminary report. *Bulletin of the World Health Organization, 54*(5), 541-553.

Hennerici, M., Bogousslavsky, J., Sacco, R., Binder, J., Chong, J., & Paciaroni, M. (2005). *Stroke*: Elsevier.

Hilal, S., Maudsley, A., Ra, J., Simon, H., Roschmann, P., Wittekoek, S., Cho, Z., & Mun, S. (1985). In vivo NMR imaging of sodium-23 in the human head. *Journal of Computer Assisted Tomography, 9*(1), 1-7.

Hilal, S., Maudsley, A., Simon, H., Perman, W., Bonn, J., Mawad, M., Silver, A., Ganti, S., Sane, P., & Chien, I. (1983). Invivo NMR imaging of tissue sodium in the intact cat before and after acute cerebral stroke. *American Journal of Neuroradiology, 4*(3), 245-249.

Hossmann, K. (1994). Viability Thresholds and the Penumbra of Focal Ischemia. *Annals of Neurology, 36*(4), 557-565.

Hubbard, P. (1970). Nonexponential nuclear magnetic relaxation by quadrupole interactions. *Journal of Chemical Physics, 53*(3), 985-987.

Hussain, M., Stobbe, R., Bhagat, Y., Emery, D., Butcher, K., Manawadu, D., Rizvi, N., Maheshwari, P., Scozzafava, J., Shuaib, A., & Beaulieu, C. (2009). Sodium imaging intensity increases with time after human ischemic stroke. *Annals of Neurology, 66*(1), 55-62.

Inglese, M., Madelin, G., Oesingmann, N., Babb, J., Wu, W., Stoeckel, B., Herbert, J., & Johnson, G. (2010). Brain tissue sodium concentration in multiple sclerosis: a sodium imaging study at 3 tesla. *Brain, 133*, 847-857.

Jaccard, G., Wimperis, S., & Bodenhausen, G. (1986). Multiple-quantum NMR spectroscopy of S=3/2 spins in isotropic phase: A new probe for multiexponential relaxation. *Journal of Chemical Physics, 85*(11), 6282-6293.

Jackson, J., Nishimura, D., & Macovski, A. (1992). Twisting radial lines with application to robust magnetic resonance imaging of irregular flow. *Magnetic Resonance in Medicine, 25*(1), 128-139.

Jacobs, M., Stearns, V., Wolff, A., Macura, K., Argani, P., Khouri, N., Tsangaris, T., Barker, P., Davidson, N., Bhujwalla, Z., Bluemke, D., & Ouwerkerk, R. (2010). Multiparametric Magnetic Resonance Imaging, Spectroscopy and Multinuclear ((23)Na) Imaging Monitoring of Preoperative Chemotherapy for Locally Advanced Breast Cancer. *Academic Radiology, 17*(12), 1477-1485.

Jauch, E., Saver, J., Adams, H., Jr., Bruno, A., Connors, J., Demaerschalk, B., Khatri, P., McMullan, P., Jr., Qureshi, A., Rosenfield, K., Scott, P., Summers, D., Wang, D., Wintermark, M., Yonas, H., Amer Heart Assoc Stroke, C., Council Cardiovasc, N., Council Peripheral Vasc, D., & Council Clinical, C. (2013). Guidelines for the Early Management of Patients With Acute Ischemic Stroke A Guideline for Healthcare Professionals From the American Heart Association/American Stroke Association. *Stroke, 44*(3), 870-947.

Jelicks, L., & Gupta, R. (1989). Observation of intracellular sodium ions by double-quantum-filtered Na-23 NMR with paramagnetic quenching of extracellular coherence by gadolinium tripolyphosphate. *Journal of Magnetic Resonance, 83*(1), 146-151.

Jelicks, L., Paul, P., Obyrne, E., & Gupta, R. (1993). Hydrogen-1, sodium-23, and carbon-13 MR spectroscopy of cartilage degradation in vitro. *Journal of Magnetic Resonance Imaging, 3*(4), 565-568.

Jones, S., Kharlamov, A., Yanovski, B., Kim, D., Easley, K., Yushmanov, V., Ziolko, S., & Boada, F. (2006). Stroke onset time using sodium MRI in rat focal cerebral ischemia. *Stroke, 37*(3), 883-888.

Joseph, P., & Summers, R. (1987). The flip-angle effect - a method for detection of Na-23 quadrupole splitting in tissue. *Magnetic Resonance in Medicine, 4*(1), 67-77.

Kalyanapuram, R., Seshan, V., & Bansal, N. (1998). Three-dimensional triple-quantum-filtered Na-23 imaging of the dog head in vivo. *Journal of Magnetic Resonance Imaging, 8*(5), 1182-1189.

Kaufman, L., Kramer, D., Crooks, L., & Ortendahl, D. (1989). Measuring signal-to-noise ratios in MR imaging. *Radiology, 173*(1), 265-267.

Keltner, J., Wong, S., & Roos, M. (1994). Three-dimensional triple-quantum-filtered imaging of 0.012 and 0.024 M sodium-23 using short repetition times. *Journal of Magnetic Resonance Series B, 104*(3), 219-229.

Kemp-Harper, R., Brown, S., Hughes, C., Styles, P., & Wimperis, S. (1997). Na-23 NMR methods for selective observation of sodium ions in ordered environments. *Progress in Nuclear Magnetic Resonance Spectroscopy, 30*, 157-181.

Kemp-Harper, R., Brown, S., Styles, P., & Wimperis, S. (1994). In-vivo NMR of sodium-ions in ordered environments. *Journal of Magnetic Resonance Series B, 105*(2), 199-203.

Kharrazian, R., & Jakob, P. (2006). Dynamics of Na-23 during completely balanced steady-state free precession. *Journal of Magnetic Resonance, 179*(1), 73-84.

Kidwell, C., Alger, J., & Saver, J. (2003). Evolving paradigms in imaging the ischemic penumbra with multimodal magnetic resonance imaging. *Stroke, 34*(11), 2729-2735.

Kidwell, C., Chalela, J., Saver, J., Starkman, S., Hill, M., Demchuk, A., Butman, J., Patronas, N., Alger, J., Latour, L., Luby, M., Baird, A., Leary, M., Tremwel, M., Ovbiagele, B., Fredieu, A., Suzuki, S., Villablanca, J., Davis, S., Dunn, B., Todd, J., Ezzeddine, M., Haymore, J., Lynch, J., Davis, U., & Warach, S. (2004). Comparison of MRI and CT for detection of acute intracerebral hemorrhage. *Journal of the American Medical Association*(15), 1823-1830.

Klatzo, I. (1987). Pathophysiological aspects of brain edema. *Acta Neuropathologica, 72*(3), 236-239.

Kline, R., Wu, E., Petrylak, D., Szabolcs, M., Alderson, P., Weisfeldt, M., Cannon, P., & Katz, J. (2000). Rapid in vivo monitoring of chemotherapeutic response using weighted sodium magnetic resonance imaging. *Clinical Cancer Research, 6*(6), 2146-2156.

Kohno, K., Hoehnberlage, M., Mies, G., Back, T., & Hossmann, K. (1995). Relationship between Diffusion-Weighted MR-Images, Cerebral Blood-Flow, and Energy-State in Experimental Brain Infarction. *Magnetic Resonance Imaging, 13*(1), 73-80.

Kopp, C., Linz, P., Wachsmuth, L., Dahlmann, A., Horbach, T., Schoefl, C., Renz, W., Santoro, D., Niendorf, T., Mueller, D., Neininger, M., Cavallaro, A., Eckardt, K.-U., Schmieder, R., Luft, F., Uder, M., & Titze, J. (2012). Na^{23} Magnetic Resonance Imaging of Tissue Sodium. *Hypertension, 59*(1), 167-172.

Lansberg, M., Thijs, V., O'Brien, M., Ali, J., de Crespigny, A., Tong, D., Moseley, M., & Albers, G. (2001). Evolution of apparent diffusion coefficient, diffusion-weighted, and T2-weighted signal intensity of acute stroke. *American Journal of Neuroradiology, 22*(4), 637-644.

Laustsen, C., Ringgaard, S., Pedersen, M., & Nielsen, N. (2010). Quadrupolar-coupling-specific binomial pulse sequences for in vivo Na-23 NMR and MRI. *Journal of Magnetic Resonance, 206*(1), 139-146.

LaVerde, G., Nemoto, E., Jungreis, C., Tanase, C., & Boada, F. (2007). Serial triple quantum sodium MRI during non-human primate focal brain ischemia. *Magnetic Resonance in Medicine, 57*(1), 201-205.

Lebihan, D., Breton, E., Lallemand, D., Grenier, P., Cabanis, E., & Lavaljeantet, M. (1986). MR imaging of intravoxel incoherent motions - application to diffusion and perfusion in neurologic disorders. *Radiology, 161*(2), 401-407.

Lin, S., Song, S., Miller, J., Ackerman, J., & Neil, J. (2001). Direct, longitudinal comparison of H-1 and Na-23 MRI after transient focal cerebral ischemia. *Stroke, 32*(4), 925-932.

Liu, T. T., & Brown, G. G. (2007). Measurement of cerebral perfusion with arterial spin labeling: Part 1. Methods. *Journal of the International Neuropsychological Society, 13*(3), 517-525.

Lu, A., Atkinson, I., Claiborne, T., Damen, F., & Thulborn, K. (2010). Quantitative sodium imaging with a flexible twisted projection pulse sequence. *Magnetic Resonance in Medicine, 63*(6), 1583-1593.

Lyon, R., Pekar, J., Moonen, C., & Mclaughlin, A. (1991). Double-quantum surface coil NMR studies of sodium and potassium in the rat brain. *Magnetic Resonance in Medicine, 18*(1), 80-92.

Madelin, G., Babb, J., Xia, D., Chang, G., Jerschow, A., & Regatte, R. (2012). Reproducibility and repeatability of quantitative sodium magnetic resonance imaging in vivo in articular cartilage at 3 T and 7 T. *Magnetic Resonance in Medicine, 68*(3), 841-849.

Makkat, S., Vandevenne, J., Verswijvel, G., Ijsewijn, T., Grieten, M., Palmers, Y., De Schepper, A., & Parizel, P. (2002). Signs of acute stroke seen on fluid-attenuated inversion recovery MR imaging. *American Journal of Roentgenology, 179*(1), 237-243.

Marchal, G., Beaudouin, V., Rioux, P., delaSayette, V., LeDoze, F., Viader, F., Derlon, J., & Baron, J. (1996). Prolonged persistence of substantial volumes of potentially viable brain tissue after stroke - A correlative PET-CT study with voxel-based data analysis. *Stroke, 27*(4), 599-606.

Matthies, C., Nagel, A., Schad, L., & Bachert, P. (2010). Reduction of B-0 inhomogeneity effects in triple-quantum-filtered sodium imaging. *Journal of Magnetic Resonance, 202*(2), 239-244.

Meier, P., & Zierler, K. (1954). On the Theory of the Indicator-Dilution Method for Measurement of Blood Flow and Volume. *Journal of Applied Physiology, 6*(12), 731-744.

Mellon, E., Pilkinton, D., Clark, C., Elliott, M., Witschey, W., Borthakur, A., & Reddy, R. (2009). Sodium MR Imaging Detection of Mild Alzheimer Disease: Preliminary Study. *American Journal of Neuroradiology, 30*(5), 978-984.

Mitchell, P., Wilkinson, I. D., Hoggard, N., Paley, M. N. J., Jellinek, D. A., Powell, T., Romanowski, C., Hodgson, T., & Griffiths, P. D. (2001). Detection of subarachnoid haemorrhage with magnetic resonance imaging. *Journal of Neurology Neurosurgery and Psychiatry, 70*(2), 205-211.

Moritani, T., Ekholm, S., & Westesson, P. (2009). *Diffusion-Weighted MR Imaging of the Brain* (2nd ed.): Springer.

Moseley, M., Chew, W., Nishimura, M., Richards, T., Murphy-Boesch, J., Young, G., Marschner, T., Pitts, L., & James, T. (1985). In-vivo sodium-23 magnetic resonance surface coil imaging observing experimental cerebral ischemia in the rat. *Magnetic Resonance Imaging, 3*(4), 383-388.

Moseley, M., Cohen, Y., Mintorovitch, J., Chileuitt, L., Shimizu, H., Kucharczyk, J., Wendland, M., & Weinstein, P. (1990). Early Detection of Regional Cerebral-Ischemia in Cats - Comparison of Diffusion-Weighted and T2-Weighted MRI and Spectroscopy. *Magnetic Resonance in Medicine, 14*(2), 330-346.

Muller, N., Bodenhausen, G., & Ernst, R. (1987). Relaxation-Induced Violations of Coherence Transfer Selection-Rules in Nuclear-Magnetic-Resonance. *Journal of Magnetic Resonance, 75*(2), 297-334.

Nagel, A., Amarteifio, E., Lehmann-Horn, F., Jurkat-Rott, K., Semmler, W., Schad, L., & Weber, M.-A. (2011a). 3 Tesla Sodium Inversion Recovery Magnetic Resonance Imaging Allows for Improved Visualization of Intracellular Sodium Content Changes in Muscular Channelopathies. *Investigative Radiology, 46*(12), 759-766.

Nagel, A., Bock, M., Hartmann, C., Gerigk, L., Neumann, J., Weber, M., Bendszus, M., Radbruch, A., Wick, W., Schlemmer, H., Semmler, W., & Biller, A. (2011b). The potential of relaxation-weighted sodium magnetic resonance imaging as demonstrated on brain tumors. *Investigative Radiology, 46*(9), 539-547.

Nave, C. (2010). Electric Quadrupole Moments of Nuclei Retrieved Sept 15, 2011, from http://hyperphysics.phy-astr.gsu.edu/hbase/nuclear/elequad.html

Navon, G. (1993). Complete elimination of the extracellular Na-23 NMR signal in triple quantum filtered spectra of rat hearts in the presence of shift-reagents. *Magnetic Resonance in Medicine, 30*(4), 503-506.

Nielles-Vallespin, S., Weber, M., Bock, M., Bongers, A., Speier, P., Combs, S., Wohrle, J., Lehmann-Horn, F., Essig, M., & Schad, L. (2007). 3D radial projection technique with ultrashort echo times for sodium MRI: Clinical applications in human brain and skeletal muscle. *Magnetic Resonance in Medicine, 57*(1), 74-81.

Nishimura, D. (2010). *Principles of Magnetic Resonance Imaging* Stanford University.

Ooms, K., Cannella, M., Vega, A., Marcolongo, M., & Polenova, T. (2008). Na-23 TQF NMR imaging for the study of spinal disc tissue. *Journal of Magnetic Resonance, 195*(1), 112-115.

Oppenheim, C., Logak, M., Dormont, D., Lehericy, S., Manai, R., Samson, Y., Marsault, C., & Rancurel, G. (2000). Diagnosis of acute ischaemic stroke with fluid-attenuated inversion recovery and diffusion-weighted sequences. *Neuroradiology, 42*(8), 602-607.

Ostergaard, L., Weisskoff, R., Chesler, D., Gyldensted, C., & Rosen, B. (1996). High resolution measurement of cerebral blood flow using intravascular tracer bolus passages .1. Mathematical approach and statistical analysis. *Magnetic Resonance in Medicine, 36*(5), 715-725.

Ouwerkerk, R., Bleich, K., Gillen, J., Pomper, M., & Bottomley, P. (2003). Tissue sodium concentration in human brain tumors as measured with Na-23 MR imaging. *Radiology, 227*(2), 529-537.

Ovbiagele, B., & Saver, J. (2006). Cerebral white matter hyperintensities on MRI: Current concepts and therapeutic implications. *Cerebrovascular Diseases, 22*(2-3), 83-90.

Parizel, P. M., Makkat, S., Van Miert, E., Van Goethem, J. W., van den Hauwe, L., & De Schepper, A. M. (2001). Intracranial hemorrhage: principles of CT and MRI interpretation. *European Radiology, 11*(9), 1770-1783.

Patel, M., Edelman, R., & Warach, S. (1996). Detection of hyperacute primary intraparenchymal hemorrhage by magnetic resonance imaging. *Stroke, 27*(12), 2321-2324.

Pekar, J., & Leigh, J. (1986). Detection of Biexponential Relaxation in Na-23 Facilitated by Double-Quantum Filtering. *Journal of Magnetic Resonance, 69*(3), 582-584.

Perkins, C., Kahya, E., Roque, C., Roche, P., & Newman, G. (2001). Fluid-attenuated inversion recovery and diffusion- and perfusion-weighted MRI abnormalities in 117 consecutive patients with stroke symptoms. *Stroke, 32*(12), 2774-2781.

Powers, W. (1991). Cerebral hemodynamics in ischemic cerebrovascular disease. *Annals of Neurology, 29*(3), 231-240.

Prince, L., Miller, S., Pohost, G., & Elgavish, G. (1992). The longitudinal relaxation time (T1) of the intracellular Na23 NMR signal in the isolated perfused rat heart during hypoxia and reoxygenation. *Magnetic Resonance in Medicine, 23*(2), 376-382.

Qian, Y., & Boada, F. (2010). *In vivo triple-quantum (TQ) sodium MRI on the human brain: SNR benefits at 7T.* Paper presented at the 18th Annual Meeting of ISMRM, Stockholm, Sweden.

Ra, J., Hilal, S., & Cho, Z. (1986). A method for invivo MR imaging of the short T2 component of Na-23. *Magnetic Resonance in Medicine, 3*(2), 296-302.

Ratkowsky, D. (1990). *Handbook of nonlinear regression models*. New York: Marcel Dekker Inc.

Reddy, R., Bolinger, L., Shinnar, M., Noyszewski, E., & Leigh, J. (1995). Detection of residual quadrupolar interaction in human skeletal muscle and brain in-vivo via multiple-quantum filtered sodium NMR spectra. *Magnetic Resonance in Medicine, 33*(1), 134-139.

Reddy, R., Insko, E., & Leigh, J. (1997a). Triple quantum sodium imaging of articular cartilage. *Magnetic Resonance in Medicine, 38*(2), 279-284.

Reddy, R., Insko, E., Noyszewski, E., Dandora, R., Kneeland, J., & Leigh, J. (1998). Sodium MRI of human articular cartilage in vivo. *Magnetic Resonance in Medicine, 39*(5), 697-701.

Reddy, R., Li, S., Noyszewski, E., Kneeland, J., & Leigh, J. (1997b). In vivo sodium multiple quantum spectroscopy of human articular cartilage. *Magnetic Resonance in Medicine, 38*(2), 207-214.

Reddy, R., Shinnar, M., Wang, Z., & Leigh, J. (1994). Multiple-quantum filters of spin-3/2 with pulses of arbitrary flip angle. *Journal of Magnetic Resonance Series B, 104*(2), 148-152.

Ricci, P., Burdette, J., Elster, A., & Reboussin, D. (1999). A comparison of fast spin-echo, fluid-attenuated inversion-recovery, and diffusion-weighted MR imaging in the first 10 days after cerebral infarction. *American Journal of Neuroradiology, 20*(8), 1535-1542.

Robb, R. (2001). The Biomedical Imaging Resource at Mayo Clinic. *Ieee Transactions on Medical Imaging, 20*(9), 854-867.

Roberts, T., & Rowley, H. (2003). Diffusion weighted magnetic resonance imaging in stroke. *European Journal of Radiology, 45*(3), 185-194.

Rooney, W., & Springer, C. (1991). A comprehensive approach to the analysis and interpretation of the resonances of spins 3/2 from living systems. *NMR in Biomedicine, 4*(5), 209-226.

Rosen, B., Belliveau, J., Vevea, J., & Brady, T. (1990). Perfusion imaging with NMR contrast agents. *Magnetic Resonance in Medicine, 14*(2), 249-265.

Rowley, H. (2001). The four Ps of acute stroke imaging: Parenchyma, pipes, perfusion, and penumbra. *American Journal of Neuroradiology, 22*(4), 599-601.

Schlaug, G., Benfield, A., Baird, A., Siewert, B., Lovblad, K., Parker, R., Edelman, R., & Warach, S. (1999). The ischemic penumbra - operationally defined by diffusion and perfusion MRI. *Neurology, 53*(7), 1528-1537.

Schlaug, G., Siewert, B., Benfield, A., Edelman, R., & Warach, S. (1997). Time course of the apparent diffusion coefficient (ADC) abnormality in human stroke. *Neurology, 49*(1), 113-119.

Schroth, G., & Klose, U. (1992). Cerebrospinal fluid flow II. Physiology of respiration-related pulsations. *Neuroradiology, 35*(1), 10-15.

Serena, J., Davalos, A., Segura, T., Mostacero, E., Castillo, J., & Spanish Neurological, S. (2003). Stroke on awakening: Looking for a more rational management. *Cerebrovascular Diseases, 16*(2), 128-133.

Shimizu, T., Naritomi, H., & Sawada, T. (1993). Sequential changes on Na-23 MRI after cerebral infarction. *Neuroradiology, 35*(6), 416-419.

Shporer, M., & Civan, M. (1972). Nuclear magnetic resonance of sodium-23 linoleate water - basis for an alternative interpretation of sodium-23 spectra within cells. *Biophysical Journal, 12*(1), 114-122.

Siemonsen, S., Mouridsen, K., Holst, B., Ries, T., Finsterbusch, J., Thomalla, G., Ostergaard, L., & Fiehler, J. (2009). Quantitative T2 Values Predict Time From Symptom Onset in Acute Stroke Patients. *Stroke, 40*(5), 1612-1616.

Sorensen, A., & Reimer, P. (2000). *Cerebral MR perfusion imaging: principles and current applications*: Thieme.

Springer, C. (1987). Measurement of metal cation compartmentalization in tissue by high-resolution cation NMR. *Annual Review of Biophysics and Biophysical Chemistry, 16*, 375-399.

Springer, C. (1996). Biological systems: spin-3/2 nuclei. In D. M. Grant & R. K. Harris (Eds.), *Encyclopedia of nuclear magnetic resonance* (pp. 940-951). New York: John Wiley & Sons.

Stejskal, E., & Tanner, J. (1965). Spin diffusion measurements: spin echoes in the presence of a time-dependent field gradient. *Journal of Chemical Physics, 42*(1), 288-292.

Stobbe, R. (2010). *Sodium MRI optimization for the human head with application to acute stroke.* Doctor of Philosophy, University of Alberta, Edmonton. Retrieved from http://search.proquest.com/docview/305232040?accountid=14474 ProQuest Dissertations & Theses Full Text database.

Stobbe, R., & Beaulieu, C. (2005). In vivo sodium magnetic resonance imaging of the human brain using soft inversion recovery fluid attenuation. *Magnetic Resonance in Medicine, 54*(5), 1305-1310.

Stobbe, R., & Beaulieu, C. (2006). *Sodium relaxometry (Part 2): Towards the characterization of the sodium NMR environment in the human brain using a novel relaxomety technique* Paper presented at the 14th Annual Meeting ISMRM, Seattle.

Stobbe, R., & Beaulieu, C. (2008a). Advantage of sampling density weighted apodization over postacquisition filtering apodization for sodium MRI of the human brain. *Magnetic Resonance in Medicine, 60*(4), 981-986.

Stobbe, R., & Beaulieu, C. (2008b). Sodium imaging optimization under specific absorption rate constraint. *Magnetic Resonance in Medicine, 59*(2), 345-355.

Stobbe, R., & Beaulieu, C. (2009). *Sodium 'invisibility' in single quantum sodium imaging of the human brain.* Paper presented at the 17th Annual Meeting ISMRM, Honolulu, Hawaii.

Tanase, C., & Boada, F. (2005). Triple-quantum-filtered imaging of sodium in presence of B-0 inhomogeneities. *Journal of Magnetic Resonance, 174*(2), 270-278.

Tauskela, J., Dizon, J., Whang, J., & Katz, J. (1997). Evaluation of multiple-quantum-filtered Na-23 NMR in monitoring intracellular Na content in the isolated perfused rat heart in the absence of a chemical-shift reagent. *Journal of Magnetic Resonance, 127*(1), 115-127.

The National Institute of Neurological Disorders and Stroke rt-PA Stroke Study Group. (1995). Tissue plasminogen activator for acute ischemic stroke. *The New England Journal of Medicine, 333*(24), 1581-1587.

Thomalla, G., Rossbach, P., Rosenkranz, M., Siemonsen, S., Krutzelmann, A., Fiehler, J., & Gerloff, C. (2009). Negative Fluid-Attenuated Inversion Recovery Imaging Identifies Acute Ischemic Stroke at 3 Hours or Less. *Annals of Neurology, 65*(6), 724-732.

Thompson, H., Whalen, R., Starmer, C., & McIntosh, H. (1964). Indicator transit time considered as gamma variate. *Circulation Research, 14*(6), 502-515.

Thulborn, K., Davis, D., Adams, H., Gindin, T., & Zhou, J. (1999a). Quantitative tissue sodium concentration mapping of the growth of focal cerebral tumors with sodium magnetic resonance imaging. *Magnetic Resonance in Medicine, 41*(2), 351-359.

Thulborn, K., Davis, D., Snyder, J., Yonas, H., & Kassam, A. (2005). Sodium MR imaging of acute and subacute stroke for assessment of tissue viability. *Neuroimaging Clinics of North America, 15*(3), 639-653.

Thulborn, K., Gindin, T., Davis, D., & Erb, P. (1999b). Comprehensive MR imaging protocol for stroke management: Tissue sodium concentration as a measure of tissue viability in nonhuman primate studies and in clinical studies. *Radiology, 213*(1), 156-166.

Thulborn, K., Lu, A., Atkinson, I., Damen, F., & Villano, J. (2009). Quantitative sodium MR imaging and sodium bioscales for the management of brain tumors. *Neuroimaging Clinics of North America, 19*(4), 615-624.

Tsang, A., Stobbe, R., Asdaghi, N., Hussain, M., Bhagat, Y., Beaulieu, C., Emery, D., & Butcher, K. (2011). Relationship Between Sodium Intensity and Perfusion Deficits in Acute Ischemic Stroke. *Journal of Magnetic Resonance Imaging, 33*(1), 41-47.

Tsang, A., Stobbe, R., & Beaulieu, C. (2009). *Triple-quantum-filtered sodium MRI of the human brain at 4.7T.* Paper presented at the ISMRM, Hawaii, USA.

Tsang, A., Stobbe, R., & Beaulieu, C. (2012). Triple quantum filtered sodium imaging of the human brain at 4.7T. *Magnetic Resonance in Medicine, 67,* 1633-1643.

Turski, P., Houston, L., Perman, W., Hald, J., Turski, D., Strother, C., & Sackett, J. (1987). Experimental and human brain neoplasms - detection with invivo sodium MR imaging. *Radiology, 163*(1), 245-249.

Tyson, R., Sutherland, G., & Peeling, J. (1996). ^{23}Na nuclear magnetic resonance spectral changes during and after forebrain ischemia in hypoglycemic, normoglycemic, and hyperglycemic rats. *Stroke, 27*(5), 957-964.

van der Maarel, J. (2003). Thermal relaxation and coherence dynamics of spin 3/2. I. Static and fluctuating quadrupolar interactions in the multipole basis. *Concepts in Magnetic Resonance Part A, 19A*(2), 97-116.

Van Der Veen, J., Slegt, S., Creyghton, J., Mehlkopf, A., & Bovee, W. (1993). Optimal pulse angles for the detection of sodium multiple-quantum coherences filtered by phase cycling and gradients. *Journal of Magnetic Resonance, 101,* 87-90.

Vander, A., Sherman, J., & Luciano, D. (2001). *Human physiology: The mechanisms of body function* (Eighth ed.). New York: McGraw-Hill.

Villringer, A., Rosen, B., Belliveau, J., Ackerman, J., Lauffer, R., Buxton, R., Chao, Y., Wedeen, V., & Brady, T. (1988). Dynamic imaging with Lanthanide chelates in normal brain - contrast due to magnetic susceptibility effects. *Magnetic Resonance in Medicine, 6*(2), 164-174.

Wang, Y., Hu, W. X., Perez-Trepichio, A., Ng, T., Furlan, A., Majors, A., & Jones, S. (2000). Brain tissue sodium is a ticking clock telling time after arterial occlusion in rat focal cerebral ischemia. *Stroke, 31*(6), 1386-1391.

Weinmann, H., Brasch, R., Press, W., & Wesbey, G. (1984). Characterisitics of gadolinium-DTPA complex - a potential NMR contrast agent. *American Journal of Roentgenology, 142*(3), 619-624.

Weisskoff, R., Zuo, C., Boxerman, J., & Rosen, B. (1994). Microscopic susceptibility variation and transverse relaxation - theory and experiment. *Magnetic Resonance in Medicine, 31*(6), 601-610.

Wimperis, S., Cole, P., & Styles, P. (1992). Triple-quantum-filtration NMR imaging of 200 mM sodium at 1.9 Tesla. *Journal of Magnetic Resonance, 98*(3), 628-636.

Wimperis, S., & Wood, B. (1991). Triple-quantum sodium imaging. *Journal of Magnetic Resonance, 95*(2), 428-436.

Winter, P., & Bansal, N. (2001a). TmDOTP5- as a Na-23 shift reagent for the subcutaneously implanted 9L gliosarcoma in rats. *Magnetic Resonance in Medicine, 45*(3), 436-442.

Winter, P., & Bansal, N. (2001b). Triple-quantum-filtered Na-23 NMR spectroscopy of subcutaneously implanted 9L gliosarcoma in the rat in the presence of TmDOTP5-. *Journal of Magnetic Resonance, 152*(1), 70-78.

Woessner, D. (2001). NMR relaxation of spin-3/2 nuclei: effects of structure, order, and dynamics in aqueous heterogeneous systems. *Concepts in Magnetic Resonance, 13*(5), 294-325.

Woessner, D., & Bansal, N. (1998). Temporal characteristics of NMR signals from spin 3/2 nuclei of incompletely disordered systems. *Journal of Magnetic Resonance, 133*(1), 21-35.

Wu, O., Ostergaard, L., & Sorensen, A. (2005). Technical aspects of perfusion-weighted imaging. *Neuroimaging Clinics of North America, 15*(3), 623-637.

Wu, O., Ostergaard, L., Weisskoff, R., Benner, T., Rosen, B., & Sorensen, A. (2003). Tracer arrival timing-insensitive technique for estimating flow in MR perfusion-weighted imaging using singular value decomposition with a block-circulant deconvolution matrix. *Magnetic Resonance in Medicine, 50*(1), 164-174.

Yoshita, M., Fletcher, E., & DeCarli, C. (2005). Current concepts of analysis of cerebral white matter hyperintensities on magnetic resonance imaging. *Topics in magnetic resonance imaging, 16*(6), 399-407.

Young, W., Rappaport, Z., Chalif, D., & Flamm, E. (1987). Regional brain sodium, potassium, and water changes in the rate middle cerebral artery occlusion model of ischemia. *Stroke, 18*(4), 751-759.

Yu, S. (2003). Na+, K+-ATPase: the new face of an old player in pathogenesis and apoptotic/hybrid cell death. *Biochemical Pharmacology, 66*(8), 1601-1609.

Yuh, W., Crain, M., Loes, D., Greene, G., Ryals, T., & Sato, Y. (1991). MR imaging of cerebral ischemia: findings in the first 24 hours. *American Journal of Neuroradiology, 12*(4), 621-629.

Yushmanov, V., Yanovski, B., Kharlamov, A., LaVerde, G., Boada, F., & Jones, S. (2009). Sodium Mapping in Focal Cerebral Ischemia in the Rat by Quantitative Na-23 MRI. *Journal of Magnetic Resonance Imaging, 29*(4), 962-966.

Zaaraoui, W., Konstandin, S., Audoin, B., Nagel, A., Rico, A., Malikova, I., Soulier, E., Viout, P., Confort-Gouny, S., Cozzone, P., Pelletier, J., Schad, L., & Ranjeva, J. (2012). Distribution of Brain Sodium Accumulation Correlates with Disability in Multiple Sclerosis: A Cross-sectional Na-23 MR Imaging Study. *Radiology, 264*(3), 859-867.